CFD Modelling of Bioprocesses: Integrating Mechanical Mixing, Aeration and Dynamic Rheology

by

María Constanza Sadino Riquelme

A thesis submitted in partial fulfillment of the requirements for the degree of

Doctor of Philosophy

in

CHEMICAL ENGINEERING

Department of Chemical and Materials Engineering
University of Alberta

ABSTRACT

Bioprocesses currently have a huge importance in worldwide sustainable development. However, the design of bioreactors based on experimental and empirical knowledge poses a challenge for the industrial biotechnology. Thus, CFD has gained attention as a design tool.

Although CFD modelling has previously been applied to study bioprocesses where mechanical mixing and aerations are key, the fact that the broth rheology changes over time has been mostly ignored. Additionally, many inaccurate practices have been used for the CFD models adaptation. In consequence, the obtained results have a limited scope and the level of confidence in such works is severely reduced at best.

The goal of this thesis is to adapt and validate a CFD model to predict the effect of the dynamic interaction between stirring, aeration and changing fluid rheology for bioreactors. The methodology consists of an experimental approach as well as a modelling approach. The microbial alginate production is selected as case study.

Experimentally, the bioprocess is reproduced in a stirred and aerated batch reactor. The process kinetics is characterized and the importance of reporting statistical data for an unbiased analysis of the parameters uncertainty and process reproducibility is shown. The density and rheological parameters of the broth are estimated at different stages of the fermentation, confirming that its rheology evolves from Newtonian to pseudoplastic.

Batch and continuous abiotic systems are implemented, using non-Newtonian and Newtonian fluids, to mimic the fluid dynamics of the fermentation at different stages. It is concluded that, under unaerated conditions, the impeller interaction decreases as the viscosity

increases; while, when aeration is included, the formation and breakaway of air cavities modifies the fluid dynamics. Additionally, it is proved that the probes affect the impeller torque. The similarity between the torque curves of the continuous systems and the fermentation supports the idea that their underlying mixing mechanisms are similar. Therefore, the CFD modelling of the batch abiotic systems would help to understand the evolving fluid dynamics of the microbial alginate batch production.

Regarding modelling accuracy, the CFD models are proved to be able to capture the effect of the probes on the fluid dynamics of the stirred tank. Therefore, these tank's internal elements should not be neglected. The simplification of the liquid level as a flat and fixed surface should not be applied either. The headspace should be implemented, especially for a process with aeration or when unaerated conditions can lead to a surface vortex. Regarding the numerical accuracy, the sliding mesh approach should be used instead of multiple reference frames. The SST k-omega, k-kl-omega and laminar models are shown to work for modelling a stirred tank with a flow in the turbulent, transitional and laminar regime, respectively. Thus, different single-phase CFD models are successfully validated for a stirred tank without aeration, to be able to simulate a changing fluid rheology as well as an evolving flow regime. When including the aeration, it is concluded that the mixture model is not able to predict the interface shape as well as the Eulerian model. However, only the mixture model shows to be numerically stable.

The CFD models are applied to study the evolution of the fermentation fluid flow patterns, velocity field, dead zones and vortical structures. Precessional vortices are identified as responsible for the unstable flow patterns identified at the earlier stages of the fermentation. A stable parallel flow pattern accounts for the higher mixing times and dead

zones at the final stage. Under the applied operating condition, the aeration affects the meso and macromixing mechanisms.

Overall, this work presents a standardized framework for the modelling of mixing tanks and contributes with a detailed analysis of the effect of a fermentation broth with a changing rheology on the fluid dynamics of a stirred bioprocess, under aerated and unaerated conditions.

PREFACE

The research conducted for this thesis forms part of an international research collaboration, led by A. Donoso-Bravo, Professor at the Universidad Técnica Federico Santa María (Chile) and researcher at Cetaqua (Chile), with Professor R.E. Hayes being the lead collaborator at the University of Alberta. The experimental methodology referred to in Chapters 2 and 3 was designed by myself, with the assistance of J. Rivas, Professor A. Donoso-Bravo, Professor D. Jeison and Professor R.E. Hayes. The computational methodology referred to in Chapters 4 to 7 was designed by myself, with the assistance of Professor A. Donoso-Bravo, Professor D. Jeison and Professor R.E. Hayes. The data analysis in Chapters 2 to 7 and concluding analysis in Chapter 8 are my original work, as well as the literature review in Chapter 1.

Some of Chapter 2 of this thesis has been published as M.C. Sadino-Riquelme, J. Rivas, D. Jeison, R.E. Hayes, and A. Donoso-Bravo, "Making Sense of Parameter Estimation and Model Simulation in Bioprocesses," Biotechnology and Bioengineering, vol. 117, issue 5, 1357-1366. I was responsible for the data collection and analysis as well as the manuscript composition. J. Rivas assisted with the data collection. Professor A. Donoso-Bravo, Professor D. Jeison and Professor R.E. Hayes contributed to manuscript edits and were involved with concept formation and manuscript composition. Professor R.E. Hayes was the supervisory author.

Some of Chapters 3 and 4 of this thesis have been published as M.C. Sadino-Riquelme, J. Rivas, D. Jeison, A. Donoso-Bravo, and R.E. Hayes, "Computational Modelling of Mixing Tanks for Bioprocesses: Developing a Comprehensive Workflow," The Canadian Journal of Chemical Engineering, in press. I was responsible for the data collection and analysis as well as the manuscript composition. J. Rivas assisted with the experimental data collection. Professor A. Donoso-Bravo, Professor D. Jeison and Professor R.E. Hayes contributed to manuscript edits and were involved with concept formation and manuscript composition. Professor R.E. Hayes was the supervisory author.

Con amor para mi mamá, María Gloria Riquelme Fuentes,
quien siempre me anima a aventurarme en la vida.

With love to my mom, María Gloria Riquelme Fuentes,
who always encourages me to adventure in life.

ACKNOWLEDGEMENTS

I would like to acknowledge Dr. Robert E. Hayes, Dr. Andrés Donoso-Bravo and Dr. David Jeison, for the opportunity of being part of their collaborative project. Their supervision, guidance, and support were key for the successful design and development of this research. Also, I would like to express my gratitude to José Rivas, who helped me with the experiments' implementation and data collection.

I wish to thank the professors Dr. Alexandra Komrakova, Dr. Natalia Semagina, Dr. Petr Nikrityuk and Dr. Carlos Lange for their advice towards the improvement of my research. Also, to the professors Dr. Joe Mmbaga and Dr. Anthony Yeung for trusting me as Teaching Assistant and Grader.

I will be eternally grateful to my family, my mom María Gloria Riquelme Fuentes and my brother Cristóbal Sadino Riquelme, for their love, support and patience. I love them with all my heart. I thank my cousins, aunts and uncles for all the welcoming and farewell gatherings, for their good wishes and prayers. Also, I would like to thank my friends Yanxi Hu and Begoña Urtubia, for a friendship that does not know of spatial nor temporal boundaries, and to Daniela Moraga, in whom I found the support and company of a sister.

Finally, I acknowledge ANID for granting me a Doctoral Scholarship (Becas Chile/72180040) and funding the execution of the experiments (FONDECYT/1180498). Additionally, I acknowledge the support provided by the Natural Sciences and Engineering Research Council of Canada and Compute Canada by granting the use of their clusters, and the support provided by the School of Biochemical Engineering of the Pontifical Catholic University of Valparaiso (Chile) by allowing the use of their laboratory installations.

TABLE OF CONTENTS

LIST OF TABLES

LIST OF FIGURES

NOMENCLATURE

a_1	constant [ ]
b	baffle width [m]
C_1, C_2, C_3	impeller spacing [m]
$C_{1\varepsilon}, C_{2\varepsilon}, C_\eta$	constant [ ]
$C_{\omega 1}, C_{\omega 2}, C_{\omega 3}, C_{\omega R}$	constant [ ]
c	nongrowth-related alginate formation parameter [g/(g·h)]
D_T, D_L	dissipation rate [m^2/s^3]
D	impeller diameter [m]
D_ω	cross-diffusion term [$kg/m^3 \cdot s^2$]
DF	degrees of freedom [ ]
DOT	dissolved oxygen tension [%]
E	validation comparison error [%]
$\vec{F}$	external body force [$kg/m^2 \cdot s^2$]
F_2	blending function [ ]
f	model output
f_o	vector with the derivative of f with respect to model parameters
f_ω, f_W	damping functions [ ]
$f_Z(t_i, \theta)$	predicted (model-based) value of Z at time t_i
G_k	generation of turbulence kinetic energy [$kg/m \cdot s^3$]
G_ω	generation of specific dissipation rate [$kg/m^3 \cdot s^2$]
$\vec{g}$	gravity acceleration [m/s^2]
H	liquid level [m]
H_0	null hypothesis statement

$\bar{\bar{I}}$	unit tensor [ ]
$\hat{\jmath}$	matrix derived from Jacobian matrix decomposition
K	consistency coefficient [Pa·s^n]
k	turbulence kinetic energy [m^2/s^2]
k_L	laminar kinetic energy [m^2/s^2]
k_s	proportionality constant [ ]
L	impeller blade length [m]
l	turbulence length scale [m]
M	size of data set [ ]
m	growth-related alginate formation parameter [g/g]
N	impeller rotation speed [s^{-1}]
N_P	power number [ ]
n	Power Law index [ ]
OD_{540}	optical density at 540 nm [ ]
P	alginate concentration [g/L]
P_k	production of turbulent kinetic energy [m^2/s^3]
P_{k_L}	production of laminar kinetic energy [m^2/s^3]
P_0	power consumption under unaerated conditions [W]
P_g	power consumption under aerated conditions [W]
p	static pressure [kg/m·s^2]
p_θ	number of parameters [ ]
Q	airflow rate [m^3/s]
R, R_{NAT}	energy transfer [m^2/s^3]
$\vec{R}_{ij}$	interaction force between phases [kg/m^2·s^2]
Re	Reynolds number for Newtonian fluid [ ]
Re^*	Reynolds number for non-Newtonian fluid [ ]

S	sucrose concentration [g/L]
S_R	strain rate magnitude [1/s]
s^2	estimate of the variance
T	tank diameter [m]
$T_{AVG_{exp}}$	time-averaged experimental torque [N·m]
$T_{AVG_{sim}}$	time-averaged simulated torque [N·m]
T_{emp,P_0}	empirically estimated torque value under unaerated conditions [N·m]
T_{emp,P_g}	empirically estimated torque value under aerated conditions [N·m]
$T_{SD_{exp}}$	standard deviation of $T_{AVG_{exp}}$ [N·m]
$T_{SD_{sim}}$	standard deviation of $T_{AVG_{sim}}$ [N·m]
T_{test}	test statistic [ ]
t	fermentation time (kinetic model) [h] fluid flow time (transport equations) [s]
$t_{M-p_\theta}^{\alpha_{test}/2}$	t-distribution value [ ]
Δt	time step [s]
U_{Exp}	experimental uncertainty [%]
U_{grid}	grid convergence uncertainty [%]
U_V	validation uncertainty [%]
$U_{\Delta t}$	time convergence uncertainty [%]
u	radial velocity [m/s]
$VM_{AVG_{sim}}$	time-averaged simulated velocity magnitude [m/s]
$VM_{SD_{sim}}$	standard deviation of $VM_{AVG_{sim}}$ [m/s]
V_{max}	maximum velocity magnitude [m/s]
V_{tip}	impeller tip velocity [m/s]
$\vec{v}$	fluid velocity vector [m/s]

v^*	friction velocity [m/s]
W	impeller blade width [m]
w_z	weighting function for variable Z in the least-squares equation
X	biomass concentration [g/L]
X_{max}	maximum attainable cell concentration [g/L]
x	spatial dimension [m]
Y_k	dissipation of turbulence kinetic energy [kg/m·s^3]
Y_ω	dissipation of specific dissipation rate [kg/m^3·s^2]
Y^+	non-dimensional distance [ ]
y	dimensional wall distance [m]
y_{Z_i}	experimental value of Z at time t_i
Z	denotes X, P or S
z	axial distance from the tank bottom [m]

Greek Letters

α	growth-related sucrose consumption parameter [g/g]
α^*	coefficient [ ]
α_T	turbulent diffusivity [m^2/s]
α_{test}	level of significance [ ]
β	nongrowth-related sucrose consumption parameter [g/(g·h)]
$\dot{\gamma}$	shear rate [s^{-1}]
ε	turbulence energy dissipation rate [m^2/s^3]
η	Newtonian fluid viscosity [mPa·s]
η_{ap}	non-Newtonian fluid apparent viscosity [mPa·s]
η_t	turbulent viscosity [kg/m·s]
θ	vector of kinetic model parameters

κ	bulk viscosity [kg/m·s]
λ_K	Kolmogorov length scale [m]
μ	specific cell growth rate [h^{-1}]
ρ	fluid density [kg/m^3]
σ_ε	turbulent Prandtl number for turbulence energy dissipation rate [ ]
σ_k	turbulent Prandtl number for turbulence kinetic energy [ ]
σ_ω	turbulent Prandtl number for specific dissipation rate [ ]
τ	shear stress [Pa]
$\bar{\bar{\tau}}$	stress tensor [Pa]
φ	volume fraction [ ]
ω	specific dissipation rate [1/s]
Ω	volume [m^3]

Abbreviations

A. vinelandii	*Azotobacter vinelandii*
ASR	activated sludge reactor
BC	boundary condition
CAD	Canadian dollar currency
CFD	computational fluid dynamics
CI	confidence intervals
CSTR	continuous stirred tank reactor
DOT	dissolved oxygen tension
EUR	Euro currency
GCI	grid convergence index
IC	initial condition
LES	large eddy simulation

MRF	multiple reference frames
Newt	Newtonian fluid
PI	prediction intervals
RANS	Reynolds-averaged Navier–Stokes
RSM	Reynolds stress model
SM	sliding mesh
SST	shear-stress
STR	stirred tank reactor

1 INTRODUCTION

1.1 Background and Motivation

A bioprocess is the culture of microorganisms that converts a carbon source and other organic and inorganic molecules into a value-added product. This transformation process typically occurs in large-scale bioreactors under controlled operating conditions.

At present, bioprocesses have a huge importance in the worldwide economy, especially in the area of sustainable development. Products such as biofuels, biopharmaceuticals and food ingredients, as well as services such as water treatment and waste management are in high demand. In Canada alone, bioproduct revenues increased from CAD$1.3 billion to CAD$4.3 billion between 2009 and 2015 (Natural Resources Canada, 2019). Moreover, it is expected that the global demand for bioproducts will increase over the next few years, as shown in Table 1.1. Nevertheless, the bioprocesses that supply these products or services are not optimal, especially when large-scale bioreactors are used, posing a big challenge for the industrial biotechnology (Mudde et al., 2017; Noorman & Heijnen, 2017).

Table 1.1. Bioproduct demand expected for 2035 (table adapted from Mudde et al., 2017).

Product	**Annual Production [million tons]**	**Annual Market Size [billion EUR]**
Bioethanol	250	125
Energy from biomass	6.400	300
Food ingredients	10	15
Bioplastics	40	80
Pharma products	0.2	280

The bioprocess kinetics depend on various factors, such as the characteristics of the microorganisms, the reactor configuration, the culture medium and the operating conditions.

The microorganisms are sensitive to the changes in their surroundings, so the onset of heterogeneities in the bioreactor affects their growth dynamics and activity, modifying the yield of the process and compromising its stability (Schügerl & Bellgardt, 2012).

As occurs with other processes, bioprocesses are initially designed and studied at lab-scale, and then scale-up criteria are applied to build the final industrial-scale reactor. Nevertheless, such criteria, originally developed for chemical reactors, do not incorporate constraints related to the microorganism maintenance. Therefore, the heterogeneous environment that arises in large-scale bioreactors causes the reduction of the bioprocess yield. The process at industrial scale may even become economically unfeasible (Kuschel et al., 2017; Mudde et al., 2017; Noorman & Heijnen, 2017).

1.1.1 Mixing a bioprocess: why it is different than mixing a chemical process?

The mixing processes in a stirred tank can be divided, according to the spatial scale at which they occur, into macromixing, mesomixing and micromixing. The macromixing occurs on the scale of the entire reactor and determines the environment for the mesomixing and micromixing (Baldyga & Pohorecki, 1995). The mesomixing arises on a smaller scale and corresponds to the spatial evolution of the fluid caused by the turbulent diffusion and the disintegration of large eddies into smaller eddies (Baldyga & Pohorecki, 1995; Baldyga et al., 1997). The micromixing happens on the smallest scale, which comprises the eddies smaller than the Kolmogorov length scale, due to the deformation of fluid elements (ex. blobs) and molecular diffusion (Baldyga & Pohorecki, 1995).

Chemical reactions are a molecular scale process. Therefore, in a stirred chemical reactor, the micromixing has a direct influence over them and is able to change the properties and quality of the overall chemical process (Baldyga & Pohorecki, 1995). When the chemical reactions are faster than the micromixing process, there are triggered concentration gradients that give rise to heterogeneities throughout the reactor (Baldyga & Bourne, 1984). This can be accompanied by temperature gradients, in which case the fluid density and viscosity could vary significantly across the tank and, therefore, give different micromixing rates in different zones (Baldyga et al., 1998). Although not directly, the mesomixing and macromixing also

affect the chemical reactions, as their interaction change the environment where the micromixing happens (Baldyga & Pohorecki, 1995).

In the case of bioprocesses, the biochemical reactions occur inside of microorganisms, which are the entities that experience the environmental changes (Delvigne et al., 2017). As the cells circulate inside the bioreactor, they are subjected to continuously changing conditions, such as significant gradients of substrate, pH and temperature (Lencastre Fernandes et al., 2011; Delafosse et al., 2015; Haringa et al., 2017). Even if the inoculated cells come from a pure culture with the same genetic information, the dynamic conditions will trigger a heterogeneity in the cell population which will decrease the performance of the bioprocess. In a bench-scale reactor, those changes could be negligible because the mixing is almost ideal, but that does not apply for larger scale reactors where the mixing is limited and the heterogeneities in the extracellular environment become significant (Lencastre Fernandes et al., 2011).

Furthermore, during a bioprocess, the cell culture is subjected to hydromechanical shear stresses due to the contact with the impellers (in case of mechanical agitation), the bubble movement and the turbulent flow in general. Depending on the cell culture shear-sensitivity threshold and the exposure time and frequency to those fluctuating stresses, the bioprocess performance could be negatively affected (Delafosse et al., 2015).

Hence, it is key to characterize the evolution of the mixing mechanisms over a bioprocess. However, the implementation of large-scale bioreactors with investigative purposes is a very time consuming and costly activity, not to mention that the experimental characterization of such a system is difficult. So, alternatives must be considered to study the large-scale bioprocesses, such as a Computational Fluid Dynamics (CFD) modelling approach.

1.1.2 CFD modelling

Computational Fluid Dynamics allows the numerical resolution of the governing equations of fluid flow, mass transfer and heat transfer by means of computer-based simulation (Versteeg & Malalasekera, 2007). This modelling approach is a promising tool to study, predict and optimize bioprocesses. As a computational method, CFD modelling allows the evaluation of

different scenarios to identify the most important variables and parameters in a bioprocess, without the expenses that an experimental procedure requires. Moreover, CFD can couple the biochemical reaction dynamics with the fluid dynamics to gain an integral representation of the bioprocess (Mudde et al., 2017; Noorman & Heijnen, 2017).

So far, CFD modelling has been applied to study several bioprocesses, performed in different bioreactor configurations, as summarized in Table 1.2. Particularly, it has been used to study various bioprocesses in mechanically stirred tanks, such as anaerobic digestion, biohydrogen production, cellulose hydrolysis, and animal cell culture.

1.2 CFD Modelling Applied to Stirred Bioprocesses

Although reliable simulations of the mixing process are computationally expensive, taking days for each simulation, CFD models have gained attention in the task of reactor characterization and design for processes where mechanical mixing and aerations are key. Using this computational approach, some issues that are relevant for bioprocesses have been addressed. Nevertheless, important features have been neglected or highly simplified in most of the researches, some as relevant as the culture medium rheology characterization. This is clearly reflected in Table 1.2, where it can be seen that many of the models have assumed that the culture medium behaves like water. Therefore, the knowledge about the studied issues has a limited scope, as the applied modelling assumptions do not match properly the real conditions of the system.

Additionally, many numerical assumptions and practices are used for geometry and grid construction, model configuration and analysis of results. Although many papers do address the validity of some of these assumptions, there are few if any examples where *all* of the essential criteria for a correct model are discussed. Thus, the level of confidence in such work is severely reduced at best.

Table 1.2. Summary of the reviewed bioprocess CFD models published until 2018 (CSTR: continuous stirred tank reactor; STR: stirred tank reactor; ASR: activated sludge reactor; Newt.: Newtonian fluid).

Article	Bioprocess as Motivation	Bioreactor Type	Mixed	Aerated	Broth Rheology
Gunyol and Mudde (2009)	None in particular	STR	Yes	No	Newt. (water)
Wang et al. (2010a)	Toluene waste gas treatment	Airlift reactor	No	Yes	Not specified
Wang et al. (2010b)	Biohydrogen production	Granular sludge bed	No	No	Mixed liquid
Delafosse et al. (2014)	None in particular	STR	Yes	No	Newt. (water)
Hong et al. (2014)	Yeast production	Gas-inducing reactor	Yes	No	Not specified
Delafosse et al. (2015)	None in particular	STR	Yes	No	Newt. (water)
Hou et al. (2016)	Lignocellulose pre-treatment	STR	Yes	No	Non-Newt. (several cases)
McClure et al. (2016)	Yeast fermentation	Bubble column	No	Yes	Not specified
Srirugsa et al. (2017)	Biohydrogen formation	CSTR	Yes	No	Newtonian
Kuschel et al. (2017)	Bacterial culture	STR	Yes	No	Not specified
Bach et al. (2017)	Cellulose synthesis	STR	Yes	No	Newt. (water), Non-Newt. (several cases)
Zhang et al. (2018)	Wastewater treatment	Anaerobic reactor	No	No	Not specified
Nalband and Jalilnejad (2018)	Naphthalene degradation	Airlift reactor	No	Yes	Newt. (water)
Climent et al. (2018)	Wastewater treatment	ASR	Yes	No	Non-Newt.
Kazemzadeh et al. (2018)	Animal cell culture	STR	Yes	Yes	Newt. (water)
Lu et al. (2018)	Mammalian cell culture	Shaking reactor	No	No	Newt. (water)
Rasouli et al. (2018)	Anaerobic digestion	Plug-flow reactor	Yes	No	Newt. (3 cases)
Sánchez et al. (2018)	Wastewater treatment	ASR	Yes	Yes	Not specified
Fan et al. (2018)	Aerobic granulation	STR	Yes	Yes	Newt. (water)

1.2.1 Mechanical mixing

The stirred tank reactor in batch mode is the configuration most used for industrial fermentations (Mudde et al., 2017; Shin et al., 2018). As a consequence, the bioreactors equipped with impellers have been widely studied using CFD models. The development of those models helps to get a better insight into the hydrodynamics of the system. For example, Srirugsa et al. (2017) compared the performance of two types of impellers at different speeds based on the flow patterns and the formation of dead zones. Similarly, Kazemzadeh et al. (2018) observed the effect of the impeller speed on the shear rate and the appearance of vortices inside the tank. Using another approach, Bach et al. (2017) performed a mixing time analysis based on tracer experiments for different impeller speeds. Lately, Haringa et al. (2018a; 2018b) modelled a multi-impeller tank to study the effects of the inter-compartment interaction on mixing time.

A few CFD studies have focussed on determining the turbulence model that fits best the flow characteristics of a bioreactor. Gunyol and Mudde (2009) and Zhang et al. (2018) concluded that the standard k-epsilon model gave good predictions for a mechanically stirred bioreactor, in comparison with other turbulence models for RANS equation closure (such as RNG k-epsilon, k-omega and RSM). However, Wu (2012) obtained results where LES performed better than the RANS based models. On the other hand, Haringa et al. (2018b) found a similar performance for LES and realizable k-epsilon models, both of which outperformed RSM. As was highlighted by Delvigne et al. (2017), using the standard k-epsilon or other RANS model allows us to know only the large scales of the flow fields, while the effect of the smaller eddies is put into the simulation via a modelling method, affecting the prediction of the mesomixing process. Additionally, k-epsilon models are not suitable for modelling the anisotropic turbulence that arises close to the impellers (Haringa et al., 2018a). Nevertheless, because of the smaller computational cost, many of the CFD models applied to bioprocesses use the standard or RNG k-epsilon turbulence model, even in the most recent publications (see, for example, Bach et al., 2017; Kuschel et al., 2017; Fan et al., 2018; Kazemzadeh et al., 2018; Lu et al., 2018; Nalband & Jalilnejad, 2018; Rasouli et al., 2018; Sánchez et al., 2018). It is important to mention that, for the k-epsilon models, the near-wall grid and the wall treatment selection are particularly important for the modelling of

the turbulent boundary layer (Ansys, 2009). However, these two factors are often not reported in detail or not mentioned, so it is unknown how they have been addressed (Gelves et al., 2014; Fan et al., 2018; Haringa et al., 2018a; Niño et al., 2018; Ebrahimi et al., 2019; Spann et al., 2019; Verma et al., 2019; Zhu et al., 2019; Chezeau et al., 2020).

Two modelling approaches could be used to simulate the impeller rotation, multiple reference frames (MRF) and sliding mesh (SM). Both methods require the separation of the rotating impeller zones from the rest of the tank. However, MRF uses a steady-state formulation, while SM uses a transient one. MRF simulates the agitation of the domain without moving the impellers, so only one relative position between the impellers and baffles is simulated and its interaction is approximated. On the contrary, the SM accounts for the transient effects that are caused by the actual rotation of the impellers (Ansys, 2009). Haringa et al. (2018a, 2018b), showed that SM can capture the flow macro-instabilities while MRF cannot. Thus, even when both methods may generate valid torque predictions, the fluid flow and mixing patterns will not be accurately predicted by MRF. When those variables are of interest, the SM approach must be used. Nevertheless, recent publications use the MRF approach (Bergamo et al., 2020; Chezeau et al., 2020; Cappello et al., 2021).

A common bioreactor design for turbulent mixing is a cylindrical baffled tank with one or more impellers. Probes (for measurements and/or sampling) and a gas sparger are often present. The computational domain is geometrically complex, which makes grid generation challenging, and the solution time-consuming. Complex grids can introduce spurious numerical artifacts. Therefore, domain simplification is common, which reduces the grid size and complexity. Some recent CFD stirred tank models have simplified the three-dimensional tank domain to an angular section, justifying this simplification for symmetry reasons (Shi & Rzehak, 2018; Liangchao et al., 2019; Spann et al., 2019). Probes in the fermenter have been eliminated from the domain in many cases (Noorman, 2011; Spann et al., 2019; Verma et al., 2019; Chezeau et al., 2020). Even the sparger in aerated tanks has been ignored (Noorman, 2011; Spann et al., 2019). These simplifications can significantly affect the flow field prediction.

The difficulties of implementing the domain grid often overshadow the importance of the time-step size in transient simulations. Some publications assessed the grid but not the

time step (Haringa et al., 2018a; Kazemzadeh et al., 2018; Jegatheeswaran et al., 2019; Russell et al., 2019; Jegatheeswaran & Ein-Mozaffari, 2020). Other articles used a heuristic based on the impeller speed to set the upper limit of the time-step size (Zhu et al., 2019). Albeit this can be a good starting point to select an initial time step, the time-step sensitivity should be studied.

Some researchers have stated that 20 to 30 impeller revolutions are necessary to reach the stationary state of a transient model (Ng et al., 1998; Micale et al., 1999). However, this number depends on the reactor configuration, operating conditions and fluid characteristics, so more revolutions may be needed (Jegatheeswaran et al., 2019). Therefore, the transient evolution of the relevant variables should be monitored, as recently done by Spann et al. (2019) and Verma et al. (2019).

1.2.2 Fluid rheology

In many fermentation processes, the culture medium behaves as a pseudoplastic non-Newtonian fluid due to the content and nature of microorganisms, and the presence of solids or polymeric substances. Some examples of such processes are fungi cultivation, wastewater treatment and production of extracellular biopolymers (Doran, 1995). In such cases, an accurate characterization of the rheology of the fluid is essential, because the estimation of the viscosity has a significant effect on the mixing rate, the mass transfer, the heat removal and the formation of caverns around the impeller (Noorman, 2011). However, most of the bioprocess CFD models developed so far considered the liquid medium as water (see Table 1.2), neglecting the influence that the substrate, products and/or microorganisms have on the rheology of the culture medium. Even substrates widely documented as non-Newtonian, such as sludge and manure, have been simplified as Newtonian fluids in CFD models of anaerobic digestion (Sadino-Riquelme et al., 2018).

Furthermore, when those bioprocesses are running in batch mode, the rheological properties of the culture medium change over time as the fermentation evolves. However, the rheological characteristics of the culture medium have been applied as a static property in the CFD models of stirred tanks. Only a few researches have taken into account the evolution of the parameters. Hou et al. (2016) dealt with a system with changing rheological properties,

by simulating separately different stages of the process of lignocellulose biomass degradation, to study its effect on the power consumption and mixing time. Similarly did Bach et al. (2017) to study the distribution of the volumetric mass transfer coefficient. Nonetheless, the former used the MRF approach to simulate the impeller rotation while the latter used SM but with only half tank as the domain.

Therefore, the fluid dynamics has not been accurately analyzed for stirred bioreactors mixing fluids with an evolving pseudoplastic behaviour.

1.2.3 Aeration

Many bioprocesses are aerobic, which means that they require a supply of oxygen. This gas is released as air bubbles from a sparger or a pipe placed inside the tank. Then, the bubbles transfer oxygen to the liquid medium as they move through the tank. Different factors affect the oxygen mass transfer process, such as the power input of the gas, the type and speed of the impeller and the viscosity of the culture medium (Mudde et al., 2017; Rosseburg et al., 2018). Some of these factors, and their consequences on a bioprocess, have been studied using CFD models. For example, Fan et al. (2018) and Kazemzadeh et al. (2018) studied how the impeller speed and the gas flow rate influenced the gas holdup and the bubble size distribution in a reactor for aerobic granulation and animal cell culture, respectively. In both cases, the liquid phase was modelled as water. However, the aerobic granulation is known to have a shear-thinning culture medium as a result of the grown of filamentous bacteria (Fan et al., 2018).

Recent studies have used CFD models to analyze the effect of the rheology on the gas holdup and air cavities formation of aerated stirred tanks (Jamshidzadeh et al., 2020; Cappello et al., 2021). However, further developments are needed regarding CFD modelling and the integration of the main factors that determine the evolution of the fluid dynamics of a stirred bioprocess: the mechanical mixing, the aeration and the changing fluid rheology.

1.3 Research Objectives

The aim of this research was **to adapt and validate a CFD model to predict the effect of the dynamic interaction between stirring, aeration and fluid rheology for bioreactors**.

As steps towards this aim, the objectives of this research were:

1. To characterize experimentally the kinetic and fluid dynamics of an aerated stirred bioprocess with changing rheology.
2. To develop a workflow for numerically and modelling accurate adaptation of CFD single-phase models for bioreactors with mechanical mixing.
3. To develop a workflow for numerically and modelling accurate adaptation of CFD multi-phase models for bioreactor with aeration and mechanical mixing.
4. To analyze the effect of the fluid rheology on the fluid dynamics of a stirred tank, without and with aeration.
5. To relate the effects of the interaction between stirring, aeration and fluid rheology on the development of a bioprocess.

1.4 Research Approach

To fulfill the objectives of the research, the microbial alginate production was selected as case study. Alginate is a polysaccharide that can be secreted by bacteria such as *Azotobacter vinelandii*. Due to its viscosity and gelling properties, alginate is used as a stabilizer and gelling agent in the food, beverage and pharmaceutical industries. It is estimated that the annual production of this compound is at least 30,000 tonnes (Hay et al., 2013). Nevertheless, the microbial production of this compound faces some difficulties because the culture medium becomes pseudoplastic and its apparent viscosity increases gradually as the alginate is secreted concentration increases inside the reactor. The process requires aeration, however, the oxygen mass transfer, as well as the mass transfer of other metabolites, is impaired by the highly viscous culture medium, adversely affecting the production of the biopolymer (Sabra & Zeng, 2009). For this reason, this process was selected to study the effect of the changing rheology on the fluid dynamics of an aerated and stirred bioprocess.

The microbial alginate production process was studied based on an experimental approach as well as a modelling approach. Experimentally, the fermentation was reproduced in a 4.0 L stirred batch reactor to characterize the kinetics and fluid dynamics of the bioprocess and the rheology of the culture medium. Additionally, abiotic systems mimicking the culture medium, at different stages of the fermentation, were implemented to further study the effect of the mechanical mixing, aeration and fluid rheology on the bioprocess fluid dynamics.

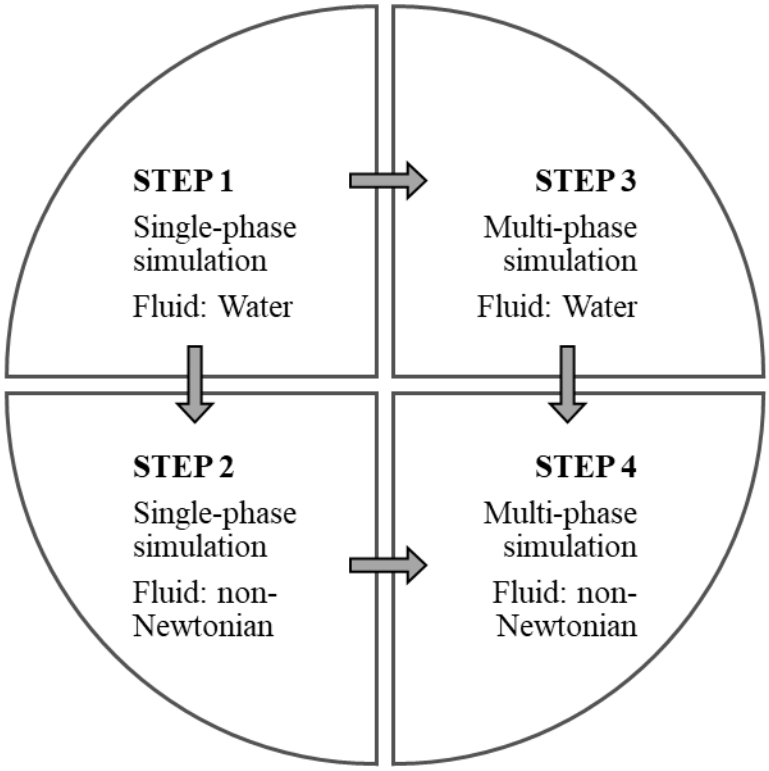

Figure 1.1. Step-by-step methodology applied to adapt the CFD models of the stirred tank.

The fluid dynamics of the alginate production was studied through the computational modelling of the abiotic systems. The adaptation of the CFD models was based on the use of industry standard commercial software, ANSYS FLUENT. To achieve the proposed objective, a step-by-step methodology was applied (see Figure 1.1). First, the single-phase model of the stirred tank mixing water was built. At this step, the domain of the 4.0 L lab-scale reactor, the grid and the numerical settings were extensively examined. In particular,

the effect of the probes on the system fluid dynamics was studied. Next, the CFD model was modified to simulate the mixing of non-Newtonian pseudoplastic fluids. Afterwards, a multi-phase model was adapted to simulate the stirred tank mixing water under aerated conditions. The domain, the grid and the numerical settings were again extensively examined to accomplish the new modelling needs. Finally, the CFD multi-phase model was modified to simulate the mixing of non-Newtonian pseudoplastic fluids. All the models were experimentally validated based on the impeller torque.

The experimental characterization of the fermentation and the results of the single-phase and multi-phase simulations were used to analyze the effect of the changing rheology on a stirred and aerated bioprocess.

The experiments were done in Chile, in the facilities of the Pontifical Catholic University of Valparaiso (*Pontificia Universidad Católica de Valparaíso*). The CFD simulations were run in the Compute Canada clusters, Graham and Cedar.

1.5 Research Scope

Although the scale of the studied fermenter is smaller than the typical industrial volumes, which vary between 10,000 and 200,000 L, the analysis presented in this work can be applied to the design of large-scale reactors by means of dimensionless and scale-down analyses. Furthermore, the experimental and modelling results aid in the understanding of the effect of the tank geometrical configuration and operating conditions on the fluid dynamics of a stirred tank, regardless of its size.

This work sets up some guidelines for more accurate CFD models of stirred tanks for bioprocess and contributes to a framework for standardized modelling, examining the workflow used to set up a model (from the domain implementation to the simulation completion criteria), to study the grid and time-step size (including the refinement criteria and the procedure followed for the simulations with the refined grids), and to conduct verification and validation of the model. The CFD models described in this work were set up using ANSYS Fluent, therefore the methodology contains some terminology particular to this software. However, the concerns addressed in this thesis are generally applicable to any software that uses the finite volume discretization method.

The use of CFD modelling as a tool to characterize the contribution of the mixing mechanisms over the fermentation stages, as the rheology changes, would contribute to designing optimal stage-specific solutions to improve the mass transfer and, therefore, the bioprocess yield. Thus, this work would be a significant contribution to bioprocess computational-based research and bioreactor engineering design.

1.6 Thesis Structure

The thesis is organized as follows. Chapters 2 and 3 are focused on the laboratory experiments and Chapters 4 to 6 are focused on the CFD models. In every chapter, the respective methodology and results are described and discussed. In particular, Chapter 2 addresses the microbial alginate batch fermentation. The mimicking abiotic systems are studied in Chapter 3. Chapter 4 addresses the first step of the CFD modelling process, that is, the single-phase model of the stirred tank mixing water. Chapter 5 reports the second step of the CFD modelling process, that is, the single-phase model of the stirred tank mixing non-Newtonian fluids. Chapter 6 and Chapter 7 deal, respectively, with the third and fourth step of the CFD modelling process, that is, the multi-phase models of the stirred tank. In Chapter 8, and final, are presented the overall conclusions of this work and recommendations for further research.

2 ALGINATE BATCH PRODUCTION[1]

The microbial alginate batch production was experimentally reproduced in a stirred tank. The kinetics, as well as the rheology of the bioprocess, were characterized over the fermentation process. The methodology, results and discussion are as follows.

2.1 Material and Methods

2.1.1 Stirred vessel configuration

The stirred reactor used in this study was a 5.0 L fermenter (BioFlo 3000, New Brunswick Scientific, USA) with a working volume of 4.0 L. The reactor was equipped with a dual Rushton turbine, four baffles, four probes and a sparger. A torsion angle-type torque meter (RWT 421-EE 100 Nm) was attached to the impeller shaft and connected to a computer to record the torque data. The reactor and its dimensions are shown in Figure 2.1. The position and dimensions of the probes and sparger are detailed in Appendix A.

2.1.2 Alginate fermentation

The bacterial alginate batch fermentation was studied in the described bioreactor. *Azotobacter vinelandii* (ATCC9046) strain was used. Three independent fermentations were performed, under the same conditions. The fermenter was inoculated with 400 ml of inoculum. The conditions of the inoculum preparation are described in Appendix B.

The reactor was stirred at 400 rpm and the aeration rate was 4 L/min (1 vvm). It is important to mention that the rotational speed was set up as high as possible to promote the homogenization of the culture medium and the dispersion of air throughout the tank, but not as high as to incur mechanical damage to the microorganisms by the shear stresses.

The pH was controlled at 7.2 (probe 405-DPAS-SC-K8S; Mettler Toledo, Malaysia) by the addition of NaOH (2 M) and the temperature was maintained at 30°C (thermometer

[1] Part of this chapter is published in Making Sense of Parameter Estimation and Model Simulation in Bioprocesses, Sadino-Riquelme, M. C., Rivas, J., Jeison, D., Hayes, R. E., & Donoso-Bravo, A., Biotechnology and Bioengineering, 117(5), Wiley Periodicals, Inc. © 2020, John Wiley and Sons.

provided with the fermenter) using a heat transfer jacket. The dissolved oxygen tension (DOT), measured by a polarographic oxygen probe (InPro 6800; Mettler Toledo), was not controlled. To reduce foaming, a silicone-based antifoaming agent (Loba Chemie, India) at a concentration of 30% (v/v) was used. The antifoaming agent was added manually, after the inoculation, as needed to prevent overflow of the foam over the course of the fermentation.

Samples of 30 ml were withdrawn, at different times, for analytical measurements of biomass, alginate and sucrose concentration, and to characterize the broth density and rheology. The biomass concentration was measured through the optical density at 540 nm (OD_{540}) in a spectrophotometer (Jenway 6715; Cole-Parmer, Canada), using a calibration plot of OD_{540} versus dry weight biomass concentration. The alginate concentration was determined gravimetrically, based on the methodology of Peña et al. (1997). The sucrose concentration was determined based on an assay for reducing power with dinitrosalicylic acid reagent, after acid hydrolysis (Miller, 1959). The OD_{540} of the resultant solution, suitable diluted, was measured in a spectrophotometer (Jenway 6715; Cole-Parmer, Canada). Methodological details and calibration curves are in Appendix C.

The density was estimated using the mass to volume ratio. The rheological characterization was done using a cone and plate viscometer (Brookfield DV-II+, UL spindle) with a temperature bath at 30°C. The spindle rotational speed was varied between 1 and 100 rpm, keeping a torque value between 10 and 99%. The Power-Law model parameters, consistency coefficient (K) and Power Law index (n), were fitted from the shear rate ($\dot{\gamma}$) versus shear stress (τ) curve, according to Equation 2.1. Detailed rheological data are given in Appendix D. Equation 2.2 was used to estimate the fluid apparent viscosity[2] (η_{ap}).

$$\tau = K\dot{\gamma}^n \tag{2.1}$$

$$\eta_{ap} = K\dot{\gamma}^{n-1} \tag{2.2}$$

The torque data were recorded over the whole fermentation. The torque measured for the impeller rotating in the empty tank (blank) was subtracted from the data to eliminate the shaft friction effect.

[2] Usually, the viscosity is represented by μ. However, in this work, μ represents the specific cell growth rate. Therefore, to avoid confusions, the viscosity and apparent viscosity are represented, respectively, by η and η_{ap}.

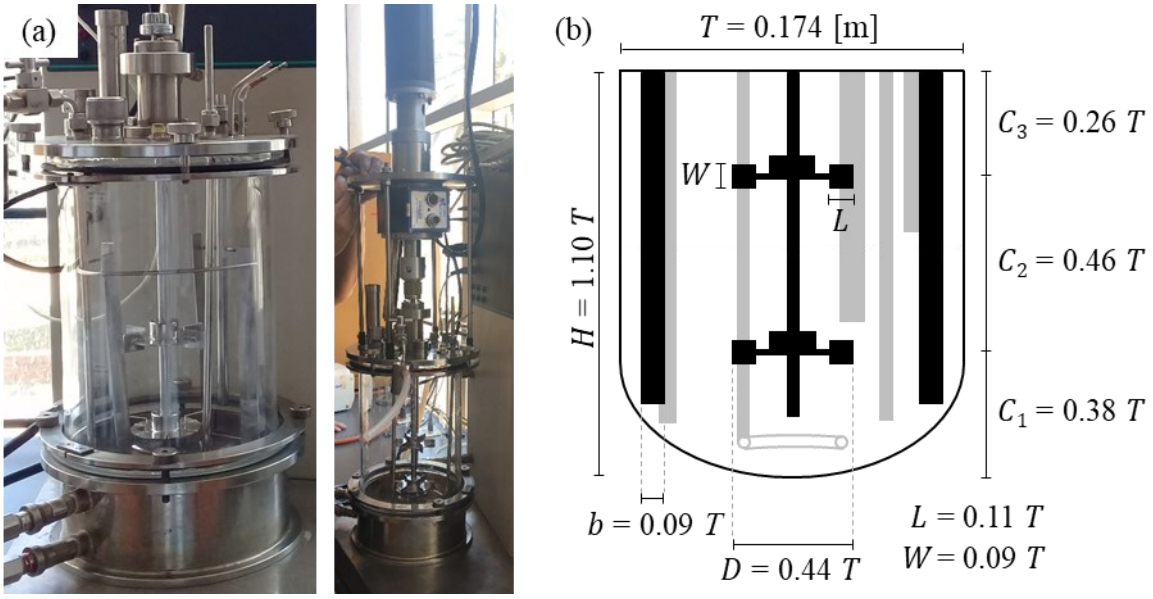

Figure 2.1. Tank used for the study. (a) Photos of the tank, (b) diagram of the tank dimensions. In (b), the baffles and impeller are shown in black, and the probes and sparger are shown in grey. Order of the elements in grey, from the left to the right side: sampling probe, sparger, pH probe, temperature probe and oxygen probe. Figure adapted from Sadino-Riquelme et al. (2020), reprinted with permission of John Wiley and Sons.

2.1.3 Kinetic model

The alginate fermentation with *A. vinelandii* was modelled using the mechanistic kinetic scheme proposed by Klimek and Ollis (1980). This model describes the biomass proliferation with the logistic rate equation, the product formation with the Luedeking-Piret model and the substrate consumption with a modified form of the Luedeking-Piret equation. The equations for the material balances for alginate production in a batch system are given by Equation 2.3-2.5 (Klimek & Ollis, 1980).

$$\frac{dX}{dt} = \mu X\left(1.0 - \frac{X}{X_{max}}\right) \tag{2.3}$$

$$\frac{dP}{dt} = cX + m\frac{dX}{dt} \tag{2.4}$$

$$\frac{dS}{dt} = -\alpha\frac{dX}{dt} - \beta X \tag{2.5}$$

where X, P and S are the biomass, alginate and sucrose concentration, respectively; t, the fermentation time; X_{max} and μ, parameters for the maximum attainable cell concentration and the specific cell growth rate, respectively; c and m, nongrowth and growth-related alginate formation parameters; and α and β, sucrose consumption parameters.

It is important to mention that the kinetic model does not account for product inhibition effects on the process.

2.1.4 Parameter fitting

The model representation and parameter estimation were carried out using Matlab®. The set of ordinary differential equations was solved using the toolbox ODE15s, which is a quasi-constant step size solver based on the numerical differentiation formulas proposed by Klopfenstein (Shampine & Reichelt, 1997). Two rounds of parameter estimation were executed. First, the whole set of six parameters was estimated. After that, based on hypothesis test results, one parameter was fixed and the other five were fitted. The parameter values were obtained by a nonlinear weighted non-robust regression technique, based on the Levenberg-Marquardt nonlinear least-squares algorithm, implemented in the *nlinfit* function. This function is designed for models with a single dependent variable and a single objective function. Therefore, the objective function was formulated in terms of the three dependent variables (X, P, S), using appropriate weighting functions to reduce any bias caused by the different magnitude of the variables, as shown in Equation 2.6. The weights (w_Z) were defined as described by Equation 2.7, where Z denotes X, P or S. This way, the multiple nonlinear regression problem is handled as a simple nonlinear regression problem.

$$\begin{aligned}\sum_{i=1}^{M} w_X\left[y_{X_i} - f_X(t_i,\theta)\right]^2 + \sum_{i=1}^{M} w_S\left[y_{S_i} - f_S(t_i,\theta)\right]^2 \\ + \sum_{i=1}^{M} w_P\left[y_{P_i} - f_P(t_i,\theta)\right]^2\end{aligned} \tag{2.6}$$

$$w_Z = \frac{1}{max(Z_i)} \tag{2.7}$$

The fitted parameters values are those that minimize the weighted least-squares equation shown in Equation 2.6, where θ is the vector of parameters, and y_{Z_i} and $f_Z(t_i, \theta)$ are, respectively, the experimental and estimated (using the kinetic model) value for the dependent variable Z at time t_i. M is the total number of experimental data points. Regarding the experimental data, the initial sugar concentration was set to 20 g/L in agreement with the fresh culture medium preparation protocol, while the initial concentration of alginate and biomass correspond to experimental measures values.

The parameters were computed for each of the batch culture data triplicates and for the average of all of them. As termination criterion for the iterative minimization process, a convergence tolerance of 10^{-8} was used for the relative change between two consecutive computed weighted least-squares values. It was verified that the termination criterion had been met in each case.

2.1.5 Confidence and prediction intervals

To quantify the model's uncertainty, it is advisable to provide a range that is statistically likely to contain the representative parameter within a certain level of confidence. For instance, if 95% confidence intervals (CI) are used, it means that if the experiment is run numerous times, the provided range will contain the mean value of the parameter in 95% of the cases (NIST/SEMATECH, 2003). For this study, the 95% CI of the parameters were calculated with the Matlab® function *nlparci,* using the following inputs: the estimated parameters, the residuals of the fitted model and the Jacobian matrix of the kinetic model, all of which were obtained previously as an output of the function *nlinfit*.

The ability of a mathematical model to predict the response of a process is affected by the propagation of the uncertainty of the estimated parameters. Thus, it would be more accurate to report a 95% CI of the model simulation along with single mean value for the predicted variable. These intervals are called prediction intervals (PI) to avoid confusion with the CI of the parameters. The 95% PI for the outputs of the kinetic model were calculated with the Matlab® function *nlpredci.* It requires the same inputs as the function *nlparci,* in addition to the regression model and the independent variable (time) for which is desired to predict the dependent variables (X, P, S). More information about these functions can be

found online in the documentation of MathWorks®. A description of the theory behind those functions is given in Appendix E.

The CI, as well as the parameters, were computed for each of the batch culture data triplicates and for their average. The PI were estimated only for the average of the experimental runs.

2.1.6 Hypothesis test

To check if the parameter values are statistically significantly different from zero, a two-tailed hypothesis test was performed. Thus, for each fitted parameter its p-value was calculated. The p-value represents the probability of obtaining the estimated value, subject to the null hypothesis $H_0: \theta_r = 0$, which states that the true value of the parameter θ_r is zero. So, when the p-value is under a certain level of significance, usually fixed at 0.05, the null hypothesis is rejected and the alternative hypothesis, which states that the parameter is different from zero, is accepted. Whenever the p-value is over the level of significance it means that the null hypothesis cannot be rejected. An analogous procedure can be used to check whether a parameter value is statistically different from a specific non-zero value. For this purpose, the Matlab® function *linhyptest* was used. This function requires the following inputs: the estimated parameters and its covariance matrix, both obtained as outputs of the function *nlinfit*; the value of the null hypothesis (zero or other specific value); and the degrees of freedom of the covariance matrix. This hypothesis test, as well as the CI and PI methodology, is based on the asymptotic theory of nonlinear least-squares estimation and assumes that the parameters estimates have an asymptotic normal distribution. More theoretical details can be referred to Seber and Wild (1989).

Furthermore, to compare the estimated values for each parameter, a two-sample t-Test for equal means (NIST/SEMATECH, 2003) was performed, which considers unpaired data and two samples with different variances and independent data. The p-value for this two-tailed test was calculated using the Matlab® function *tcdf*. This function computes the t-Student cumulative distribution function and uses two inputs: the value of the test statistic and its degrees of freedom, both estimated as explained in Appendix E.

2.2 Results and Discussions

2.2.1 Batch growth kinetics

The values of the dissolved oxygen tension and biomass, alginate and sucrose concentration are shown in Figure 2.2. Due to a technical problem, the DOT was monitored only for cultures #1 and #2. In both cases, the DOT decreased to zero and remained there during the cell growth phase. Díaz-Barrera et al. (2007) reported similar DOT evolution curves for batch cultures of *A. vinelandii* performed in a bioreactor with a working volume of 2.0 L stirred by dual Rushton turbines, without DOT control. However, in that study, the maximum DOT at the stationary phase was 80%, less than the value obtained in this research.

Over most of the growth phase, the biomass and alginate kinetics behaved the same for all of the triplicates. However, the cultures reached different maximum values for the alginate and biomass concentration at the stationary phase. While culture #2 reached the highest maximum cell concentration, culture #1 had the largest maximum alginate concentration. The maximum cell concentration varies less among the triplicates (25% variation relative to culture #2) than the maximum alginate concentration does (50% variation relative to culture #1). The error associated with the experimental measurement of alginate also contributes to the curve's deviation. Despite those differences, the sugar consumption kinetic is almost identical for the three fermentations. In each case, the alginate production seems to be mainly growth-associated, as slight or null increments were detected during the stationary phase. Similar kinetics were obtained by Peña et al. (2000), who produced alginate in batch cultures using a bioreactor with a working volume of 1.0 L and stirred by three Rushton turbines.

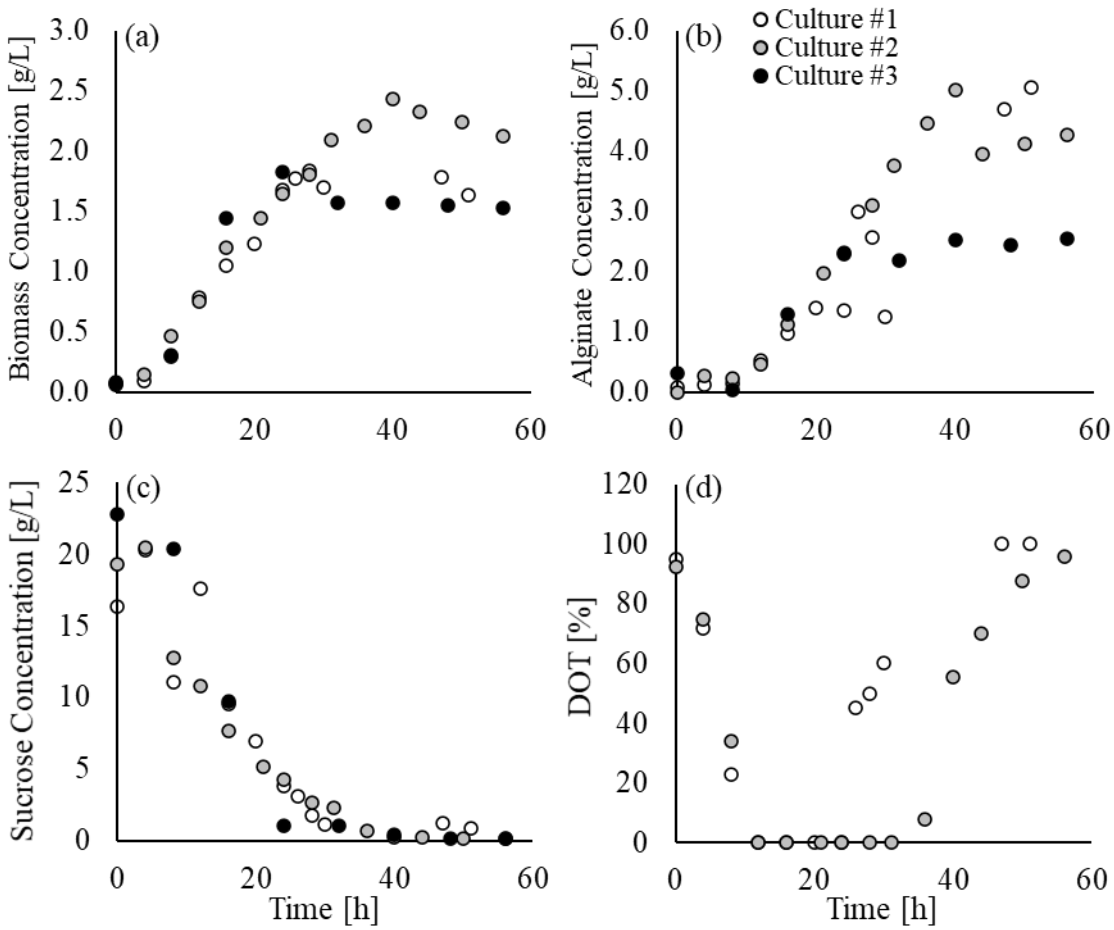

Figure 2.2. Kinetics of (a) biomass growth, (b) alginate production, (c) sucrose consumption and (d) DOT, during the batch culture conducted in a stirred fermenter. Data in triplicate: white, grey and black circles for culture #1, #2 and #3, respectively. Figure from Sadino-Riquelme et al. (2020), reprinted with permission of John Wiley and Sons.

2.2.2 Parameter fitting and confidence intervals

The model proposed by Klimek and Ollis (1980) was fitted for the experimental data of each triplicate and the average of them. First, the mean value of the six model parameters and their 95% CI were obtained (see Table 2.1). While μ is the parameter with less variation on its mean value (12% difference relative to the culture with the lowest mean), β is the one with the highest variation (8170% difference relative to the culture with the lowest mean), when comparing the results of the three cultures. Although these comparisons may give some hints

about the differences between the different runs of the fermentation, the uncertainty of the parameters should be assessed before analyzing the physical meaning of the results.

Table 2.1. Mean value and 95% confidence intervals of the kinetics parameters, when all the six parameters are fitted, for each culture and the averaged triplicates. The CI are expressed in the units of the parameter and as the percent difference of the half width of the interval relative to the corresponding mean value. Table from Sadino-Riquelme et al. (2020), reprinted with permission of John Wiley and Sons.

Parameter	**Culture #1**		**Culture #2**		**Culture #3**		**Averaged Triplicates**	
	Value	**95% CI**	**Value**	**95% CI**	**Value**	**95% CI**	**Value**	**95% CI**
$\mu\ [h^{-1}]$	0.263	[0.227, 0.299] 13.7%	0.244	[0.214, 0.274] 12.3%	0.273	[0.203, 0.342] 25.3%	0.219	[0.193, 0.245] 11.9%
$X_{max}\ [g/L]$	1.806	[1.623, 1.989] 10.1%	2.169	[1.993, 2.344] 8.1%	1.661	[1.466, 1.857] 11.8%	1.922	[1.779, 2.064] 7.4%
$c\ [g/(g \cdot h)]$	0.070	[0.047, 0.094] 34.3%	0.024	[0.006, 0.042] 75%	0.012	[-0.002, 0.026] 117%	0.033	[0.019, 0.048] 45.5%
$m\ [g/g]$	0.448	[-0.025, 0.921] 106%	1.366	[0.950, 1.781] 30.4%	0.943	[0.522, 1.365] 44.8%	0.927	[0.539, 1.314] 41.7%
$\alpha\ [g/g]$	10.52	[8.302, 12.73] 21%	9.667	[7.78, 11.56] 19.6%	2.384	[-6.593, 11.36] 377%	10.17	[8.308, 12.02] 18.2%
$\beta\ [g/(g \cdot h)]$	0.014	[-0.089, 0.118] 743%	-0.010	[-0.088, 0.068] 780%	0.807	[-0.001, 1.615] 100%	0.012	[-0.056, 0.080] 567%

A desirable feature for the results of a model fitting is to obtain narrow CI, which implies a low level of uncertainty for the mean value of the parameter. For that, the percent difference of the half width of the interval with respect to the mean value of the parameter should be small. The size of an acceptable CI may be an arbitrary decision, which also depends on the process, as its variability and the error of the measurement techniques vary from case to case. This is especially true for biological processes, where variability is an intrinsic characteristic. In any event, a value of less than 50% could be considered a

reasonable difference, and less than 30% would be, according to our experience and criteria, ideal. Considering that, the CI obtained for μ and X_{max} are highly satisfactory for all the triplicates and for their average; while c, m and α present unsatisfactory results for one or two of the cultures, but still acceptable results for the averaged triplicates. However, β, which has the largest CI in comparison with all the parameters, has an unacceptable relative size in all the cases. Furthermore, its CI contains the zero in all the cases, raising the question as to whether this parameter is likely to be equal to zero. Thus, the hypothesis test was performed for each parameter to check the null hypothesis H_0: $\theta_r = 0$. Is important to recall that the possible outputs of a hypothesis test are to reject (p-value < 0.05) or not to reject (p-value > 0.05) the null hypothesis, but never to accept the null hypothesis. In other words, if the null hypothesis is not rejected, it means that the test output is inconclusive about the real value of the parameter. Thus, the results show that β cannot be rejected as equal to zero, as the p-value > 0.05 for each culture as well as for the average of all of them (see Table 2.2). For the other parameters, the null hypothesis was rejected based on the criterion that the p-value < 0.05 for the averaged triplicates and, at least, for two of the triplicates (as individual cases). Particularly, c was proved to be different from zero, which means that alginate is only partially growth-associated, which was not an obvious conclusion since the tendency of the experimental data showed otherwise.

According to the hypothesis test, there is not enough statistical evidence to affirm that β is different from zero (the test output was inconclusive). Therefore, to take the decision whether to fix this parameter value to zero, biological as well as mathematical arguments must be considered. From the biological perspective, recall the physical meaning of the parameter: β represents the rate of sucrose consumption for the bacteria's maintenance activities. So, its value cannot be null, but the term associated with it can be assumed to be negligible in comparison with the consumption of substrate for the biomass growth. On the other hand, from a mathematical point of view, a parameter with a large CI affects the model reliability. For a given data set, it is generally accepted that minimizing the number of parameters leads to an improved quality of parameter estimation. Thus, it was decided to study how fixing β as 0 g/(g·h) would affect the kinetic parameters fitting.

Table 2.2. Hypothesis test results (p-value) performed over the parameters individually, when the six parameters are fitted. Null hypothesis: H_0: $\theta_r = 0$. The * indicates p-value over the level of significance 0.05. Table from Sadino-Riquelme et al. (2020), reprinted with permission of John Wiley and Sons.

Parameter	**Culture #1**	**Culture #2**	**Culture #3**	**Averaged Triplicates**
μ	1.1e-14	1.7e-17	5.2e-07	4.4e-24
X_{max}	7.2e-18	4.2e-23	1.3e-11	3.4e-34
c	1.5e-06	0.0089	0.0904*	2.9e-05
m	0.065*	1.3e-07	2.5e-04	1.2e-05
α	2.5e-10	5.8e-12	0.5798*	1.2e-05
β	0.7783*	0.7904*	0.0503*	0.7327*

Figure 2.3 compares the mean values and 95% CI for the parameters of the kinetic model, obtained in both cases, without fixing β and fixing its value as 0 g/(g·h). As can be seen, for the cases of X_{max}, c and m, for each culture triplicate as well as for the average of all of them, the mean value and CI did not change significantly. While, for the parameters μ and α, fixing β as zero allowed us to narrow the CI, especially those wider related to culture #3, reducing the uncertainty of the model. Therefore, from this point and on, β was set to 0 g/(g·h) and only the subset of parameters μ, X_{max}, c, m and α was considered for the model fitting and uncertainty propagation.

As a side comment, it must be said that the lack of impact when changing the value of β and its large 95% CI are indicators that it could be a parameter of low sensitivity, which means that a large change in its value will affect slightly or not at all the model outputs. Although sensitivity analysis is beyond the scope of the present study, others are encouraged to perform this kind of analysis, especially when a new kinetic model is proposed.

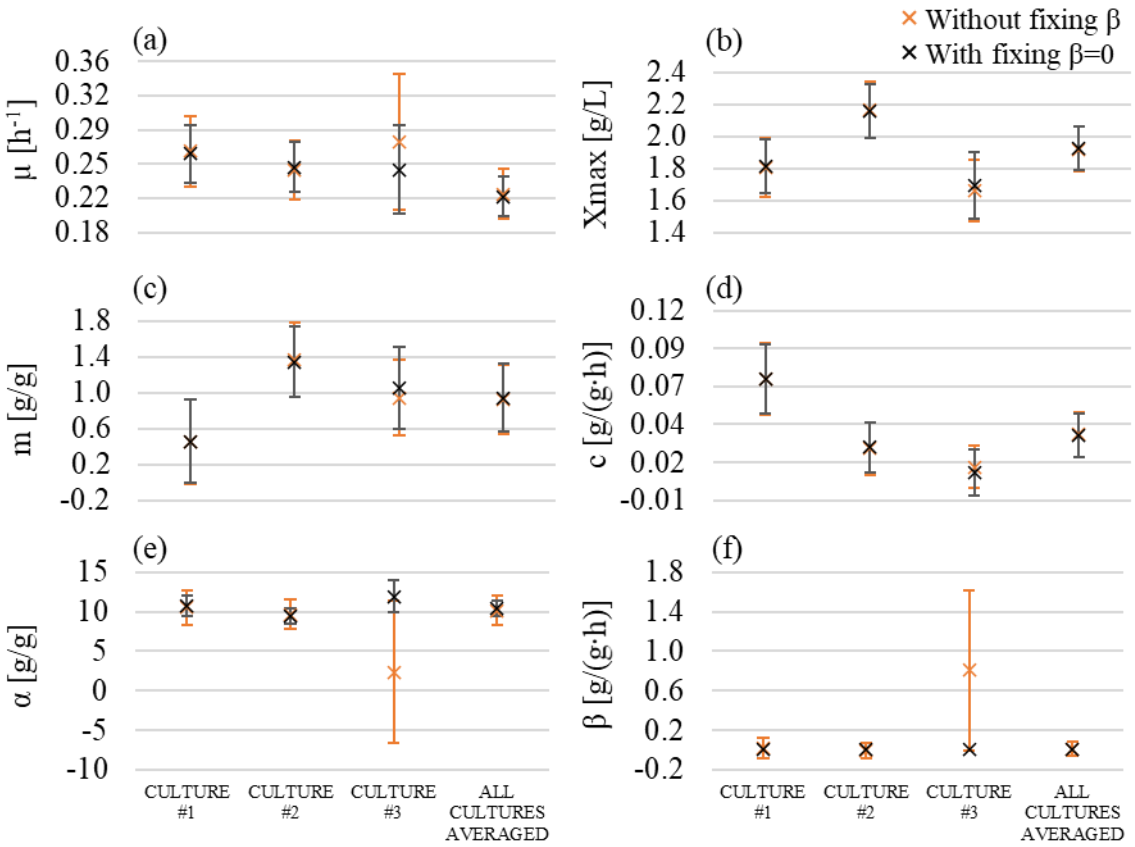

Figure 2.3. Comparison of 95% confidence intervals, without fixing β (orange marker) and fixing β=0 g/(g·h) (black marker), for the kinetic parameters associated to: (a) specific growth rate, (b) maximum cell concentration, (c) growth and (d) nongrowth-related polymer formation, and (e) growth and (f) nongrowth-related substrate consumption. Figure from Sadino-Riquelme et al. (2020), reprinted with permission of John Wiley and Sons.

Now that the uncertainty in the parameters has been analyzed and improved, an evaluation of whether the parameters between cultures are significantly different from a statistical point of view is carried out. Usually, the conclusion that two parameters are not significantly different is based on overlapped CI (visual inspection). However, that approach is not completely correct. Although not overlapping CI are related to significantly different parameter means, the opposite is not always true, as the visual inspection methodology is more conservative than a hypothesis test (Nicholls, 2016; Cumming et al., 2007). Therefore, the two-sample t-Test for equal means was performed. The *p*-value was obtained for each

parameter, comparing its mean value for culture #1 vs culture #2, culture #1 vs culture #3 and culture #1 vs culture #3, respectively (see Table 2.3). Based on this test, it is not possible to discard that the mean value of μ is the same for all the triplicates. Similarly occurs for α when the cultures #2 and #3 are compared with culture #1. On the other hand, it can be concluded that the maximum cell concentration (X_{max}) of the cultures #1 and #3 are significantly different from culture #2, which is about 30% higher. For the parameters m and c, the results indicate that the alginate production may not be statistically different between cultures #2 and #3 but is significantly different between cultures #1 and #2.

Table 2.3. Two-sample t-Test for equal means results (p-value), when β =0 g/(g·h) and only five parameters are fitted. The * indicates p-value over the level of significance 0.05. Table from Sadino-Riquelme et al. (2020), reprinted with permission of John Wiley and Sons.

Parameter	**Cultures #1 vs #2**	**Cultures #1 vs #3**	**Cultures #2 vs #3**
μ	0.4776*	0.5352*	0.9232*
X_{max}	0.0043	0.3598*	0.0007
c	0.0020	0.00003	0.1399*
m	0.0040	0.0612*	0.3172*
α	0.0991*	0.3026*	0.0249

Regarding the parameters fitted using the averaged triplicates, they cannot be compared with each culture using the two-sample t-Test for equal means, because this hypothesis test only can be used to compare mean values obtained from independent data, and the average cannot be considered independent from the elements that were averaged. However, it is interesting to note that the 95% CI obtained from the averaged triplicated are narrower than those obtained with each triplicate, improving the quality of the estimation for all the parameters. This is consistent with the fact that averaging multiple repetitions of an experiment helps to diminish the impact of the experimental errors and the process

variability. Thus, the estimation of parameters based on multiple independent repetitions of a fermentation is encouraged.

As mentioned in the motivation, process reproducibility could be based on the obtention of similar parameters between different runs. As there are several parameters in a model, it is considered that this should be based on the more relevant parameters for the process goals. In this case, that would be the parameters related with the biomass growth (μ) and most of the alginate production (m). c is not considered in this analysis, as the alginate produced during the stationary phase is negligible in comparison with the one accumulated during the growth phase. As shown in Table 2.3, μ is not significantly different between the cultures, and m is significantly different only between the cultures #1 and #2, however, Figure 2.2 shows that both cultures reached similar maximum alginate concentration. So far, that tells us that this process is highly reproducible, however, more independent runs, for different operating conditions should be tested to confirm such hypothesis.

2.2.3 Prediction intervals

As the parameters are more likely to be any value in the 95% CI instead of the exact mean value estimated through least square regression, the question arises of how that uncertainty is propagated into the model outputs. Therefore, the 95% PI were estimated for the outputs of the model, for the averaged triplicates, setting the parameter β=0 g/(g·h) (see Figure 2.4). From the graphs, it is observed that 53% of the total averaged experimental data lie between the intervals. Specifically, 45% of the biomass data, 32% of the alginate and 82% of the sucrose data are within their respective prediction intervals. Furthermore, the data points which fall outside of the prediction are close to the intervals and follow its trend. All these indicate that the kinetic model can not only predict the tendency of the kinetic of the fermentation, but also it can estimate with considerable certainty the dynamics of the concentration of its components, at least in a lab-scale well mixed reactor.

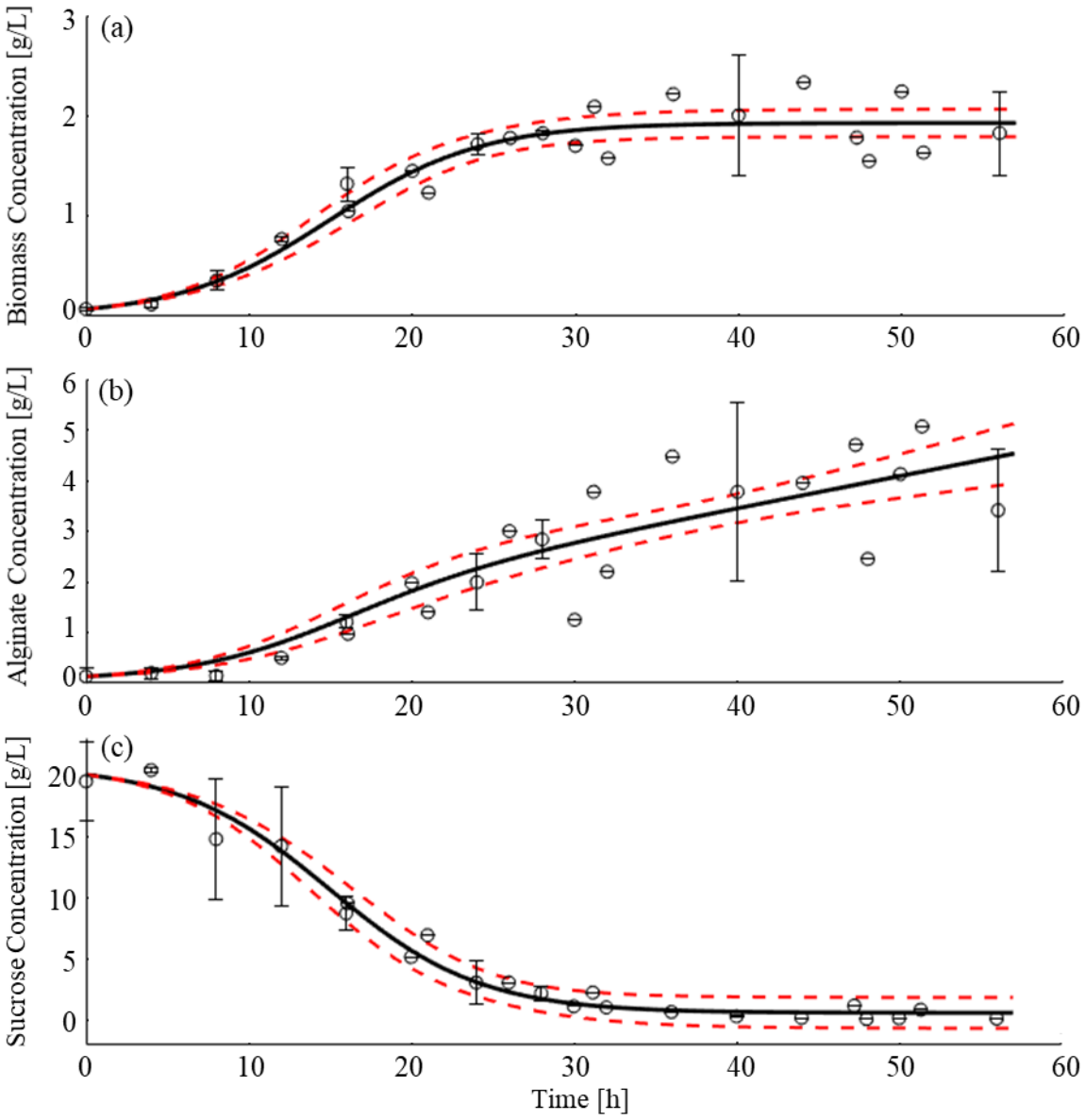

Figure 2.4. 95% prediction intervals for the concentration of biomass (a), alginate (b) and sucrose (c), using the average of the experimental data and setting β=0 g/(g·h). The solid and dashed lines correspond to the mean value and the 95% prediction interval, respectively. The circles and the error bars represent the averaged experimental data and its standard deviation. Figure from Sadino-Riquelme et al. (2020), reprinted with permission of John Wiley and Sons.

It is important to remark that, in this study, the approach used to fit the parameters and estimate CI and PI does not account for all the possible sources of uncertainty. Only the uncertainty of the model and its parameters were considered. Other sources may have an important effect on the model application. As is well known, every experimental data set possess some level of uncertainty related to sampling procedure, measuring methodology and measuring instrument. Although it is possible to add such uncertainty into the least square regression methodology for the parameters estimation and propagate it into the model outputs (Anane et al., 2019), to estimate the measurements uncertainty is per se a difficult task. For example, in the sampling procedure during *A. vinelandii* fermentation, the higher viscosity of the culture medium may hinder the homogenization of the tank, hampering the take of a representative sample, even more towards the end of the process when the alginate concentration is higher. In any case, the impact of data uncertainty is considered through the addition of standard deviation intervals to the experimental data, which accounts together for the measurement errors as well as the intrinsic variability of the process. But it is important to keep in mind that including that uncertainty into the model may result in larger CI and PI to keep the same confidence level on the inferences.

2.2.4 Perspective of application of statistical analysis

As mentioned earlier, some researchers have reported kinetic parameters for the model proposed by Klimek and Ollis (1980), fitted from experimental data of alginate production in batch cultures of *A. vinelandii*. Mainly, the specific growth rate of *A. vinelandii* has been reported (see Table 2.4). However, in general, it is not specified whether the parameters were estimated using a regression methodology or an alternative method, such as the one proposed by Klimek and Ollis (1980) based on a mix of visual and plot intersection estimations. That information is important and should be rigorously described in the articles when reporting fitted parameters for bioprocess kinetic models.

Just for illustrative purposes, the reported values from literature are compared. Based on the results reported by Peña et al. (2008) and Peña et al. (2011), using the two-sample t-Test for equal means, it is possible to conclude that the growth kinetic is not significantly different (p-value=0.37) between the studied experimental systems, shake flask and stirred

tank, at some defined operating conditions. Therefore, it can be affirmed that it is possible to obtain similar growth kinetics on systems with different scales and mixing approaches. This result added to more similar analysis may help to build an unbiased and strong background for scale-up design in bioprocesses.

Table 2.4. Data reported in the literature for the mean value of the specific growth rate, in units of [h^{-1}]. Standard deviations intervals are given if reported in the original article. Table from Sadino-Riquelme et al. (2020), reprinted with permission of John Wiley and Sons.

System	**Peña et al. (2000)**	**Reyes et al. (2003)**	**Peña et al. (2007)**	**Peña et al. (2008)**	**Peña et al. (2011)**
Shake flask		0.090 ± 0.002	0.09		0.11 ± 0.009
Stirred tank	0.07			0.13 ± 0.02	
	0.11	0.160 ± 0.009			
	0.14	0.123 ± 0.005			
	0.20	0.113 ± 0.004			
	0.20	0.093 ± 0.003			
	0.23				

On the other hand, even when Peña et al. (2007) and Peña et al. (2011) reported data for the same kind of system, it is not possible to conclude if the growth rates are significantly different or not, because one standard deviation was not reported. Similarly, it also occurs if the result of Peña et al. (2000) is compared with the present study (μ=0.216 h^{-1}, using the averaged triplicates). In those cases, the *linhyptest* function could be used to analyze if the mean value obtained for a parameter is significantly different from a specific value. However, this result is not as strong as the one that could be obtained using the two-sample t-Test for equal means, if both results were reported with standard deviations, as this method considers the uncertainty of both estimated parameters.

2.2.5 Physical and rheological characterization

The rheological characterization of the fermentation samples confirms the non-Newtonian pseudoplastic behaviour of the culture medium, because the power-law index decreases below 1 as the alginate concentration increases (see Figure 2.5a). Exceptions were found at alginate concentrations below 1 g/L when the culture medium behaves as a Newtonian fluid with a viscosity similar to water. On the other hand, the consistency coefficient shows a trend to increase with the alginate concentration, but with very dispersed values (see Figure 2.5b). The density also shows scattered values but within a narrow range between 1,000 and 1,040 kg/m^3 (see Figure 2.5c).

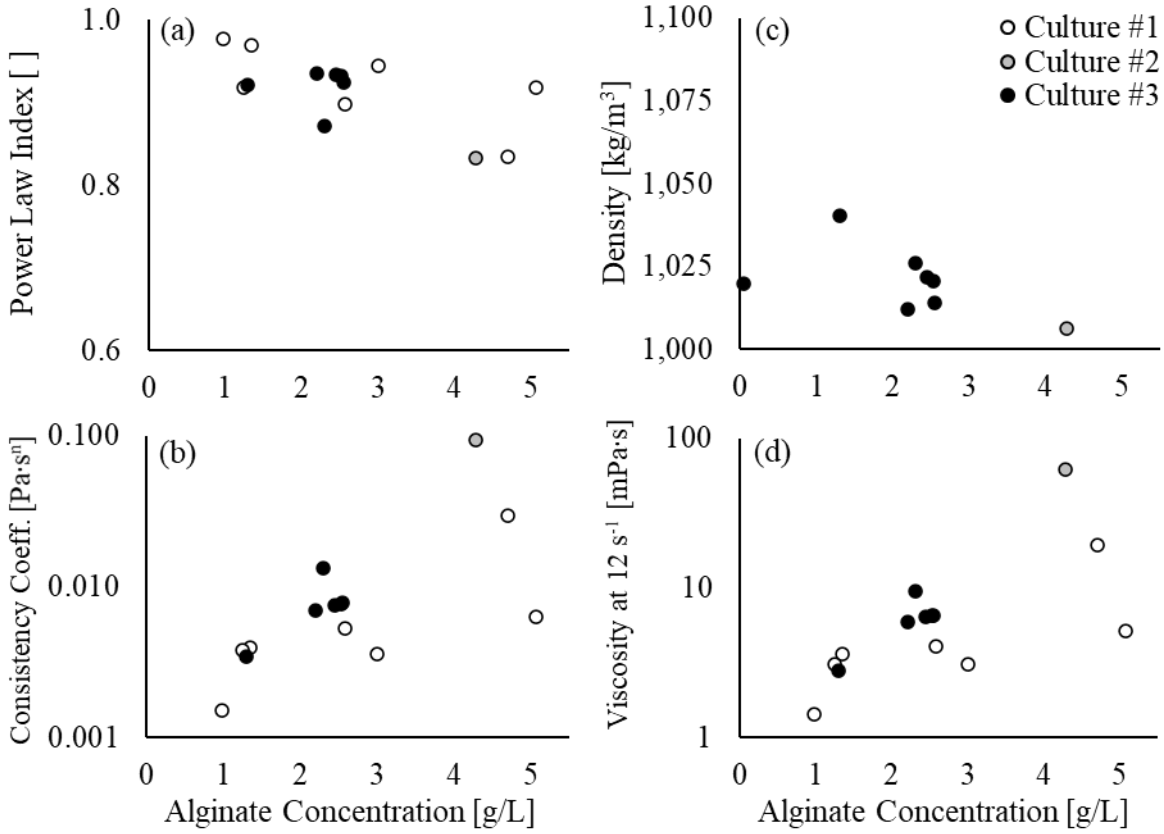

Figure 2.5. Evolution of the rheological parameters and density during the microbial alginate batch production, (a) power-law index, (b) consistency coefficient, (c) density and (d) viscosity at 12 s^{-1}, as a function of alginate concentration. Data in white, grey and black circles for culture #1, #2 and #3, respectively.

The highest viscosity of the culture medium was associated to an alginate concentration around 4.5 g/L and varied between 19 and 62 mPa·s (at a shear rate of 12 s^{-1}) among the cultures (see Figure 2.5d). This is in good agreement with Peña et al. (2000) that reported viscosities between 20 and 420 mPa·s (at 12 s^{-1}), for 4 g/L of alginate in a 1.0 L system stirred at 300 rpm by three Rushton turbines under different controlled DOT values.

It is important to mention that the sampling from the cultures became more difficult as the alginate concentration increased, because the mixing close to the sampler probe becomes poorer, and, therefore, the sample may not represent adequately other parts of the system. Furthermore, despite the existence of a pH control unit, the pH of the culture medium increased during the fermentations. This may also be due to the mixing problems triggered by the high viscosity of alginate. All these may cause variations in the process itself as well. Indeed, the characteristics of the alginate aggregates varied during the process. This was observed after the precipitation and resuspension of alginate from the broth samples. For culture #1, the alginate aggregate of the samples at time 30 and 51 h had a disaggregated and compact look, respectively (see Figure 2.6). This variation may respond to a different molecular composition of the alginate that can affect its intrinsic viscosity and gelling property (Clementi, 1997). A compact aspect was observed for most of the resuspended alginate aggregates of culture #2 (see Appendix F).

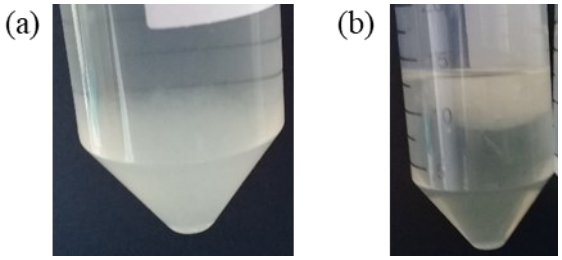

Figure 2.6. Alginate aggregates re-suspended from samples of the culture #1 taken after (a) 30 h and (b) 51 h since the inoculation.

Also, it is important to mention that the samples for rheological characterization from culture #1 were frozen because the viscometer was not available while developing the fermentation. Later, a small comparative analysis showed up that the freezing-defrosting

process could affect the rheology of the fluid. Therefore, the samples for the rheological characterization of cultures #2 and #3 were not frozen but analyzed immediately after the sampling.

2.2.6 Torque characterization

Due to the fermentation broth opacity (see Appendix G), the shaft torque measurement was the most suitable technique that could be used to monitor the fluid dynamics inside the bioreactor, during the microbial alginate production. Unfortunately, the torque measurements registered during culture #1, had to be discarded due to a technical problem. The torque showed similar behaviour for cultures #2 and #3 as the curves are separated by an (almost) constant gap, except at around the minute 30 (see Figure 2.7). That bigger gap was caused by an earthquake that occurred during the culture #3.

Both torque curves, in Figure 2.7, show significant small oscillations, as part of bigger oscillations. This could be explained by the interaction of different factors, such as mechanical mixing, aeration and rheological changes. However, due to the complexity of the system, it is difficult to identify how each of these factors contributes to the bioreactor fluid dynamics and, therefore, to its torque curve. Therefore, it was necessary to study abiotic systems to be able to isolate the effect of those factors at different stages of the fermentation process.

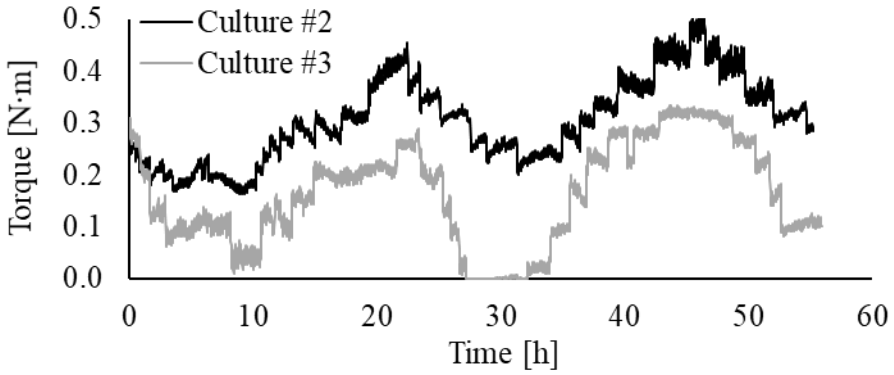

Figure 2.7. Impeller torque evolution during the microbial alginate batch production. Data in black and grey line for culture #2 and #3, respectively.

2.2.7 Foam

During the fermentation, although droplets of an antifoam agent were added to the culture medium, a layer of foam could be found on the liquid surface from the very beginning of the process (see Appendix G). The stability of the foam layer may be attributed to the alginate itself because polysaccharides are considered foam-stabilising agents (Doran, 1995).

The presence of foam, as well as the addition of antifoam agent, could have affected the fermentation kinetics. Cells can be trapped in the foam layer leading to cell damage and death, reducing the biomass (Doran, 1995; Paul et al., 2003). Also, the thick foam layer could hinder the mass transfer of acid/base, fed from the lid of the tank for the pH control, delaying its entrance to the culture medium, a similar effect is discussed for the entrance of tracer through a layer of foam in Section 3.2.3. However, the use of antifoam, to avoid the previous issues, has its own drawbacks. It has been reported that the antifoams could increase the coalescence fluid properties and reduce the volumetric mass transfer coefficient of oxygen, affecting both the mass transfer coefficient and the interfacial area (Doran, 1995).

It is important to mention that the addition of antifoam did not affect the volume of the culture medium significantly as only a few drops were added as needed to prevent overflow of the foam.

3 EXPERIMENTAL ABIOTIC SYSTEMS[3]

Based on the rheological characterization of the culture medium, five abiotic systems were chosen to mimic the fluid dynamics at different stages of the fermentation. Thus, the effect of the mechanical mixing and aeration on the fluid dynamics was studied and how this effect depends on the fluid rheology. The methodology, results and discussion are as follows.

3.1 Material and Methods

3.1.1 Fluids

Three fluids were chosen to mimic the fluid dynamics of the fermentation broth at the beginning, intermediate and final stages of the alginate production. Distilled water was selected due to its similarity with the culture medium at time 0 h. To mimic the pseudoplastic behaviour that develops in the culture medium when the alginate concentration increases, two solutions were chosen, named Xanthan Sol A and Xanthan Sol B, which were prepared with distilled water and xanthan gum at a concentration of 0.75 and 0.25 mg/mL, respectively. Xanthan Sol A was selected because its viscosity moves between 20 and 100 mPa·s at low shear rates, as expected for the final stage of the fermentation. Under a same shear rate, Xanthan Sol B has a lower viscosity than Xanthan Sol A, so Xanthan Sol B was used to represent an intermediate stage of the process. Specifically, at a shear rate of 12 s^{-1}, the viscosity of Xanthan Sol A and Xanthan Sol B was 33 and 8 mPa·s, respectively.

To study separately the effect of the viscosity and the pseudoplastic non-Newtonian behaviour of the fluid, two additional Newtonian fluids were studied, PEG Sol A and PEG Sol B. PEG Sol A and PEG Sol B were prepared, respectively, with Polyethylene glycol 300 ROTIPURAN® Ph.Eur. (Carl Roth, Germany) without dilution and diluted 2-fold in distilled water. The rheological and physical properties of the fluids used for the batch abiotic systems

[3] Part of this chapter is published in Computational Modelling of Mixing Tanks for Bioprocesses: Developing a Comprehensive Workflow, Sadino-Riquelme, M. C., Rivas, J., Jeison, D., Donoso-Bravo, A. & Hayes, R. E., The Canadian Journal of Chemical Engineering, Canadian Society for Chemical Engineering © 2021, John Wiley and Sons.

are described in Table 3.1. Details about the rheological characterization are given in Appendix H.

Table 3.1. Rheological and physical characterization of the fluids selected for the abiotic systems, at 30°C.

Fluid	Density [kg/m^3]	Viscosity [mPa·s]	Consistency coefficient [Pa·s^n]	Power Law index [ ]
Xanthan Sol A	1,023	-	0.1173	0.4840
Xanthan Sol B	1,006	-	0.0193	0.6416
PEG Sol A	1,142	67	-	-
PEG Sol B	1,090	9.8	-	-
Water	998	1	-	-

3.1.2 Batch abiotic systems

For each abiotic system, the reactor was filled with 4.0 L of fluid and the temperature was controlled at 30 °C. As during the fermentation, the dual impeller rotated at 400 rpm. For each fluid, two operating conditions were used, with and without aeration. The aeration rate was 4 L/min (1 vvm).

Two tank configurations were compared, with and without the probes. The sparger was kept in the tank for both cases. For the configuration with the probes, the torque, mixing time and bubbles diameter were studied for all the five fluids.

For each experiment without aeration, the torque was recorded for between 10 and 16 minutes, with the system initially at rest. After that time, the aeration was started, and the torque was recorded for others 10 to 16 minutes. In each case, the average ($T_{AVG_{exp}}$) and standard deviation ($T_{SD_{exp}}$) of the experimental torque were calculated over the last six minutes of data to characterize the stationary state of the system. To eliminate the shaft friction effect (zeroing), the torque measured for the impeller rotating in the empty tank was registered by the torque meter software, to be automatically subtracted from the data.

For each abiotic system with aeration, the mixing time was measured using a colorimetric method. It was also measured for the system with water without aeration. Methylene blue was used as tracer. The mixing process was recorded, using a white background. A camera GoPro Hero 6 (240 fps in 1080p) was used for that purpose. The images were analyzed with the software ImageJ. The mixing time was estimated based on the mean grey value changes (Rosseburg et al., 2018). Data treatment is detailed in Appendix I.

Additionally, for the experiments with aeration, the systems were filmed to study the air bubble diameter. A camera GoPro Hero 6 was used for that purpose. The images were analyzed with the software ImageJ. Data treatment is detailed in Appendix J.

For the tank configuration without the probes, the torque was measured for the systems with Water, PEG Sol A and PEG Sol B. The methodology underwent two modifications: each experiment was run three times under the same conditions (triplicates) and the blank for the torque zeroing was calculated with the same procedure used to measure the impeller torque of the abiotic systems. That is, the torque of the impeller rotating in the empty tank was registered for 10 minutes, and the blank was calculated as the average over the last 6 minutes of data. The blank was measured every three experiments, to keep track of any change in the torque meter calibration, and the subtraction of the blank from the data was done manually.

To check the correctness of the torque measurements, an empirical estimation of the torque value was made based on the correlation between the Reynolds number of a stirred system and its power number (N_P) that, in turn, depends on the torque of the impeller shaft. The Reynolds number for Newtonian fluid (Re) was calculated using Equation 3.1, where ρ, η, N and D are, respectively, the fluid density, the fluid viscosity, the impeller speed and the impeller diameter. The Reynolds number for non-Newtonian fluid (Re^*) was calculated using Equation 3.2 as proposed by Metzner and Otto (1957), where k_s is the proportionality constant between the mean fluid shear rate and the impeller speed and its values was assumed equal to 11, based on the evidence provided by Metzner et al. (1961). Afterwards, N_P was calculated as two-fold the power number read from the power curve correlation in Newtonian fluids for a flat six-blade disk style single impeller reported by Bates et al. (1963). The applied two-fold factor is used due to the dual impeller configuration of the batch abiotic

systems, and it implies that a stable parallel flow pattern is assumed. Thus, the calculated N_P provides an estimation of the upper limit of the actual power number of the system, which may be lower due to the effect of the impeller spacing on the flow field (Rutherford et al., 1996). According to Metzner et al. (1961), the pseudoplastic fluids are described by the same power curve as the Newtonian fluids when $Re^* \leq 15$ or $Re^* \geq 200$. Thus, the same power curve was validly used to estimate the N_P for each of the five batch abiotic systems. Next, the power consumption for the unaerated (P_0) and aerated (P_g) conditions were estimated using, respectively, Equation 3.3 and 3.4. In Equation 3.4, Q represents the airflow rate. Finally, the empirical torque value was calculated for the unaerated (T_{emp,P_0}) and aerated (T_{emp,P_g}) systems using, respectively, Equation 3.5 and 3.6.

Importantly, Equation 3.4 was originally developed by Michel and Miller (1962) for Newtonian fluids in fully baffled tanks with a flat bottom and a single flat-blade impeller, and it was successfully applied to pseudoplastic fluids by Badino et al. (2001). Thus, Equation 3.4 uses the coefficients values reported by Badino et al. (2001).

$$Re = \frac{\rho N D^2}{\eta} \tag{3.1}$$

$$Re^* = \frac{\rho N^{2-n} D^2}{K k_s^{n-1}} \tag{3.2}$$

$$P_0 = \rho N_P N^3 D^5 \tag{3.3}$$

$$P_g = 0.832 \left(\frac{P_0^2 N D^3}{Q^{0.56}} \right)^{0.44} \tag{3.4}$$

$$T_{emp,P_0} = \frac{P_0}{2\pi N} \tag{3.5}$$

$$T_{emp,P_g} = \frac{P_g}{2\pi N} \tag{3.6}$$

3.1.3 Continuous abiotic systems

To mimic the dynamic change of viscosity during alginate production, two continuous abiotic systems were implemented. Only the tank configuration with the probes was used for the experimental set up (see Figure 3.1). For the Xanthan system, the tank was filled with 4.0 L of Xanthan Sol B and continuously fed with Xanthan Sol A. The tank was stirred at 400 rpm and aerated at 1 vvm. The input and output flows were controlled with a pump. The measured outflow was $8 \cdot 10^{-7}$ m^3/s. The liquid level was observed to remain constant. The experiment duration was 90 minutes, and the torque was recorded during the whole process. The zeroing option of the torque meter software was used. Samples (20 mL) were taken at the outflow every 10 minutes, and its density, rheological parameters and viscosity were analyzed following the same procedure as with the broth samples. Detailed rheological data are in Appendix K. Likewise, was run the PEG system. In this case, the tank was filled with 4 L of PEG Sol B and fed with PEG Sol A. The measured outflow was $9 \cdot 10^{-7}$ m^3/s.

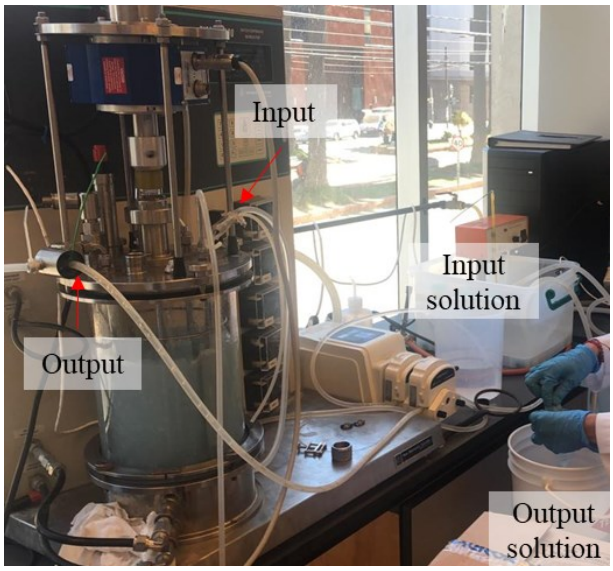

Figure 3.1. Experimental continuous abiotic system.

It is important to mention that the abiotic systems do not account for the presence of microorganisms, which can locally modify the culture medium rheological properties, such as happens with the formation of microbial clumps and the secretion of metabolites that affect the pH.

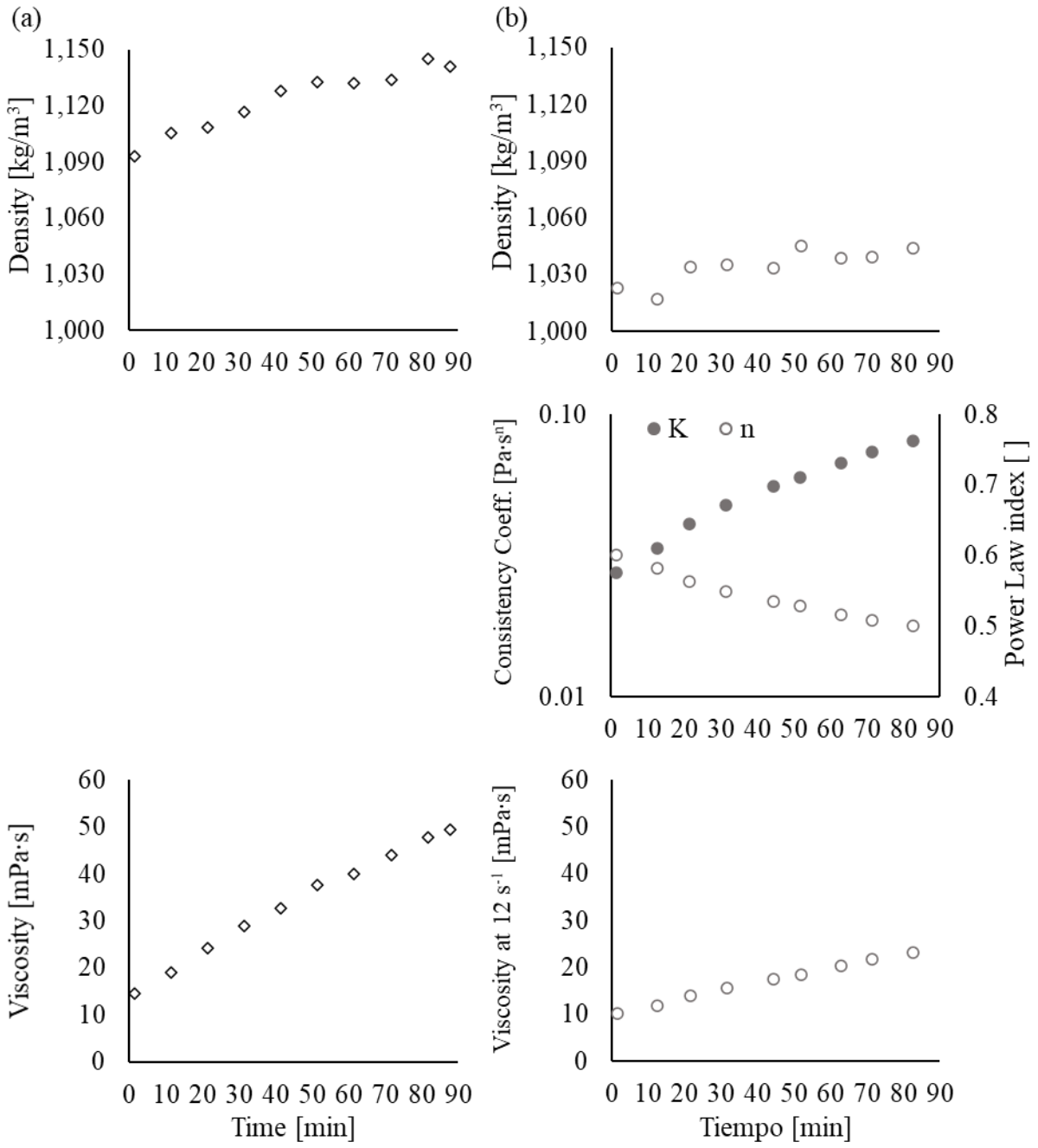

Figure 3.2. Evolution of the rheological and physical properties of the samples taken at the outflow of the continuous abiotic systems. (a) PEG system and (b) Xanthan system.

3.2 Results and Discussions

3.2.1 Physical and rheological characterization

For the PEG continuous abiotic system, as planned, the density and viscosity increased steadily over the experiment (see Figure 3.2a). The fluid density for the PEG system was higher than for the fermentation broth. The maximum difference was 14%, considering the lowest broth density versus the highest PEG density. More importantly, the PEG viscosity varied within the same range as the broth of the culture #2, at a shear rate of 12 s-1. That is, the PEG system mimics the viscosity changes that occurred over the course of the microbial alginate production.

For the Xanthan continuous abiotic system, the analysis showed that, as planned, the fluid properties changed over time in a similar way to the broth properties over the fermentation process (see Figure 3.2b). The density of the Xanthan system varied within the same range as the broth density. The consistency coefficient of the outflow increased steadily, while the power-law exponent decreased. In particular, the viscosity of the system evolved similarly to the viscosity of the culture #1 (at 12 s^{-1}). That is, the Xanthan system closely mimics the rheological changes that occurred during the microbial alginate production.

3.2.2 Torque characterization

The Reynolds number calculated for the batch abiotic systems indicates that the system with water was in the turbulent regime, while the other systems were in the transitional regime (see Table 3.2). If the flow pattern of the batch systems were parallel, torque values similar to those reported in Table 3.2 would be expected, for the unaerated and aerated conditions. However, the tank geometry used in this work differs from the standard conditions that are assumed by the empirical correlations. A different flow pattern could be onset on the batch abiotic systems by the effect of the tank rounded bottom and the impeller spacing, which would reduce the torque (Rutherford et al., 1996). Furthermore, the use of probes could also affect the impeller torque, but its effect has not been reported in the literature.

Table 3.2. Empirical characterization of the batch abiotic systems, without and with aeration.

Abiotic System	**Reynolds number** [ ]	N_P [ ]	T_{emp,P_0} [N·m]	T_{emp,P_g} [N·m]
Water	38,937	10.0	0.185	0.100
PEG Sol A	662	7.26	0.154	0.085
PEG Sol B	4,333	9.26	0.187	0.101
Xanthan Sol A	3,121	8.92	0.169	0.092
Xanthan Sol B	9,474	9.90	0.185	0.099

Table 3.3 and Table 3.4 summarize the torque measurements for the batch abiotic systems using the tank configuration without and with the probes, respectively. As expected, the measured torque values tabulated in Table 3.3 are lower than the corresponding empirically estimated values in Table 3.2. However, the same condition is not true for all the values in Table 3.4. The initial torque measurements for PEG Sol A, with probes, were 44 and 72% higher than the empirically estimated value, respectively, for the unaerated and aerated conditions. To discard whether it was a measurement error or an effect of the probes, the torque was measured again for PEG Sol A with probes. The zeroing methodology described for the tank configuration without probes was used for the new measurements. The triplicates of the new data were consistently different from the initial measurements and matched closely to the empirically estimated values. Therefore, the initial data for PEG Sol A with probes were discarded, and the measurement error was attributed to an incorrect calibration of the torque meter. The torque values measured for PEG Sol B and Xanthan Sol A, with probes and under aerated condition, are also different from the expected value. The former is higher than the empirically estimated value, and the latter is significantly lower than the empirically estimated value. The repetition of both measurements would be advisable but was not possible to be performed.

Table 3.3. Torque measured for the batch abiotic systems, without and with aeration, using the tank configuration without probes. Torque is given as $T_{AVG_{exp}} \pm T_{SD_{exp}}$, in units of [N·m].

Abiotic System	Without aeration	With aeration
Water	0.0977 ± 0.0033	0.0738 ± 0.0043
	0.0943 ± 0.0039	0.0710 ± 0.0042
	0.1135 ± 0.0101	0.0803 ± 0.0041
PEG Sol A	0.1466 ± 0.0169	0.0864 ± 0.0035
	0.1234 ± 0.0053	0.0912 ± 0.0049
	0.1390 ± 0.0050	0.0712 ± 0.0036
PEG Sol B	0.1280 ± 0.0050	0.0837 ± 0.0038
	0.1371 ± 0.0052	0.0849 ± 0.0038
	0.1217 ± 0.0048	0.0728 ± 0.0034

Table 3.4. Torque measured for the batch abiotic systems, without and with aeration, using the tank configuration with probes. Data with ** was discarded and data with * should be repeated. Torque is given as $T_{AVG_{exp}} \pm T_{SD_{exp}}$, in units of [N·m].

Abiotic System	Without aeration	With aeration
Water	0.1172 ± 0.0061	0.0678 ± 0.0123
PEG Sol A	0.2220 ± 0.0062**	0.1463 ± 0.0046**
	0.1695 ± 0.0054	0.0947 ± 0.0040
	0.1635 ± 0.0050	0.0934 ± 0.0073
	0.1679 ± 0.0060	0.0929 ± 0.0038
PEG Sol B	0.1765 ± 0.0076	0.1258 ± 0.0076*
Xanthan Sol A	0.1360 ± 0.0056	0.0377 ± 0.0109*
Xanthan Sol B	0.1311 ± 0.0076	0.0975 ± 0.0100

The study of the batch abiotic systems allows us to understand the impact of the mechanical mixing and aeration on the torque and how the extent of that impact depends on the fluid characteristics, whether rheological properties or viscosity. Under unaerated conditions, the system with water had a lower torque than the other systems, regardless of the tank configuration. Similarly, though a slight difference, Xanthan Sol A had a higher torque than Xanthan Sol B in the tank with probes, and PEG Sol A had a higher torque than PEG Sol B in the tank without probes. That is in agreement with the fluid viscosity differences. Interestingly, based on Figure 3.3, it was observed that, under the same operating conditions, the system with the highest viscosity (PEG Sol A) got a power number expected for dual-impellers with a parallel flow and the system with the lowest viscosity (water) got a power number more similar to a simple-impeller tank, while the other systems were in an intermediate situation. Therefore, it is proposed that the viscosity had a fundamental role in the flow pattern definition as it determined the level of interaction between the impellers. Particularly, the impeller interaction decreased as the viscosity increased.

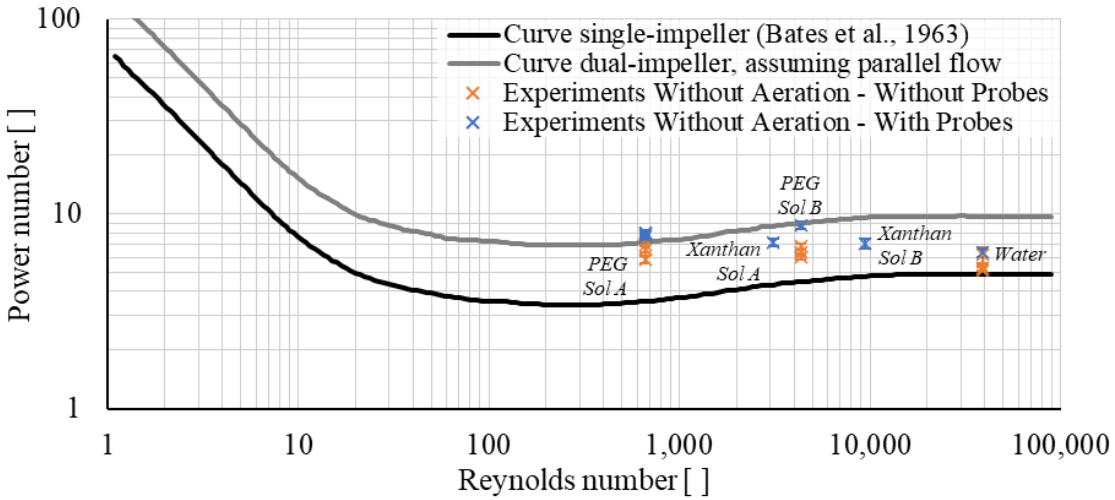

Figure 3.3. Power number curve analysis of the batch abiotic systems without aeration.

On the other hand, regardless of the tank configuration, the batch abiotic systems with aeration experienced a torque reduction, which is a consequence of air cavities formation behind the blades (Nienow, 1998). When the analysis is focused on the aerated systems with Newtonian fluids, using the tank without probes, it can be seen that the aeration blurs the

effect of the fluid viscosity differences on the measured torque value. However, it means that the torque reduction was related, up to a certain level, with the fluid viscosity, because PEG Sol A and PEG Sol B suffered a higher torque reduction (38-39%) than water (26%). This is in agreement with a reported phenomenon that links a higher fluid viscosity to the formation of bigger and more stables air cavities and, therefore, a more significant torque reduction (Nienow, 1998). For the experiments with aeration in the tank with the probes, the torque reduction was more significant in the case of Xanthan Sol A (72%) than in the other cases (26-44%), so much so that its torque became the lowest one. This could be explained by the high fluid viscosity, as before. However, the torque reduction for PEG Sol A was only of 44%, although its high viscosity. If a measurement error is discarded, the torque reduction for Xanthan Sol A may be attributed to additional factors, such as its pseudoplasticity.

Regarding the effect of the tank configuration, the probes increased the torque for the unaerated systems. The systems with water, PEG Sol A and PEG Sol B registered a torque increment of 15, 23 and 37%, respectively. For the aerated systems, the effect of the probes on the torque is not conclusive. While for the system with water the torque with probes was 9.6% lower than without them, for PEG Sol A and PEG Sol B the torque with probes was 13% and 56% higher than without them. However, for the cases with water and PEG Sol A, the torque reduction was higher with the probes than without them, while for PEG Sol B it was lower. The different responses of the systems with aeration could be related to the effect of the probes on the onset of macro-instabilities that affects the dynamic of the air cavities formation and breakaway, as discussed in Chapter 5. Overall, these results show the importance of including the probes in any system mimicking a bioprocess, whether experimental or computational.

The temporal evolution of the torque for the continuous abiotic systems and the batch abiotic systems, for the cases with water, Xanthan Sol B and Xanthan Sol A, was analyzed to gain a deeper understanding of the impact of the interaction of the changing rheological behaviour with the mechanical mixing and aeration on the torque (see Figure 3.4). Only the results obtained in the tank with probes are considered for this analysis. The torque evolution for the batch abiotic systems not included in Figure 3.4 can be found in Appendix L which also includes details related to the torque data treatment.

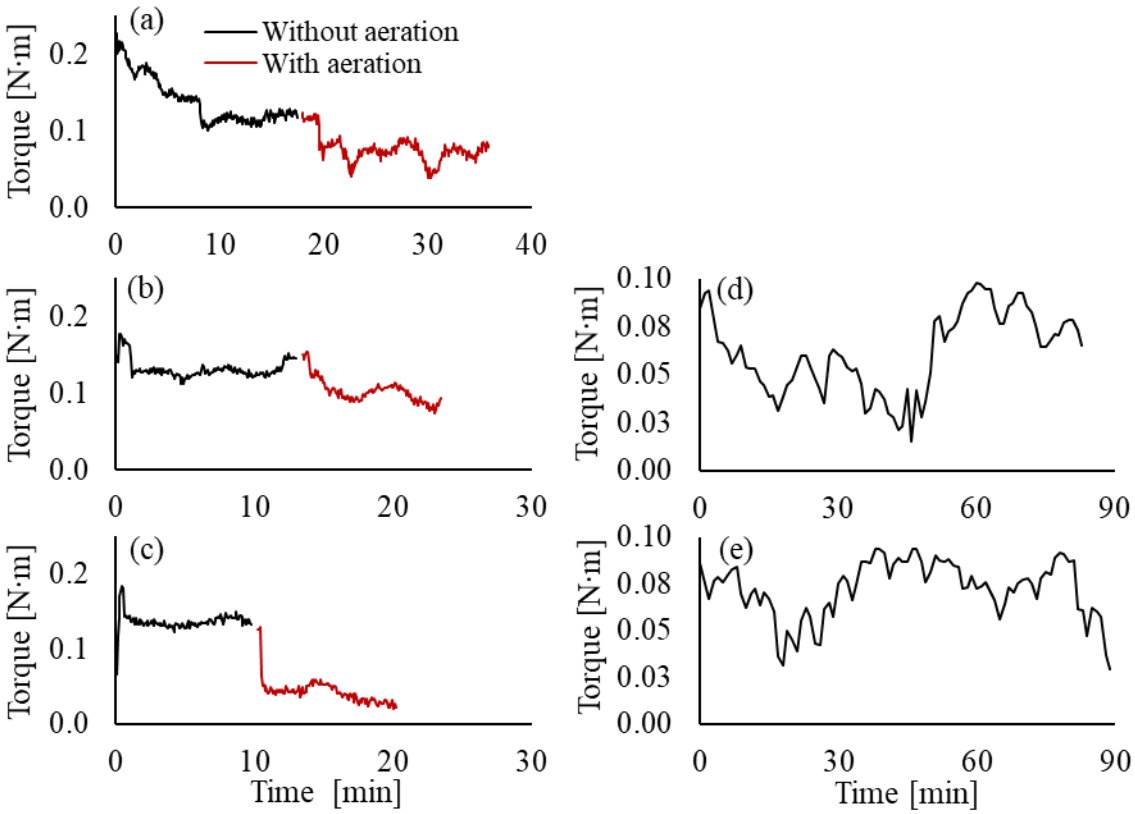

Figure 3.4. Impeller torque evolution in the tank with the probes. Batch abiotic systems with (a) water, (b) Xanthan Sol B, and (c) Xanthan Sol A; and continuous abiotic systems with (d) Xanthan and (e) PEG.

Among the unaerated batch abiotic systems with xanthan solution and water, it is possible to see that the torque was less stable in the case with water. It may be explained by the onset of flow macro-instabilities along the impeller shaft as discussed in Chapter 5. Besides, bigger torque oscillations were identified for the case with water with aeration in comparison to without aeration. It is hypothesized that those oscillations relate to the growth of the air cavities and their following size reduction when their volume surpasses the limits of the edges of the blades or are breakaway by some flow macro-instability. The fluid viscosity differences may explain that, in the narrow time span studied for the batch abiotic systems, it can be identified only two of those oscillations for the case with water and none (or maybe one) for the cases with xanthan solution.

The torque curve of the continuous Xanthan system moves, as expected, between the values already registered for the batch systems Xanthan Sol B and Xanthan Sol A under aerated conditions. Similarly, the highest torque registered for the PEG system recalls the torque of the batch system PEG Sol A under aerated conditions. Being consistent with the hypothesis made based on the batch abiotic aerated systems, it is proposed that the oscillations that occur around every 10 minutes in the continuous Xanthan system could be related to the growth and reduction of the air cavities size. A similar dynamic is hypothesized for the PEG system but, in this case, the time spanned by the oscillations varied during the experiment, from around 4 minutes during the first 30 minutes to around 8 minutes later on. This variation could be explained by the evolving viscosity, as the viscosity changed more significantly over the experiment with the PEG system than with the Xanthan System.

The similarity between the torque curves of the fermentation and the continuous system supports the idea that their underlying mixing mechanisms are similar and, therefore, studying computationally the batch abiotic systems would help to understand the fluid dynamics of the microbial alginate batch production.

3.2.3 Mixing time

Table 3.5 shows the mixing time estimated for the batch abiotic systems. Based on the mixing times for the cases with water, it is concluded that the aeration increased the mixing time under the applied operating conditions. According to the literature, this result implies that the impeller agitation was dominating the bulk flow, and the air was being dispersed and recirculated (Nienow, 1998). This agrees with the visual observations made during the experiments, not only for the system with water but also for all the aerated abiotic systems.

Among the systems with aeration, the one with Xanthan Sol A had the highest mixing time, which was significantly different from the other results. In the case of the batch system with Xanthan Sol A, the tracer looked like strands and some strands remained trapped in the baffles, for a long time, extending the mixing process. In particular, the mixing time of Xanthan Sol A was about 700 times bigger than the mixing time of Xanthan Sol B. Thus, it could be expected a similar increment of the mixing time over the microbial alginate batch production. For the systems with Newtonian fluids, it was expected that PEG sol B would

have a mixing time bigger than water but smaller than PEG Sol A. However, the result shows something different. Nevertheless, it is believed that the mixing time for PEG Sol B was overestimated because the tracer remained resting on the foam, delaying the entry of the tracer into the fluid.

Table 3.5. Mixing time estimated for the aerated batch abiotic systems, in units of [s].

Abiotic system	Aeration	Mixing Time
Water	No	0.86
Water	Yes	3.24
PEG Sol A	Yes	3.70
PEG Sol B	Yes	4.21
Xanthan Sol A	Yes	674
Xanthan Sol B	Yes	1.26

3.2.4 Bubbles diameter

The Sauter-mean bubble diameter was calculated for each batch abiotic system with aeration (see Table 3.6). As expected, the higher the viscosity, the higher the bubble diameter, because the coalescence process is favoured under this fluid characteristic (Nienow, 1998).

Table 3.6. Sauter-mean bubble diameter estimated for the aerated batch abiotic systems, in units of [mm].

Abiotic System	Sauter-mean Diameter
Water	4.9
PEG Sol A	7.4
PEG Sol B	5.2
Xanthan Sol A	8.8
Xanthan Sol B	5.6

4 CFD SINGLE-PHASE MODELLING – NEWTONIAN FLUID[4]

The CFD modelling of the different batch abiotic systems was considered relevant to identify the limitations and capabilities of this computational approach to model the evolution of the alginate fermentation fluid dynamics caused by the broth rheological changes. The single-phase simulation of the system with water without aeration was addressed first, which is referred to as Step 1. In this step, the impact that the common assumptions and practices have upon the results of the CFD modelling of mechanically mixed tanks in the bioprocess field was analyzed. In this chapter, in addition to the study of the effect of eliminating the probes on the flow field, the workflow used to set up the model, to study the grid and time-step size, and to conduct verification and validation of the model is described in detail.

At an initial stage of Step 1, the batch abiotic systems with PEG Sol A and PEG Sol B were modelled, as well as the case with water. Those preliminary models and results are detailed in Appendix M.

4.1 Material and Methods

4.1.1 CFD domain

To study the effect of the probes, two three-dimensional domains were built using Ansys Design Modeler (Workbench 18.2). The domain without the probes, called GeomA, included only the sparger ring (see Figure 4.1a). GeomB contained the entire sparger besides all the four probes of the experimental system (see Figure 4.1b).

Both domains were divided into smaller bodies to implement the rotating zones around the impellers and gain control over the grid structure and sizing (see Figure 4.2). The upper stationary bodies were assembled into one part, except for the upper stationary zones with probes bottom sections of the domain GeomB.

[4] Part of this chapter is published in Computational Modelling of Mixing Tanks for Bioprocesses: Developing a Comprehensive Workflow, Sadino-Riquelme, M. C., Rivas, J., Jeison, D., Donoso-Bravo, A. & Hayes, R. E., The Canadian Journal of Chemical Engineering, Canadian Society for Chemical Engineering © 2021, John Wiley and Sons.

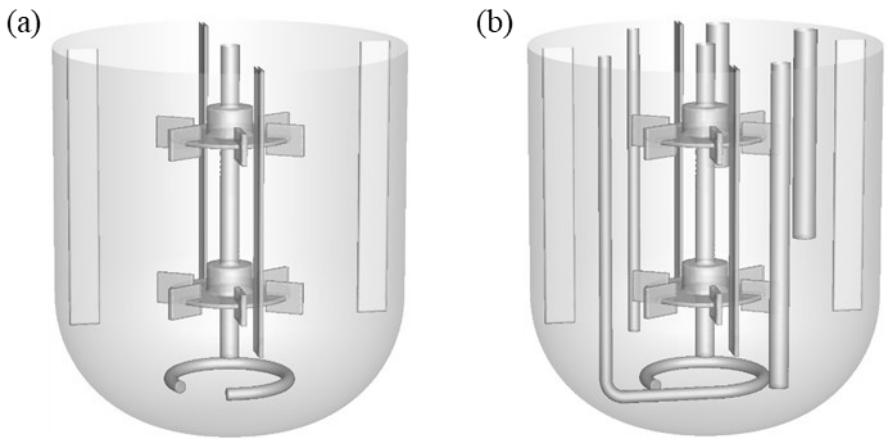

Figure 4.1. Tank CFD domain of (a) GeomA and (b) GeomB. Figure adapted from Sadino-Riquelme et al. (2021), reprinted with permission of John Wiley and Sons.

4.1.2 Coarse domain grid

A coarse grid was implemented in Ansys Meshing (Workbench 18.2) for each domain. CFD and Fluent were selected, respectively, under the physics and solver options. For the general sizing settings, the curvature function was set with medium relevance centre. A target skewness of 0.6 was defined for quality. The maximum face size, minimum size and maximum tetrahedral size were modified from their default values to 2 mm, 1 mm and 2 mm, respectively.

The following meshing methods were applied: multi-zone method with hexahedral elements, tetrahedron patch conforming method, and sweep method with triangular elements. The method used for each body is specified in Figure 4.2. Edge, face and body sizing methods were used to refine the grid locally. Inflation layers were implemented next to each wall using the total thickness inflation option, with 15 layers and a 1.2 growth rate. More details are given in Appendix N. Using these features, the coarse grids resulted in 2,615,336 and 2,843,027 nodes for GeomA and GeomB, respectively (see Figure 4.3).

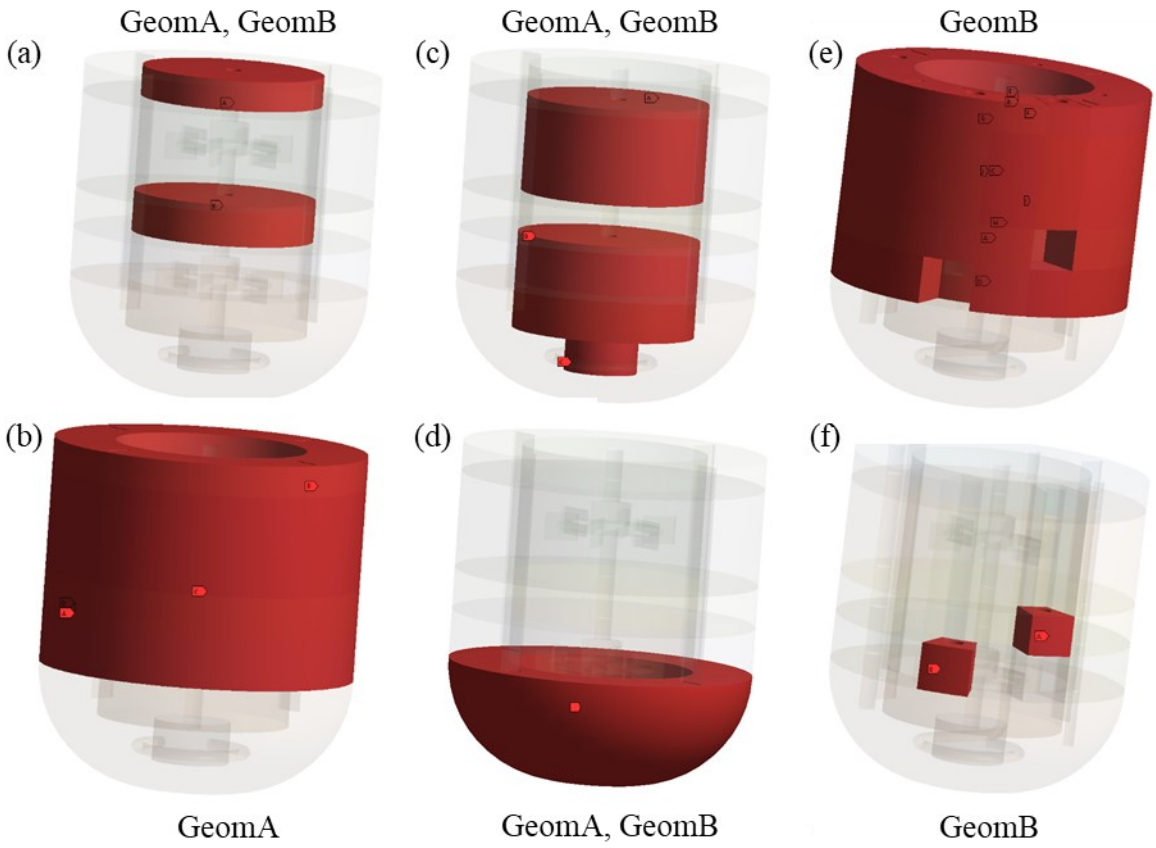

Figure 4.2. Bodies of the domain GeomA and meshing methods implemented: (a) upper and middle axis zones, multizone method with hexahedral elements; (b) upper stationary zones, sweep method with triangular elements for face meshing; (c) impeller and lower axis zones, tetrahedrons patch conforming method; and (d) lower stationary zone, tetrahedrons patch conforming method. Bodies of the domain GeomB that differ from GeomA, and meshing methods implemented: (e) upper stationary zones without probes bottom section, with triangular elements for face meshing; and (f) upper stationary zones with probes bottom section, tetrahedrons patch conforming method. Figure from Sadino-Riquelme et al. (2021), reprinted with permission of John Wiley and Sons.

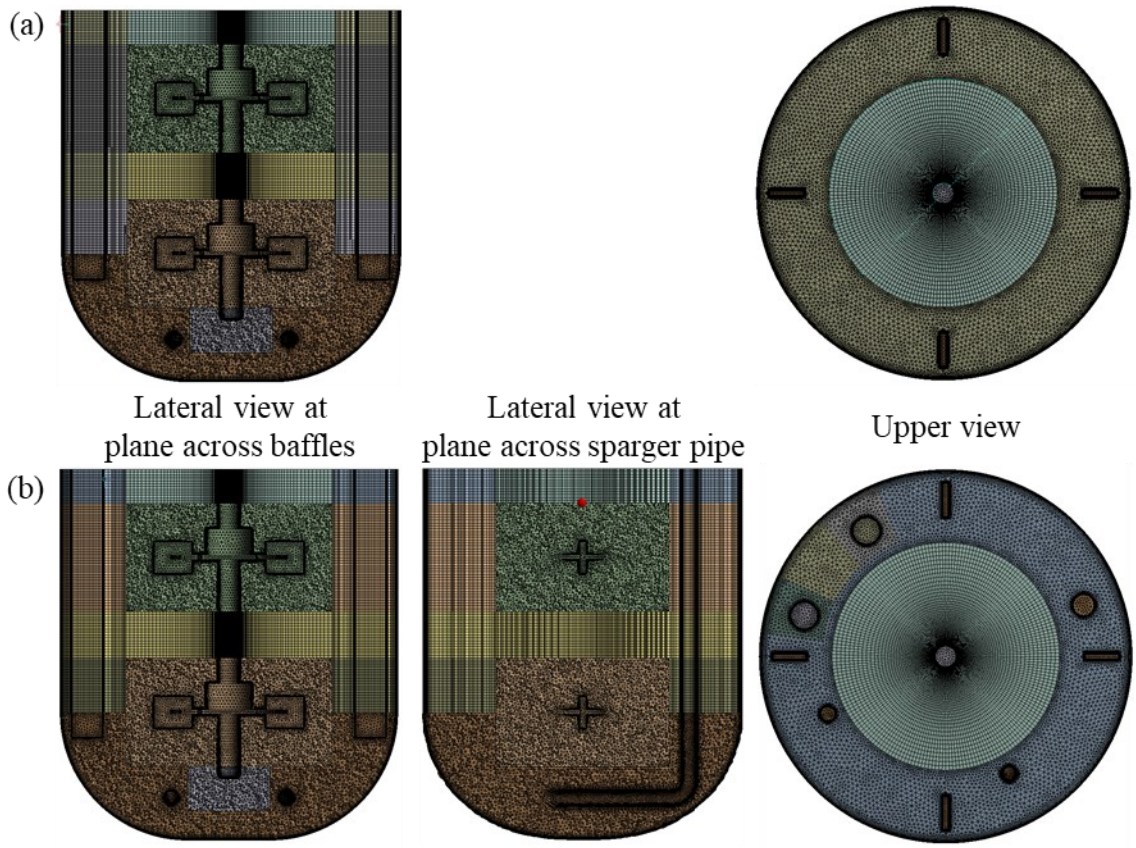

Figure 4.3. Lateral and upper views of the coarse grid implemented for the domains (a) GeomA and (b) GeomB. Figure from Sadino-Riquelme et al. (2021), reprinted with permission of John Wiley and Sons.

4.1.3 CFD model settings

The CFD models were adapted in Ansys Fluent (versions 18.2 and 2019R3). The following assumptions were considered to model the batch abiotic system with water without aeration: constant temperature, flat liquid-air interface surface, and free of air entrapment from the interface. Thus, the described system is single-phase, and the fluid physical properties are static and homogeneous. The assumptions related to the liquid-air interface are not physically accurate and were removed afterwards, using a multi-phase model (see Chapter 6).

The fluid was characterized as water, using the built-in library data. To simulate the mixing, the transient SM method was used, with a rotating velocity of 400 rpm for each moving zone. Two sets of numerical settings were compared, here called the k-epsilon set

and the SST k-omega set. The configuration of both sets is given in Table 4.1 and Table 4.2. The governing conservation equations of the CFD model can be referred to in Appendix O.

Table 4.1. Numerical settings shared by the k-epsilon and SST k-omega sets.

Precision	Double
Coupling scheme	SIMPLE
Solver	Pressure-based with absolute velocity formulation
Body Forces	Gravity
Time Step Size	0.0004 s
Iterations	Maximum 60 per time step. It was activated the option to stop the iterations when all residuals were below 10^{-5} simultaneously.
Boundary conditions	
Top wall	Symmetry
Impeller and axis walls	Relative velocity to moving zone 0 rpm
Other walls	No-slip condition
Under-relaxation factors	
Density	0.7
Body forces	0.7
Turbulent viscosity	0.8
Others	default value

Hereinafter, for ease of reference of the four models being studied, they will be named according to the domain and set of settings. Thus, GeomA-kε and GeomA-SSTkω correspond to the models that use the domain GeomA with, respectively, the k-epsilon set and the SST k-omega set. Similarly, the models that use the domain GeomB are named GeomB-kε and GeomB-SSTkω.

Table 4.2. Numerical settings not shared by the k-epsilon and SST k-omega sets.

	k-epsilon set	**SST k-omega set**
Turbulence model	Standard k-epsilon	Shear-Stress (SST) k-omega with production limiter
Near-wall treatment	Enhanced wall treatment	-
Initial conditions	From rest k=0.1; ε=0.1	Solution obtained with the k-epsilon set after 30 impeller turns
Discretization methods*		
Gradient	Least-squares cell-based	Green Gauss node-based
Pressure	Second-order	PRESTO
Transient formulation	Second-order implicit	Second-order implicit
Others	Second-order upwind	Second-order upwind
*with warped-face gradient correction		

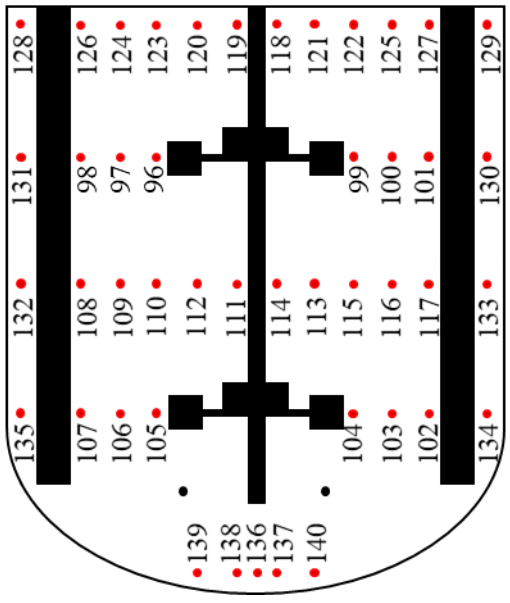

Figure 4.4. Map of the monitored points. The points were symmetrically distributed over a vertical plane, which crosses two baffles and cuts the reactor by half. Figure adapted from Sadino-Riquelme et al. (2021), reprinted with permission of John Wiley and Sons.

4.1.4 Simulation completion criteria

The velocity magnitude at different points and the impeller torque were recorded after every time step. The monitoring points were placed on a vertical central plane (see Figure 4.4). The data were used to identify the achievement of the stationary state and to detect numerical issues. The residual values were tracked after every iteration, along with any alert of cells with turbulent viscosity ratio exceeding the maximum allowed value (10^5). At the end of each time step, residuals values below 10^{-5} were expected (convergence criterion).

4.1.5 Grid and time-step size analysis

For the grid study, two progressively refined grids were built starting from the coarse one, here named medium and fine grid, respectively. The grid refinement was done keeping a node ratio of approximately 1.3 between consecutive grids, for the entire domain as well as for each body, to ensure a progressive and systematic refinement (Ferziger et al., 2002). The medium and fine grids for GeomA had 3,365,649 and 4,401,802 nodes, respectively; and the medium and fine grids for GeomB had 3,646,519 and 4,726,656 nodes, respectively. Also, it was checked that the quality was similar between the consecutive grids of both domains (see Appendix P).

A grid independence study was performed to verify the results of GeomA-kε and GeomB-kε. The models were solved using the medium and fine grids. In each case, the coarse grid solution of the corresponding domain was used to interpolate an initial condition. The simulations used the coarse time step, 0.0004 s. The methodology is detailed in Figure 4.5a.

The grid independence study was also performed to verify the result of GeomB-SSTkω. However, the methodology used to assess the grid for the k-epsilon set did not work in this case. Thus, it was necessary to apply a new methodology, where the interpolation of data from the coarse to the finer grids was done using the k-epsilon set results, and the SST k-omega was applied later. Furthermore, the simulations were run using the fine time step, 0.0002 s. The details are shown in Figure 4.5b.

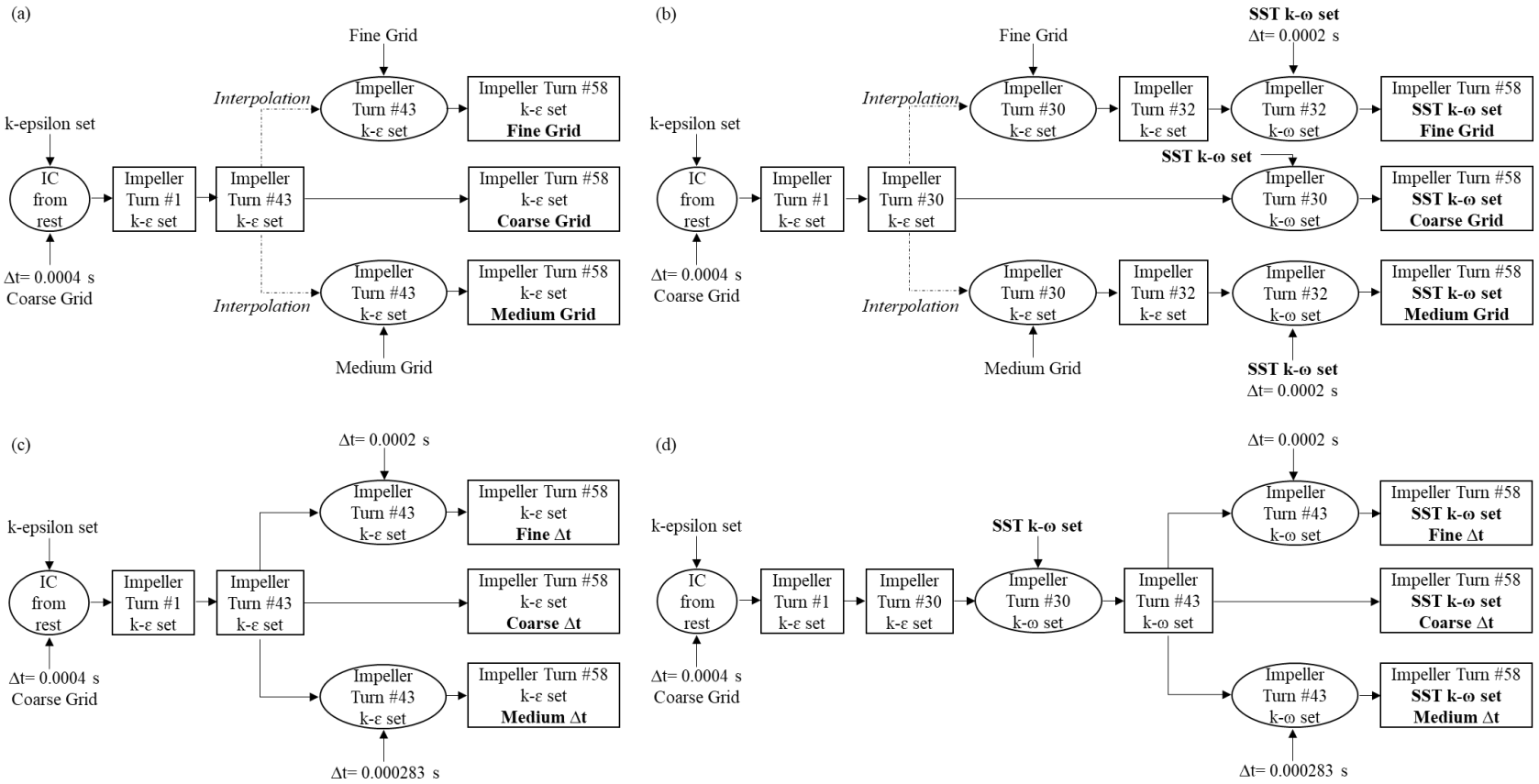

Figure 4.5. Methodologies applied for the (a, b) grid and (c, d) time-step size studies. (a, b) were used to study the solution obtained with GeomA-kε and GeomB-kε. (c, d) were applied to study the solution obtained with GeomB-SSTkω. Figure from Sadino-Riquelme et al. (2021), reprinted with permission of John Wiley and Sons.

To study the time-step size, two additional time steps were used: 0.000283 and 0.0002s, called medium and fine time steps, respectively. Thus, a refinement ratio of 1.4 was maintained between consecutive time steps. To solve the model with these new time steps, the solution obtained with the coarse grid of the corresponding domain was used as initial condition. The simulations were run using the coarse grid. The time-step size was studied for the results of GeomA-kε and GeomB-kε (see Figure 4.5c) and GeomB-SSTkω (see Figure 4.5d).

For each simulation, the impeller torque was calculated as the average ($T_{AVG_{sim}}$) and standard deviation ($T_{SD_{sim}}$) of the data computed over the last 10 impeller turns. Similarly, was calculated the time-average velocity magnitude ($VM_{AVG_{sim}} \pm VM_{SD_{sim}}$) at the monitored points.

4.1.6 CFD model verification and validation

For the verification and validation of the models, the methods described by Coleman and Stern (1997) were used. The grid convergence uncertainty (U_{grid}) was estimated based on the grid convergence metric, given by Equation 4.1.

$$U_{grid} = \frac{T_{AVG_{sim,fine}} - T_{AVG_{sim,medium}}}{T_{AVG_{sim,medium}}} \cdot 100\% \tag{4.1}$$

where $T_{AVG_{sim,fine}}$ and $T_{AVG_{sim,medium}}$ correspond to $T_{AVG_{sim}}$ of, respectively, the fine and medium grid. Similarly, the uncertainty related to the time convergence ($U_{\Delta t}$) was estimated, using the torque computed with the fine and medium time step.

$$E = \frac{T_{AVG_{sim,coarse}} - T_{AVG_{exp}}}{T_{AVG_{exp}}} \cdot 100\% \tag{4.2}$$

$$U_V{}^2 = U_{grid}{}^2 + U_{\Delta t}{}^2 + U_{Exp}{}^2 \tag{4.3}$$

For the validation of the models, the comparison error (E) between the simulated and experimental torque was estimated according to Equation 4.2. The validation uncertainty (U_V) was estimated by Equation 4.3, where U_{Exp} corresponds to the uncertainty related to the

experimental torque data. Other sources of modelling and numerical uncertainties were not included in the analysis.

Also, for a more robust validation, the velocity profiles obtained for GeomA were compared with experimental data reported by Micale et al. (1999).

4.2 Results and Discussions

4.2.1 Domain grid

The grid affects both numerical resolution and computational time. One reason to eliminate the probes would be to reduce the cost associated with the inflation layers around their walls. However, the implemented grid, using a domain divided into smaller bodies to separate zones with a regular shape from those with an irregular one, allowed us to keep a similar number of nodes in the GeomB's grid compared to the GeomA's grid, which is an advantage as it can be obtained an accurate solution without increasing significantly the computational time (see Table 4.3). This highlights the importance of building the geometry to be an accurate representation of the physical system as well as to facilitate the implementation of the grid.

Table 4.3. Computing time required to simulate one time-step of the model with k-epsilon set, in units of [min]. Time registered for the simulations run in the Compute Canada clusters Cedar (48 cpu)*, Graham (64 cpu)$^{+}$, and Graham (16 cpu)$^{++}$. Table from Sadino-Riquelme et al. (2021), reprinted with permission of John Wiley and Sons.

Time step	**Domain grid**			***Domain***
	Coarse	**Medium**	**Fine**	
Coarse	1.67 *	2.16 *	2.66 *	***GeomA***
	1.75 *	4.75 $^{++}$	3.16 *	***GeomB***
Medium	1.58 *			***GeomA***
	1.30 $^{+}$			***GeomB***
Fine	1.58 *			***GeomA***
	1.30 $^{+}$			***GeomB***

The grid quality is important in CFD models, however, few have reported quality indices (Cudak, 2019). Three metrics are particularly relevant: orthogonal quality, aspect ratio and skewness. The orthogonal quality ranges between 0 and 1; the minimum value should be larger than 0.01, with the average close to 1. The skewness index also varies between 0 and 1, and the maximum and average values should be below 0.95 and 0.33, respectively. The aspect ratio can take values from 1 with no upper limit. Far from the walls, the aspect ratio should not be much higher than 5, while close to the walls (that is, where the inflation layers are located), the aspect ratio has no restrictions provided that the simulation does not include the energy equation (Ansys, 2009). All these recommendations were met by the coarse grid of each domain. Additionally, it was required that the quality of the coarse grid of GeomA and GeomB were similar, to eliminate the grid quality as a source of differences between the simulations' results (see Appendix P). Also, it was verified that the quality indices did not vary significantly during the refinement of the grids, to avoid the addition of a new source of numerical error in the grid study (see Appendix P).

During the grid development, it is very important to check the onset of cells that exceed the maximum allowed turbulent viscosity ratio during a simulation. The moving impeller zones were meshed with tetrahedral cells and, therefore, it was difficult to reduce the skewness to the degree required to control or eliminate the outbreak of non-physical high turbulent viscosity ratio. Even for a grid complying with the minimum quality requirements, it was identified that cells with a high skewness and located in the interface between the moving and the stationary zones were particularly prone to present intermittently a high turbulent viscosity ratio. It is hypothesized that the grid motion can be responsible for this intermittent effect, as it may cause that two cells meet in a mismatch position, impairing the information transport. Therefore, the grid of the interface between those zones is key when SM is used.

One way to identify cells with non-physical high turbulent viscosity ratio, aside from the warning that the software may display, is checking the contour of turbulent viscosity ratio at cells in different planes. High values of turbulent viscosity ratio located in zones that are not related to the higher velocities could be artifacts that are triggered numerically. These characteristics are illustrated in Figure 4.6.

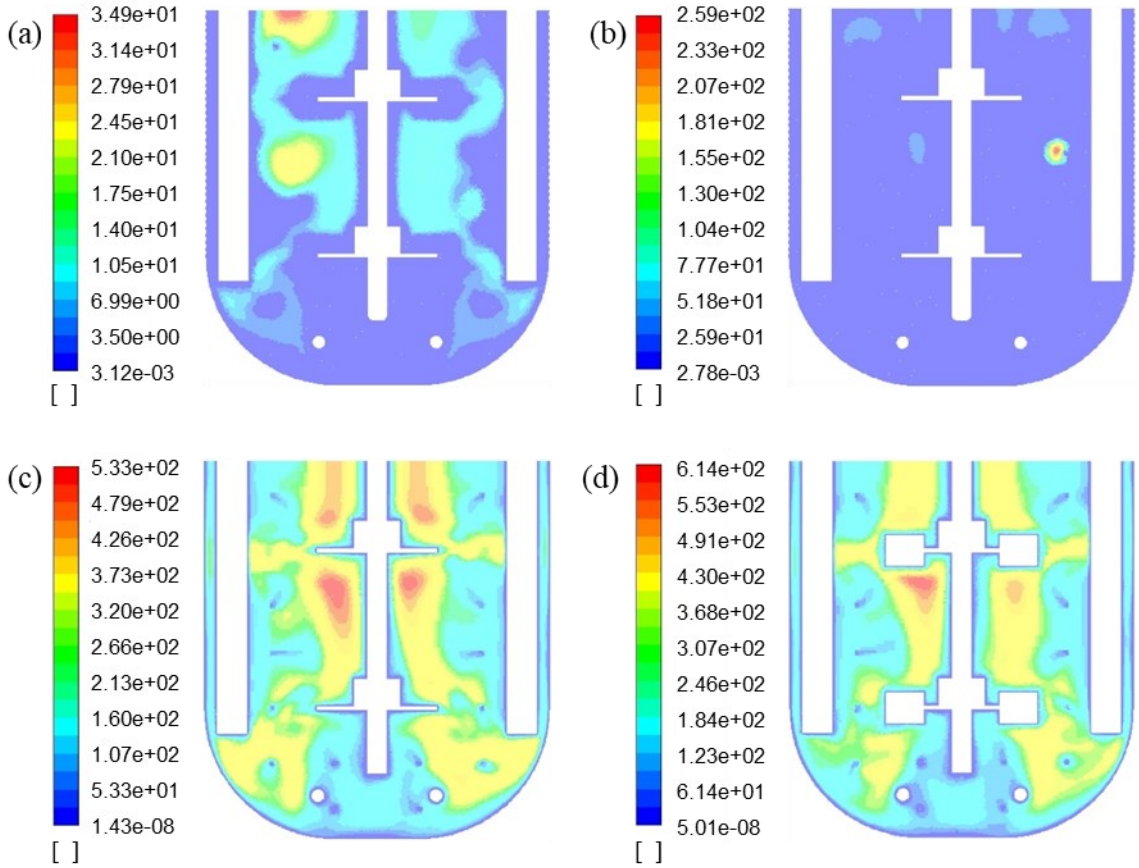

Figure 4.6. Contours of instantaneous turbulent viscosity ratio of results with (a, b) non-physical high turbulent viscosity ratio and (c, d) high turbulent viscosity ratio related to the system's physics. Two planes across the baffles are shown: (a, c) YZ and (b, d) XY plane. Figure adapted from Sadino-Riquelme et al. (2021), reprinted with permission of John Wiley and Sons.

When using the coarse grid, the simulation of GeomA-kε did not show cells with a non-physical high turbulent viscosity ratio, neither did GeomA-SSTkω nor GeomB-SSTkω. On the contrary, GeomB-kε had this problem in one cell, appearing intermittently in fewer than one hundred iterations out of 18,750 iterations. As both coarse grids have the same skewness quality, it is confirmed that this factor by itself did not determine the appearance of non-physical high turbulent viscosity ratio. Moreover, when GeomB-kε with the coarse grid was run with the fine time step, the non-physical high turbulent viscosity ratio disappeared. Therefore, the study of the time step is as relevant as the analysis of the grid. Returning to the

GeomB-kε simulation with high turbulent viscosity ratio, as it did not propagate to more cells and appeared in less than 1% of the iterations, it was considered that it does not affect the results, which is also substantiated by the rigorous grid and time-step analysis (see Section 4.2.5).

4.2.2 Near-wall treatment

The near-wall treatment, which is required for the modelling of the turbulent boundary layer, should be selected based on the near-wall Y^+values (see Appendix O). This parameter allows us to identify whether the nodes near the wall are in the viscous sublayer ($Y^+ < 5$), the buffer region ($5 < Y^+ < 30$), or the logarithmic region ($30 < Y^+ < 300$) of the boundary layer. For modelling purposes, the near-wall grid should ensure that the nodes near the wall are either in the logarithmic region or the viscous sublayer. In the former case, the near-wall treatment approach based on the logarithmic law of the wall, so-called standard wall functions in Ansys Fluent, should be used. For the latter case, the enhanced wall treatment is available on Ansys Fluent, which combines a two-layer model with enhanced wall functions (Ansys, 2009).

However, in many CFD models that have used the k-epsilon model, the near-wall treatment does not cite the obtained Y^+ value (Gelves et al., 2014; Haringa et al., 2018a; Niño et al., 2018), and sometimes neither the wall function nor the inflations layers are described (Fan et al., 2018; Haringa et al., 2018a; Ebrahimi et al., 2019; Spann et al., 2019; Verma et al., 2019; Zhu et al., 2019; Chezeau et al., 2020). Therefore, in this work, the effect of using an inappropriate wall treatment was explored.

Preliminary simulations with water showed that using standard wall functions instead of enhanced wall treatment, when Y^+ is less than 5, would affect the prediction of the time-averaged velocities, both next to the walls and far from them, especially in the zones between the impellers and close to the liquid level, where the standard wall functions would underpredict the time-averaged velocities as much as 54% and 32%, respectively (see Figure 4.7a). This effect was also identified when a non-Newtonian fluid was simulated. In this case, the velocities close to the impellers were significantly affected too, being overpredicted as much as 20% for the upper impeller and underpredicted as much as 33% for the lower one

(see Figure 4.7b). These significant deviations of the predicted velocities can impair the study of the local and global mixing.

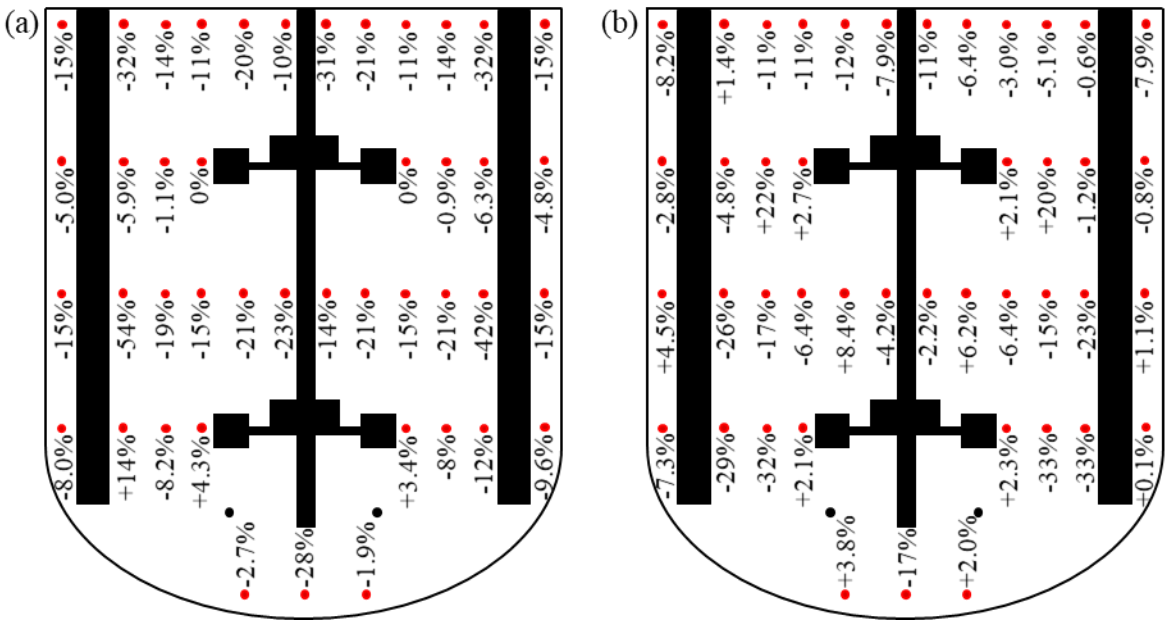

Figure 4.7. Analysis of under(-)/over(+) prediction of $VM_{AVG_{sim}}$ when standard wall functions is used instead of enhanced wall treatment, despite Y^+ is less than 5. Two fluids were used: (a) water and (b) non-Newtonian fluid (ρ 1,006 kg/m3; K 0.19 Pa·s^n; n 0.64). The analysis was based on preliminary simulations with GeomA. Figure from Sadino-Riquelme et al. (2021), reprinted with permission of John Wiley and Sons.

Table 4.4. Range of Y^+ next to the walls, for the simulations with the k-epsilon set.

Walls	**GeomA**	**GeomB**
Exterior walls	0.13 – 2.4	0.09 – 2.0
Impeller and axis	0.01 – 5.4	0.01 – 5.6
Baffles	0.08 – 1.6	0.06 – 1.6
Probes	-	0.06 – 2.3
Sparger	0.52 – 2.6 (ring)	0.15 – 2.5

In this work, for the simulations with the k-epsilon set, the Y^+ value was within 0.1 and 5 next to all of the walls of the domain (see Table 4.4), which means that the enhanced wall treatment should be used (Ansys, 2009).

It is important to notice that, according to preliminary simulations, the inflation layers are necessary around all the walls, not only the impeller walls.

4.2.3 Numerical settings

Two modelling approaches could be used to simulate the impeller rotation, MRF and SM. Both methods require the separation of the rotating impeller zones from the rest of the tank. However, MRF uses a steady-state formulation, while SM uses a transient one. MRF simulates the agitation of the domain without moving the impellers, so only one relative position between the impellers and baffles is simulated and its interaction is approximated. On the contrary, the SM accounts for the transient effects that are caused by the actual rotation of the impellers (Ansys, 2009). Simulations using both methods showed that their effect on the velocity magnitude prediction is significant (see Figure 4.8). This comparison was also made by Haringa et al. (2018a; 2018b), where it was shown that SM can capture flow macro-instabilities while MRF cannot. Thus, even when both methods may generate valid torque predictions, the fluid flow and mixing patterns will not be accurately predicted by MRF. When those variables are of interest, the SM approach must be used. SM could be used from the beginning of a simulation or MRF could be used to converge faster to an initial solution and later change to SM. In the later case, it may still require the extension of the simulation for several impeller's turns to recover the dynamic of the macro-instabilities of the system. Therefore, both options may be of use, according to the need and purpose of the study. In this work, SM was set from the beginning as it provides a more accurate understanding of how the system's fluid dynamics evolve.

The appearance of a high non-physical turbulent viscosity ratio, discussed in Section 4.2.1, can be related to the limitations of the numerical settings to simulate the fluid dynamics of the system. Indeed, for GeomB, when the k-epsilon set was substituted by the SST k-omega set, the high non-physical turbulent viscosity ratio disappeared.

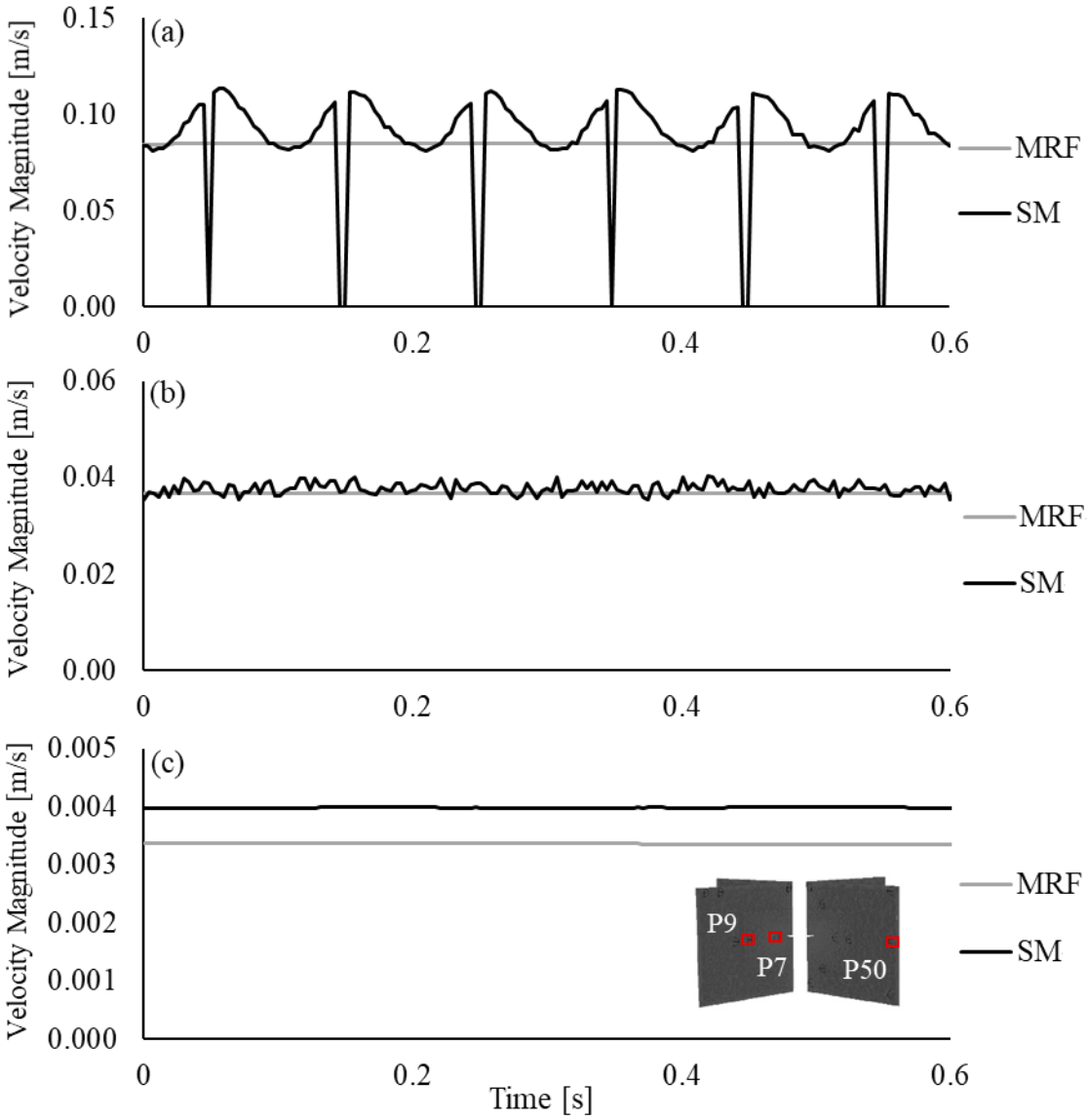

Figure 4.8. Velocity temporal profile in stationary state for preliminary simulations of a stirred tank, obtained with the MRF and SM methods, for monitored points: (a) P7, next to the impeller; (b) P9; and (c) P50, next to the exterior wall. Figure from Sadino-Riquelme et al. (2021), reprinted with permission of John Wiley and Sons.

Theoretically, the SST k-omega set has advantages for the simulation of a stirred tank with turbulent flow compared to the k-epsilon set. The turbulence model SST k-omega works better than k-epsilon to solve flows with high-pressure gradients. Also, PRESTO may be more beneficial than the second-order discretization scheme in cases with high-speed rotating

flows and flows in strongly curved domains (Ansys, 2009). However, the implementation of these settings was not straightforward. When the SST k-omega model was set with the least-squares cell-based scheme, the simulation diverged. Theoretically, for irregular unstructured grids, the accuracy of the least-squares cell-based gradient is similar to the accuracy of the Green Gauss node-based gradient scheme (Ansys, 2009), however, the SST k-omega model was only successfully implemented with the Green Gauss node-based gradient scheme.

It is important to mention that it was not possible to initialize from rest a simulation with the SST k-omega set. Conversely, when the solution obtained with the k-epsilon set was used as initial condition, the simulation ran successfully. It may be because the numerical settings of the SST k-omega set required a more robust initial condition.

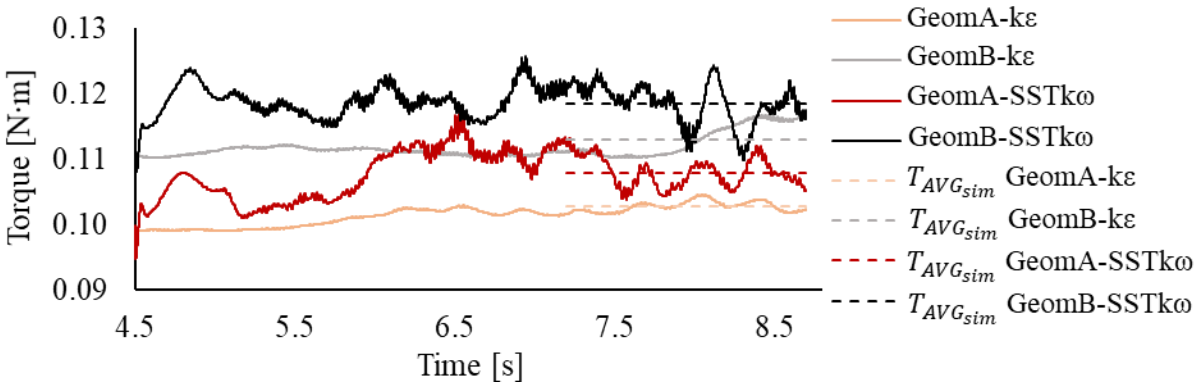

Figure 4.9. Torque temporal evolution simulated with the k-epsilon and SST k-omega sets, for GeomA and GeomB, with the coarse grid and time step. The $T_{AVG_{sim}}$ values are plotted against the flow time of the last 10 impeller turns. Figure from Sadino-Riquelme et al. (2021), reprinted with permission of John Wiley and Sons.

The effects of the different numerical sets are apparent on the torque for both domains (see Figure 4.9). The torque simulated with the SST k-omega set showed more oscillations than the one with the k-epsilon set. That may be explained by the turbulence model, as the k-epsilon model adds numerical diffusion, smoothing the gradients, which does not occur as much with the SST k-omega model. For both domains, the torque obtained with the SST k-omega set is higher than the one obtained with the k-epsilon set, during the whole simulation frame time (except for a short time for GeomB). However, regardless of the settings, GeomB

has a higher torque than GeomA. Interestingly, the difference between the averaged torques of GeomB-kε and GeomA-kε is similar to the difference between GeomB-SSTkω and GeomA-SSTkω. Thus, even when the k-epsilon set may not be as accurate as the SST k-omega set to simulate the fluid dynamics, it is sufficient to capture the torque difference between both tank configurations.

4.2.4 Simulation completion criteria

The residual values should be verified and reported, which is not always done (Noorman, 2011; Srirugsa et al., 2017; Li et al., 2018; Wiedemann et al., 2018; Cudak, 2019; Ebrahimi et al., 2019; Russell et al., 2019; Verma et al., 2019). In this work, all the simulations reached residuals values below 10^{-5} at every time step.

From the graphs of the monitored variables, non-physical oscillations and numerical instabilities were discarded. Interestingly, it was observed that 20 or 30 impeller turns (simulated from rest) were not enough to have a clear understanding of the fluid flow patterns in stationary state, especially because it was found that such state is not stable for the system under study, which means that in some periods of time the velocity and torque can be higher or lower than in other periods (see Figure 4.9). This finding was important to set up the criterion for the calculation of the averaged torque because, if it is calculated from different short periods, the comparison may lead to a wrong conclusion. Thus, first, the torque data need to be free of the influence of the initial condition and the initial transient state of the system and, second, the average and standard deviation should consider a flow-time-frame big enough to incorporate several torque oscillations. That is why $T_{AVG_{sim}}$ and $T_{SD_{sim}}$ were calculated over the simulated data of the last 10 impeller turns, after 48 simulated impeller turns.

4.2.5 Grid and time-step size analysis

The time-step size study is as important as the domain grid study. If the time step is too large, the effect of the impeller passage will not be well captured and the flow patterns will not be accurately predicted. Furthermore, even if an implicit formulation is being used to solve the

system of equations (which is theoretically unconditionally stable), a large time step could trigger the model divergence due to the aggregation of errors. Thus, the time-step size should always be studied.

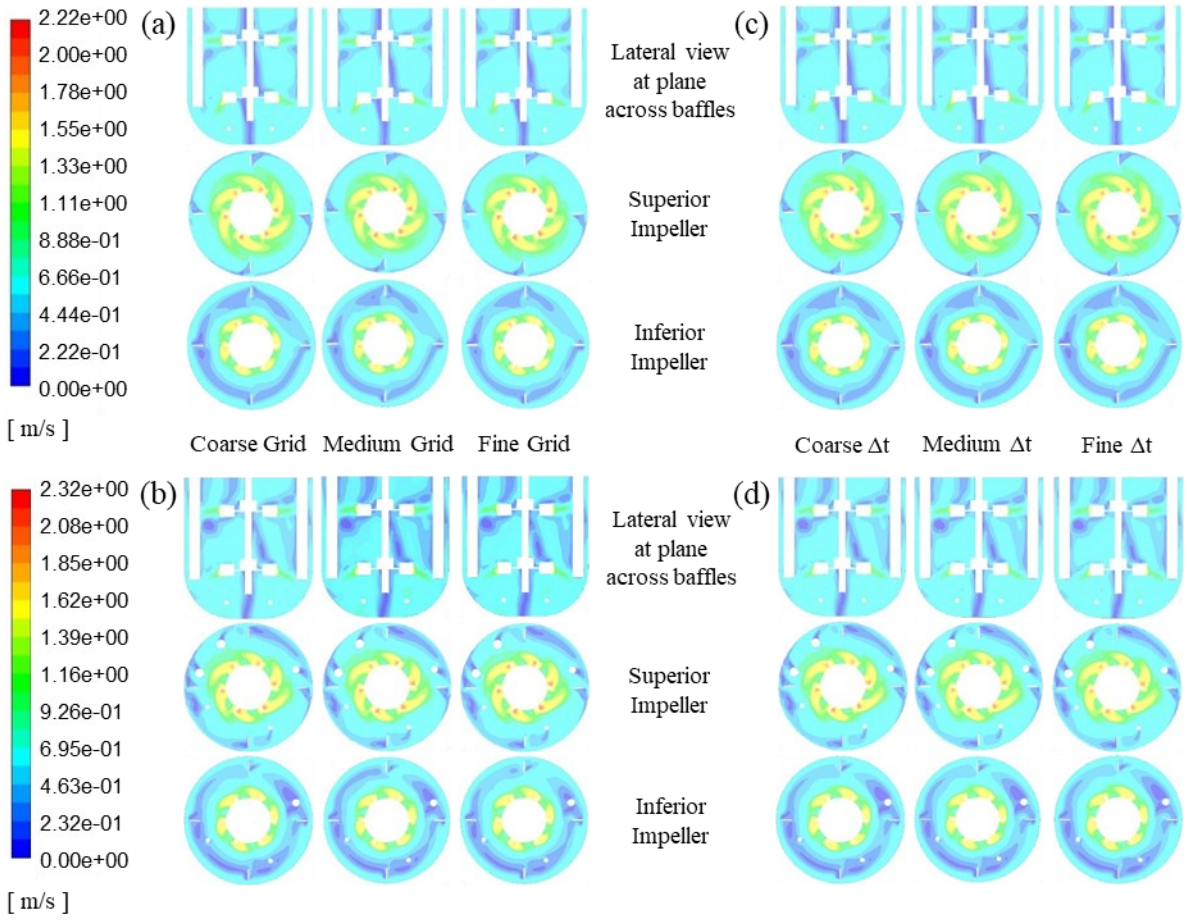

Figure 4.10. Sensitivity analysis of the instantaneous velocity magnitude contours simulated with (a, c) GeomA and (b, d) GeomB. (a, b) Grid study and (c, d) time-step size study. Contours were computed at the end of each simulation. Results were obtained with the k-epsilon set. Figure adapted from Sadino-Riquelme et al. (2021), reprinted with permission of John Wiley and Sons.

Qualitatively, for GeomA and GeomB, an analysis of the velocity magnitude contours negates the appearance of new features in the flow field as the grid or time step is refined, which is a positive sign of grid and time-step size independence (see Figure 4.10).

For GeomA-kε and GeomB-kε, $T_{AVG_{sim}}$ varies less than 3% when using the refined time steps and grids in comparison to the coarse ones (see Table 4.5). Similarly occurs for GeomB-SSTkω (see Table 4.5). If, additionally, it is considered the oscillating nature of the impeller torque, captured by $T_{SD_{sim}}$, the differences between the different grids and time steps are even smaller.

Table 4.5. Grid and time-step size study conducted over the simulated torque. Torque is given as $T_{AVG_{sim}} \pm T_{SD_{sim}}$, in units of [N·m]. Table from Sadino-Riquelme et al. (2021), reprinted with permission of John Wiley and Sons.

Time Step	**Domain Grid**			***Model***
	Coarse	**Medium**	**Fine**	
Coarse	0.1028 ± 0.0008	0.1025 ± 0.0008	0.1026 ± 0.0009	***GeomA-kε***
	0.1130 ± 0.0024	0.1128 ± 0.0024	0.1126 ± 0.0025	***GeomB-kε***
	0.1185 ± 0.0031			***GeomB-SSTkω***
	0.1080 ± 0.0022			***GeomA-SSTkω***
Medium	0.1032 ± 0.0008			***GeomA-kε***
	0.1133 ± 0.0024			***GeomB-kε***
	0.1186 ± 0.0031			***GeomB-SSTkω***
Fine	0.1037 ± 0.0008			***GeomA-kε***
	0.1137 ± 0.0024			***GeomB-kε***
	0.1183 ± 0.0028	0.1157 ± 0.0025	0.1151 ± 0.0020	***GeomB-SSTkω***

Furthermore, for the four models, the instantaneous torque computed on the impeller (moving walls) versus on the stationary walls were compared, for the different grids and time steps (see Table 4.6), as done by Cortada-Garcia et al. (2017). These two torque values are equal due to the conservation of angular momentum, hence small differences are expected for grid-independent results. Torque differences as high as 3.2% were found for GeomA-kε and GeomB-kε. A similar torque difference was obtained for Cortada-Garcia et al. (2017) for its optimal grid (3-4%). Bigger differences were found for GeomB-SSTkω, however, as these are of the same order of magnitude that the differences obtained using the k-epsilon set, the

grid was not discarded. Nevertheless, to make sure that the grid and time-step size were not affecting the flow field prediction, an additional analysis was made for GeomB-SSTkω. The effect of the grid and time-step refinement on the velocity magnitude at different points of GeomB was studied (see Table 4.7). For each monitored point, the differences in $VM_{AVG_{sim}}$ were mostly within the range of the temporal oscillations (captured by $VM_{SD_{sim}}$), suggesting that the velocities are independent of the grid and time-step size.

Table 4.6. Grid and time-step size study conducted over the instantaneous torque computed at the end of each simulation. Torque on impeller and difference with the torque on the stationary walls, given as [N·m] / [%]. Table from Sadino-Riquelme et al. (2021), reprinted with permission of John Wiley and Sons.

Time Step	**Domain Grid**			***Model***
	Coarse	**Medium**	**Fine**	
Coarse	0.1023 / 1.8	0.1023 / 3.2	0.1025 / 3.2	***GeomA-kε***
	0.1167 / 1.4	0.1164 / 0.4	0.1166 / 0.9	***GeomB-kε***
	0.1176 / 6.6			***GeomB-SSTkω***
	0.1053 / 5.5			***GeomA-SSTkω***
Medium	0.1029 / 2.0			***GeomA-kε***
	0.1170 / 1.4			***GeomB-kε***
	0.1194 / 4.2			***GeomB-SSTkω***
Fine	0.1049 / 0.7			***GeomA-kε***
	0.1174 / 1.3			***GeomB-kε***
	0.1222 / 0.1	0.1121 / 3.1	0.1135 / 1.9	***GeomB-SSTkω***

Thus, it was strongly demonstrated that the results obtained for GeomB-kε and GeomB-SSTkω are independent of the grid and time-step size. This was also demonstrated for GeomA-kε. Neither the grid nor the time-step size for GeomA-SSTkω was studied, however, as the complexity of this model is bounded by GeomA-kε and GeomB-SSTkω, and the independence of the results was proved for both cases, it is assumed that the results obtained with GeomA-SSTkω are independent of the grid and time-step size too.

Table 4.7. Sensitivity analysis of the velocity magnitude at different monitoring points, for GeomB-SSTkω. Velocity magnitude is given as $VM_{AVG_{sim}} \pm VM_{SD_{sim}}$, in units of [m/s]. Table from Sadino-Riquelme et al. (2021), reprinted with permission of John Wiley and Sons.

Grid/Time Step	Point-99	Point-104	Point-136	Point-122	Point-131
Coarse/coarse	1.611 ± 0.417	1.470 ± 0.351	0.117 ± 0.050	0.625 ± 0.056	0.354 ± 0.088
Medium/fine	1.629 ± 0.424	1.483 ± 0.355	0.101 ± 0.033	0.667 ± 0.036	0.260 ± 0.055
Fine/fine	1.642 ± 0.444	1.493 ± 0.396	0.089 ± 0.033	0.631 ± 0.052	0.358 ± 0.039
Coarse/medium	1.613 ± 0.413	1.467 ± 0.340	0.121 ± 0.055	0.624 ± 0.049	0.348 ± 0.094
Coarse/fine	1.608 ± 0.408	1.462 ± 0.330	0.123 ± 0.048	0.621 ± 0.042	0.353 ± 0.082

It is important to mention that the results in Table 4.5 are not in the asymptotic range of convergence. However, it is widely recognized that the impellers' shape makes the tank geometry complex, and, for complex geometries, it can be hard to get solutions in the asymptotic range (Coleman & Stern, 1997). That is why this work has taken the analysis of grid and time-step further than in most of the published articles. Thus, although the results are not in the asymptotic range of convergence, it was proved that the results are independent of the grid and time-step size.

4.2.6 Verification and validation

Neither the order-of-accuracy verification nor the Richardson extrapolation analysis was conducted because the results obtained were not in the asymptotic range. For the same reason, the grid convergence uncertainty was estimated based on the grid convergence metric instead of the grid convergence index (GCI), as the latter requires the order-of-accuracy estimation (Coleman & Stern, 1997). Table 4.8 summarizes the uncertainties estimated for each model. U_{exp} was estimated as 8.2%, based on the standard deviation of the triplicated torque measurements made for GeomA (see Table 3.3), and was considered equal for all the models. Comparing the factors of the validation uncertainty, the experimental data contributes the most.

Table 4.8. CFD models uncertainties estimation, in units of [%]. Table from Sadino-Riquelme et al. (2021), reprinted with permission of John Wiley and Sons.

Model	U_{grid}	$U_{\Delta t}$	U_V
GeomA-kε	0.10	0.48	8.2
GeomB-kε	0.18	0.35	8.2
GeomB-SSTkω	0.52	0.25	8.2

To validate each model based on the torque variable, $T_{AVG_{sim,coarse}}$ was compared with $T_{AVG_{exp}}$ (see Table 4.9). In the case of GeomA, the average of the experimental measurements was considered for the analysis. With $|E| < U_V$, the model validation has been achieved, at an 8.2% level, for the four models. Based on the reasoning used in Section 4.2.5, it was assumed that U_V is around 8.2% for GeomA-SSTkω too.

Table 4.9. Validation of the models against experimental torque data. $|E|$ is given as [%]. Table from Sadino-Riquelme et al. (2021), reprinted with permission of John Wiley and Sons.

Domain	**k-epsilon set**	**SST k-omega set**
GeomA	0.95	6.1
GeomB	3.6	1.1

Axial profiles of the radial velocity at three different radial locations in GeomA-kε and GeomA-SSTkω were compared with experimental data obtained from the work of Micale et al. (1999), who studied a tank with dual Rushton turbines and a flat bottom (see Figure 4.11). A perfect prediction of the experimental data cannot be expected due to the geometrical differences in the bottom shape and the spacing between the impellers. Nevertheless, in the superior impeller zone, which could be expected to be less influenced by the bottom shape, the simulations predict closely the experimental radial velocity. For the lower impeller, the amplitude of the peaks was closely predicted at the distances 0.083T and 0.223T from the

impeller tip, although they occur at a different height from the tank bottom. The radial velocities predicted for the zone between the impellers differ more notoriously from the experimental data. This can be explained by the smaller impeller spacing of the system under study in this work. Comparing the numerical settings, in general, the k-omega set predicts bigger velocity peaks than the k-epsilon set and, also, it predicts lower a lower velocity nadir in the zone between the impellers. It would be necessary to study the time-averaged axial profiles to discard whether those differences respond to the analysis of instantaneous values of different moments in the flow field.

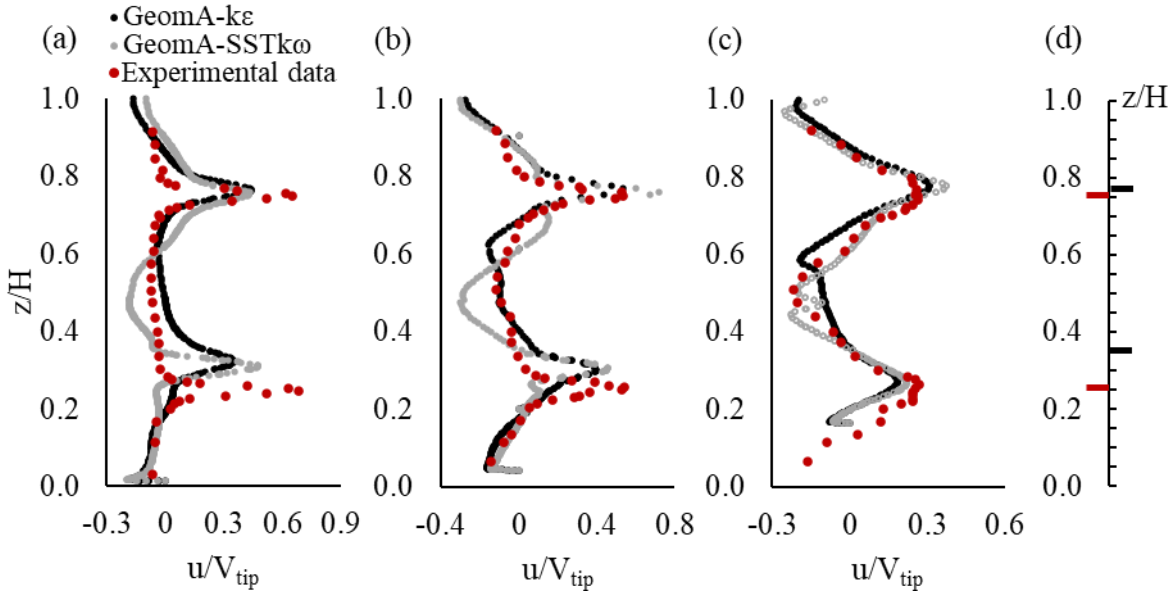

Figure 4.11. Comparison of axial profile of the radial velocity in a plane midway between baffles at different radial distances from the impeller tip: (a) 0.013T, (b) 0.083T, and (c) 0.223T. Experimental data (orange circles) from Micale et al. (1999). In (d) is shown the impeller heights of the experimental system, on the left side, and the CFD domain, on the right side. The predicted profiles correspond to instantaneous data computed at the end of the simulations with GeomA-kε (black circles) and GeomA-SSTkω (grey circles). Figure from Sadino-Riquelme et al. (2021), reprinted with permission of John Wiley and Sons.

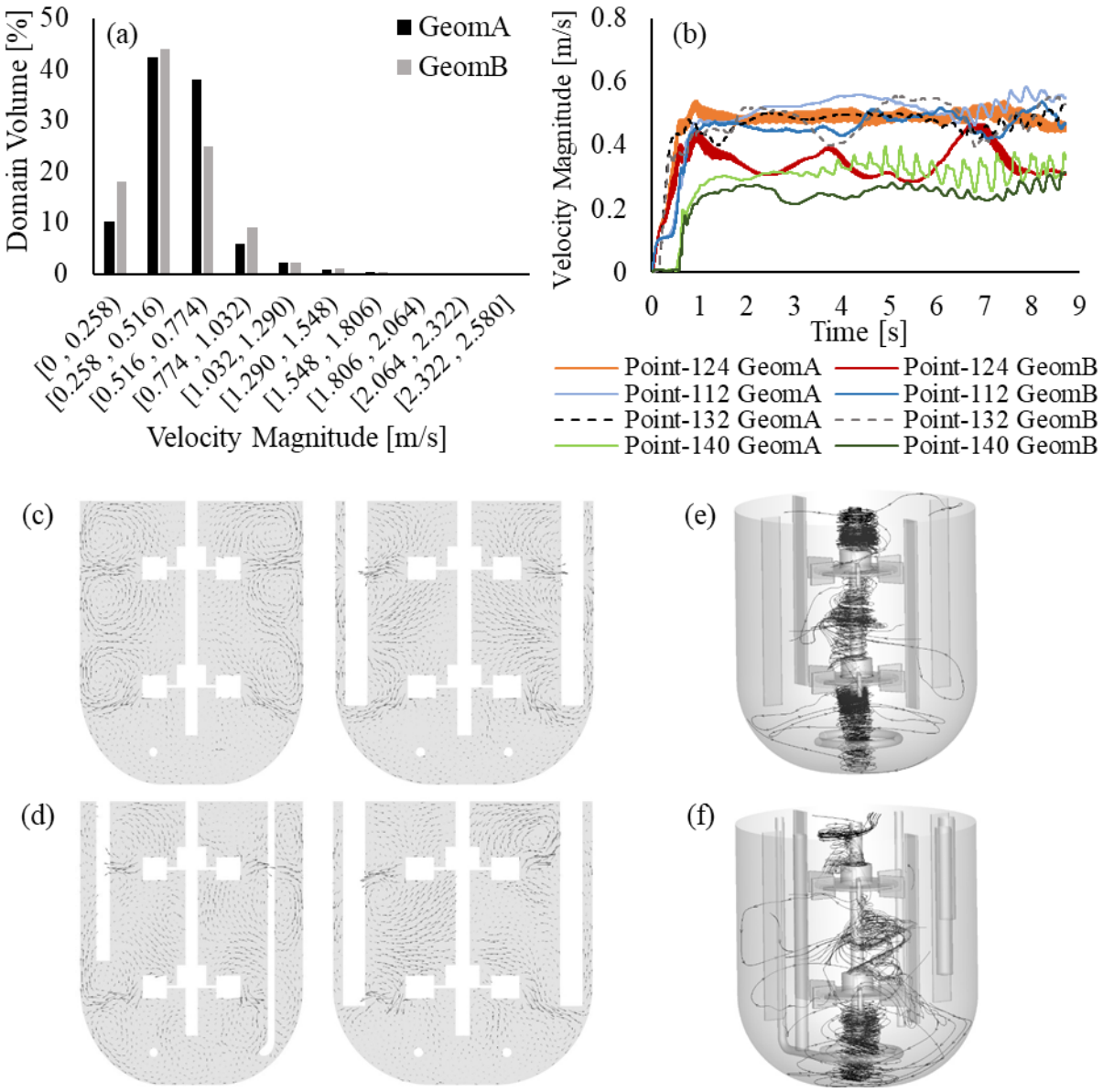

Figure 4.12. Effect of probes. Comparison of (a) instantaneous velocity magnitude distribution, (b) velocity magnitude temporal profile for different monitoring points, (c, d) instantaneous velocity vectors at two different planes for (c) GeomA and (d) GeomB, and (e, f) instantaneous precessional vortex for (e) GeomA and (f) GeomB. Results were obtained with the SST k-omega set. Instantaneous data was computed at the end of the corresponding simulation. Figure adapted from Sadino-Riquelme et al. (2021), reprinted with permission of John Wiley and Sons.

4.2.7 Domain simplification

For both sets of settings, $T_{AVG_{sim}}$ of GeomA is lower than for GeomB (see Figure 4.9). This result demonstrates, first, that the probes affect the prediction of the torque (therefore, they would affect the estimation of the impeller power consumption) and, second, that the models were able to capture the same effect of the probes on the flow field than the experiments. When comparing the velocity magnitude contours, it is apparent that GeomA shows a different flow field than GeomB (see Figure 4.10). Specifically, the probes trigger bigger zones with lower velocities (see Figure 4.12a), as these elements break down the momentum transferred from the impellers. The analysis of velocity magnitude temporal profiles shows that the probes significantly modify the local velocities, especially away from the impellers (see Figure 4.12b). That effect was also verified based on a comparison of the time-averaged velocity magnitude at different monitoring points of both domains (see Table 4.10), from which is possible to confirm that the effect of the probes on the velocity magnitude is negligible close to the impellers but very significant close to the exterior walls. Even more importantly, the probes modify the stable parallel flow pattern in GeomA into an unstable one in GeomB (see Figure 4.12c-d), due to a deflection of the precessional vortex axis between the impellers (see Figure 4.12e-f). The modification of the flow pattern causes changes in the mixing time and power consumption (Rutherford et al., 1996).

Table 4.10. Effect of the probes on the velocity magnitude for the SST k-omega set. Velocity magnitude is given as $VM_{AVG_{sim}} \pm VM_{SD_{sim}}$, in units of [m/s]. Table from Sadino-Riquelme et al. (2021), reprinted with permission of John Wiley and Sons.

Domain	Point-99	Point-104	Point-136	Point-122	Point-131
GeomA	1.5680 ± 0.5384	1.4249 ± 0.3387	0.0579 ± 0.0474	0.5204 ± 0.0870	0.5471 ± 0.0460
GeomB	1.6110 ± 0.4172	1.4695 ± 0.3505	0.1170 ± 0.0500	0.6246 ± 0.0559	0.3536 ± 0.0877

Thus, based on all of the evidence, and regardless of the numerical settings, the probes have a strong influence on the fluid dynamics simulations. Therefore, the estimation of important design parameters would be significantly affected if the probes were eliminated

from the model, such as local and global mixing times, which would impair the prediction of species mass transfer or reaction rates. The effect of the probes could be even more significant when the fluid is highly viscous or has a pseudoplastic behaviour, which is common in the bioprocesses field. In fact, experimentally, a difference of 23% for the torque measured with and without probes, when mixing at 400 rpm a liquid with a viscosity around 70 times higher than that of water, was found, while the same torque difference for water is 15%. Therefore, the CFD domain should include the probes or, at least, the validation procedure should consider the modelling uncertainty that the probes elimination adds to the results.

Regarding the domain simplification based on the tank symmetry, the temporal velocity profile shows that the velocity magnitude is not the same for all the pairs of symmetric points (see Figure 4.13). This evidence supports the fact that, although in the absence of probes the tank geometry might be considered to be symmetric around the impeller axis, the system does not have a symmetrical flow field, especially under turbulent conditions, therefore a domain reduced in this manner will give misleading results, as also discussed by Haringa et al. (2018a).

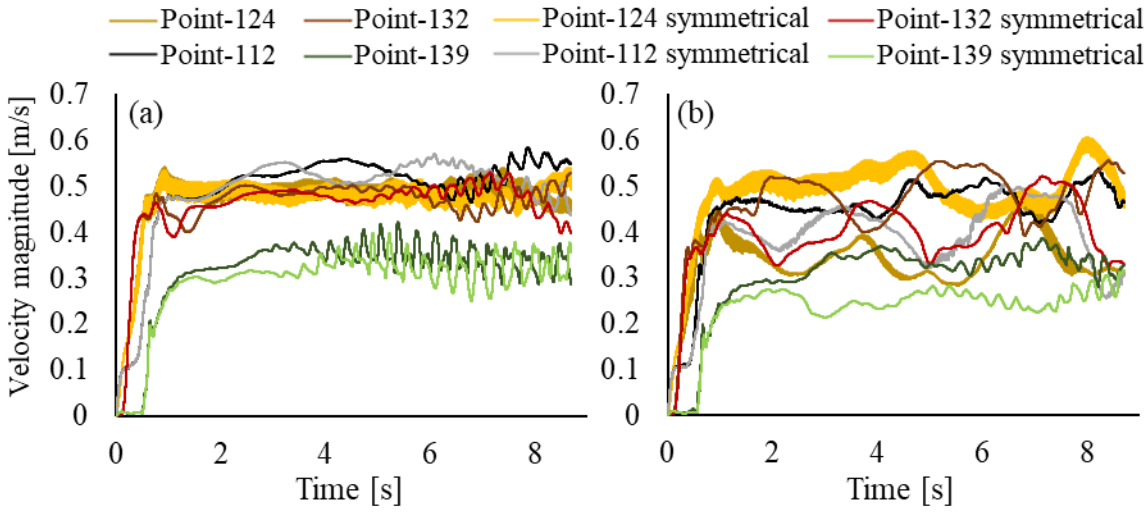

Figure 4.13. Comparison of the velocity magnitude temporal profile on pairs of symmetrical points for (a) GeomA and (b) GeomB. Profiles obtained with the k-epsilon set. Figure adapted from Sadino-Riquelme et al. (2021), reprinted with permission of John Wiley and Sons.

5 CFD SINGLE-PHASE MODELLING – NON-NEWTONIAN FLUID

Based on the learning gathered during the adaptation of the model for the batch abiotic system with water, the systems with non-Newtonian fluids without aeration were addressed next, which is referred to as Step 2. In this step, the effect of the interaction between the impeller mixing and a changing fluid rheology was characterized. In this chapter, CFD modelling is applied to study the evolution of the fermentation fluid flow patterns, velocity field, dead zones and vortical structures, under unaerated conditions.

5.1 Material and Methods

5.1.1 CFD domain and mesh

Only the domain of GeomB was used, which includes all of the internal elements of the tank, with the coarse grid. The geometry and mesh implementation were studied in Chapter 4.

5.1.2 CFD model settings

The CFD models were adapted in Ansys Fluent (version 2019R3). The following assumptions were considered to model the batch abiotic systems with non-Newtonian fluids, without aeration: constant temperature, flat liquid-air interface surface, and free of air entrapment from the interface. In line with the experimental results, the fluids were characterized as pseudoplastic, using the Power Law model. Thus, the described systems are single-phase, and the fluid density is static and homogeneous, while the fluid viscosity depends on the rheological parameters and the local shear rates. The assumptions related to the liquid-air interface were removed afterwards, using a multi-phase model (see Chapter 7).

The rheological and physical properties used to model the fluid of the batch abiotic systems with Xanthan Sol A and Xanthan Sol B are given in Table 3.1. The mixing of a third non-Newtonian pseudoplastic fluid, referred to as Xanthan Sol C, was modelled to evaluate the effect of a higher viscosity on the system fluid dynamics. Xanthan Sol C was characterized with the same rheological and physical properties as Xanthan Sol A, except for

the consistency coefficient that was defined as 1.1731 Pa·s^n, which is one order of magnitude higher than for Xanthan Sol A. Furthermore, to set up the non-Newtonian Power Law model, the software Ansys Fluent requires the specification of lower and upper viscosity limits. The values listed in Table 5.1 were used for that purpose.

Table 5.1. Viscosity limits used to set up the Power Law model on Fluent, in units of [Pa·s].

Fluid	**Lower limit**	**Upper limit**
Xanthan Sol A	10^{-5}	1
Xanthan Sol B	10^{-5}	1
Xanthan Sol C	0.001	300

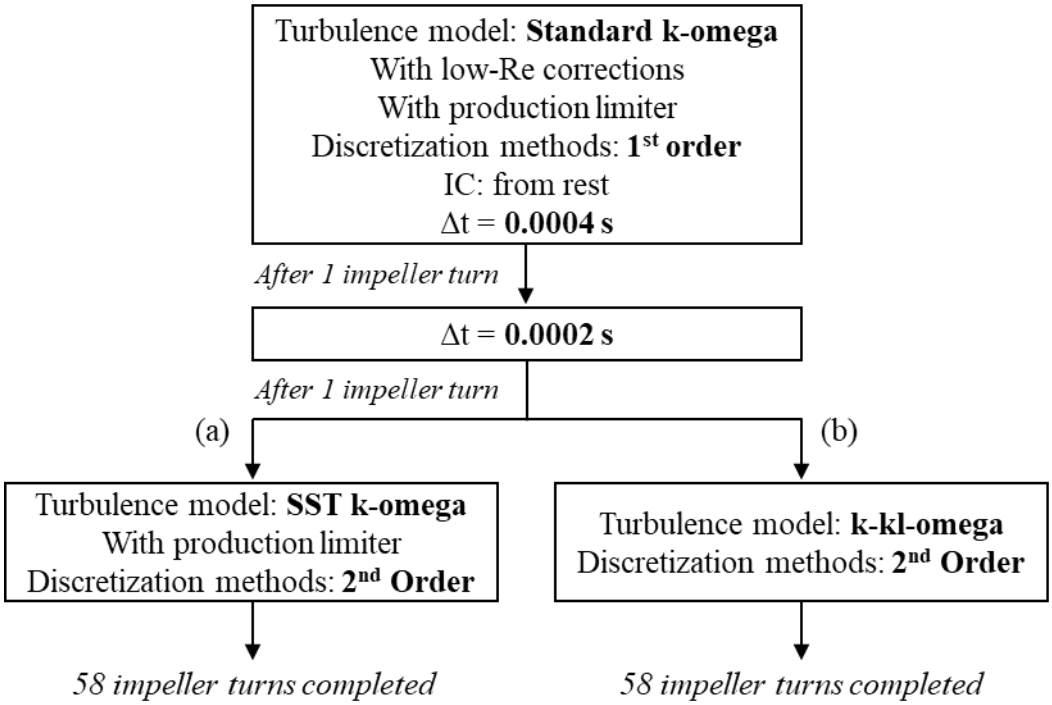

Figure 5.1. Flow diagram of the numerical configuration used to model the batch abiotic systems with Xanthan Sol A and Xanthan Sol B, using the (a) SST k-omega turbulence model and (b) k-kl-omega transition model.

Table 5.2. CFD settings shared by the models of Xanthan Sol A and Xanthan Sol B.

Precision	Double
Coupling scheme	SIMPLE
Solver	Pressure-based with absolute velocity formulation
Body Forces	Gravity
Iterations	Maximum 80 per time step. It was activated the option to stop the iterations when all residuals were below 10^{-5} simultaneously.
Initial conditions	Velocity 0 m/s in all directions (that is, from rest) Turbulence parameters k = 0.1; ω=1
Boundary conditions	
Top wall	Symmetry
Impeller and axis walls	Relative velocity to moving zone 0 rpm
Other walls	No-slip condition
Discretization methods*	
Gradient	Green Gauss node-based
Pressure	PRESTO
*with warped-face gradient correction	
Under-relaxation factors	
Pressure	0.2
Density	0.7
Body forces	0.7
Turbulent viscosity	0.8
Others	Default value

As well as for the case with water, the transient SM method was used to simulate the mixing, with a rotating velocity of 400 rpm for each moving zone. To model the batch abiotic systems Xanthan Sol A and Xanthan Sol B, two numerical configurations were evaluated, one with the SST k-omega turbulence model and the other with the k-kl-omega transition

model. The governing conservation equations of the CFD models can be found in Appendix O.

In both cases, the simulations were initialized using the standard k-omega model and, after completing two impeller turns, the turbulence model was shifted. Additionally, other settings were modified throughout the simulations, such as the discretization methods (except for pressure and gradient) and the time-step size, as detailed in Figure 5.1. The remaining settings were not modified and were the same for both configurations (see Table 5.2).

In the case of Xanthan Sol C, anticipating the future need of studying the effect of the aeration, a multi-phase Eulerian model with implicit volume fraction parameters formulation was used. Xanthan Sol C and air were defined as primary and secondary phases, respectively. However, the volume fraction of air was set equal to zero for the whole domain and the volume fraction equation was disabled. Thus, in practice, a multi-phase model was adapted to represent a single-phase system.

The simulation of Xanthan Sol C was initialized using the standard k-omega model (with low-Re correction, shear flow corrections and production limiter) with first-order discretization methods (except for pressure and gradient). After completing ten impeller turns, the turbulence model was shifted to laminar and the discretization methods to second-order. The remaining settings were set up as given in Table 5.3.

The use of the k-kl-omega transition model and laminar model was based on the analysis of the Reynolds number and the turbulent viscosity ratio of each batch abiotic system, as these parameters indicate whether the fluid flow is in the turbulent, transitional, or laminar regime. This numerical aspect is further discussed in Section 5.2.1.

It is important to mention that, for Step 2, the same simulation completion criteria described for Step 1 were used (see Chapter 4). For validation purposes, for each simulation, the impeller torque was calculated as $T_{AVG_{sim}} \pm T_{SD_{sim}}$ over the last 10 impeller turns.

Table 5.3. CFD settings used for Xanthan Sol C.

Precision	Double		
Coupling scheme	Phase coupled SIMPLE		
Solver	Pressure-based with absolute velocity formulation		
Body Forces	Gravity		
Time-step size	0.0004 s		
Iterations	Maximum 60 per time step. It was activated the option to stop the iterations when all residuals were below 10^{-5} simultaneously.		
Initial conditions	Velocity 0 m/s in all directions (that is, from rest) Turbulence parameters k = 0.1; ε=0.1		
Boundary conditions			
Top wall	Degassing		
Impeller and axis walls	Relative velocity to moving zone 0 rpm		
Other walls	No-slip condition		
Interphase interactions			
Interfacial area	ia-symmetric		
Others	None		
Discretization methods*			
Gradient	Green Gauss node-based		
Pressure	PRESTO		
*with warped-face gradient correction			
Under-relaxation factors			
Pressure	0.2	Turbulent kinetic energy	0.5
Density	0.7	Specific dissipation rate	0.5
Body forces	0.5	Turbulent viscosity	0.8
Momentum	0.5	Others	Default value

Hereinafter, for ease of reference of the models with non-Newtonian fluids, they will be named according to the fluid and the turbulence model used by the CFD configuration. Thus, XSolA-SSTkω and XSolA-kklω correspond to the models for Xanthan Sol A with, respectively, the SST k-omega and the k-kl-omega models. Similarly named are the models for Xanthan Sol B, XSolB-SSTkω and XSolB-kklω. Furthermore, the model adapted for the batch abiotic system with water (see Chapter 4), originally named as GeomB-SSTkω, was renamed as Water-SSTkω, for the purposes of this chapter.

5.1.3 Analysis of mixing mechanisms

To investigate the macro and mesomixing mechanisms, the existence of vortical structures was analyzed, based on the simulated data, using the software Tecplot. The precessing vortex cores were extracted using the method of the velocity gradient eigenmodes. To visualize their directionality, streamtraces were drawn from the vortex cores. On the other hand, the trailing vortices were drawn as iso-surfaces of constant vorticity magnitude at 300, 240 and 180 s^{-1}.

Furthermore, the maximum turbulence length scale (l) was estimated, using a user-defined function with Equation 5.1. Similarly, to investigate the micromixing, the minimum Kolmogorov length scale (λ_K) was estimated, using a user-defined function with Equation 5.2. For the non-Newtonian fluids, the viscosity was calculated according to Equation 5.3.

$$l = 0.09^{3/4} \cdot \frac{k^{3/2}}{\varepsilon} \tag{5.1}$$

$$\lambda_K = \left(\frac{(\eta/\rho)^3}{\varepsilon} \right)^{1/4} \tag{5.2}$$

$$\eta = \frac{\tau}{\dot{\gamma}} \tag{5.3}$$

5.2 Results and Discussions

5.2.1 CFD settings analysis

For an accurate simulation of the mixing process, all of the internal elements of the bioreactor were included in the CFD domain, even the probes, because it was previously

proved that they affect the fluid flow patterns. Furthermore, to have an insight into the macro-instabilities, transient simulations are necessary (see Section 4.2.3). All of these factors add to the complexity of the CFD models, requiring a small time-step to achieve a convergent, numerically stable, and time-step size independent simulation. That is the reason why, with the existing computational capabilities, it is not possible to simulate the continuous abiotic systems within a reasonable period of time and, therefore, the strategy of simulating the batch abiotic systems, to approach the fermentation process stages, remains the only realistic option for now.

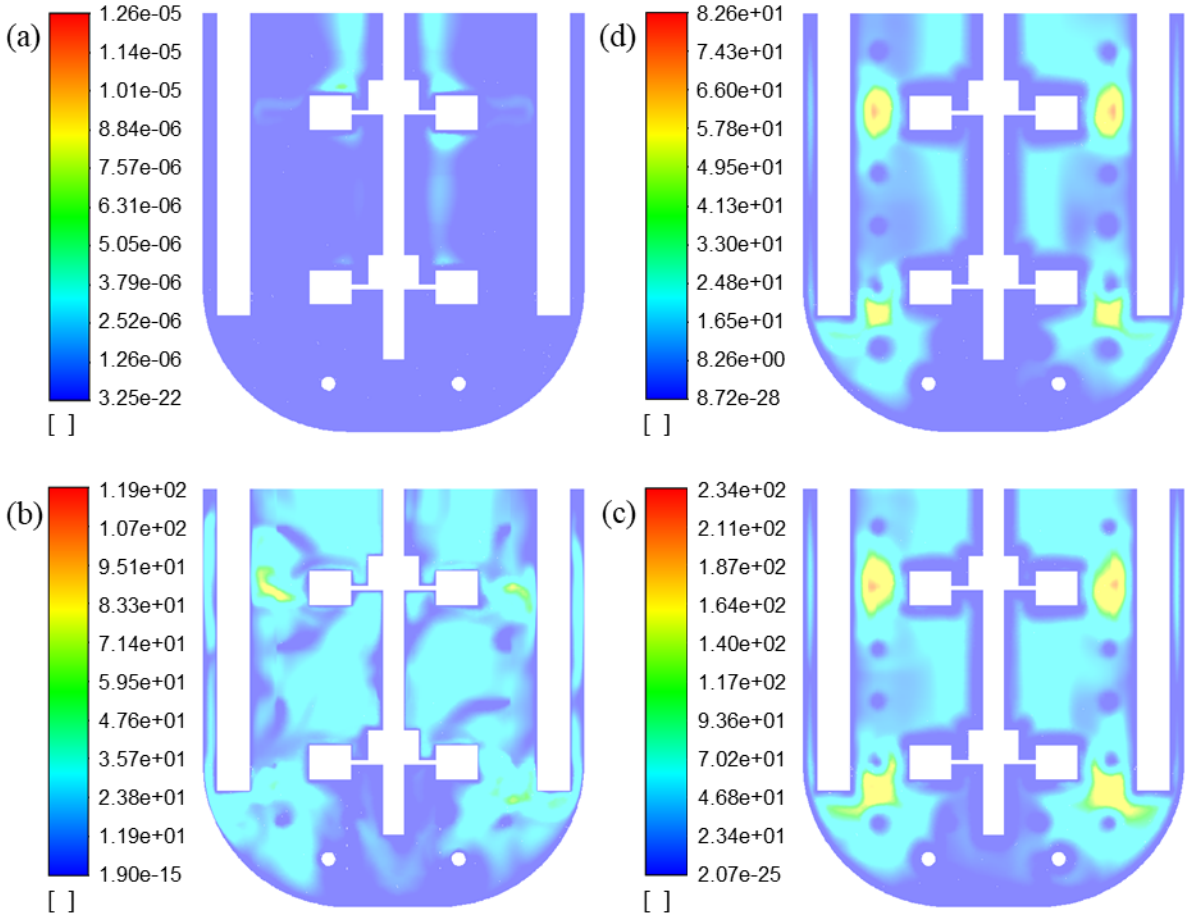

Figure 5.2. Contours of instantaneous turbulent viscosity ratio, at plane YZ, simulated for the batch abiotic systems with non-Newtonian fluids. (a) Xanthan Sol C, after 10 impeller turns with standard k-omega; (b) XSolB-SSTkω, after 58 impeller turns; (c) XSolB-kklω, after 58 impeller turns; and (d) XSolA-kklω, after 58 impeller turns.

The residual values were verified for all the simulations. In the case of XSolA-SSTkω, initially the residual for the turbulence parameter ω converged intermittently, to finally stop converging during the simulation of the 6th impeller turn, while all the other residuals were below 10^{-5} at every time step. For XSolB-SSTkω, all the residuals were below 10^{-5} at every time step, except the residual of the parameter ω which did not converge in a few time steps (approximately 17 out of 750 time-steps). In the cases of XSolA-SSTkω and XSolB-SSTkω, although the parameter ω did not meet the convergence criterion, the order of magnitude of its residual was still acceptable (10^{-5}). For all the other simulations of Step 2, the residuals values were below 10^{-5} at every time step. Furthermore, based on the monitored variables, numerical instabilities were discarded, and it was ensured that the systems were in stationary state over the last 10 impeller turns. Also, the Y^+ values were checked (see Appendix Q).

According to the analysis of the Reynolds number, calculated using Equation 3.2, the systems with Xanthan Sol C, Xanthan Sol B and Xanthan Sol A are all in the transitional flow regime ($10 \leq Re^* \leq 10^4$). However, the analysis of the turbulent viscosity ratio allowed us to conclude differently (see Figure 5.2). For this study, it was accepted, as a rule of thumb, that a turbulent viscosity ratio above 10 and below 5 indicates, respectively, a turbulent and a laminar flow regime, while a value between 5 and 10 corresponds to a transitional regime. Therefore, for Xanthan Sol C, even though Re^*=312, the flow actually corresponds to a laminar regime based on the turbulent viscosity ratio. In the case of Xanthan Sol A, the turbulent viscosity ratio values have a broader distribution, spanning the three flow regimes, but prevail the zones in the laminar and transitional regimes. As previously described, the simulation with XSolA-SSTkω had convergence issues related with the parameter ω, which has been attributed to the use of a turbulent model to characterize a system where the turbulent regime is not predominant. In consequence, the model XSolA-SSTkω was discarded and only XSolA-kklω was used to study the system Xanthan Sol A. With respect to Xanthan Sol B, the turbulent viscosity ratio values span the three flow regimes as well, but the turbulent regime is more prevalent than for Xanthan Sol A. So much so that the results obtained with XSolB-SSTkω and XSolB-kklω are very similar, in agreement with the fact that the Reynolds number of Xanthan Sol B is very close to the limit between the transitional and turbulent range. As there is not enough information to ensure which one of the models

adapted for Xanthan Sol B is better than the other one, the results of both are considered in this study. It is hypothesized that, probably, the real behaviour of the system Xanthan Sol B is at some point in between the predictions of XSolB-SSTkω and XSolB-kklω.

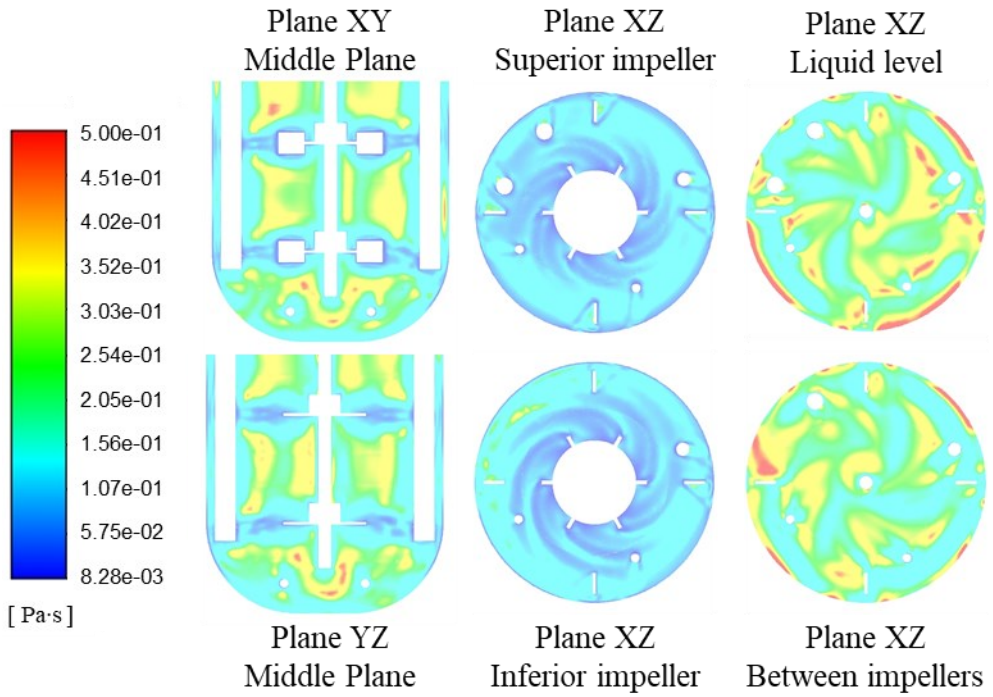

Figure 5.3. Contours of instantaneous viscosity simulated for the batch abiotic system with Xanthan Sol C, with the preliminary lower and upper viscosity limits (0.001 and 0.5 Pa·s, respectively), after 20 impeller turns.

As mentioned before, ANSYS Fluent requires inputting a lower and upper viscosity limit for the non-Newtonian Power Law model. In other words, a Power Law fluid is handled like a Carreau fluid. Therefore, it is important to set up limits that will not artificially influence the simulation of the mixing system. This was evident for the case with Xanthan Sol C, for which preliminarily the upper limit was set as 0.5 Pa·s. However, after the simulation of several impeller turns, the contours at different planes showed that the viscosity reached the maximum allowed value in several zones (see Figure 5.3). This observation raised the question of whether the applied upper limit was too low. During the experimental characterization of Xanthan Sol A, the maximum measured viscosity was 0.2 Pa·s at a shear

rate of 0.36 s^{-1}, but lower shear rates can be found in the bioreactor and, therefore, higher viscosities. According to the literature, Xanthan solutions can reach viscosities up to 8 and 200 Pa·s at 0.1 and 0.001 s^{-1}, respectively (Xue & Sethi, 2012; Zhong et al., 2013). Based on this, the simulation for Xanthan Sol C was re-started, using 300 Pa·s as the upper limit. Similar attention was given to the lower viscosity limit. Thus, it was ensured that the applied viscosity limits did not affect the results obtained with the models of the batch abiotic systems with non-Newtonian fluids (see Table 5.4). See viscosity contours in Appendix Q.

Table 5.4. Minimum, maximum and volume-average instantaneous values of the simulated viscosity for the systems with non-Newtonian fluids, computed after 58 impeller turns. Viscosity is given in units of [Pa·s].

Fluid	Minimum	Maximum	Volume-average
XSolA-kklω	0.00052	0.2694	0.01979
XSolB-kklω	0.00044	0.0189	0.00555
XSolB-SSTkω	0.00045	0.0273	0.00498
XSolC-lam	0.00818	5.8260	0.20724

5.2.2 CFD model validation

Observing Figure 5.4, it is apparent that the CFD models successfully predicted the effect that the fluid viscosity has on the torque. In particular, the models XSolA-kklω and XSolB-kklω satisfactorily captured the effect of the fluid rheology on the torque for the non-Newtonian systems in the transitional flow regime. This is a relevant result because it is the first time that the k-kl-omega transition model is evaluated for the simulation of stirred tanks.

To validate the model of each batch abiotic system with non-Newtonian fluids, $T_{AVG_{sim}}$ was compared with $T_{AVG_{exp}}$, obtaining $|E|$ below 5% (see Table 5.5). These are small errors in comparison to the ones obtained by Ebrahimi et al. (2019), which vary between 5.7% and 14.9% for the simulations of dual impellers mixing water with Re between 11,700 and 35,000. It is important to notice that the cited article used power values for validation

purposes, which is analogous to using torque, based on their linear relationship (see Equation 3.5). In the case of XSolC-lam, although not having experimental data to compare with, it can be expected to observe a higher relative error, related to the use of a multi-phase model with single-phase conditions, according to the analysis presented in Section 6.2.1.

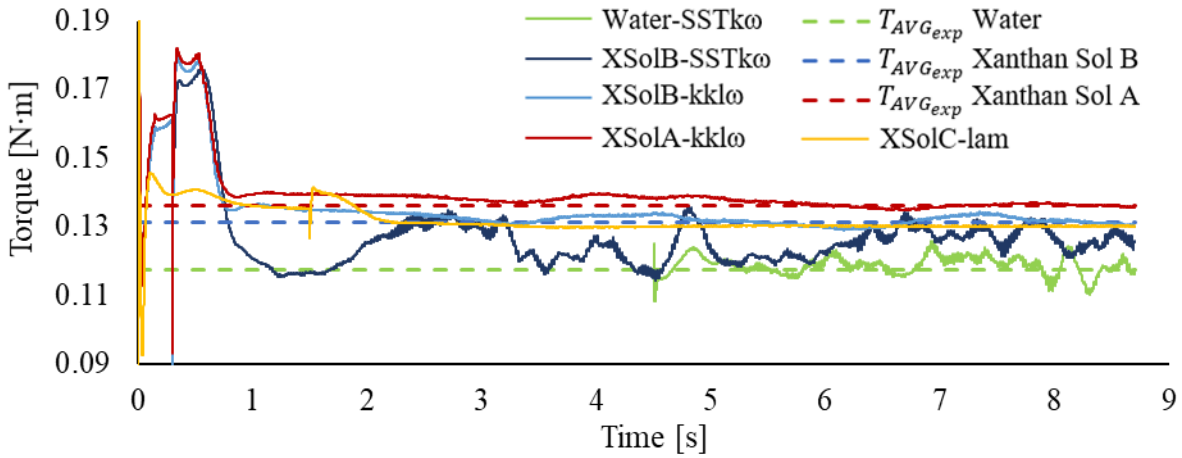

Figure 5.4. Torque temporal evolution simulated for the batch abiotic systems with non-Newtonian fluids. The $T_{AVG_{exp}}$ values are plotted against the flow time.

Previously, for the verification analysis of the model Water-SSTkω, U_V was estimated as equal to 8.2% (see Section 4.2.6). Assuming that the validation uncertainty is the same for the batch abiotic systems with non-Newtonian fluids, with $|E| < U_V$, the CFD models for Xanthan Sol A and Xanthan Sol B are successfully validated, at 8.2% uncertainty level.

Table 5.5. Validation of the models for the batch abiotic systems with non-Newtonian fluids. Simulated torque is given as $T_{AVG_{sim}} \pm T_{SD_{sim}}$, in units of [N·m], and |E| is given as [%].

Model	**Torque**	$\|E\|$
XSolA-kklω	0.1364 ± 0.0003	0.3
XSolB-kklω	0.1320 ± 0.0011	0.7
XSolB-SSTkω	0.1269 ± 0.0029	3.2
XSolC-lam	0.1301 ± 0.0001	-

Additionally, it is interesting to notice that a lower torque for Xanthan Sol C than for Xanthan Sol A and Xanthan Sol B was predicted. Considering that Xanthan Sol C has a significantly higher viscosity than the other fluids, this result may appear erroneous, but it is not. Actually, it is in agreement with the power number curve behaviour, as Xanthan Sol C has Re^{*}=236 which corresponds to a power number smaller than for the other systems and, therefore, to a smaller torque. Thus, the model XSolC-lam is assumed as valid too.

5.2.3 Analysis of mixing mechanisms

Based on the analysis of the flow regime, it can be expected that the mixing process of the system with Xanthan Sol C will depend more on the micromixing than on the macro or mesomixing scales, contrary to what is predicted for the other systems. A comparative analysis of the turbulence length scale and Kolmogorov scale also supports that hypothesis (see Table 5.6). Furthermore, the Kolmogorov scale for Xanthan Sol B (as mentioned before, it is hypothesized that the real behaviour of the system Xanthan Sol B is at some point in between the predictions of XSolB-SSTkω and XSolB-kklω), as well as for water, would be around 50% lower than for Xanthan Sol A. This scale would explain the significantly higher mixing time of the system Xanthan Sol A in comparison to the other systems experimentally studied.

Table 5.6. Instantaneous minimum Kolmogorov scale and maximum turbulence length scale, computed after 58 impeller turns, in units of [m].

Model	Kolmogorov Scale	Turbulence Length Scale
XSolA-kklω	1.85e-05	0.065
XSolB-SSTkω	4.06e-06	0.004
XSolB-kklω	1.42e-05	0.060
XSolC-lam	0.001	0.0002
Water-SSTkω	8.76e-06	0.004

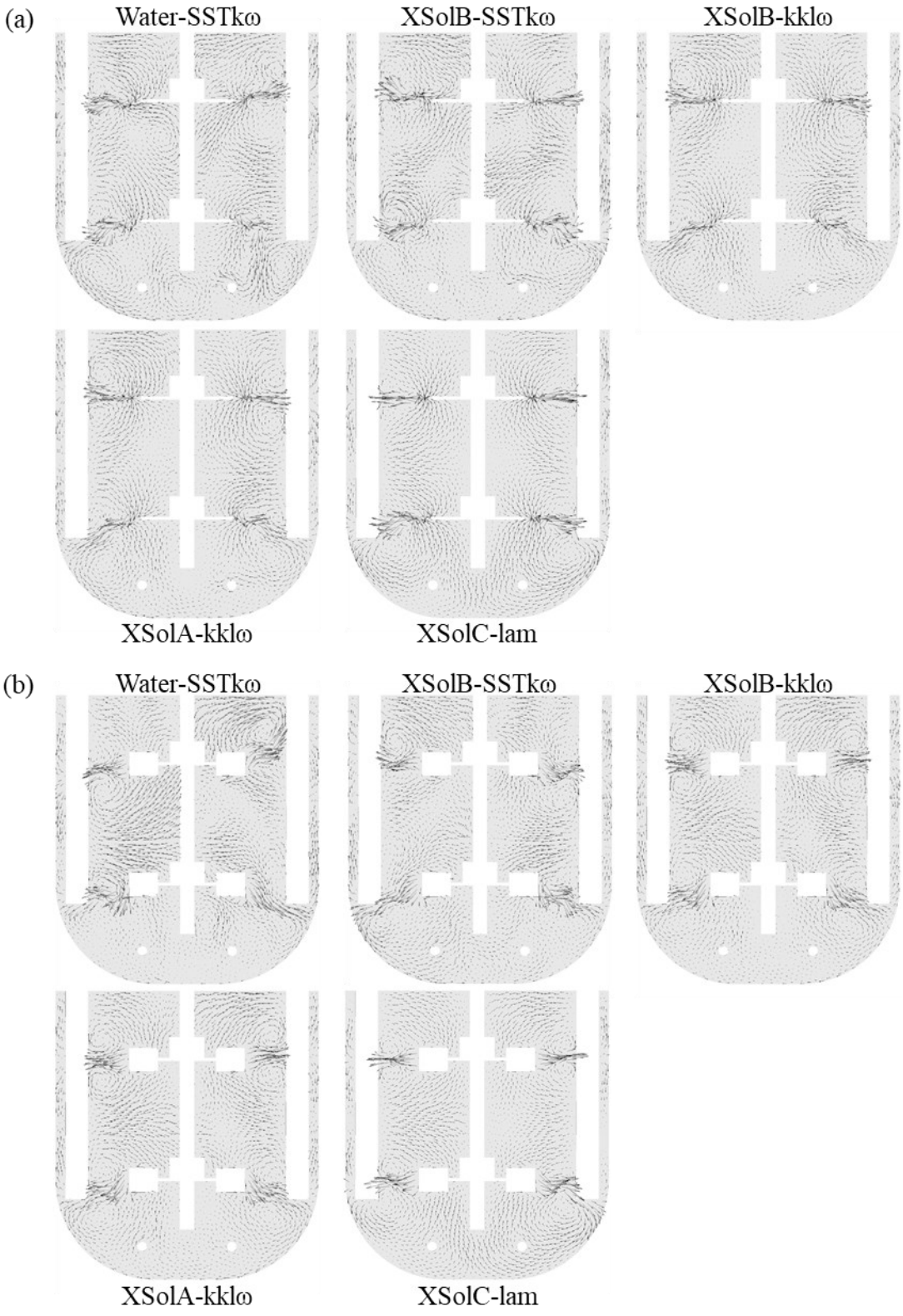

Figure 5.5. Comparison of the instantaneous velocity vectors, after the simulation of 58 impeller turns, between the different batch abiotic systems, at (a) YZ and (b) XY planes.

The velocity vectors of the systems were compared with those described by Rutherford et al. (1996) for stable flow patterns in a dual-Rushton turbine stirred vessel. Based on the behaviour of the vectors between the upper and lower impellers and at the bottom of the fermenter, it is concluded that the systems with water and Xanthan Sol B do not have stable flow patterns, while the system with Xanthan Sol C has a parallel stable flow. In the case of Xanthan Sol A, the criterion of a parallel pattern is met by the zone between the impellers but not by the bottom zone (see Figure 5.5). The flow patterns can also be studied from the examination of the lower and upper impeller torque. Both torque values are expected to be similar in a system with a parallel flow, meaning that the impellers are working independently of each other. As expected, this condition is only fulfilled by Xanthan Sol C (see Table 5.7).

Table 5.7. Instantaneous lower and upper impeller torque values, computed after 58 impeller turns, in units of [N·m].

Model	**Upper impeller**	**Lower impeller**
XSolA-kklω	0.07599	0.05960
XSolB-SSTkω	0.06917	0.05621
XSolB-kklω	0.07332	0.05676
XSolC-lam	0.06631	0.06378
Water-SSTkω	0.06558	0.05197

The flow patterns are of importance because they affect the mixing time. Among the stable patterns, a parallel flow would have a weaker interchange between the upper and lower zones of the tank, increasing the mixing time, but unstable flow patterns have been related to the highest mixing times (Rutherford et al., 1996). In this work, however, the lowest mixing times are associated with unstable flow patterns. Nevertheless, this is not necessarily contradicting the conclusions made by Rutherford et al. (1996), as those conclusions were based on experiments with the same fluid, while, in this case, the fluids are significantly

different and in different turbulence regimes. In any event, modifying the flow of the system Xanthan Sol A from parallel to merging could help to reduce the mixing time.

Among the three abiotic systems experimentally studied, the velocity not only changed in direction but also in magnitude. A comparative analysis of the instantaneous velocity magnitude contours shows a significant reduction of the velocity close to the walls, the liquid surface and between the impellers, as the fluid becomes more pseudoplastic (see Figure 5.6a); while the time-averaged contours reveal that the higher velocities span less area, but more symmetrically, around the impellers (see Figure 5.6b). The latter is a consequence of the direction of the impeller discharge stream. The impeller discharge stream for the system with water has axial and radial components, while it is mostly radial for the other fluids. In terms of the mixing time, that may not be detrimental for the system Xanthan Sol B but it is a disadvantage for the case with Xanthan Sol A. Adding an axial component to the impeller discharge stream of Xanthan Sol A, could help to reduce the stagnant zones and mixing time.

Over the fermentation process, an additional factor can impair the homogenization of the system, which is the stagnation of the fluid into dead zones. In this work, the definition of dead zone used by Vesvikar and Al-Dahhan (2005) was applied. This definition considers the zones with velocity magnitude lower than 5% of the maximum velocity magnitude (V_{max}) of the system. Based on this concept, when the broth properties evolve from water to Xanthan Sol B and Xanthan Sol A, although there is a significant increment of fluid volume with velocities below 20% V_{max}, it does not significantly affect the dead zone volume (see Figure 5.7a). On the other hand, if the broth properties evolve to Xanthan Sol C, the dead zones span 14% of the system volume, which is almost 5-fold higher than for water (see Figure 5.7b). The contours of velocity magnitude of Xanthan Sol C are shown in Appendix Q.

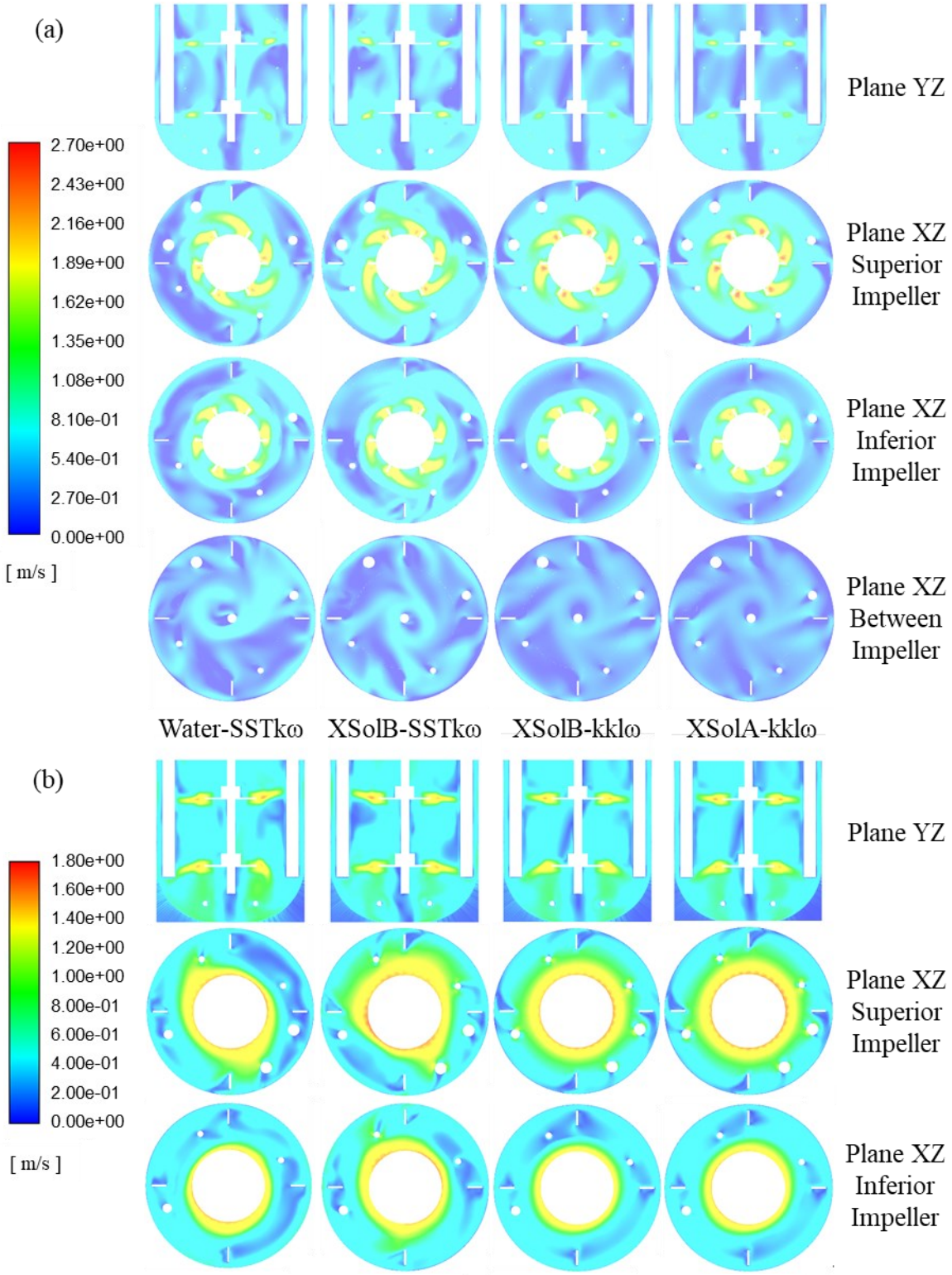

Figure 5.6. Comparison of the velocity magnitude. Contours of (a) instantaneous values, after the simulation of 58 impeller turns, and (b) time-averaged values over the last impeller turn.

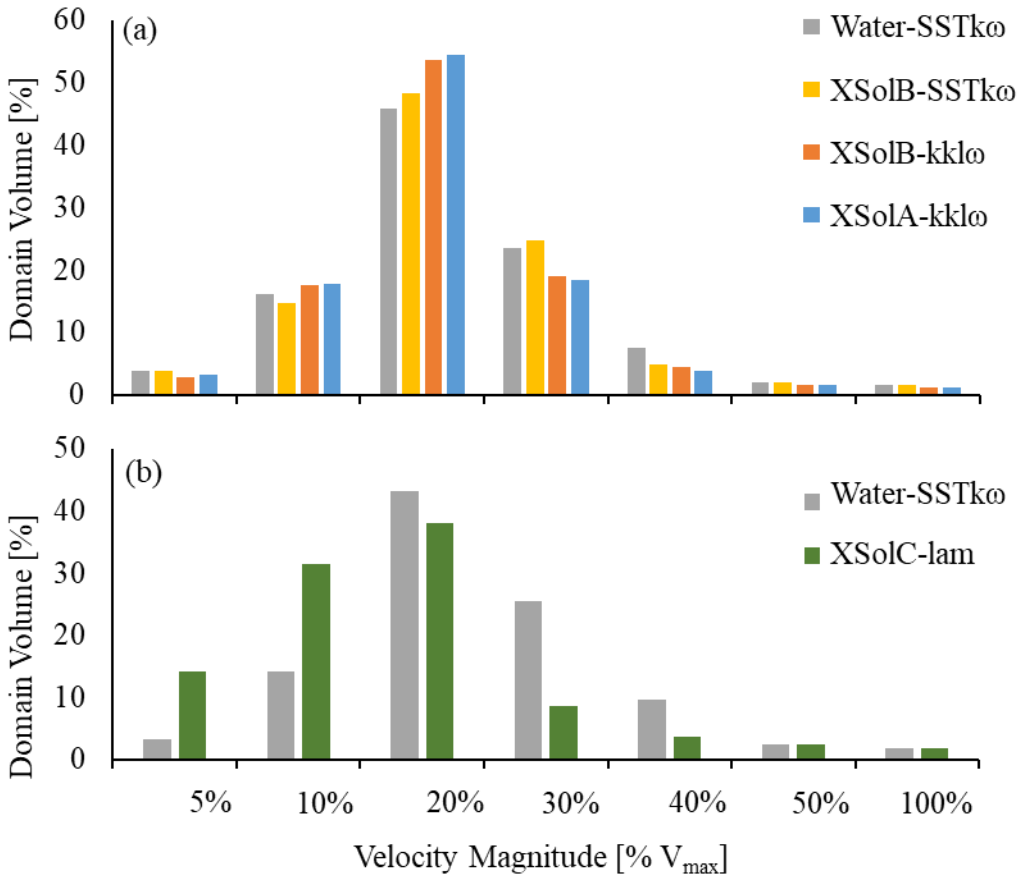

Figure 5.7. Analysis of velocity magnitude distribution for the quantification of dead zones volume increment, when the system evolves (a) from water to Xanthan Sol B and Xanthan Sol A, and (b) from water to Xanthan Sol C.

The rotation of the Rushton turbines creates several vortical structures that enhance the mixing process by creating flow instabilities. The trailing vortices are formed just behind the blades and affect the flow due to their periodic passage (see Figure 5.8a-b). For the systems with Xanthan solutions, the trailing vortices dissipated at a shorter radial distance from the shaft than for the case with water, due to the higher viscosities that dissipate the energy of the trailing vortices into heat. Besides, the vertical separation distance between the trailing vortices of each blade is stretched as the fluid is more pseudoplastic. Overall, the trailing vortices of the superior impeller are slightly different from those of the inferior impeller.

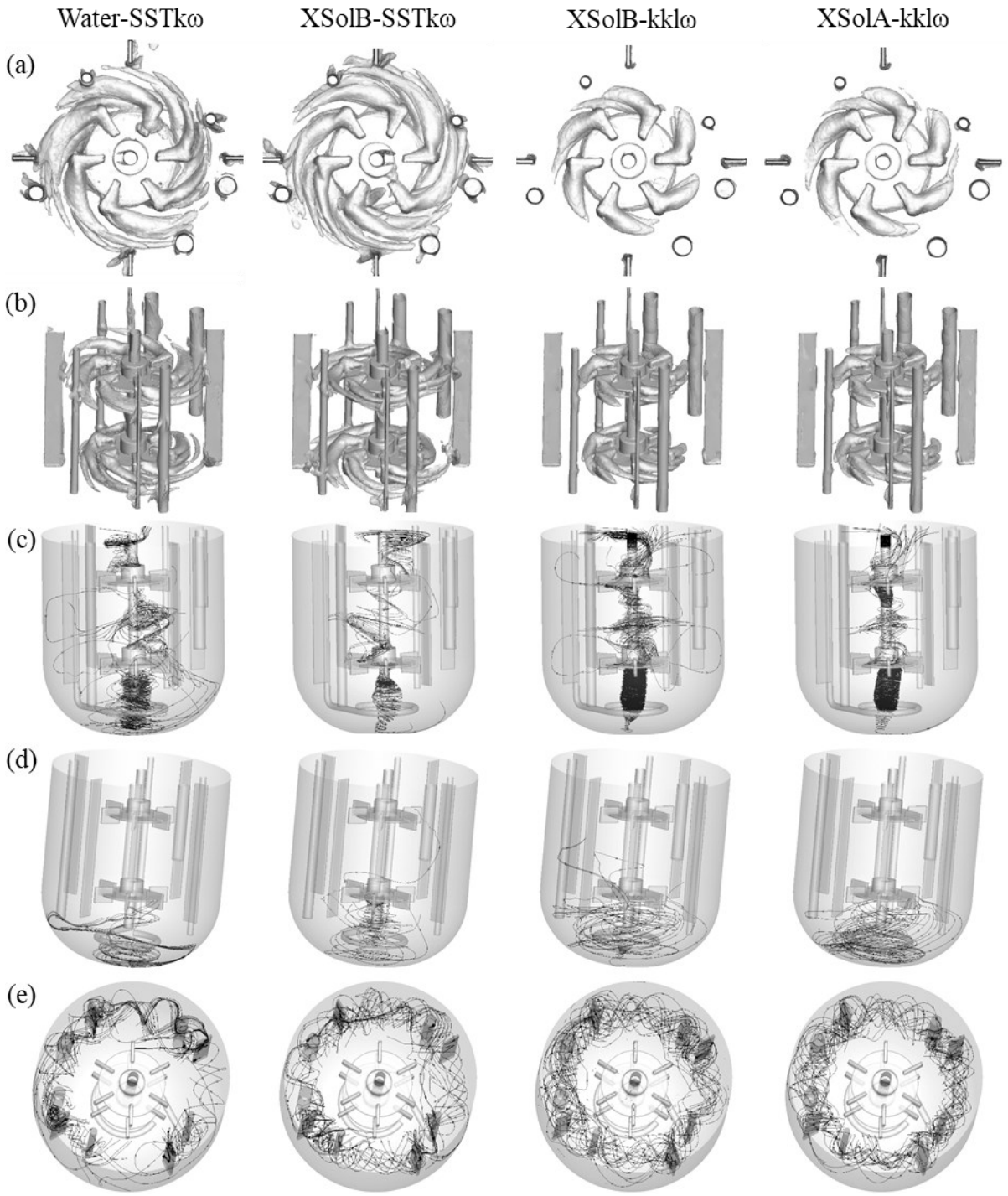

Figure 5.8. Visualization of the instantaneous vortical structures, after the simulation of 58 impeller turns. (a) Upper view of trailing vortices; (b) lateral view of trailing vortices; (c) precessional vortices around the axis; (d) Ekman pumping; and (e) vortices around probes, baffles and sparger pipe.

An additional vortical structure can be found around the impeller axis (see Figure 5.8c). It is an effect of a phenomenon called the Ekman Layer, where the pressure gradient force, the Coriolis force and the turbulent drag play a fundamental role. The difference between the vorticity in the bulk of the fluid and the tank bottom generates a vertical velocity that, in the systems studied for this work, pumps the fluid upwards (see Figure 5.8d). Such a phenomenon is called Ekman pumping or Ekman blowing, and it can be associated with a precessional vortex type of macro-instability (Lavezzo et al., 2009). This feature is an advantage when there are particles that need to be suspended, such as the microorganisms inside the bioreactor. Furthermore, the unstable flow patterns of the abiotic systems with water and Xanthan Sol B can be explained by the behaviour of the vortices around the axis, especially by its asymmetric shape around the shaft, in the zone between the impellers.

Other vortical structures are formed around the probes, baffles, and sparger (see Figure 5.8e). It is important to highlight the existence of these vortices because most of the time these elements are not included in the CFD domain, however, as shown here, they play a role in the fluid dynamics at a mesomixing scale.

Also, the vortex around the impeller axis would explain the flow pattern differences observed in the tank bottom, when comparing Xanthan Sol C with the other batch abiotic systems (see Figure 5.9).

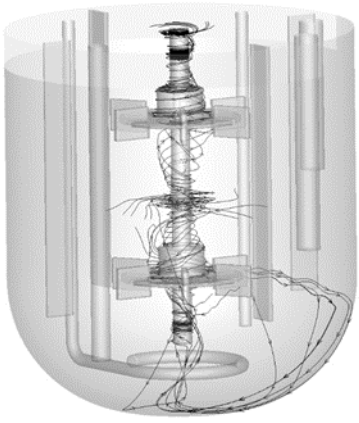

Figure 5.9. Visualization of the instantaneous precessional vortices around the axis of Xanthan Sol C, after the simulation of 58 impeller turns.

Based on the experimental and computational results, it is hypothesized that the aeration would modify the trailing vortices and the Ekman pumping by the onset of the air cavities and the modification of the pressure gradients in the bottom zone of the tank, respectively. In fact, these changes could be the reason behind the increment in the mixing time for the abiotic system with water when including the aeration. Regarding the vortices between the baffles, it is not expected they would change with the aeration. On the contrary, those vortices would affect the bubbles' pathlines. Currently, the CFD models with aeration are being adapted to study the veracity of these hypotheses.

6 CFD MULTI-PHASE MODELLING – NEWTONIAN FLUID

The CFD modelling of the batch abiotic systems under aerated conditions was considered relevant to identify the limitations and capabilities of this computational approach to model the effect of the dynamic interaction between the broth rheology and the aeration on the fluid dynamics of the alginate fermentation. The multi-phase simulation of the system with water was addressed first, which is referred to as Step 3. In this step, the impact that the common assumption of a flat liquid level has upon the results of the CFD modelling of mechanically mixed tanks was analyzed. In this chapter, the evaluated workflows to set up the models, without and with aeration, are described in detail. Additionally, the CFD models are applied to study the effect of the onset of a surface vortex and air cavities on the mixing mechanisms.

At an initial stage of Step 3, the batch abiotic systems with PEG Sol A and PEG Sol B were modelled, as well as the case with water. Those preliminary models and results are detailed in Appendix R.

6.1 Material and Methods

6.1.1 CFD domain

To study the effect of the flat liquid level assumption, two three-dimensional domains were used, without and with headspace. For the former, GeomB was used, whose geometry implementation was described in Chapter 4. For the latter, GeomB was modified into a new domain, called GeomC. Specifically, the exterior wall and the impeller axis were extended 16 cm upward. The probes, baffles and the sparger tube were also extended, but only 5.5 cm upward. Thus, while GeomB considers only the volume of the liquid with a flat and fixed upper level; GeomC includes a headspace for air, enabling a free surface modelling of the liquid level. As in the experimental system, the headspace was enclosed by a lid, where a hole (1 cm diameter) was placed to allow the air to escape. The part of the domain that GeomC has in common with GeomB (hereinafter named shared domain) preserved the geometrical configuration of the latter. In particular, both domains have four holes equally sized (1 mm diameter) on the upper surface of the sparger ring (see Figure 6.1).

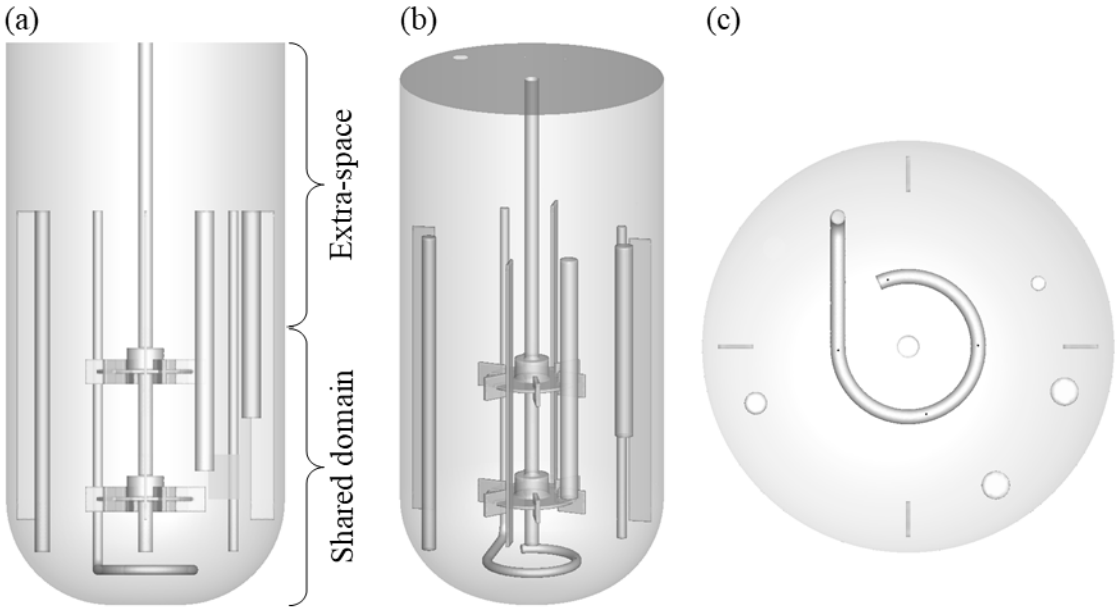

Figure 6.1. Tank CFD domain of GeomC. (a) Identification of shared domain and extra-space; (b) side view, including the lid hole; and (c) upper view of the sparger holes.

For GeomC, the extra-space was divided into smaller bodies, to be able to control the mesh implementation (see Figure 6.2). The shared domain preserved the divisions used for GeomB. The bodies of the lower and middle external zones were assembled into one part together with the upper stationary bodies of the shared domain.

6.1.2 Grids

For GeomB, the coarse grid, described in Chapter 4, was used. For GeomC, a grid was implemented in Ansys Meshing (Workbench 18.2), using mostly the same settings as for GeomB. The grid of the shared domain suffered no modifications, except for the upper axis zone and the superior upper stationary zone; whose sizing methods were modified to refine the grid related to the computation of the free surface. For the grid of the extra-space, the following methods were applied: multizone method with hexahedral elements, multizone method with prism elements, tetrahedrons patch conforming method, and the sweep method with triangular elements (see Figure 6.2). As well as for GeomB, sizing methods and inflation layers were used for the grid of GeomC.

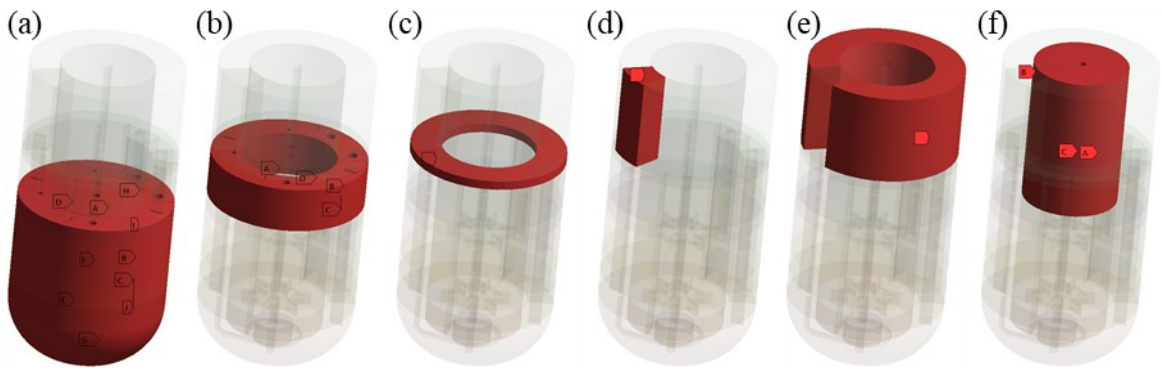

Figure 6.2. Bodies of the domain GeomC. (a) bodies of the shared domain. Bodies of the extra-space and meshing methods implemented: (b) lower external zone, sweep method with triangular elements; (c) middle external zone, tetrahedrons patch conforming method; (d) upper external zone with lid hole, multizone method with prism elements; (e) upper external zone without lid hole, multizone method with hexahedral elements; and (f) internal zone, multizone method with hexahedral elements.

Using these features, the grid of GeomC resulted in 5,182,784 nodes (see Figure 6.3). More details are giving in Appendix S.

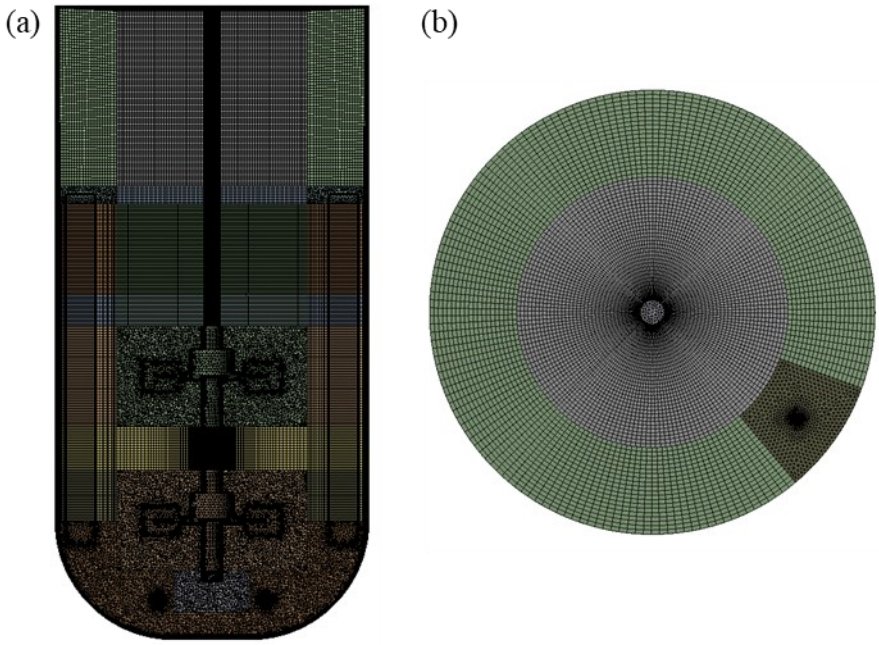

Figure 6.3. Coarse grid implemented for the domain GeomC. (a) Lateral and (b) upper views.

6.1.3 GeomB: CFD model settings

The following assumptions were considered to model the batch abiotic system with water as multi-phase, using the domain GeomB: constant temperature, the upper liquid-air interface is flat and fixed at the initial liquid level, air enters only through the sparger holes, air exits across the upper liquid surface, and air bubbles have a constant monosize. Thus, the fluids' physical properties are static and homogeneous. It is important to notice that the liquid does not inlet nor outlet the system.

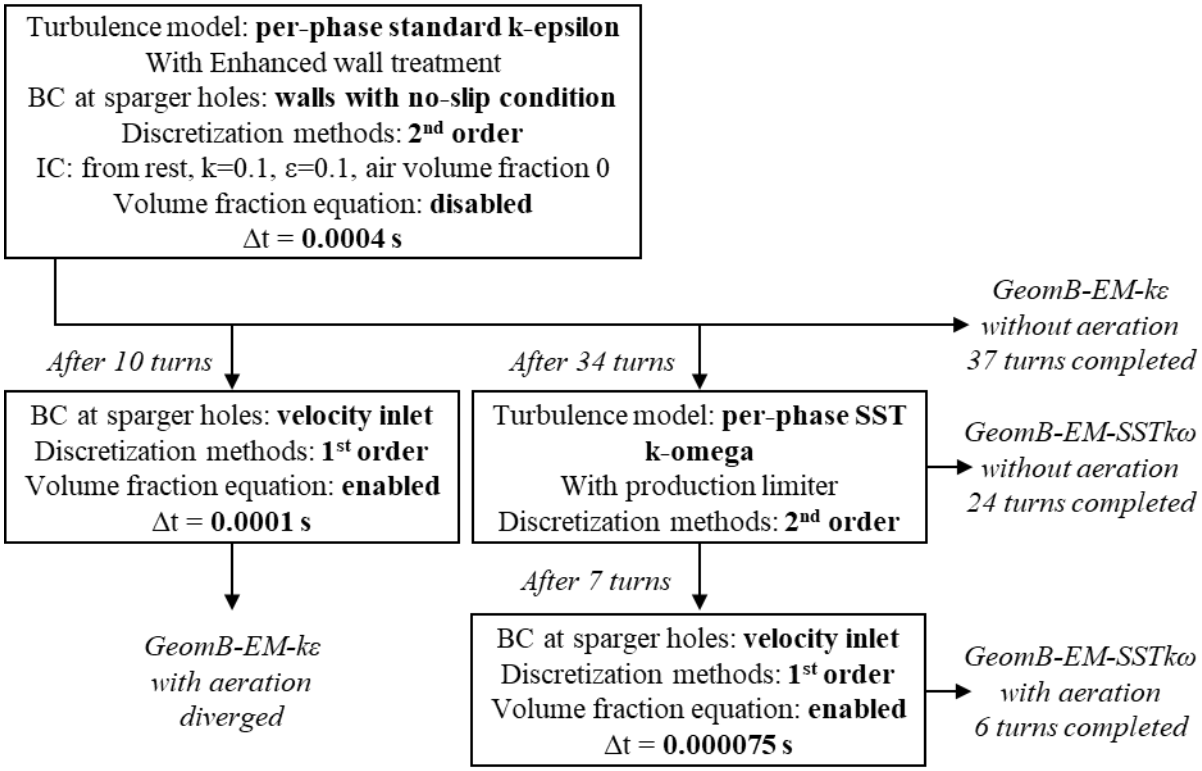

Figure 6.4. Flow diagram of the numerical configuration of the CFD models of the batch abiotic system with water, using the domain GeomB, under unaerated and aerated conditions.

Analogously to Step 1, two configurations using the Eulerian multi-phase model were evaluated, here called the k-epsilon set and the SST k-omega set, which were adapted in ANSYS Fluent version 18.2 and 2019R3, respectively. Water was defined as the primary phase, and air as the secondary phase. The fluids were characterized using the built-in library data. The air bubble diameter was set based on experimental data from Table 3.6. As with the

single-phase models, the SM approach was used to simulate the mixing, with a rotating velocity of 400 rpm for each moving zone.

Hereinafter, for ease of reference, the multi-phase models of the batch abiotic system with water will be named after the corresponding domain, multi-phase model, and turbulence model. Thus, GeomB-EM-kε and GeomB-EM-SSTkω, are the models that use the domain GeomB, the Eulerian model and, respectively, the k-epsilon and the SST k-omega set.

Table 6.1. Additional setting differences between GeomB-EM-kε and GeomB-EM-SSTkω.

	GeomB-EM-kε	**GeomB-EM-SSTkω**
Iterations	50 per time step	Maximum 60 per time step. It was activated the option to stop the iterations when all residuals were below 10^{-5} simultaneously
Phase interaction		
Interfacial area	ia-particle	ia-symmetric
BC velocity inlet[+]		
Velocity water	0 m/s	0 m/s
Velocity air	21.15 m/s (upwards)	21.15 m/s (upwards)
Turbulent intensity	5%	5%
	Length scale: 7e-05 m	Hydraulic diameter: 0.001 m
Volume fraction air	1	1
[+] Only applies for the simulations with aeration, at the sparger holes		
Discretization methods[*]		
Gradient	Least-squares cell-based	Green Gauss node-based
Volume	Modified HRIC	Modified HRIC
Pressure	(Default in Fluent 18.2)	PRESTO
[*]with warped-face gradient correction		

Table 6.2. Numerical settings shared by GeomB-EM-kε and GeomB-EM-SSTkω.

Precision	Double
Solver	Pressure-based with absolute velocity formulation
Multi-phase model	Eulerian model with implicit volume fraction parameters formulation
Coupling scheme	Phase Coupled SIMPLE
Phase interaction	
Drag	Universal drag
Surface tension	71 mN/m (Engineering ToolBox, 2004)
Others	None
Body Forces	Gravity
Operating conditions	
Operating density	Air density
Reference pressure	1 atm at the liquid level
Boundary conditions	
Top wall	Degassing
Impeller and axis walls	Relative velocity to moving zone 0 rpm
Other walls	No-slip condition
Under-relaxation factors	
Density	0.7
Body forces	0.7
Turbulent viscosity	0.8
Others	Default value

For an accurate study of the effect of the aeration, both multi-phase configurations were used to simulate the system without aeration, before activating the air inlet. The workflow for the adaptation of the models was as shown in Figure 6.4, where some of the main settings changes are outlined, such as discretization methods (except for pressure, gradient and volume fraction), the boundary condition on the sparger holes and the time-step

size. Other setting differences, between GeomB-EM-kε and GeomB-EM-SSTkω, are given in Table 6.1. The remaining settings were the same for both configurations (see Table 6.2). The governing conservation equations of a multi-phase CFD model can be referred to in Appendix T.

6.1.4 GeomC: CFD model settings

The assumptions used for the models with GeomC are the same as with GeomB, except that the upper liquid-air interface is a free surface able to entrap air into the liquid, and air can enter and exit the system through the hole on the lid.

Two configurations were adapted in ANSYS Fluent version 2019R3, one with the Eulerian multi-phase model and the other one with the mixture multi-phase model, here called GeomC-EM-SSTkω and GeomC-MM-SSTkω, respectively. The governing conservation equations of the CFD models can be found in Appendix T.

GeomC-EM-SSTkω without aeration used the same configuration as GeomB-EM-SSTkω with aeration, except for the settings described in Table 6.3.

It is important to mention that GeomC-EM-SSTkω without aeration presented numerical issues, as is discussed in Section 6.2.3. In consequence, the aeration was not incorporated to this model. On the other hand, using the configuration of GeomC-MM-SSTkω, it was possible to simulate the system without and with aeration.

For GeomC-MM-SSTkω, as for GeomC-EM-SSTkω, water and air were defined as primary and secondary phases, respectively. Both fluids were characterized using the built-in library data. The air bubble diameter was set based on experimental data from Table 3.6. The SM approach was used to simulate the mixing, with a rotating velocity of 400 rpm for each moving zone.

Table 6.3. Numerical settings used for GeomC-EM-SSTkω without aeration that differ from the model for GeomB-EM-SSTkω with aeration.

Phase interaction	
Drag	Universal drag, with Brucato modification
Surface tension	71 mN/m (Engineering ToolBox, 2004)
Turbulent dispersion	Diffusion in VoF (included after the first 1250 time steps)
Turbulence interaction	Simonin et al. (included after the first 1275 time steps)
Time Step Size	0.0001 s (from the initial condition) 0.00005 s (modified after the first 1250 time steps)
Operating conditions	
Reference pressure	1 atm at x_1=-0.05640303 m, x_2=-0.04162827 m, x_3=0.39 m
Initial conditions	From rest, k = 0, ε=0, air volume fraction 0 Patch in extra-space: air volume fraction 1 For original bodies: water velocity and turbulence parameters were interpolated from the solution of GeomB-EM-SSTkω without aeration
Boundary conditions	
Sparger holes	Wall with no-slip condition
Lid hole	Pressure outlet Gauge pressure: 0 Pa Backflow direction: normal to the boundary Backflow turbulent intensity: 1% Backflow hydraulic diameter: 0.01 m Backflow volume fraction: 1 (air)
Other walls	No-slip condition
Under-relaxation factors	
Momentum	0.5

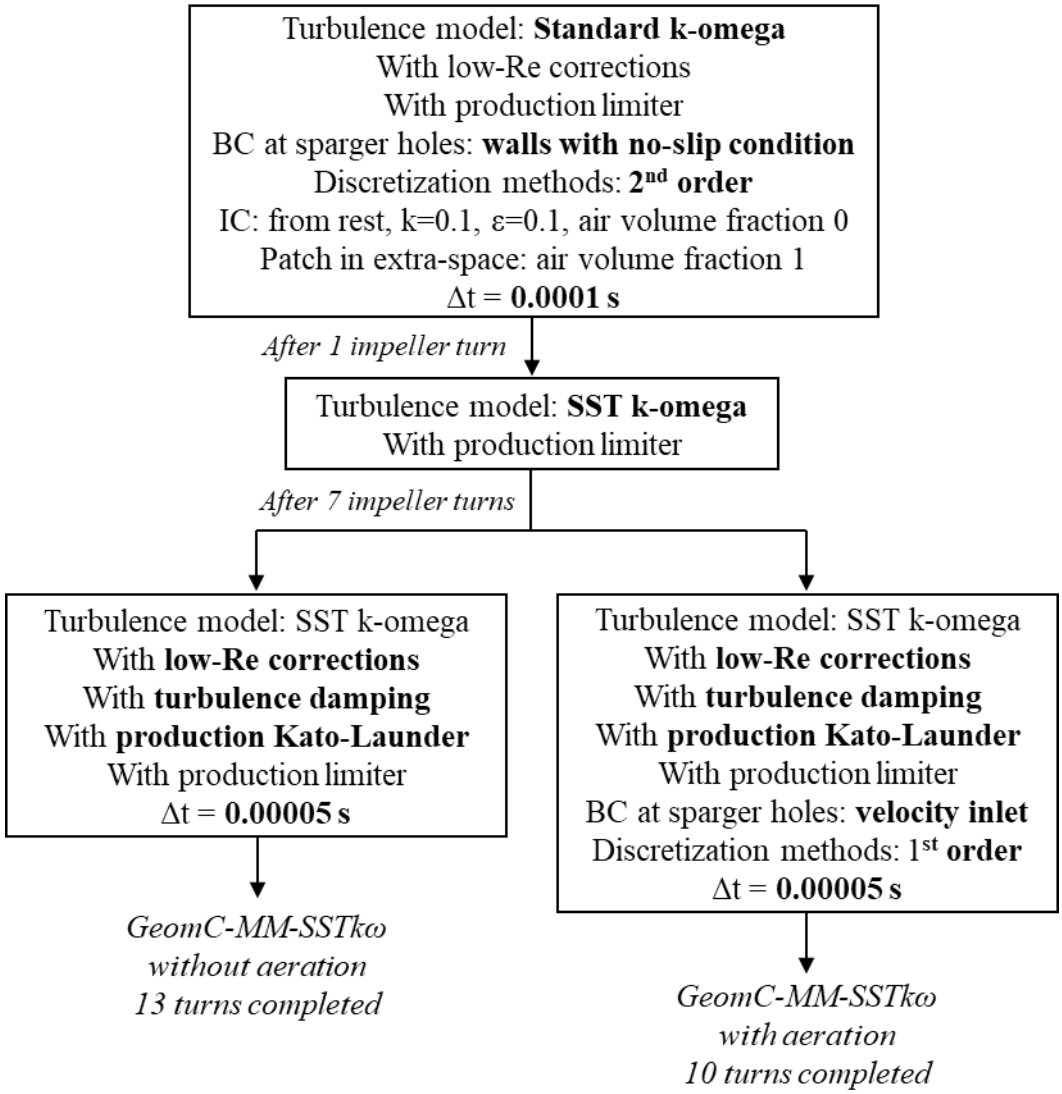

Figure 6.5. Flow diagram of the numerical configuration of the CFD models of the batch abiotic system with water, using domain GeomC, under unaerated and aerated conditions.

The simulation for GeomC-MM-SSTkω without aeration was initialized using the standard k-omega model and, after completing one impeller turn, the turbulence model was shifted to SST k-omega. Additionally, other settings were modified throughout the simulations, without and with aeration, such as the discretization methods (except for pressure, volume fraction and gradient), the boundary condition on the sparger holes and the time-step size, as detailed in Figure 6.5. The remaining settings of GeomC-MM-SSTkω were the same without aeration as well as with aeration (see Table 6.4).

Table 6.4. Settings shared by GeomC-MM-SSTkω with aeration and GeomC-MM-SSTkω without aeration.

Precision	Double		
Solver	Pressure-based with absolute velocity formulation		
Multi-phase model	Mixture model with implicit volume fraction parameters formulation. Dispersed interface. Slip velocity was activated		
Coupling scheme	PISO with skewness correction 0 and neighbour correction 1		
Phase interaction			
Drag	Symmetric	Surface tension	Continuum force, 71 mN/m
Slip	none	Interfacial area	ia-symmetric
Body Forces	Gravity		
Iterations	Maximum 80 per time step. The iterations stopped when all residuals were below 10^{-5} simultaneously.		
Operating conditions			
Operating density	Air density		
Reference pressure	1 atm at x_1=-0.05640303 m, x_2=-0.04162827 m, x_3=0.39 m		
Boundary conditions			
Impeller and axis walls	Relative velocity to moving zone 0 rpm		
Lid hole	Pressure outlet		
Other walls	No-slip condition		
Discretization methods*			
Gradient	Green Gauss node-based		
Volume	QUICK		
Pressure	PRESTO		
*with warped-face gradient correction			
Under-relaxation factors			
Pressure	0.2	Body forces	0.7
Density	0.7	Others	Default value
Turbulent viscosity	0.8		

A detailed description of the settings used for the boundary conditions, velocity inlet and pressure outlet, used for GeomC-MM-SSTkω, is given in Table 6.5.

Table 6.5. BC velocity inlet and pressure outlet used for GeomC-MM-SSTkω.

BC velocity inlet[+]	**BC pressure outlet**[*]
Velocity water: 0 m/s	Gauge pressure: 0 Pa
Velocity air: 21.15 m/s, normal to boundary	Backflow direction: normal to boundary
Turbulent intensity: 3%	Backflow turbulent intensity: 3%
Hydraulic diameter: 0.001 m	Backflow hydraulic diameter: 0.01 m
Volume fraction air: 1	Backflow air volume fraction: 1

[+] Only applies for the simulations with aeration, at the sparger holes

[*] Applied for the simulations with and without aeration, at the lid hole

6.1.5 Simulation completion criteria and validation

As well as for the single-phase models, the velocity magnitude at different points and the impeller torque were recorded after every time step. The monitoring points were placed on a vertical central plane (see Figure 4.4). The residual values were tracked after every iteration, along with any alert of cells with turbulent viscosity ratio exceeding the maximum allowed value (10^5). At the end of each time step, residuals values below 10^{-5} were expected.

In the case of the simulations with GeomB, the flow rate of air through the liquid level was monitored. For GeomC, the maximum velocity, for air and water, was registered for each body of the domain, and the flow rate of air through the sparger holes was monitored. The data were used to identify the achievement of the stationary state and to detect numerical issues.

For validation purposes, for each simulation, the impeller torque was calculated as $T_{AVG_{sim}} \pm T_{SD_{sim}}$ over the last 10 impeller turns.

6.1.6 Analysis of mixing mechanisms

The mixing mechanisms were analyzed using the software Tecplot. The precessing vortex cores were extracted using the method of the velocity gradient eigenmodes, and the trailing vortices were drawn as iso-surfaces of constant vorticity magnitude at 300, 240 and 180 s^{-1}.

6.2 Results and Discussions

6.2.1 Single vs multi-phase model without aeration

A comparative analysis of a multi-phase simulation without aeration versus a single-phase simulation is highly relevant to assess the consequences of the different numerical methods, that are required to model the aeration, on the prediction of the system fluid dynamics. Such analysis would allow us to differentiate and measure the physical from the numerical effects of the aeration on the system's main variables, such as the velocity and torque. Therefore, the results obtained with GeomB-kε and GeomB-SSTkω (see Chapter 4) were compared with GeomB-EM-kε and GeomB-EM-SSTkω without aeration.

For GeomB-EM-kε without aeration, all the variables reached residuals values below 10^{-5}, except for the continuity equation that went as low as $5 \cdot 10^{-4}$. The Y^+ values next to the walls confirmed the need for the enhanced wall treatment (see Appendix U). As well as for GeomB-kε, there was one cell with a turbulent viscosity ratio above 10^5 but, in this case, the alert related to this numerical issue appears with a higher frequency. The numerical problems became even more significant when the aeration was included, so much so that the simulation GeomB-EM-kε with aeration diverged.

Several settings were changed, one at a time, to assess their impact on the convergence behaviour of GeomB-EM-kε. Settings such as turbulence model, under-relaxation factors, discretization methods, airflow rate, air inlet velocity parameters, and time-step size were evaluated. Thus, the configuration of the STT k-omega set was identified as advantageous for the adaptation of CFD multi-phase models for the batch abiotic system with water. Specifically, using GeomB-EM-SSTkω without aeration, all the residuals reached values below 10^{-5}. Furthermore, there were no alerts of cells with turbulent viscosity ratio above 10^5, and the curves of the monitored variables did not show numerical instabilities.

Some of the advantages of the SST k-omega set were discussed for the single-phase modelling of a stirred tank (see Section 4.2.3). Regarding the multi-phase modelling, Karpinska and Bridgeman (2017) reported the comparison of the SST k-omega model against the k-epsilon model for the simulation of an aerated and mixed tank, obtaining better results with the former. Additionally, Karpinska and Bridgeman (2017) reported the use of the Brucato correlation to modify the drag factor for the modelling of an aerated and mixed tank. This correlation is appropriate for dilute gas-liquid flows where the drag coefficient is increased by the liquid phase turbulence (ANSYS, 2009), as would occur in a stirred tank.

Under unaerated conditions, the torque simulated with GeomB-EM-SSTkω shows more oscillations and a higher value than the torque obtained with GeomB-EM-kε. Furthermore, the torque curve of GeomB-EM-SSTkω without aeration satisfactorily moves around the value of $T_{AVG_{sim}}$, estimated for the tank with probes and without aeration, unlike GeomB-EM-kε (see Figure 6.6). A similar behaviour was observed for the single-phase models of the batch abiotic system with water.

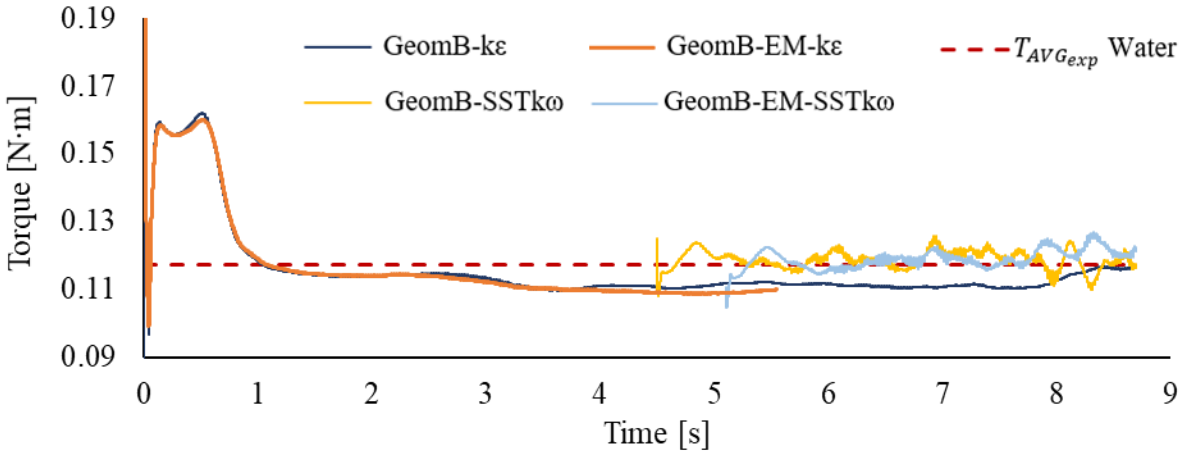

Figure 6.6. Torque temporal evolution simulated for the batch abiotic system with water, using single-phase models and multi-phase models without aeration.

For GeomB-EM-kε without aeration, $T_{AVG_{sim}}$ resulted to be 3.5% lower than the value estimated for GeomB-kε. On the contrary, for GeomB-EM-SSTkω without aeration, $T_{AVG_{sim}}$ resulted to be 1.4% higher than for GeomB-SSTkω (see Table 4.5 and Table 6.6).

Furthermore, the relative error calculated for GeomB-EM-kε and GeomB-EM-SSTkω was higher than for GeomB-kε and GeomB-SSTkω, respectively (see Table 4.9 and Table 6.6). However, for both multi-phase models without aeration $|E| < U_V$. Therefore, they are validated, at an 8.2% level. Nevertheless, GeomB-EM-SSTkω should be preferred over GeomB-EM-kε due to the numerical issues of the latter.

Table 6.6. Validation of the multi-phase models adapted for the batch abiotic system with water, under unaerated conditions. Simulated torque is given as $T_{AVG_{sim}} \pm T_{SD_{sim}}$, in units of [N·m], and |E| is given as [%].

Model	**Torque**	$\boldsymbol{\|E\|}$
GeomB-EM-kε	0.1091 ± 0.0003	6.9
GeomB-EM-SSTkω	0.1202 ± 0.0027	2.6

Regarding the prediction of the local velocities, the contours of velocity magnitude obtained for GeomB-EM-kε without aeration show slight differences from the contours obtained with GeomB-kε. (see Figure 6.7a). The more notorious difference is in the lateral view, at the interaction between the superior and inferior impellers, closed to the baffles and the axis. Similar observations can be derived when comparing GeomB-EM-SSTkω with GeomB-SSTkω (see Figure 6.7b).

Thus, for the CFD modelling of stirred tanks, it is concluded that, when using a domain without headspace, the differences between the fluid dynamics prediction obtained with a multi-phase configuration without aeration and the corresponding single-phase configuration are negligible.

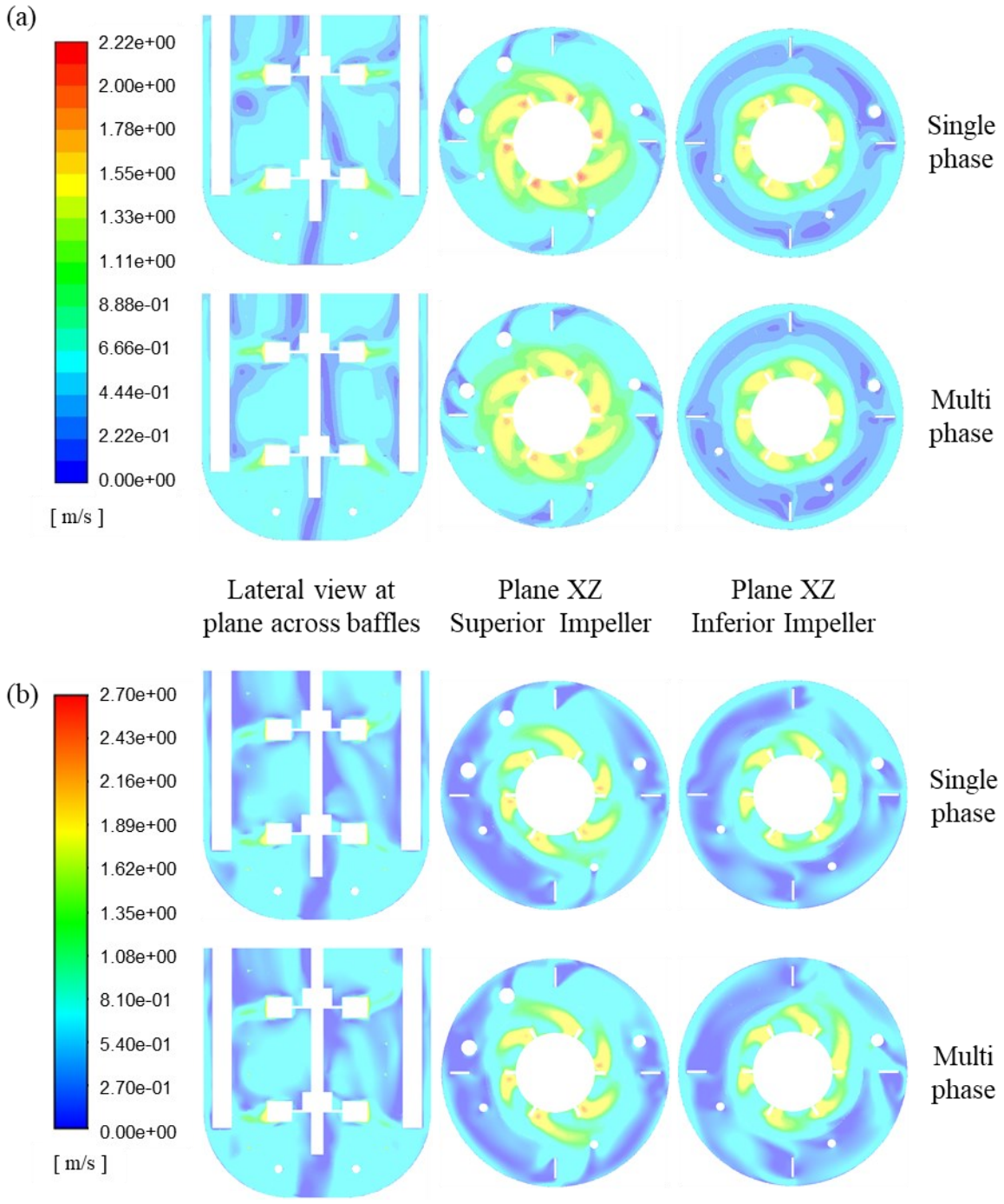

Figure 6.7. Comparison of contours of instantaneous velocity magnitude of water, simulated with a single-phase model versus a multi-phase model without aeration. Models' configuration using the (a) k-epsilon set and (b) SST k-omega set.

6.2.2 Flat upper interface: is it an accurate assumption?

As mentioned before, the simulation using the configuration GeomB-EM-kε with aeration diverged. On the contrary, for GeomB-EM-SSTkω with aeration, the simulation did not diverge. For the latter case, the turbulent viscosity ratio was below 10^5 over the whole simulation and the monitored variables did not show numerical issues. However, the convergence was unsatisfactory. During the first impeller turn, the residuals of all variables decreased below 10^{-5} for a few time steps, but later the residuals started to increase, reaching values around 10^{-2} for the continuity equation and below 10^{-4} for the other equations.

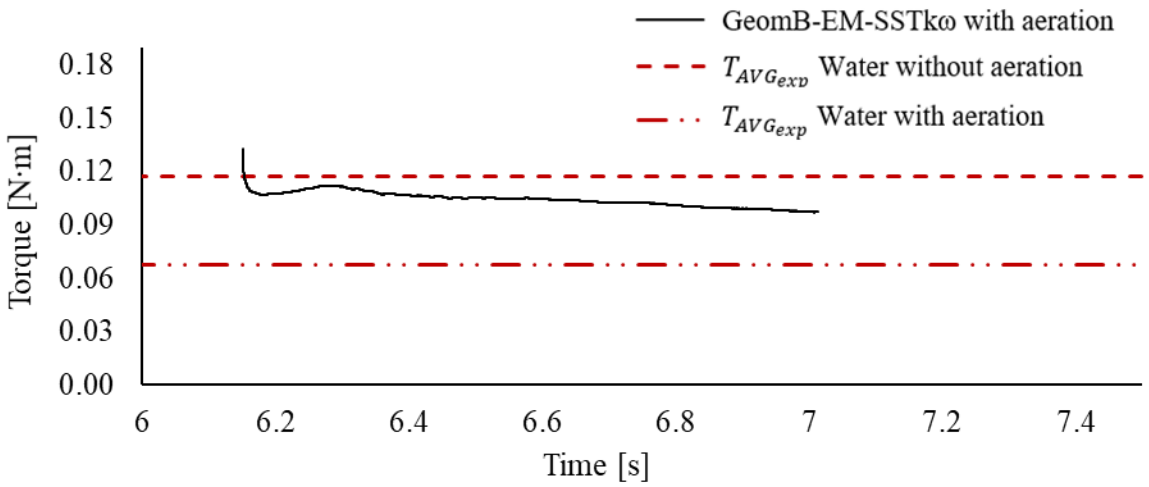

Figure 6.8. Torque temporal evolution simulated for the batch abiotic system with water, under aerated conditions, using the multi-phase model GeomB-EM-SSTkω.

For GeomB-EM-SSTkω, the simulated torque value decreased steadily, as expected, but it did not decrease enough to reach the experimental torque measured in the system with aeration (see Figure 6.8). This agrees with the fact that, for the simulated flow time, only the inferior air cavities were formed, meaning that the system would need longer to fill the upper cavities and reached the stationary state (see Figure 6.9a).

Furthermore, the model was able to capture the effect that the aeration has on the water's velocity magnitude around the lower impeller (see Figure 6.9b-c), where the shape of the trail behind the blades is deformed.

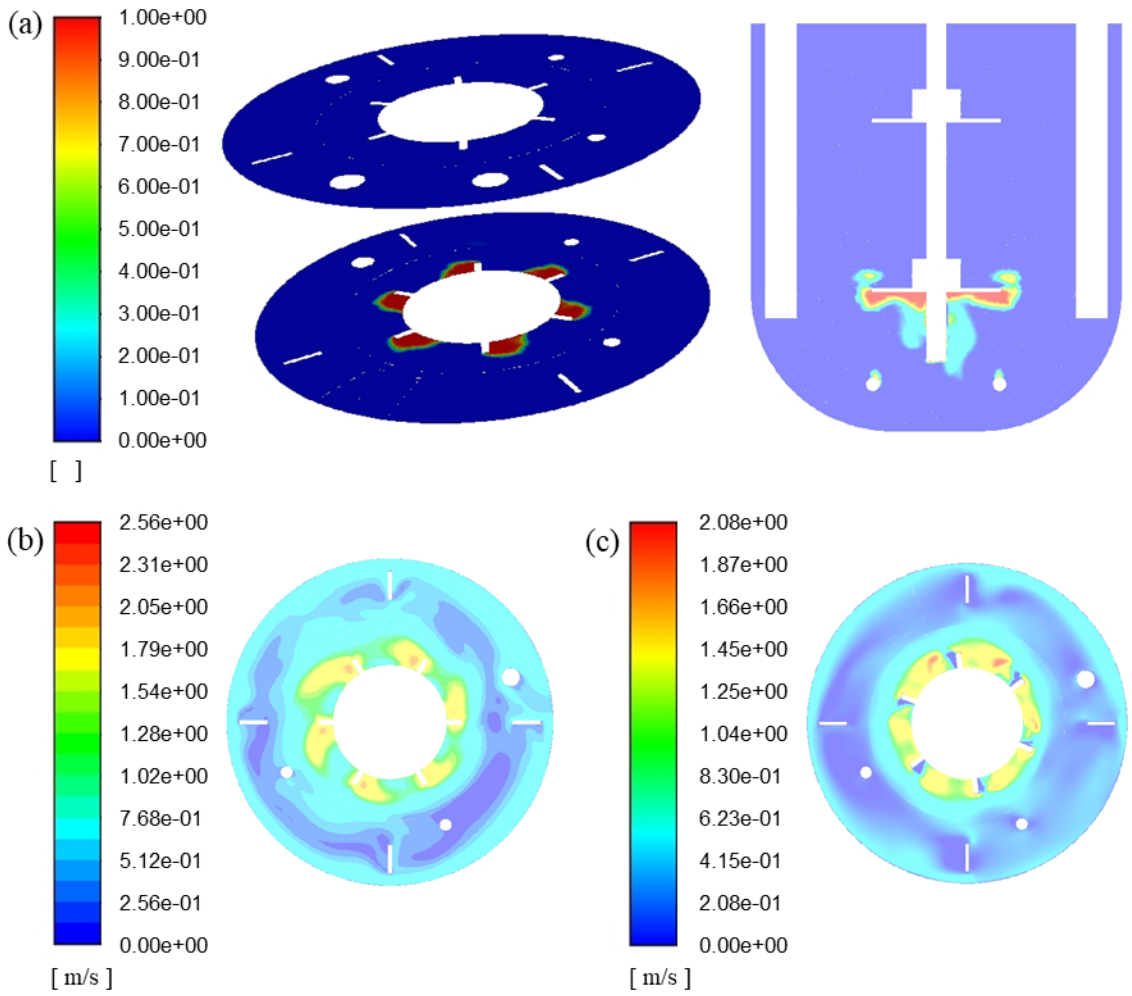

Figure 6.9. Effect of the aeration on the batch abiotic system with water, based on the results computed with GeomB-EM-SSTkω. (a) Contours of instantaneous volume fraction of air, at horizontal planes across the impellers and vertical plane across the tank center. Contours of instantaneous velocity magnitude of water at the inferior impeller, (b) just before including the aeration and (c) under aerated conditions.

However, although the simulation had not reached the stationary state of the system, the simulated flow time was not extended because the residual of the continuity equation was growing steadily, reaching unsatisfactory values. This has been attributed to numerical issues triggered by the accumulation of air behind the blades. Specifically, the residual values started to increase when the cavities of the lower impeller began to form. Afterwards, when the inferior cavities were almost filled and stop growing as fast as before, the residual values

of the continuity equation stabilized around 10^{-3}-10^{-2}, for a short flow time, after which the residual values started to increase again. It is hypothesized that, once the airflow reached the upper impeller, the upper blades started to accumulate air as well, triggering the second growth process of the residuals of the continuity equation, which would cause the divergence of the simulation.

The hypothesis is consistent with the following reasoning: air is filling part of the volume of the system, displacing water from those places. However, water has no place to move to, which means that the fluids are 'being compressed'. Nevertheless, the model assumes that the fluids are incompressible. In consequence, the residuals for the continuity equation increase because the simulation is not able to solve properly the density and pressure variables.

Based on the previous hypothesis, a stirred tank with aeration should not be modelled using a domain without a headspace. The use of this simplification would lead to numerical errors, even if the simulation does not diverge, affecting the computation of important variables for the design of a stirred and aerated tank, such as the gas hold-up.

It is important to mention that the displacement of water was actually observed during the experimentation with the batch abiotic systems with aeration. Even under unaerated conditions, the liquid-air interface was not flat, more especially for the system with water. Therefore, the domain GeomB was modified to GeomC, increasing the height of the reactor to include a headspace, to allow the water surface to move freely.

6.2.3 Headspace and multi-phase CFD settings analysis

For GeomC-EM-SSTkω without aeration, although all the residuals went below 10^{-5} after the initial stabilization, the residuals of the continuity and momentum equations for air increased to $1.3 \cdot 10^{-5}$ and $1.6 \cdot 10^{-5}$, respectively, towards the end of the first impeller turn. These residuals kept increasing when simulating the second impeller turn, leading to divergence. These results came out without alerts of turbulent viscosity ratio above 10^{-5}.

Despite the numerical problems of GeomC-EM-SSTkω without aeration, the contour of air volume fraction satisfactorily predicted the shape of the interphase between water and

air, after the simulation of the first impeller turn. It depicted a vortex similar to the one observed during the experiments, where the superior impeller was partially exposed to the air (see Figure 6.10).

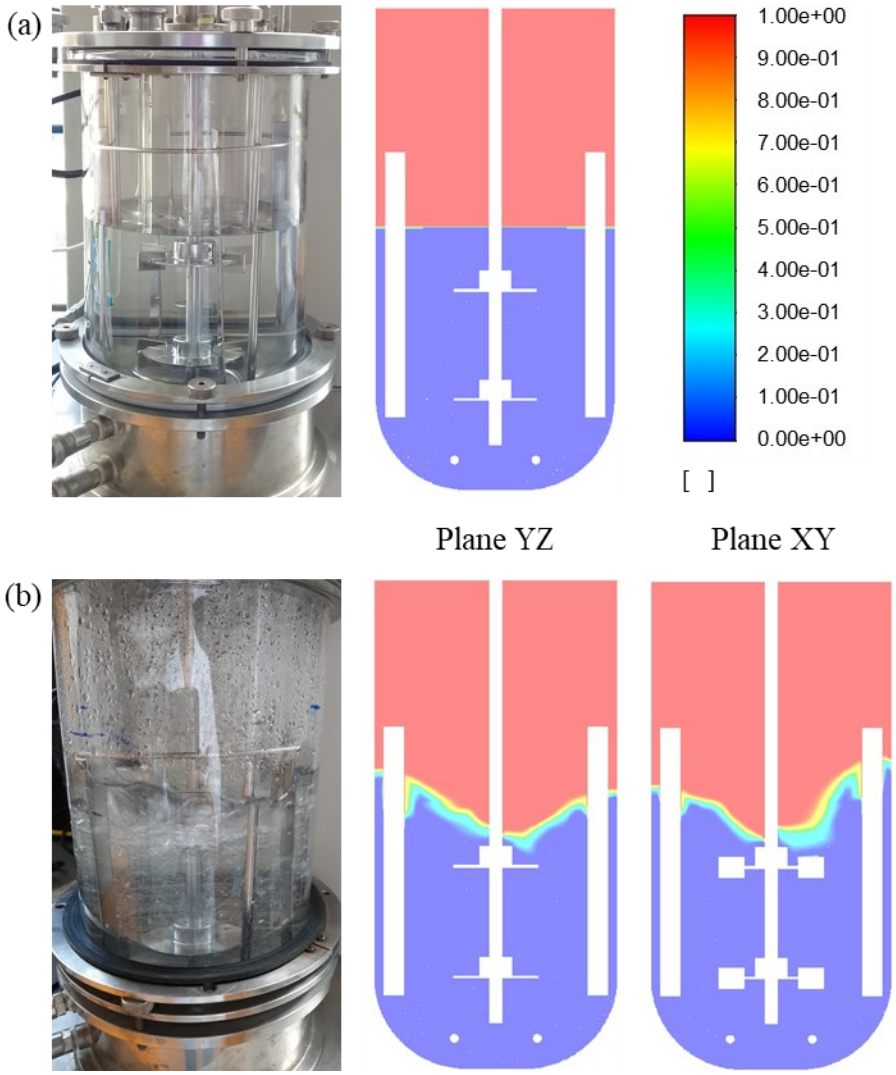

Figure 6.10. Interface surface prediction with GeomC-EM-SSTkω. Comparison between the simulated and experimental surface, formed in the abiotic system with water without aeration, (a) at rest and (b) after the first impeller turn. For the computed results, the instantaneous contours of the volume fraction of air are shown.

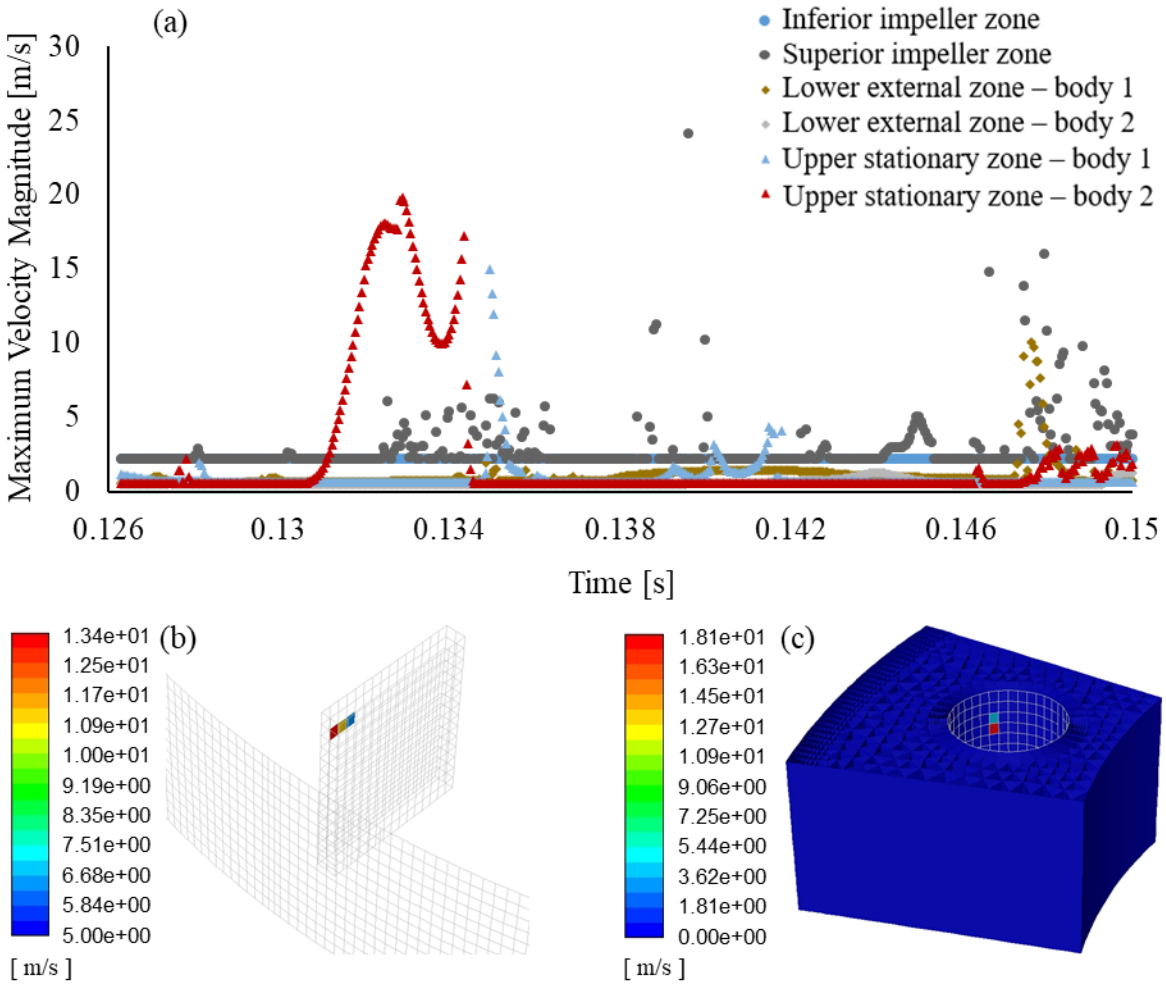

Figure 6.11. Identification of numerical error sources affecting the model GeomC-EM-SSTkω. (a) Temporal evolution of maximum velocity of water at different bodies of GeomC; mostly the curves with non-physical high values are shown. Location of cells with non-physical high velocity magnitude of water at (b) baffle wall and (c) probe wall.

Nevertheless, the numerical issues did affect the prediction of the velocity magnitude. For the stirred tank, the maximum velocity is expected to be at the impeller tip, and it should be around 2.5-2.7 m/s, according to the already validated simulations. Nonetheless, for GeomC-EM-SSTkω without aeration, the computed maximum velocities were as high as 25 m/s (see Figure 6.11a). These values were mainly registered at the bodies where the water-air interphase is located. Specifically, these high values were in cell faces next to the walls of baffles and probes, and, interestingly, they were alone (see Figure 6.11b-c). That is, the faces

of cells next to them showed regular values of velocity, like if the variable had exploded in that only identified cell. This observation raised the possibility that a refinement of the mesh next to the walls, in the identified bodies, would help to eliminate the numerical issues. However, that did not help. Several changes were tested for the model GeomC-EM-SSTkω, keeping the Eulerian multi-phase model, but none worked to eliminate the numerical problems from the simulation. Therefore, the mixture multi-phase model was evaluated next.

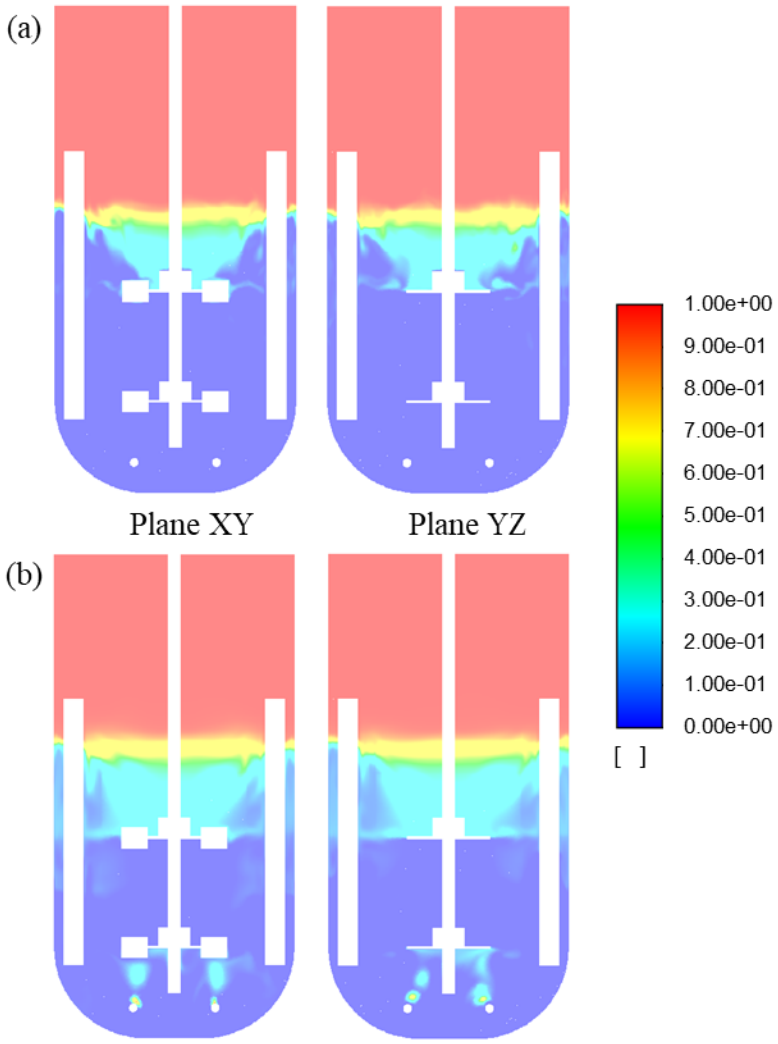

Figure 6.12. Interface surface prediction with GeomC-MM-SSTkω. Instantaneous contours of the volume fraction of air, computed for the batch abiotic system with water, (a) without aeration and (b) with aeration.

For GeomC-MM-SSTkω without aeration, all the residuals' values went below 10^{-5} after the initial stabilization, and the simulation did not present alerts of turbulent viscosity ratio above 10^5. More remarkably, the maximum velocities, monitored at the different domain's bodies, did not present high non-physical values. Similarly, this behaviour occurred for GeomC-MM-SSTkω with aeration (see Appendix U). Thus, the main drawbacks observed for the multi-phase Eulerian model were overcome by applying the mixture model. However, it is important to notice that it was necessary to activate the turbulence damping, low-Re corrections and production Kato-Launder options to avoid the divergence of the simulation with aeration. In consequence, for a fair comparison of the effect of the aeration, these options were activated for the model without aeration as well.

Although it has numerical advantages, the mixture model does not capture the surface vortex shape as well as the Eulerian model (see Figure 6.12). To improve the water-air interface sharpness, the dispersed interface model was shifted to the sharp/dispersed model, but preliminary testing simulations diverged. So, the dispersed interface model was retained.

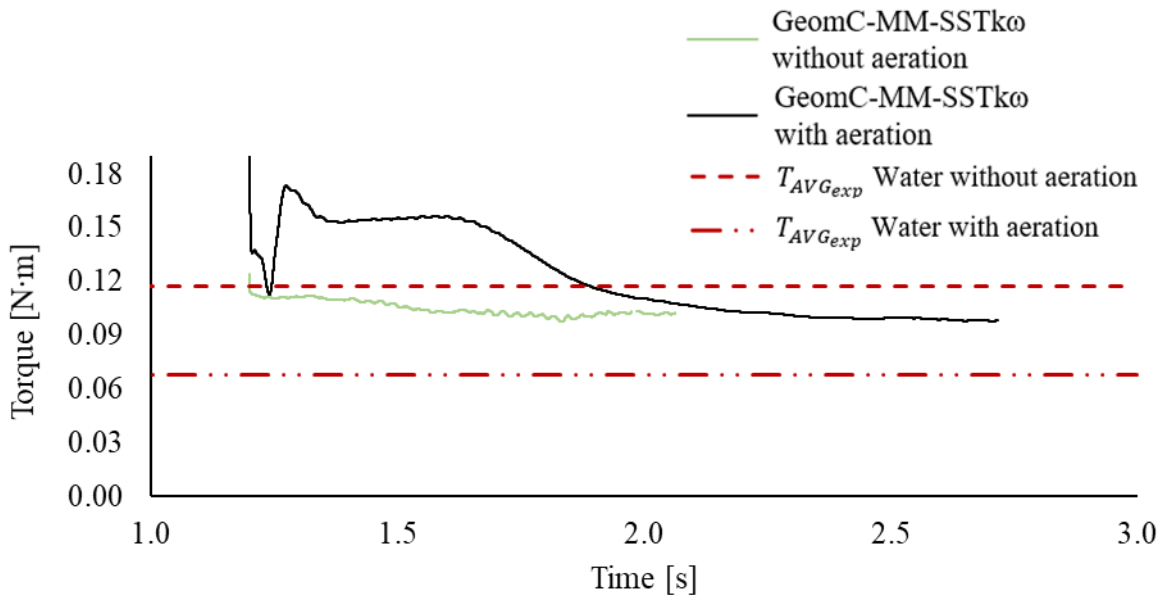

Figure 6.13. Torque temporal evolution simulated for the batch abiotic system with water, without and with aeration, using the multi-phase model GeomC-MM-SSTkω.

For GeomC-MM-SSTkω without aeration, the simulated torque curve seems to be stabilizing around a lower value than GeomB-EM-SSTkω. However, the simulation of a longer flow time is needed to confirm that and, also, to calculate the averaged torque in stationary state. Similarly, the simulation of GeomC-MM-SSTkω with aeration has to be extended, but, so far, it is able to capture the air cavities formation around the lower impeller, and the consequent displacement of water and torque reduction (see Figure 6.13).

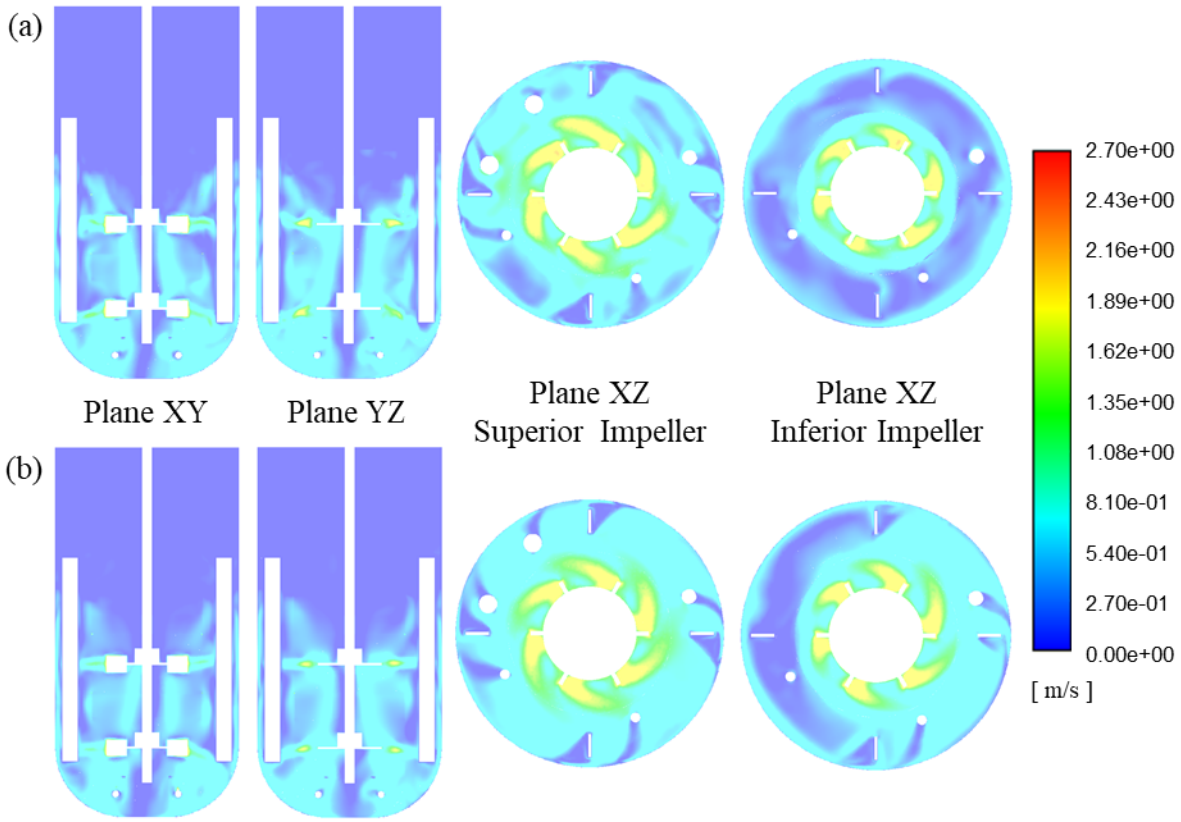

Figure 6.14. Instantaneous contours of velocity magnitude of water computed with GeomC-MM-SSTkω, (a) without and (b) with aeration.

6.2.4 Aeration and mixing mechanisms

Based on the results obtained with GeomC-MM-SSTkω, the effect of the aeration on the fluid dynamics of the stirred tank can be analyzed. It can be identified how the aeration modifies the velocity magnitude of water at different locations of the domain, such as the tank bottom and the planes across the superior and inferior impeller (see Figure 6.14). These

differences are due to the impact of the free liquid level shape and height (see Figure 6.15a-b), the undermining of the vortical structure around the impeller axis (see Figure 6.15c) and the shrinking of the trailing vortices (see Figure 6.15d and Figure 6.16). Remarkably, these resulting features of the system with aeration would explain the significantly higher mixing time measured for the batch abiotic system with water with aeration versus without it (see Table 3.5), as the vortical structures are key for the enhancement of the mixing process.

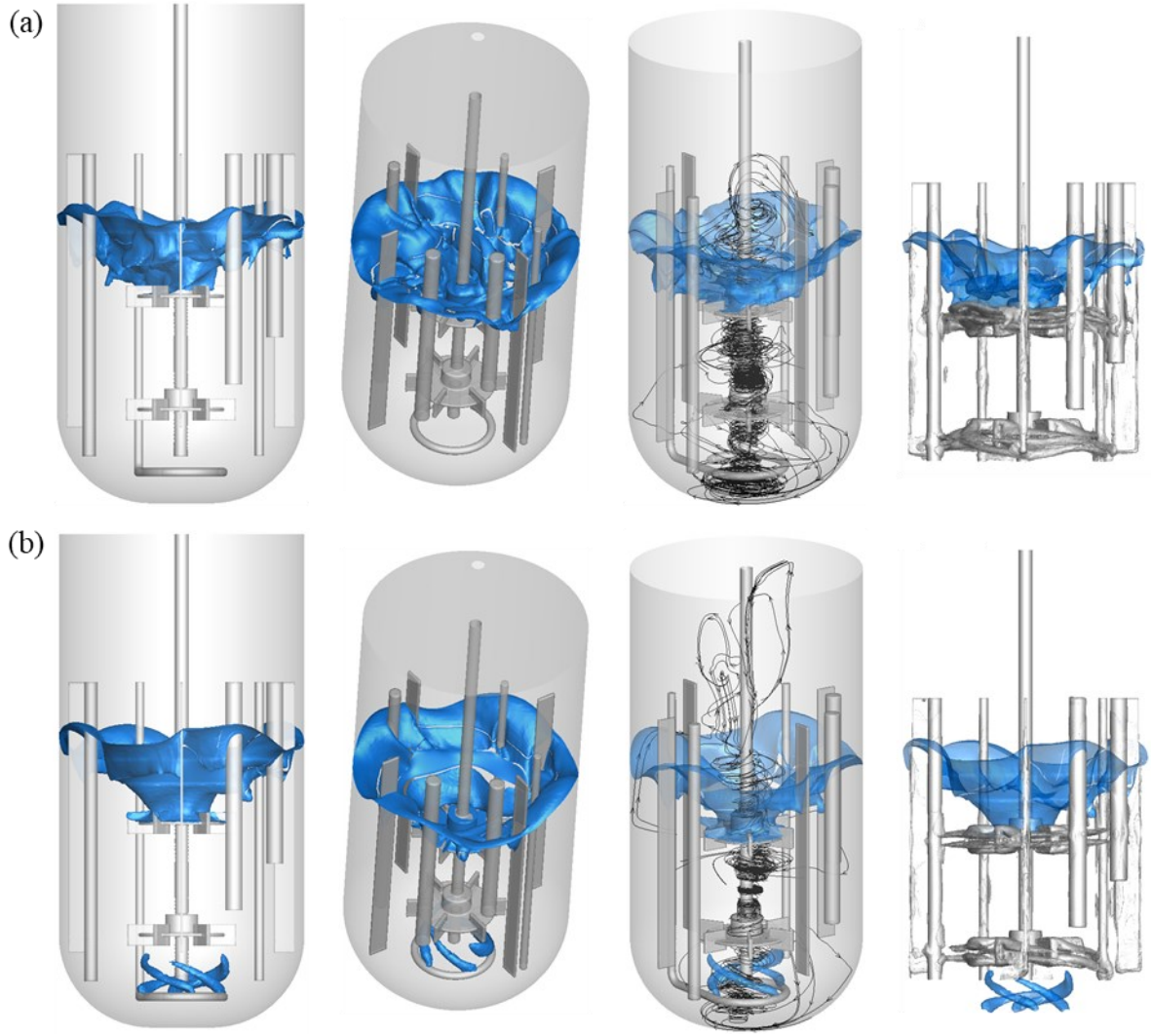

Figure 6.15. Effect of the aeration on the mixing mechanisms of the batch abiotic system with water, computed with GeomC-MM-SSTkω, (a) without and (b) with aeration. The interface was plotted as an instantaneous iso-surface of volume fraction of air equal to 0.25.

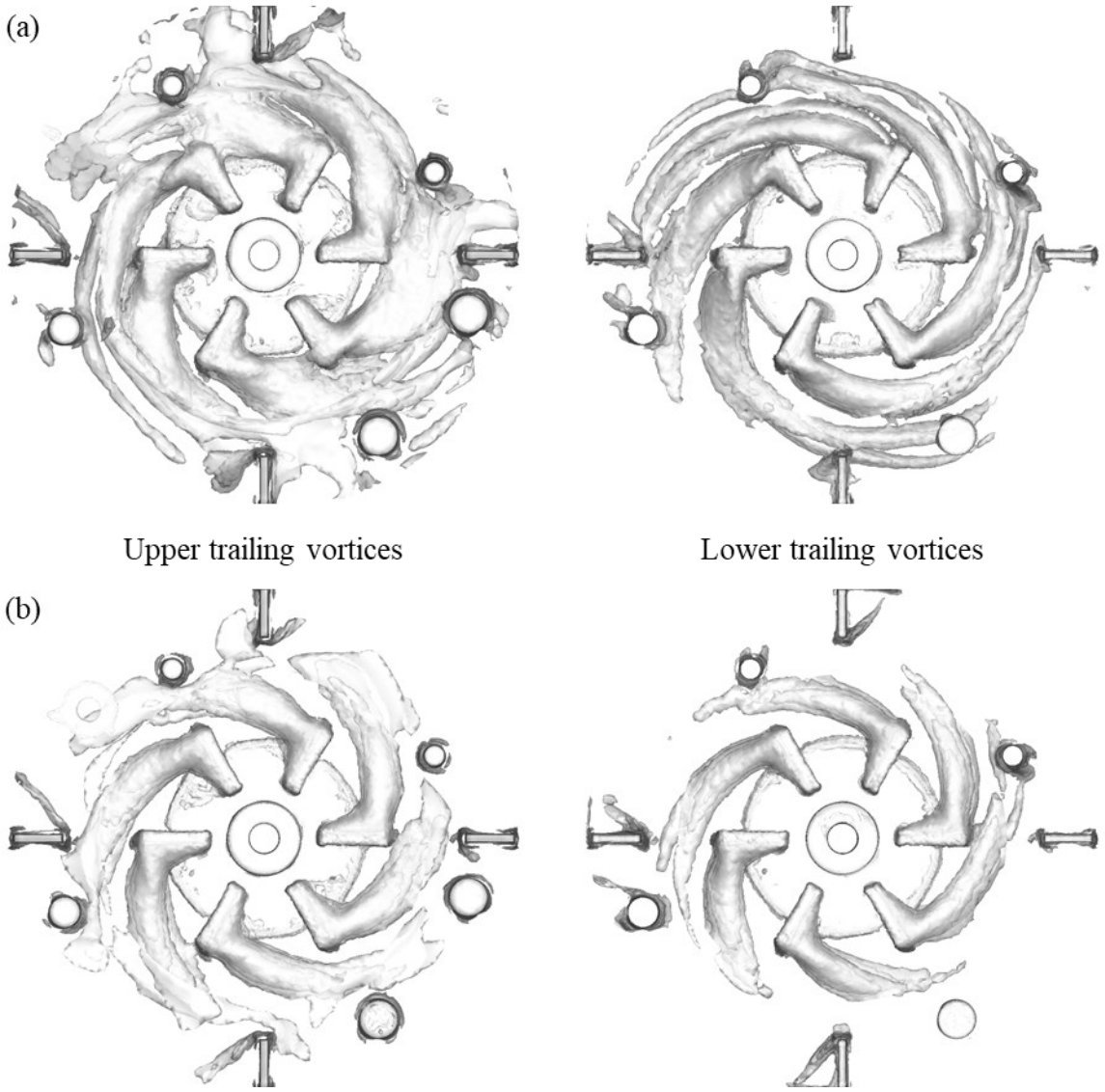

Figure 6.16. Effect of the aeration on the trailing vortices of the batch abiotic system with water, computed with GeomC-MM-SSTkω, (a) without and (b) with aeration. The vortices were plotted as an instantaneous iso-surface of vorticity magnitude.

Furthermore, the results obtained with GeomC-MM-SSTkω confirm the importance of using a domain with headspace to simulate a stirred tank. Specifically, the assumption of a flat liquid surface impairs the prediction of the fluid dynamics in the upper zone of the tank, where the liquid surface shape transforms into a surface vortex. The extent of the consequences of this inaccurate assumption can go from affecting the estimation of the

velocity magnitude next to the surface (see Figure 6.7b and Figure 6.14a), to affect the computation of the upper trailing vortices (see Figure 5.8a and Figure 6.16a). These, in turn, could impact the estimation of important variables of the fluid dynamic of the system, such as flow patterns, mixing times and gas hold-up.

However, most of the CFD models reported in the literature describe the upper liquid-gas interphase as a flat and fixed surface. Mostly, a symmetry or equivalent boundary condition was used for single-phase models (Hou et al., 2016; Cortada-Garcia et al., 2017; Haringa et al., 2018a; Wiedemann et al., 2018; Russell et al., 2019; Spann et al., 2019; Chezeau et al., 2020) or a degassing boundary condition for multi-phase systems (Kazemzadeh et al., 2018; Mendoza et al., 2018; Shi & Rzehak, 2018; Jegatheeswaran et al., 2019; Jegatheeswaran & Ein-Mozaffari, 2020). In other cases, the top surface was modelled as a no-slip boundary condition representing a lid in contact with the fluid, for single-phase (Chara et al., 2016; Liangchao et al., 2019) as well as for multi-phase simulations (Khalili et al., 2017). So far, few articles have been found where the headspace had been modelled. In the works of Zamiri and Chung (2017) and Yamamoto et al. (2019), the simulation captured the formation of a vortex in the liquid-gas surface, but the tank did not contain baffles nor probes. On the other hand, in the simulation developed by Gu et al. (2019), the operating conditions did not lead to the formation of a surface vortex. Thus, the model GeomC-MM-SSTkω, adapted for this thesis, would be a contribution, as it explores a space that has not been addressed yet by CFD modelling, that is the formation of a vortex in a system with baffles.

7 CFD MULTI-PHASE MODELLING – NON-NEWTONIAN FLUID

Based on the learning gathered during the adaptation of the single-phase models for the batch abiotic systems with non-Newtonian fluids and the adaptation of the multi-phase models for the batch abiotic system with water, the multi-phase models for the non-Newtonian systems were addressed next, which is referred to as Step 4. In this step, the effect of the dynamic interaction between the impeller mixing and changing fluid rheology was simulated with a free surface upper interface. In this chapter, the multi-phase CFD modelling without aeration, using a domain with headspace, is revised for the non-Newtonian fluids.

It is important to mention that the work presented in this chapter is the preliminary result of a work in progress. Therefore, the exploration of the models' configuration is just starting, and the settings presented here may not be final.

7.1 Material and Methods

7.1.1 CFD domain and mesh

Only the domain of GeomC was used, which includes all the internal elements of the tank and a headspace, with the coarse grid. The geometry and mesh implementation are described in Chapter 6.

7.1.2 CFD model settings

The following assumptions were considered to model the batch abiotic systems with non-Newtonian fluids, without aeration, as multi-phase: constant temperature, the upper liquid-air interface is a free surface able to entrap air into the liquid, air can enter and exit the system through the hole on the lid, and air bubbles have a constant monosize. As in Chapter 5, the non-Newtonian fluids were characterized as pseudoplastic, using the Power Law model. Thus, the air properties and water density are static and homogeneous, while the fluid viscosity depends on the rheological parameters and the local shear rates.

Two CFD models were adapted in Ansys Fluent (version 2019R3), both using the mixture multi-phase model, one for each batch abiotic systems with non-Newtonian fluid under unaerated conditions, Xanthan Sol A and Xanthan Sol B. For ease of reference, the models will be named, respectively, XSolA-GeomC-MM and XSolB-GeomC-MM.

Table 7.1. Numerical settings used for XSolA-GeomC-MM and XSolA-GeomC-MM, both without aeration, that differ from GeomC-MM-SSTkω without aeration.

Turbulence model	Transition k-kl-omega model
Phase interaction	
Surface tension model	Continuum surface force.
Surface tension coefficient	61 mN/m for XSolB-GeomC-MM (Brunchi et al., 2016) 67 mN/m for XsolA-GeomC-MM (Secouard et al., 2006)
Initial conditions	From rest, k=0.1, $k_L=10^{-6}$; ω=1, air volume fraction 0 Patch in extra-space: air volume fraction 1
BC pressure outlet	Backflow turbulent kinetic energy: 10^{-6} m^2/s^2 Backflow turbulent intensity: 3% Backflow hydraulic diameter: 0.01 m Backflow air volume fraction: 1
Time-step size	0.0001 s
Discretization methods	
Laminar kinetic energy	Second-order upwind
Under-relaxation factors	
Laminar kinetic energy	0.8

For each abiotic system, the corresponding xanthan solution was defined as the primary phase and air as the secondary phase. The rheological and physical properties used to model the fluid of the batch abiotic systems with Xanthan Sol A and Xanthan Sol B are those described in Table 3.1. The viscosity limits listed in Table 5.1 were used to set up the non-Newtonian Power Law model. The air bubble diameter was set based on experimental data

from Table 3.6. The SM approach was used to simulate the mixing, with a rotating velocity of 400 rpm for each moving zone. The remaining settings of XSolA-GeomC-MM and XSolB-GeomC-MM were the same as for GeomC-MM-SSTkω without aeration, except for the items described in Table 7.1. The governing conservation equations of the CFD models can be found in Appendix T.

It is important to mention that, for Step 4, the same simulation completion criteria described for GeomC-MM-SSTkω in Step 3 were used (see Chapter 6).

7.2 Results and Discussions

7.2.1 Multi-phase model without aeration

For XSolA-GeomC-MM and XSolB-GeomC-MM, both without aeration, all the residuals' values went below 10^{-5} after the initial stabilization, and the simulation did not present alerts of turbulent viscosity ratio above 10^{5}. Additionally, the maximum velocities, monitored at the different domain's bodies, did not present high non-physical values.

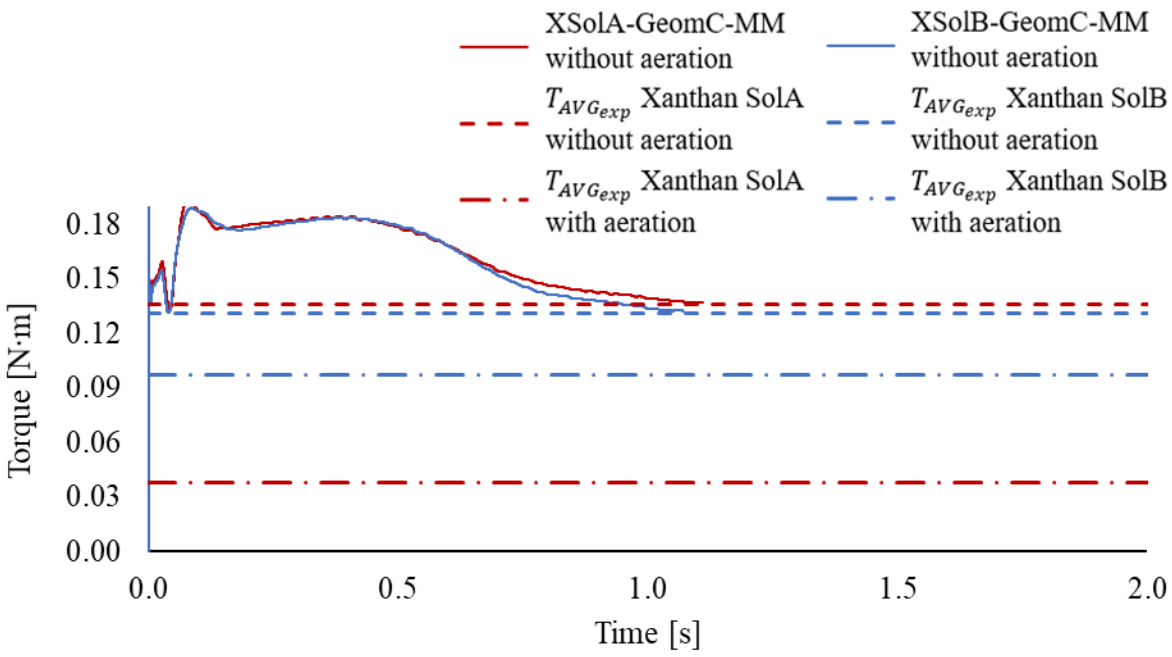

Figure 7.1. Torque temporal evolution simulated for the batch abiotic systems with Xanthan Sol A and Xanthan Sol B, without aeration, using the mixture multi-phase model and the domain GeomC.

Figure 7.2. Interface surface prediction for the batch abiotic systems with non-Newtonian fluids, using the domain GeomC. Comparison between the experimental and simulated surface, for (a) Xanthan Sol B and (b) Xanthan Sol A. For the computed results, the water-air interface was plotted as an instantaneous iso-surface of volume fraction of air equal to 0.1.

Both simulations must be extended over a longer flow time for the torque to start to stabilize (see Figure 7.1). However, so far, the simulations are able to capture the surface vortex differences between Water, Xanthan Sol B and Xantahn Sol A (see Figure 7.2).

Once the torque has stabilized, the simulation's results can be used as initial condition to evaluate the effect of the aeration on the fluid dynamics of the batch abiotic systems with non-Newtonian pseudoplastic fluids.

8 CONCLUSIONS AND RECOMMENDATIONS

The effect of the dynamic interaction between stirring, aeration and a changing broth rheology on the fluid dynamics of a bioprocess was studied. The microbial alginate production in a batch bioreactor was chosen as a case study, where the broth of the fermentation evolves from Newtonian to Non-Newtonian pseudoplastic, and it is known that the significant increase of the viscosity of the culture medium impairs the mixing and, thereby, the mass transfer.

An experimental, as well as a modelling approach, were used. Experimentally, the fermentation process was reproduced and several abiotic systems were implemented to mimic the broth at different stages of the fermentation. Advanced Computational Fluid Dynamics models were adapted to characterize further the mixing mechanisms of the abiotic system. The impact of several aspects of the CFD models on the modelling and numerical accuracy was evaluated.

In the following, the main conclusions inferred based on the experimental and modelling approaches are presented.

8.1 Experimental Characterization

The fermentation process developed as expected, the biomass and alginate concentration increased over time until reaching the stationary phase, while the sucrose concentration decreased. The parameters of the kinetic model proposed by Klimek and Ollis (1980) were fitted, and its 95% confidence intervals were estimated. A statistical analysis of the parameters' values revealed that the sucrose consumption for the bacteria's maintenance was negligible in comparison with the consumption of substrate for the biomass growth. Therefore, the parameter representing the former was assumed equal to 0 g/(g·h), reducing the number of parameters of the model and, thereby, the uncertainty associated with their fitted value. Based on additional statistical analysis, it was concluded that the process is highly reproducible, in terms of the biomass growth and alginate production kinetic, and that

the model proposed by Klimek and Ollis (1980) is able to estimate the dynamics of the concentration of the fermentation components with considerable certainty, at least in a lab-scale mixed reactor

On a more general matter, the analysis of the kinetic parameters showed the importance of describing rigorously the methodology and results when fitting the kinetic model of a bioprocess. In particular, reporting data such as standard deviation, confidence and prediction intervals allows us a statically-based unbiased analysis of the parameter uncertainty and process reproducibility.

Regarding the characterization of the fluid properties, the density and rheological parameters of the broth were estimated at different stages of the fermentation. It was confirmed that, as the alginate concentration increased, the fluid rheology evolved from Newtonian to pseudoplastic. Over the fermentation process, the Power Law index steadily decreased, while the consistency coefficient increased. The collected torque data underlined the effect of the dynamic interaction between the fluid rheology and the bioreactor mixing and aeration but did not allow us the understanding of how each of these factors contributes to the bioreactor fluid dynamics.

Based on the rheological characterization of the broth, three abiotic systems were chosen to mimic the fluid dynamics of the fermentation at the initial, intermediate and final bioprocess stages: water and two solutions of xanthan gum, with low and high apparent viscosity, respectively. Additionally, two Newtonian solutions of PEG solution were chosen, with low and high viscosity. Under the same operating conditions used for the fermentation, the mechanical mixing and aeration were experimentally studied on these abiotic systems in batch mode. The torque, the bubble diameters and the mixing time were characterized in each case. The torque captured the effect of the interaction between fluid rheology, mixing and aeration, making it the chosen modelling validation variable. Also based on the analysis of the torque, it was deduced that, under unaerated conditions, the impeller interaction decreased as the viscosity increased. On the other hand, when aeration was included, the formation and breakaway of air cavities behind the blades modified the tank's fluid dynamics. Additionally, it was proved that the probes affect the impeller torque, under both unaerated and aerated conditions. In agreement with the increment of the fluid viscosity, the

results obtained with the batch abiotic systems indicated that the fermentation had a growing bubble diameter and mixing time.

Two continuous abiotic systems were implemented to study the effect of the evolving rheology on the fluid dynamics of the stirred and aerated tank over time. The similarity between the torque curves of these systems with the curve of the fermentation supports the idea that their underlying mixing mechanisms are similar and, therefore, studying computationally the batch abiotic systems would help to understand the fluid dynamics of the microbial alginate batch production.

8.2 CFD Models Configuration

Although CFD modelling has previously been applied to study bioprocesses, many phenomena that are essential for the comprehension and optimization of bioreactors have been neglected in the reviewed published work. Therefore, for this thesis, the effect of the domain geometry, mesh implementation, and numerical settings selections were evaluated.

Regarding the domain geometry, the CFD models were proved to be able to capture the effect of the probes on the fluid dynamics of the stirred tank. Therefore, the common assumption of neglecting these internal elements should be avoided. On the other hand, the simplification of the liquid level of the fluid as a flat and fixed surface should not be applied when modelling a process under aerated conditions, or when the unaerated conditions can lead to a surface vortex, which is actually a usual feature in stirred tanks. In the former case, the lack of a headspace leads to numerical errors, even divergency, in the computation of the fluid properties and, thereby, on the prediction of important variables such as the gas hold-up. In the latter case, the domain simplification led to modelling inaccuracies, especially in the prediction of the fluid dynamics of the upper zone of the tank.

The described domain simplifications are mostly used to facilitate the mesh implementation and, also, to reduce the computation time of the simulations. However, in this thesis has been shown that the division of the tank domain into smaller bodies, to help to improve the control of the mesh implementation, is feasible for the modelling of stirred tanks. Using this strategy, all the internal elements of the tank were included in the CFD

domain, while retaining a computational time similar to the time required for the simulations with the simplified domain.

Regarding the numerical settings, the loss of accuracy in the prediction of the local velocity evolution when using the MRF approach, instead of SM, to model the stirring of the tank was shown. To model the stirred tank with water, which was within the turbulent flow regime, the SST k-omega turbulence model was proved to perform better than the standard k-epsilon. However, the former requires the use of more accurate discretization methods to solve the gradient and pressure. For the systems with non-Newtonian fluids, which were in the transitional flow regime, the k-kl-omega transition model was satisfactorily implemented. Also, an additional model was successfully adapted to simulate the stirring of a non-Newtonian fluid with a flow closer to the laminar regime, using the laminar model. Thus, different single-phase CFD model configurations were successfully validated, for a stirred fermentation without aeration, to be able to simulate a changing fluid rheology as well as an evolving flow regime. The relative error of these models moves between 0.3 and 6.1%.

The modelling of the stirred system with aeration required the exploration of the multi-phase models performance. It was concluded that the mixture model is not able to predict the shape of the liquid-air interface as well as the Eulerian model, being much more diffuse. However, the Eulerian model showed significant numerical instabilities, when using the domain with headspace to simulate the fluid dynamics of the tank without aeration. On the other hand, the mixture model worked satisfactorily to simulate the stirred tank without and with aeration, when using the same domain. Thus, the mixture model has been applied for the multi-phase modelling. Currently, three multi-phase CFD model configurations are under evaluation. Two models for the simulation of the surface vortex formation, under unaerated conditions, for a flow in the turbulent and transitional regime, respectively. A third, for the simulation of the aeration in a stirred tank in the turbulent flow regime. So far, the results of these models are promising, as they do not present numerical issues and depict surface vortices similar to those observed for the experiments.

To contribute to a framework for standardized CFD modelling of stirred and aerated bioreactors, the workflows used for the adaptation of the models presented in this thesis were described in detail. Furthermore, the importance of following good practices guidelines for

the adaptation of the CFD models was explored. Such as for the time-step size and grid study, the turbulence model and near-wall treatment selection, the simulation completion criteria and the verification and validation process.

8.3 Computational Characterization

The CFD models adapted to simulate the stirred tank allowed us a further analysis of the mixing mechanisms of the batch abiotic systems, at the macro, meso and micro levels.

For the characterization of the micromixing, the change of the turbulence and Kolmogorov length scales were studied. Thus, the Kolmogorov length scale was predicted to be 50% lower for the initial and intermediate stages of the fermentation than for the final one, explaining the significantly higher mixing time estimated for the latter stage. However, the total volume of the dead zones would remain of a similar size over the fermentation, although the volumetric distribution of the velocity magnitude was predicted to change significantly, with a reduction of the velocities across the domain.

For the characterization of the meso and macromixing, the flow patterns and vortical structures were studied. For the former, a modification from an unstable to a parallel (stable) pattern was predicted, which explains the weakening of the interaction between the upper and lower impeller. For the latter, the formation of different kinds of vortical structures was identified, such as the trailing vortices behind the blades and the vortex around the impeller axis. The evolution of the size and shape of these structures was satisfactorily associated with the worsening of the mixing process over the fermentation stages.

The effect of the aeration on the meso and macromixing mechanisms was analyzed. The reduction of the trailing vortices size and the weakening of the vortex around the axis was successfully related to the increment of the mixing time of the batch abiotic system with water when the aeration was included.

Figure 8.1 summarizes the modifications that the fluid dynamics of a bioprocess with evolving pseudoplasticity can be subjected to that may impair the fermentation results. Importantly, all these factors were characterized using CFD modelling, which implies that CFD aided design could be applied to optimize the mixing mechanisms of stirred

bioprocesses with changing fluid rheology. For example, the effect of the position of probes, impellers and air injection on the vortical structures could be studied, to identify a tank configuration that improves the mixing times and biomass suspension. Furthermore, the CFD models adapted for this work would allow the optimization of the system fluid dynamics based on the specific needs of the different fermentation stages. For example, variable operating conditions could be analyzed to counteract the effect of the increasing viscosity on the vortical structures.

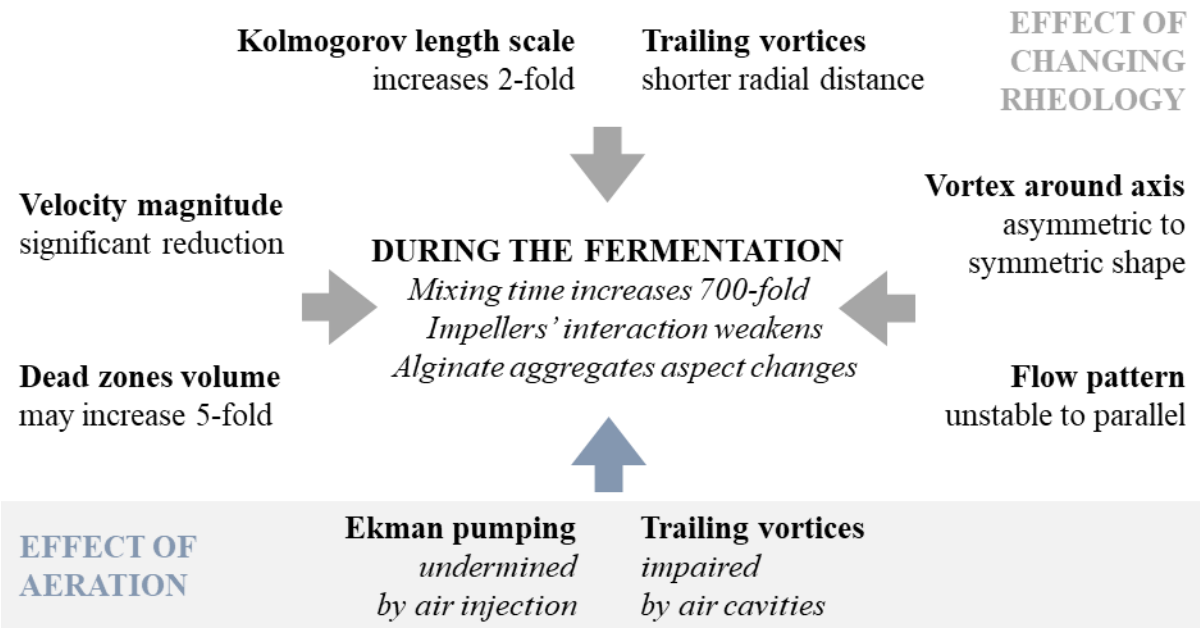

Figure 8.1. Impact of aeration and evolving fermentation broth pseudoplasticity on mixing mechanisms of stirred bioprocess.

Although these results were based on the experimental and modelling analysis of a lab-scale bioreactor, the understanding of how the changing rheology affects the mixing mechanisms and fluid dynamics of a stirred tank still applies to large-scale reactors. Moreover, the workflows built for the adaptation of the CFD models could be used for scale-up purposes, by means of a scale-down approach and dimensionless analysis.

8.4 Recommendations

To improve the numerical accuracy of the CFD models of the stirred tank with aeration presented in this thesis, the first-order discretization methods should be changed to second-order. Also, the performance of the Eulerian model could be reevaluated, using the results of the mixture model as initial condition. This strategy may help to overcome the numerical instabilities observed when initializing the simulation from rest.

To broaden the scope of the application of the CFD models of the stirred tank in the biotechnology industry, the incorporation of the bioprocess kinetics should be addressed. In that case, the relation between the evolution of the fermentation components and the broth rheology and/or viscosity should be considered. Also, the energy transport equation could be included to study the temperature distribution inside the bioreactor.

REFERENCES

Acevedo, F., Gentina, J. C., & Illanes, A. (2002). *Fundamentals of Biochemical Engineering* (3rd ed.). Ediciones Universitaria de Valparaíso, Pontificia Universidad Católica de Valparaíso.

Amooey, A. A., & Fazlollahnejad, M. (2014). Study of surface tension of binary mixtures of poly (ethylene glycol) in water and poly (propylene glycol) in ethanol and its modeling using Neural Network. *Iranian Journal of Chemical Engineering, 11*(1), 19-29.

Anane, E., Barz, T., Sin, G., Gernaey, K. V., Neubauer, P., & Bournazou, M. N. C. (2019). Output uncertainty of dynamic growth models: effect of uncertain parameter estimates on model reliability. *Biochemical Engineering Journal*, 107247. https://doi.org/10.1016/j.bej.2019.107247

ANSYS, Inc. (2009, January 23) *ANSYS FLUENT 12.0 Theory Guide*. AFS ENEA. Retrieved March 2020, from https://www.afs.enea.it/project/neptunius/docs/fluent/html/th/main_pre.htm

Bach, C., Yang, J., Larsson, H., Stocks, S. M., Gernaey, K. V., Albaek, M. O., & Krühne, U. (2017). Evaluation of mixing and mass transfer in a stirred pilot scale bioreactor utilizing CFD. *Chemical Engineering Science*, *171*, 19-26. https://doi.org/10.1016/j.ces.2017.05.001

Badino Jr, A. C., Facciotti, M. C. R., & Schmidell, W. (2001). Volumetric oxygen transfer coefficients (kLa) in batch cultivations involving non-Newtonian broths. *Biochemical Engineering Journal*, *8*(2), 111-119. https://doi.org/10.1016/S1369-703X(01)00092-4

Baldyga, J., & Bourne, J. R. (1984). A fluid mechanical approach to turbulent mixing and chemical reaction part I inadequacies of available methods. *Chemical Engineering Communications*, *28*(4-6), 231-241. https://doi.org/10.1080/00986448408940135

Bałdyga, J., & Pohorecki, R. (1995). Turbulent micromixing in chemical reactors—a review. *The Chemical Engineering Journal and the Biochemical Engineering Journal*, *58*(2), 183-195. https://doi.org/10.1016/0923-0467(95)02982-6

Bałdyga, J., Bourne, J. R., & Hearn, S. J. (1997). Interaction between chemical reactions and mixing on various scales. *Chemical Engineering Science*, *52*(4), 457-466. https://doi.org/10.1016/S0009-2509(96)00430-7

Baldyga, J., Bourne, J. R., & Walker, B. (1998). Non-isothermal micromixing in turbulent liquids: Theory and experiment. *The Canadian Journal of Chemical Engineering*, *76*(3), 641-649. https://doi.org/10.1002/cjce.5450760336

Barwick, V. J. (2003). *Preparation of calibration curves: a guide to best practice*. VAM, Teddington, UK.

Bates, R. L., Fondy, P. L., & Corpstein, R. R. (1963). Examination of some geometric parameters of impeller power. *Industrial & Engineering Chemistry Process Design and Development*, *2*(4), 310-314. https://doi.org/10.1021/i260008a011

Bergamo, U., Viccione, G., Coppola, S., Landi, A., Meda, A., & Gualtieri, C. (2020). Analysis of anaerobic digester mixing: Comparison of long shafted paddle mixing vs gas mixing. *Water Science and Technology*, *81*(7), 1406–1419. https://doi.org/10.2166/wst.2020.248

Brunchi, C. E., Bercea, M., Morariu, S., & Dascalu, M. (2016). Some properties of xanthan gum in aqueous solutions: effect of temperature and pH. *Journal of Polymer Research*, *23*(7), 1-8. https://doi.org/10.1007/s10965-016-1015-4

Cappello, V., Plais, C., Vial, C., & Augier, F. (2021). Scale-up of aerated bioreactors: CFD validation and application to the enzyme production by Trichoderma reesei. *Chemical Engineering Science*, *229*, 116033. https://doi.org/10.1016/j.ces.2020.116033

Chara, Z., Kysela, B., Konfrst, J., & Fort, I. (2016). Study of fluid flow in baffled vessels stirred by a Rushton standard impeller. *Applied Mathematics and Computation*, *272*, 614-628. https://doi.org/10.1016/j.amc.2015.06.044

Chezeau, B., Danican, A., Fontaine, J. P., & Vial, C. (2020). Characterization of the local hydromechanical stress through experimental and numerical analysis of hydrodynamics under dark fermentation operating conditions. *Chemical Engineering Journal*, *382*, 122748. https://doi.org/10.1016/j.cej.2019.122748

Clementi, F. (1997). Alginate production by Azotobacter vinelandii. *Critical Reviews in Biotechnology*, *17*(4), 327-361. https://doi.org/10.3109/07388559709146618

Climent, J., Basiero, L., Martínez-Cuenca, R., Berlanga, J. G., Julian-Lopez, B., & Chiva, S. (2018). Biological reactor retrofitting using CFD-ASM modelling. *Chemical Engineering Journal*, *348*, 1-14. https://doi.org/10.1016/j.cej.2018.04.058

Coleman, H. W., & Stern, F. (1997). Uncertainties and CFD code validation. *Journal of Fluids Engineering*, *119*(4), 795-803. https://doi.org/10.1115/1.2819500

Cortada-Garcia, M., Dore, V., Mazzei, L., & Angeli, P. (2017). Experimental and CFD studies of power consumption in the agitation of highly viscous shear thinning fluids. *Chemical Engineering Research and Design*, *119*, 171-182. https://doi.org/10.1016/j.cherd.2017.01.018

Cudak, M. (2019). Numerical analysis of hydrodynamics in a mechanically agitated gas–liquid pseudophase system. *Chemical Papers*, *73*(2), 481-489. https://doi.org/10.1007/s11696-018-0605-5

Cumming, G., Fidler, F., & Vaux, D. L. (2007). Error bars in experimental biology. *The Journal of Cell Biology*, *177*(1), 7-11. https://doi.org/10.1083/jcb.200611141

Delafosse, A., Collignon, M. L., Calvo, S., Delvigne, F., Crine, M., Thonart, P., & Toye, D. (2014). CFD-based compartment model for description of mixing in bioreactors. *Chemical Engineering Science*, *106*, 76-85. https://doi.org/10.1016/j.ces.2013.11.033

Delafosse, A., Calvo, S., Collignon, M. L., Delvigne, F., Crine, M., & Toye, D. (2015). Euler–Lagrange approach to model heterogeneities in stirred tank bioreactors–Comparison to experimental flow characterization and particle tracking. *Chemical Engineering Science*, *134*, 457-466. https://doi.org/10.1016/j.ces.2015.05.045

Delvigne, F., Takors, R., Mudde, R., van Gulik, W., & Noorman, H. (2017). Bioprocess scale-up/down as integrative enabling technology: from fluid mechanics to systems biology and beyond. *Microbial Biotechnology*, *10*(5), 1267-1274. https://doi.org/10.1111/1751-7915.12803

Díaz-Barrera, A., Peña, C., & Galindo, E. (2007). The oxygen transfer rate influences the molecular mass of the alginate produced by Azotobacter vinelandii. *Applied Microbiology and Biotechnology*, *76*(4), 903–910. https://doi.org/10.1007/s00253-007-1060-3

Doran, P. M. (1995). *Bioprocess engineering principles*. Elsevier.

Ebrahimi, M., Tamer, M., Villegas, R. M., Chiappetta, A., & Ein-Mozaffari, F. (2019). Application of CFD to Analyze the Hydrodynamic Behaviour of a Bioreactor with a Double Impeller. *Processes*, *7*(10), 694. https://doi.org/10.3390/pr7100694

Engineering ToolBox, (2004). *Surface tension of water in contact with air*. Retrieved September 24, 2019, from https://www.engineeringtoolbox.com/water-surface-tension-d_597.html

Fan, W., Yuan, L., & Qu, X. (2018). CFD simulation of hydrodynamic behaviors and aerobic sludge granulation in a stirred tank with lower ratio of height to diameter. *Biochemical Engineering Journal*, *137*, 78-94. https://doi.org/10.1016/j.bej.2018.05.012

Ferziger, J. H., Perić, M., & Street, R. L. (2002). *Computational methods for fluid dynamics* (Vol. 3, pp. 196-200). Berlin: springer.

Furst, J. (2013). Numerical simulation of transitional flows with laminar kinetic energy. *Engineering Mechanics*, *20*(5), 379-388.

Gelves, R., Dietrich, A., & Takors, R. (2014). Modeling of gas–liquid mass transfer in a stirred tank bioreactor agitated by a Rushton turbine or a new pitched blade impeller. *Bioprocess and Biosystems Engineering*, *37*(3), 365-375. https://doi.org/10.1007/s00449-013-1001-8

Gu, D., Liu, Z., Tao, C., Li, J., & Wang, Y. (2019). Numerical Simulation of Gas-Liquid Dispersion in A Stirred Tank Agitated by Punched Rigid-Flexible Impeller. *International Journal of Chemical Reactor Engineering*, *17*(4). https://doi.org/10.1515/ijcre-2018-0196

Gunyol, O., & Mudde, R. F. (2009). Computational study of hydrodynamics of a standard stirred tank reactor and a large-scale multi-impeller fermenter. *International Journal for Multiscale Computational Engineering*, *7*(6). http://doi.org/10.1615/IntJMultCompEng.v7.i6.60

Haringa, C., Noorman, H. J., & Mudde, R. F. (2017). Lagrangian modeling of hydrodynamic–kinetic interactions in (bio)chemical reactors: Practical implementation and setup guidelines. *Chemical Engineering Science*, *157*, 159–168. http://doi.org/10.1016/j.ces.2016.07.031

Haringa, C., Vandewijer, R., & Mudde, R. F. (2018a). Inter-compartment interaction in multi-impeller mixing: Part I. Experiments and multiple reference frame CFD. *Chemical Engineering Research and Design, 136*, 870–885. https://doi.org/10.1016/j.cherd.2018.06.005

Haringa, C., Vandewijer, R., & Mudde, R. F. (2018b). Inter-compartment interaction in multi-impeller mixing. Part II. Experiments, sliding mesh and large Eddy simulations. *Chemical Engineering Research and Design, 136,* 886–899. https://doi.org/10.1016/j.cherd.2018.06.007

Hay, I. D., Rehman, Z. U., Moradali, M. F., Wang, Y., & Rehm, B. H. (2013). Microbial alginate production, modification and its applications. *Microbial Biotechnology*, *6*(6), 637-650. https://doi.org/10.1111/1751-7915.12076

Hong, H. S., Cai, Z. J., Li, J. Q., Shi, D. S., Wan, W. Q., & Li, L. (2014). Simulation of gas-inducing reactor couples gas–liquid mass transfer and biochemical reaction. *Biochemical Engineering Journal*, *91*, 1-9. https://doi.org/10.1016/j.bej.2014.06.015

Hou, W., An, R., Zhang, J., & Bao, J. (2016). On-site measurement and modeling of rheological property of corn stover hydrolysate at high solids content. *Biochemical Engineering Journal*, *107*, 61-65. https://doi.org/10.1016/j.bej.2015.12.004

Jamshidzadeh, M., Ein-Mozaffari, F., & Lohi, A. (2020). Local and overall gas holdup in an aerated coaxial mixing system containing a non-Newtonian fluid. *AIChE Journal*, *66*(11), e17016. https://doi.org/10.1002/aic.17016

Jegatheeswaran, S., Kazemzadeh, A., & Ein-Mozaffari, F. (2019). Enhanced aeration efficiency in non-Newtonian fluids using coaxial mixers: High-solidity ratio central impeller with an anchor. *Chemical Engineering Journal*, *378*, 122081. https://doi.org/10.1016/j.cej.2019.122081

Jegatheeswaran, S., & Ein-Mozaffari, F. (2020). Investigation of the detrimental effect of the rotational speed on gas holdup in non-Newtonian fluids with Scaba-anchor coaxial mixer: A paradigm shift in gas-liquid mixing. *Chemical Engineering Journal*, *383*, 123118. https://doi.org/10.1016/j.cej.2019.123118

Karpinska, A. M., & Bridgeman, J. (2017). Towards a robust CFD model for aeration tanks for sewage treatment–a lab-scale study. *Engineering Applications of Computational Fluid Mechanics*, *11*(1), 371-395. https://doi.org/10.1080/19942060.2017.1307282

Kazemzadeh, A., Elias, C., Tamer, M., & Ein-Mozaffari, F. (2018). Hydrodynamic performance of a single-use aerated stirred bioreactor in animal cell culture: applications of tomography, dynamic gas disengagement (DGD), and CFD. *Bioprocess and Biosystems Engineering*, *41*(5), 679-695. https://doi.org/10.1007/s00449-018-1902-7

Khalili, F., Nasr, M. J., Kazemzadeh, A., & Ein-Mozaffari, F. (2017). Hydrodynamic performance of the ASI impeller in an aerated bioreactor containing the biopolymer solution through tomography and CFD. *Chemical Engineering Research and Design*, *125*, 190-203. https://doi.org/10.1016/j.cherd.2017.07.016

Klimek, J., & Ollis, D. F. (1980). Extracellular microbial polysaccharides: Kinetics of Pseudomonas sp.,Azotobacter vinelandii, and Aureobasidium pullulans batch fermentations. *Biotechnology and Bioengineering*, *22*(11), 2321–2342. https://doi.org/10.1002/bit.260221109

Kuschel, M., Siebler, F., & Takors, R. (2017). Lagrangian trajectories to predict the formation of population heterogeneity in large-scale bioreactors. *Bioengineering*, *4*(2), 27. https://doi.org/10.3390/bioengineering4020027

Lavezzo, V., Verzicco, R., & Soldati, A. (2009). Ekman pumping and intermittent particle resuspension in a stirred tank reactor. *Chemical Engineering Research and Design*, *87*(4), 557-564. https://doi.org/10.1016/j.cherd.2009.01.004

Lencastre Fernandes, R., Nierychlo, M., Lundin, L., Pedersen, A. E., Puentes Tellez, P. E., Dutta, A., Carlquist, M., Bolic, A., Schäpper, D., Brunetti, A. C., Helmark, S., Heins, A. L., Jensen, A. D., Nopens, I., Rottwitt, K., Szita, N., van Elsas, J. D., Nielsen, P. H., Martinussen, J., Sørensen, S. J., Lantz, A. E. & Gernaey, K. V. (2011). Experimental methods and modeling techniques for description of cell population heterogeneity. *Biotechnology Advances*, *29*(6), 575-599. https://doi.org/10.1016/j.biotechadv.2011.03.007

Li, Y., Cao, X., Geng, Z., & Zhang, M. (2018). A novel quasi plug-flow reactor design for enzymatic hydrolysis of cellulose using rheology experiment and CFD simulation. *The Canadian Journal of Chemical Engineering*, *96*(3), 770-778. https://doi.org/10.1002/cjce.22963

Liangchao, L., Ning, C., Kefeng, X., & Beiping, X. (2019). CFD Study on the Flow Field and Power Characteristics in a Rushton Turbine Stirred Tank in Laminar Regime. *International Journal of Chemical Reactor Engineering*, *17*(11). https://doi.org/10.1515/ijcre-2018-0215

Lu, Z., Wang, K., Jin, G., Huang, K., & Huang, J. (2018). CFD studies on hydrodynamic characteristics of shaking bioreactors with wide conical bottom. *Journal of Chemical Technology & Biotechnology*, *93*(3), 810-817. https://doi.org/10.1002/jctb.5431

McClure, D. D., Kavanagh, J. M., Fletcher, D. F., & Barton, G. W. (2016). Characterizing bubble column bioreactor performance using computational fluid dynamics. *Chemical Engineering Science*, *144*, 58-74. https://doi.org/10.1016/j.ces.2016.01.016

Mendoza, F., Bañales, A. L., Cid, E., Xuereb, C., Poux, M., Fletcher, D. F., & Aubin, J. (2018). Hydrodynamics in a stirred tank in the transitional flow regime. *Chemical Engineering Research and Design*, *132*, 865-880. https://doi.org/10.1016/j.cherd.2017.12.011

Metzner, A. B., & Otto, R. E. (1957). Agitation of non-Newtonian fluids. *AIChE Journal*, *3*(1), 3-10. https://doi.org/10.1002/aic.690030103

Metzner, A. B., Feehs, R. H., Ramos, H. L., Otto, R. E., & Tuthill, J. D. (1961). Agitation of viscous Newtonian and non-Newtonian fluids. *AIChE Journal*, *7*(1), 3-9. https://doi.org/10.1002/aic.690070103

Micale, G., Brucato, A., Grisafi, F., & Ciofalo, M. (1999). Prediction of flow fields in a dual-impeller stirred vessel. *AIChE Journal*, *45*(3), 445-464. https://doi.org/10.1002/aic.690450303

Michel, B. J., & Miller, S. A. (1962). Power requirements of gas-liquid agitated systems. *AIChE Journal*, *8*(2), 262-266. https://doi.org/10.1002/aic.690080226

Miller, G. L. (1959). Use of Dinitrosalicylic Acid Reagent for Determination of Reducing Sugar. *Analytical Chemistry, 31*(3), 426–28. https://doi.org/10.1021/ac60147a030

Mudde, R., Noorman, H., & Reuss, M. (2017). Bioreactor modeling. *Industrial Biotechnology: Products and Processes*, 81-128. https://doi.org/10.1002/9783527807833.ch3

Nalband, M., & Jalilnejad, E. (2018). Coupled transient CFD-inhibition kinetics modeling of naphthalene biodegradation in an airlift reactor with net draft tube. *Polycyclic Aromatic Compounds*. https://doi.org/10.1080/10406638.2017.1420668

Natural Resources Canada. (2019, August 9). *Bioenergy and Bioproducts*. NRCAN. Retrieved January 7, 2020, from https://www.nrcan.gc.ca/our-natural-resources/forests-forestry/forest-fact-book/bioenergy-bioproducts/21686

Ng, K., Fentiman, N. J., Lee, K. C., & Yianneskis, M. (1998). Assessment of sliding mesh CFD predictions and LDA measurements of the flow in a tank stirred by a Rushton impeller. *Chemical Engineering Research and Design*, *76*(6), 737-747. https://doi.org/10.1205/026387698525315

Nicholls, A. (2016). Confidence limits, error bars and method comparison in molecular modeling. Part 2: comparing methods. *Journal of Computer-aided Molecular Design*, *30*(2), 103-126. https://doi.org/10.1007/s10822-016-9904-5

Nienow, A. W. (1998). Hydrodynamics of stirred bioreactors. *Applied Mechanics Review*, *51*(1), 3-32. https://doi.org/10.1115/1.3098990

Niño, L., Peñuela, M., & Gelves, G. R. (2018). Gas-Liquid Hydrodynamics Simulation using CFD in a Helical Ribbon Impeller Applied for Non-Newtonian Fluids. *International Journal of Applied Engineering Research*, *13*(11), 9353-9359.

NIST/SEMATECH. (2003, June 1) *e-Handbook of Statistical Methods*. NIST. Retrieved June 7, 2019, from https://www.itl.nist.gov/div898/handbook/

Noorman, H. (2011). An industrial perspective on bioreactor scale-down: what we can learn from combined large-scale bioprocess and model fluid studies. *Biotechnology Journal*, *6*(8), 934-943. https://doi.org/10.1002/biot.201000406

Noorman, H. J., & Heijnen, J. J. (2017). Biochemical engineering's grand adventure. *Chemical Engineering Science*, *170*, 677-693. https://doi.org/10.1016/j.ces.2016.12.065

Paul, E. L., Atiemo-Obeng, V. A., & Kresta, S. M. (Eds.). (2003). *Handbook of industrial mixing: science and practice* (Vol. 1). John Wiley & Sons.

Peña, C., Campos, N., & Galindo, E. (1997). Changes in alginate molecular mass distributions, broth viscosity and morphology of Azotobacter vinelandii cultured in shake flasks. *Applied Microbiology and Biotechnology, 48*(4), 510–515. https://doi.org/10.1007/s002530051088

Peña, C., Trujillo-Roldán, M. A., & Galindo, E. (2000). Influence of dissolved oxygen tension and agitation speed on alginate production and its molecular weight in cultures of Azotobacter vinelandii. *Enzyme and Microbial Technology*, *27*(6), 390–398. https://doi.org/10.1016/S0141-0229(00)00221-0

Peña, C., Peter, C. P., Büchs, J., & Galindo, E. (2007). Evolution of the specific power consumption and oxygen transfer rate in alginate-producing cultures of Azotobacter vinelandii conducted in shake flasks. *Biochemical Engineering Journal*, *36*(2), 73–80. https://doi.org/10.1016/j.bej.2007.02.019

Peña, C., Millán, M., & Galindo, E. (2008). Production of alginate by Azotobacter vinelandii in a stirred fermentor simulating the evolution of power input observed in shake flasks. *Process Biochemistry*, *43*(7), 775–778. https://doi.org/10.1016/j.procbio.2008.02.013

Peña, C., Galindo, E., & Büchs, J. (2011). The viscosifying power, degree of acetylation and molecular mass of the alginate produced by Azotobacter vinelandii in shake flasks are determined by the oxygen transfer rate. *Process Biochemistry*, *46*(1), 290–297. https://doi.org/10.1016/j.procbio.2010.08.025

Rasouli, M., Mousavi, S. M., Azargoshasb, H., Jamialahmadi, O., & Ajabshirchi, Y. (2018). CFD simulation of fluid flow in a novel prototype radial mixed plug-flow reactor. *Journal of Industrial and Engineering Chemistry*, *64*, 124-133. https://doi.org/10.1016/j.jiec.2018.03.008

Reyes, C., Peña, C., & Galindo, E. (2003). Reproducing shake flasks performance in stirred fermentors: production of alginates by Azotobacter vinelandii. *Journal of Biotechnology*, *105*(1-2), 189-198. https://doi.org/10.1016/S0168-1656(03)00186-X

Rosseburg, A., Fitschen, J., Wutz, J., Wucherpfennig, T., & Schlüter, M. (2018). Hydrodynamic inhomogeneities in large scale stirred tanks–Influence on mixing time. *Chemical Engineering Science*, *188*, 208-220. https://doi.org/10.1016/j.ces.2018.05.008

Russell, A. W., Kahouadji, L., Mirpuri, K., Quarmby, A., Piccione, P. M., Matar, O. K., Luckham, P. F. & Markides, C. N. (2019). Mixing viscoplastic fluids in stirred vessels over multiple scales: A combined experimental and CFD approach. *Chemical Engineering Science*, *208*, 115129. https://doi.org/10.1016/j.ces.2019.07.047

Rutherford, K., Lee, K. C., Mahmoudi, S. M. S., & Yianneskis, M. (1996). Hydrodynamic characteristics of dual Rushton impeller stirred vessels. *AIChE Journal*, *42*(2), 332-346. https://doi.org/10.1002/aic.690420204

Sabra, W., & Zeng, A. P. (2009). Microbial production of alginates: physiology and process aspects. In *Alginates: biology and applications* (pp. 153-173). Springer, Berlin, Heidelberg. https://doi.org/10.1007/978-3-540-92679-5_7

Sadino-Riquelme, C., Hayes, R. E., Jeison, D., & Donoso-Bravo, A. (2018). Computational fluid dynamic (CFD) modelling in anaerobic digestion: General application and recent advances. *Critical Reviews in Environmental Science and Technology*, *48*(1), 39-76. https://doi.org/10.1080/10643389.2018.1440853

Sadino-Riquelme, M. C., Rivas, J., Jeison, D., Hayes, R. E., & Donoso-Bravo, A. (2020). Making sense of parameter estimation and model simulation in bioprocesses. *Biotechnology and Bioengineering*, *117*(5), 1357-1366. https://doi.org/10.1002/bit.27294

Sadino-Riquelme, M. C., Rivas, J., Jeison, D., Donoso-Bravo, A., & Hayes, R. E. (2021). Computational modelling of mixing tanks for bioprocesses: Developing a comprehensive workflow. *The Canadian Journal of Chemical Engineering*, in press. https://doi.org/10.1002/cjce.24220

Sánchez, F., Rey, H., Viedma, A., Nicolás-Pérez, F., Kaiser, A. S., & Martínez, M. (2018). CFD simulation of fluid dynamic and biokinetic processes within activated sludge reactors under intermittent aeration regime. *Water Research*, *139*, 47-57. https://doi.org/10.1016/j.watres.2018.03.067

Seber, G. A. F., & Wild, C. J. (1989). *Nonlinear regression*. John Wiley & Sons.

Secouard, S., Malhiac, C., & Grisel, M. (2006). The effect of solution surface tension on aroma compound release from aqueous xanthan solutions. *Flavour and fragrance journal*, *21*(1), 8-12. https://doi.org/10.1002/ffj.1695

Schügerl, K., & Bellgardt, K. H. (Eds.). (2012). *Bioreaction engineering: modeling and control*. Springer Science & Business Media.

Shampine, L. F., & Reichelt, M. W. (1997). The matlab ode suite. *SIAM journal on scientific computing*, *18*(1), 1-22. https://doi.org/10.1137/S1064827594276424

Shi, P., & Rzehak, R. (2018). Bubbly flow in stirred tanks: Euler-Euler/RANS modeling. *Chemical Engineering Science*, *190*, 419-435. https://doi.org/10.1016/j.ces.2018.06.001

Shin Je, L., Dae Shik, K., Jong Min, L., & Chonghun, H. (2018). Overview on Bioprocess Simulation. *Emerging Areas in Bioengineering*, *2*, 715-722. https://doi.org/10.1002/9783527803293.ch41

Spann, R., Glibstrup, J., Pellicer-Alborch, K., Junne, S., Neubauer, P., Roca, C., Kold, D., Lantz, A. E., Sin, G., Gernaey, K. V. & Krühne, U. (2019). CFD predicted pH gradients in lactic acid bacteria cultivations. *Biotechnology and Bioengineering*, *116*(4), 769-780. https://doi.org/10.1002/bit.26868

Srirugsa, T., Prasertsan, S., Theppaya, T., Leevijit, T., & Prasertsan, P. (2017). Comparative study of Rushton and paddle turbines performance for biohydrogen production from palm oil mill effluent in a continuous stirred tank reactor under thermophilic condition. *Chemical Engineering Science*, *174*, 354-364. https://doi.org/10.1016/j.ces.2017.09.024

Verma, R., Mehan, L., Kumar, R., Kumar, A., & Srivastava, A. (2019). Computational fluid dynamic analysis of hydrodynamic shear stress generated by different impeller combinations in stirred bioreactor. *Biochemical Engineering Journal*, *151*, 107312. https://doi.org/10.1016/j.bej.2019.107312

Versteeg, H. K., & Malalasekera, W. (2007). *An introduction to computational fluid dynamics: the finite volume method*. Pearson education.

Vesvikar, M. S., & Al-Dahhan, M. (2005). Flow pattern visualization in a mimic anaerobic digester using CFD. *Biotechnology and Bioengineering*, *89*(6), 719-732. https://doi.org/10.1002/bit.20388

Wang, X., Jia, X., & Wen, J. (2010a). Transient modeling of toluene waste gas biotreatment in a gas–liquid airlift loop reactor. *Chemical Engineering Journal*, *159*(1-3), 1-10. https://doi.org/10.1016/j.cej.2010.02.006

Wang, X., Ding, J., Guo, W. Q., & Ren, N. Q. (2010b). A hydrodynamics–reaction kinetics coupled model for evaluating bioreactors derived from CFD simulation. *Bioresource Technology*, *101*(24), 9749-9757. https://doi.org/10.1016/j.biortech.2010.07.115

Wiedemann, L., Conti, F., Saidi, A., Sonnleitner, M., & Goldbrunner, M. (2018). Modeling mixing in anaerobic digesters with computational fluid dynamics validated by experiments. *Chemical Engineering & Technology*, *41*(11), 2101-2110. https://doi.org/10.1002/ceat.201800083

Wu, B. (2012). Large eddy simulation of mechanical mixing in anaerobic digesters. *Biotechnology and Bioengineering*, *109*(3), 804-812. https://doi.org/10.1002/bit.24345

Xue, D., & Sethi, R. (2012). Viscoelastic gels of guar and xanthan gum mixtures provide long-term stabilization of iron micro-and nanoparticles. *Journal of Nanoparticle Research*, *14*(11), 1-14. https://doi.org/10.1007/s11051-012-1239-0

Yamamoto, T., Fang, Y., & Komarov, S. V. (2019). Surface vortex formation and free surface deformation in an unbaffled vessel stirred by on-axis and eccentric impellers. *Chemical Engineering Journal*, *367*, 25-36. https://doi.org/10.1016/j.cej.2019.02.130

Zamiri, A., & Chung, J. T. (2017). Ability of URANS approach in prediction of unsteady turbulent flows in an unbaffled stirred tank. *International Journal of Mechanical Sciences*, *133*, 178-187. https://doi.org/10.1016/j.ijmecsci.2017.08.008

Zhang, J., Chen, X., Liu, J., Huang, B., & Xu, M. (2018). Structural characteristics of a spiral symmetry stream anaerobic bioreactor based on CFD. *Biochemical Engineering Journal*, *137*, 50-61. https://doi.org/10.1016/j.bej.2018.05.016

Zhong, L., Oostrom, M., Truex, M. J., Vermeul, V. R., & Szecsody, J. E. (2013). Rheological behavior of xanthan gum solution related to shear thinning fluid delivery for subsurface remediation. *Journal of Hazardous Materials*, *244*, 160-170. https://doi.org/10.1016/j.jhazmat.2012.11.028

Zhu, Q., Xiao, H., Chen, A., Geng, S., & Huang, Q. (2019). CFD study on double-to single-loop flow pattern transition and its influence on macro mixing efficiency in fully baffled tank stirred by a Rushton turbine. *Chinese Journal of Chemical Engineering*, *27*(5), 993-1000. https://doi.org/10.1016/j.cjche.2018.10.002

APPENDICES

Appendix A. Probes and Sparger Position

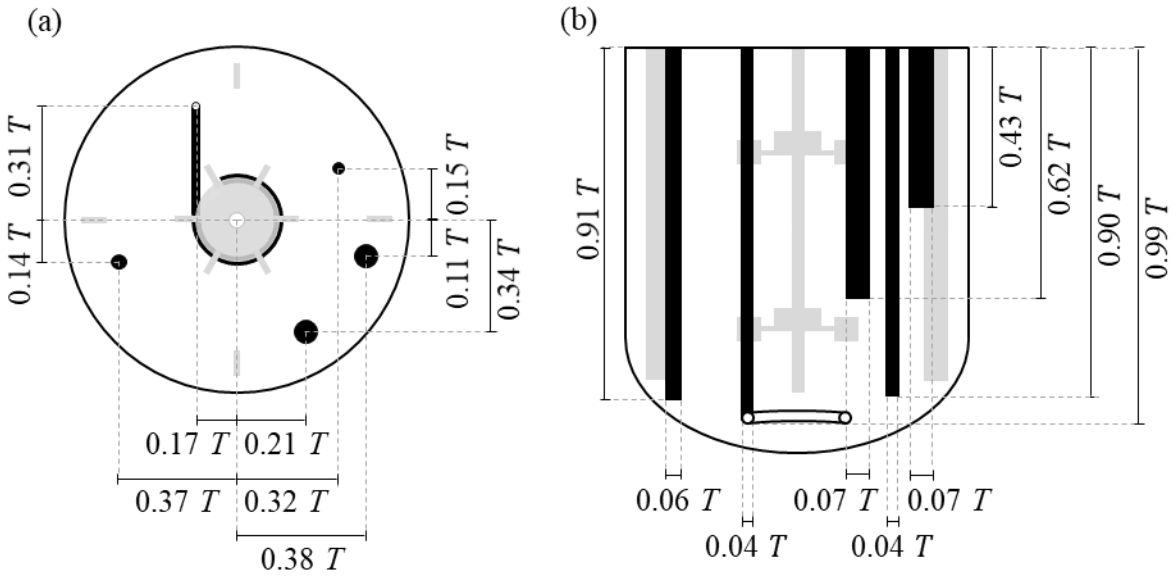

Figure A.1. Diagrams with the positions and dimensions of the probes and sparger. (a) upper and (b) lateral view of the reactor. Elements are shown in black, in the following order: sampling probe, sparger, pH probe, temperature probe and oxygen probe, from the left to the right side of the views.

Appendix B. Inoculum Preparation

The inoculum was prepared from cells stored at -80 °C in 2 mL cryovials with glycerol and modified Burk's medium (30% and 70% v/v, respectively) (Peña et al., 1997). The cryovials' cells were propagated in modified Burk's agar plates. The plates were kept at 30 °C in an incubator (IN55, Memmert, Germany) for 72 h. To propagate the inoculum for the bioreactor, bacterial colonies were taken from the plates to inoculate in 500 mL Erlenmeyer flasks containing 100 mL of culture medium. The flasks were kept for 20 h in a shaker incubator (SKIR-601, Shin Saeng, Korea) with a speed of 200 rpm at 30 °C. Finally, 40 mL of this culture were used as inoculum in a new 500 mL Erlenmeyer flask containing 360 mL of culture medium, which was incubated under the same conditions described for the other flasks for 20 h.

Appendix C. Biomass, Alginate and Sucrose Concentration

***Biomass concentration*.** A calibration curve was built to relate the OD_{540} of a culture sample with the dry weight of its biomass (Acevedo et al., 2002). For that purpose, serial dilutions were prepared from one of the 500 mL Erlenmeyer flasks cultures and the absorbance of each dilution was measured at 540 nm using distilled water as blank. Also, 20 mL of the culture broth (in duplicated) were mixed with 2 mL of EDTA (0.1 M) and 2 mL of NaCl (1 M) and then centrifuged at 6000 rpm (ROTOFIX 32A, Hettich, Germany) for 20 min. The pellet was resuspended in 10 mL of distilled water and centrifuged again. This step was repeated twice. Then, the pellet was poured into an aluminum pot, which was previously dried at 80 °C to constant weight and weighted. The pellet was dried at 80 °C to constant weight. The culture biomass concentration was estimated as the quotient between the difference of the aluminum pot dry weight with and without the pellet divided by the 20 mL volume, and the biomass concentration for the dilutions was estimated based on this. Thus, a regression equation was fitted to the data (OD_{540} vs biomass concentration) to be able to estimate indirectly the biomass concentration of the batch culture from its OD_{540} measures (Figure C.1). It is important to mention that the intercept of the regression equation was not set as zero because there was no experimental data to statistically support that decision (Barwick, 2003).

Alginate concentration. The alginate concentration was determined gravimetrically, with some variations from the methodology described by Peña et al. (1997). 4 mL of the culture broth were mixed with 0.4 mL of EDTA (0.1 M) and 0.4 mL of NaCl (1 M) and then centrifuged at 6000 rpm (ROTOFIX 32A, Hettich, Germany) during 20 min. The supernatant was mixed with 12 mL of isopropyl alcohol (technical grade). The mixture was left to rest at room temperature for 10 min to allow the precipitation. The precipitate was filtered, using a 60 mL syringe, through a 0.22 µm MCE membrane disc filters, which were previously dried at 80 °C to constant weight and weighted. To avoid the obstruction of the syringe, big alginate agglomerates were taken away before the filtration and dried together with the filtrated alginate at 80 °C to constant weight. Thus, the alginate concentration was estimated

as the quotient between the difference of the filter dry weight with and without alginate divided by the 4 mL volume.

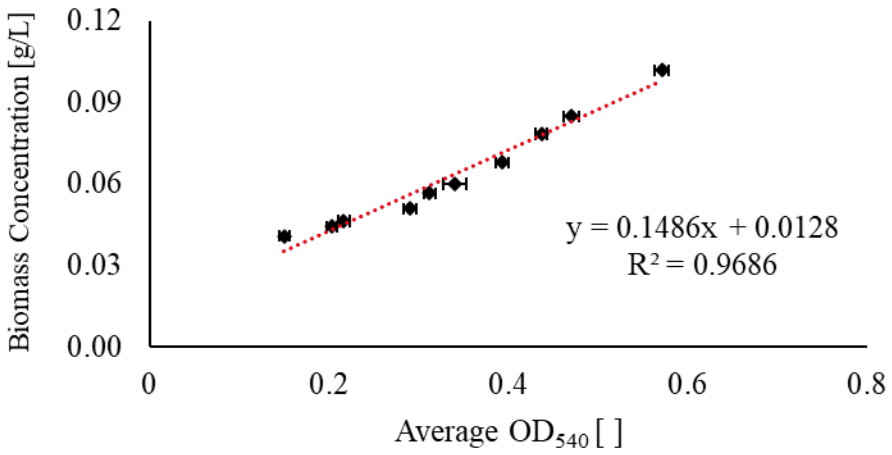

Figure C.1. Calibration curve for biomass concentration. The error bars correspond to the standard deviation. Figure from Sadino-Riquelme et al. (2020), reprinted with permission of John Wiley and Sons.

Sucrose concentration. Sucrose concentration was determined based on an assay for reducing power with dinitrosalicylic (DNS) acid reagent, after an acid hydrolysis (Miller, 1959). 1 mL of the culture broth was mixed with 0.1 mL of 37% HCl and kept at 60 °C during 10 min in a hot bath. The hydrolysis was neutralized by adding 0.9 mL of NaOH (1.7 M). 1 mL of the mixture was added to 1 mL of DNS reagent and kept at 100 °C during 5 min in a hot bath. To stop the reducing reaction, the solution was moved into an ice bath. Then, 10 mL of distilled water were added to the mixture. The absorbance of the solution was measured at 540 nm. Distilled water was used to prepare the blank. The sucrose concentration was estimated from a calibration curve, which was built following the same procedure described here but using 1 mL of sucrose solution with a known concentration of sugar, instead of culture broth. Thus, a regression equation was fitted to the data (sucrose concentration vs OD_{540}) to be able to estimate indirectly the sucrose concentration of the batch culture (Figure C.2). It is important to mention that the intercept of the regression equation was not set as zero because there was no experimental data to statistically support that decision (Barwick, 2003).

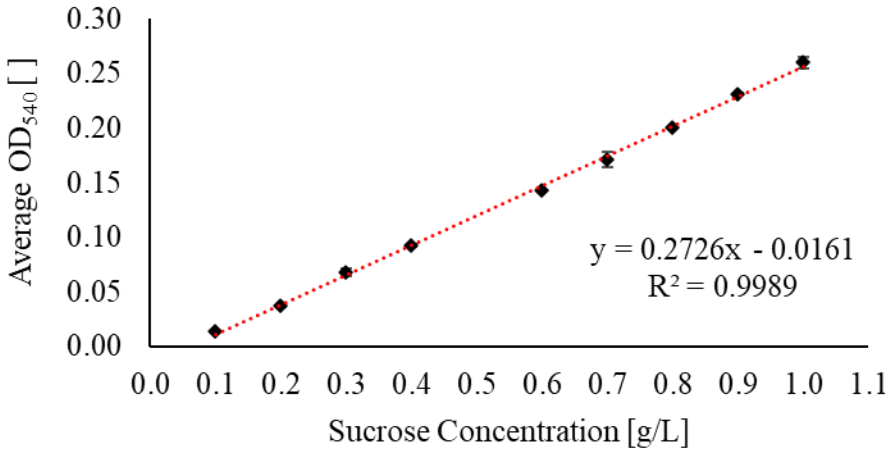

Figure C.2. Calibration curve for sucrose concentration. The error bars correspond to the standard deviation. Figure from Sadino-Riquelme et al. (2020), reprinted with permission of John Wiley and Sons.

Appendix D. Fermentation Rheological Parameters

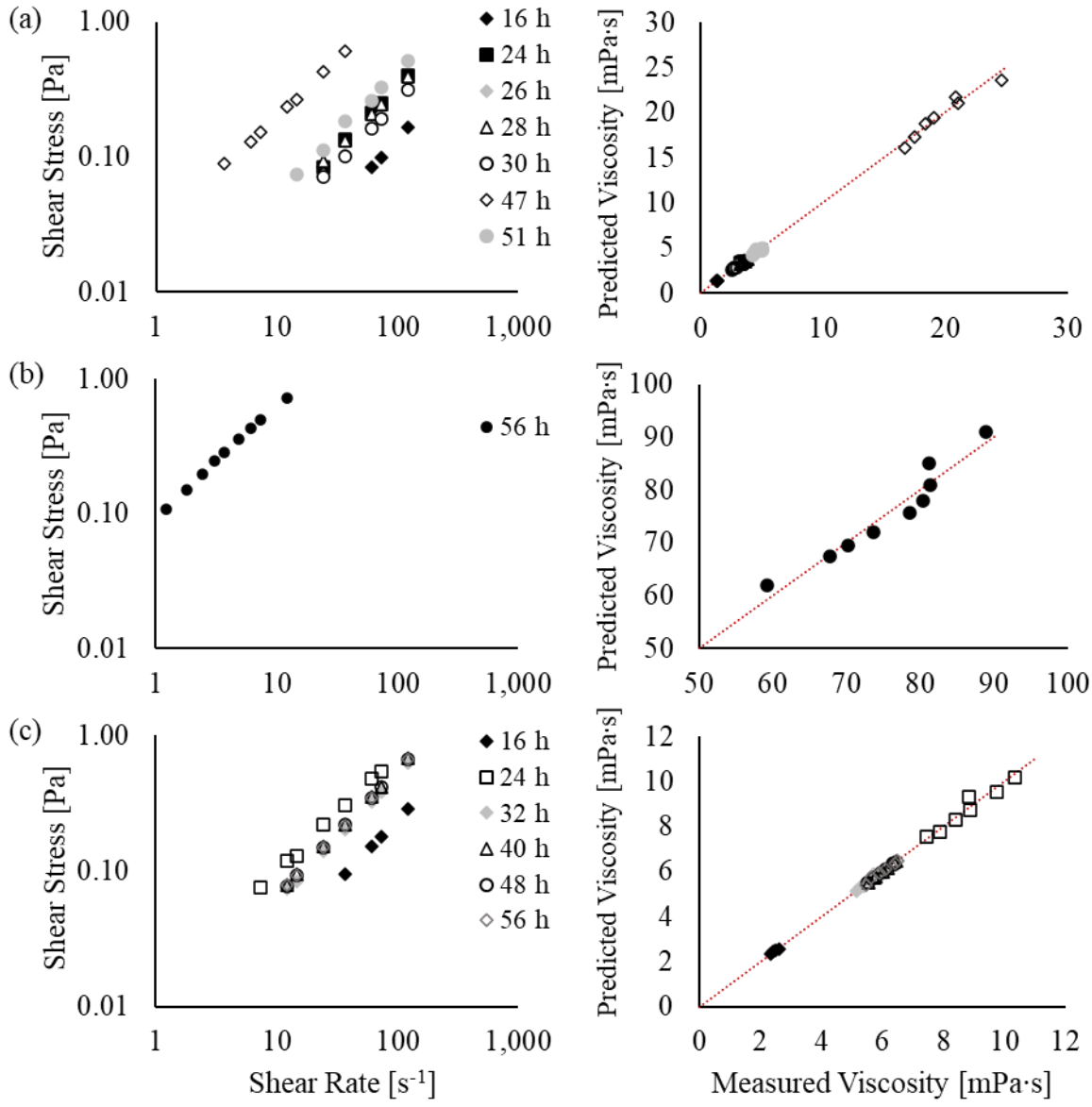

Figure D.1. Shear rate versus shear stress curve and measured viscosity versus predicted viscosity curve, for the samples taken at different times (since the inoculation) from (a) culture #1, (b) culture #2, and (c) culture #3. The predicted viscosity was calculated using the Power Law model with the parameters fitted from the corresponding shear rate versus shear stress curve ($R^2 > 0.99$, in all the cases). The red dotted line corresponds to the identity line.

Appendix E. Statistical Inferences

nlparci and *nlpredci* functions are based on the asymptotic theory of nonlinear least-squares estimation. This framework assumes that the experimental data is affected by random error with a normal distribution, with an expected value equal to zero and constant variance (Seber & Wild, 1989). Thus, the confidence and prediction intervals are estimated using Equation E.1 and E.2, respectively.

$$\widehat{\theta_r} \pm t_{M-p_\theta}^{\alpha_{test}/2} s\sqrt{\left(\hat{J}' \cdot \hat{J}\right)_{rr}^{-1}} \tag{E.1}$$

$$\hat{f} \pm t_{M-p_\theta}^{\alpha_{test}/2} s\sqrt{1 + f_o'\left(\hat{J}' \cdot \hat{J}\right)^{-1} f_o} \tag{E.2}$$

where $\hat{\theta}_r$ is the estimated mean value for the *r*-th parameter; $\hat{f}$ is the estimated mean value for the model output; M is the size of the data set; p_θ, the number of parameters; $t_{M-p_\theta}^{\alpha_{test}/2}$ is the t-distribution with $M - p_\theta$ degrees of freedom for a 100(1-α_{test})% confidence interval; $\hat{J}$ is the inverse matrix of the upper triangular matrix obtained by the orthogonal-triangular decomposition of the Jacobian matrix; $s\sqrt{\left(\hat{J}' \cdot \hat{J}\right)_{rr}^{-1}}$ is an estimated of the parameter standard deviation, calculated with the *r*-th element of the diagonal of $\left(\hat{J}' \cdot \hat{J}\right)^{-1}$ and the root of the mean square error (estimated based on the residuals of the model); and f_o is a vector with the derivative of the kinetic model with respect to each parameter, evaluated at $\hat{f}$. More theoretical details can be referred to Seber and Wild (1989).

Additionally, to compare the estimated values for each parameter, it was performed a two-sample t-Test for equal means (NIST/SEMATECH, 2003), which consider unpaired data and two samples with different variances and independent data. To illustrate this, let consider that the CI of the specific growth rate of culture #1 overlaps with CI of the same parameter for culture #2, so arises the question of whether this parameter is significantly different between these cultures or not. Then, the null hypothesis H_0: $\mu_1 = \mu_2$ was tested, where $\hat{\mu}_1$ and $\hat{\mu}_2$ are the estimated mean values of the specific growth rate for cultures #1 and #2, respectively. The test statistic (T_{test}) was estimated as shown in Equation E.3, where M_1 and

M_2 are the sample sizes and s_1^2 and s_2^2 are the sample variances, for cultures #1 and #2, respectively. It is important to note that $\hat{\mu}$ and s^2/M are both outputs of *nlinfit*, where s^2/M correspond to the diagonal values of the variance-covariance matrix. The *p*-value for this two-tailed test can be calculated using the Matlab® function *tcdf* (Equation E.4). *tcdf* computes the t-Student cumulative distribution function and for that requires two inputs: the value of T_{test} and its degrees of freedom (DF). The latter can be calculated with Equation E.5. So, when the *p*-value is under 0.05 level of significance, the null hypothesis is rejected and the alternative hypothesis, which states that the parameter means are significantly different, is accepted.

$$T_{test} = \frac{\hat{\mu}_1 - \hat{\mu}_2}{\sqrt{\frac{s_1^2}{M_1} + \frac{s_2^2}{M_2}}} \tag{E.3}$$

$$p\text{-value} = 2 \cdot tcdf(-|T_{test}|, DF) \tag{E.4}$$

$$DF = \frac{(s_1^2/M_1 \ + s_2^2/M_2)^2}{\left(\frac{s_1^2}{M_1}\right)^2/(M_1 - 1) + \left(\frac{s_2^2}{M_2}\right)^2/(M_2 - 1)} \tag{E.5}$$

Appendix F. Alginate Aggregates

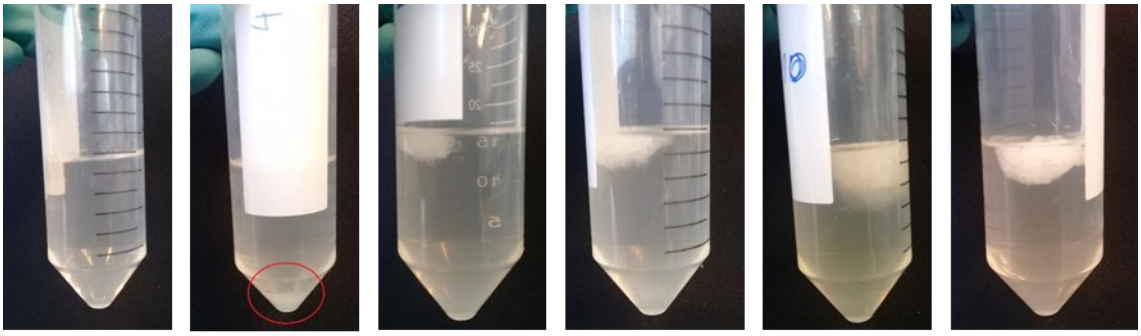

Figure F.1. Alginate aggregates re-suspended from samples of culture #2 taken at different times.

Appendix G. Fermentations Photos

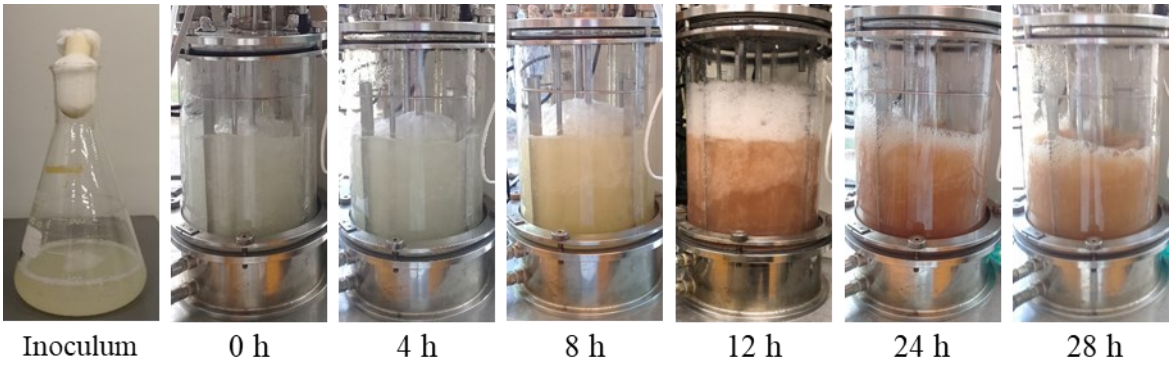

Figure G.1. Pictures of culture #1 at different times of the fermentation process.

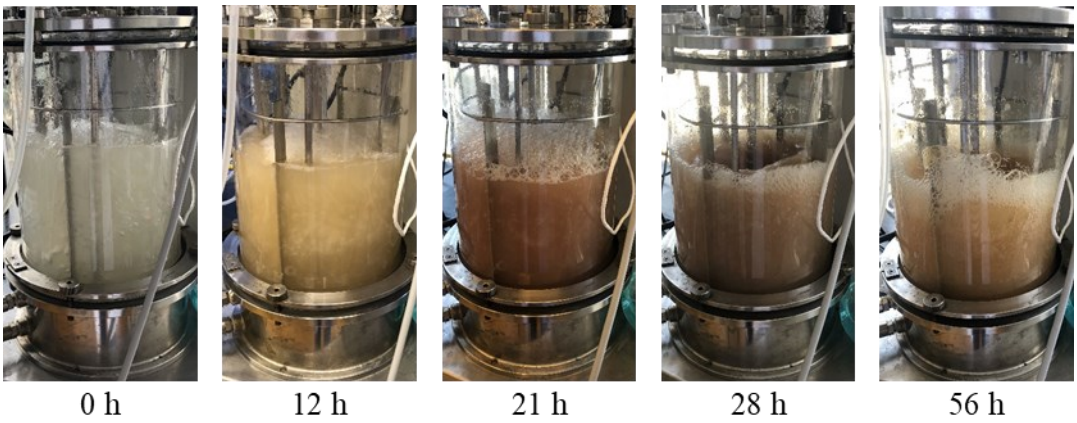

Figure G.2. Pictures of culture #2 at different times of the fermentation process.

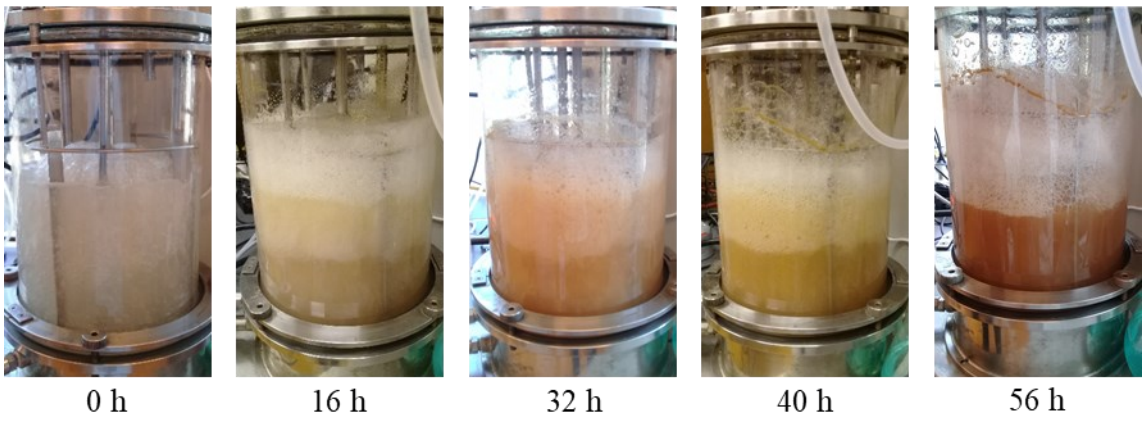

Figure G.3. Pictures of culture #3 at different stages of the fermentation process.

Appendix H. Xanthan Solutions Rheological Parameters

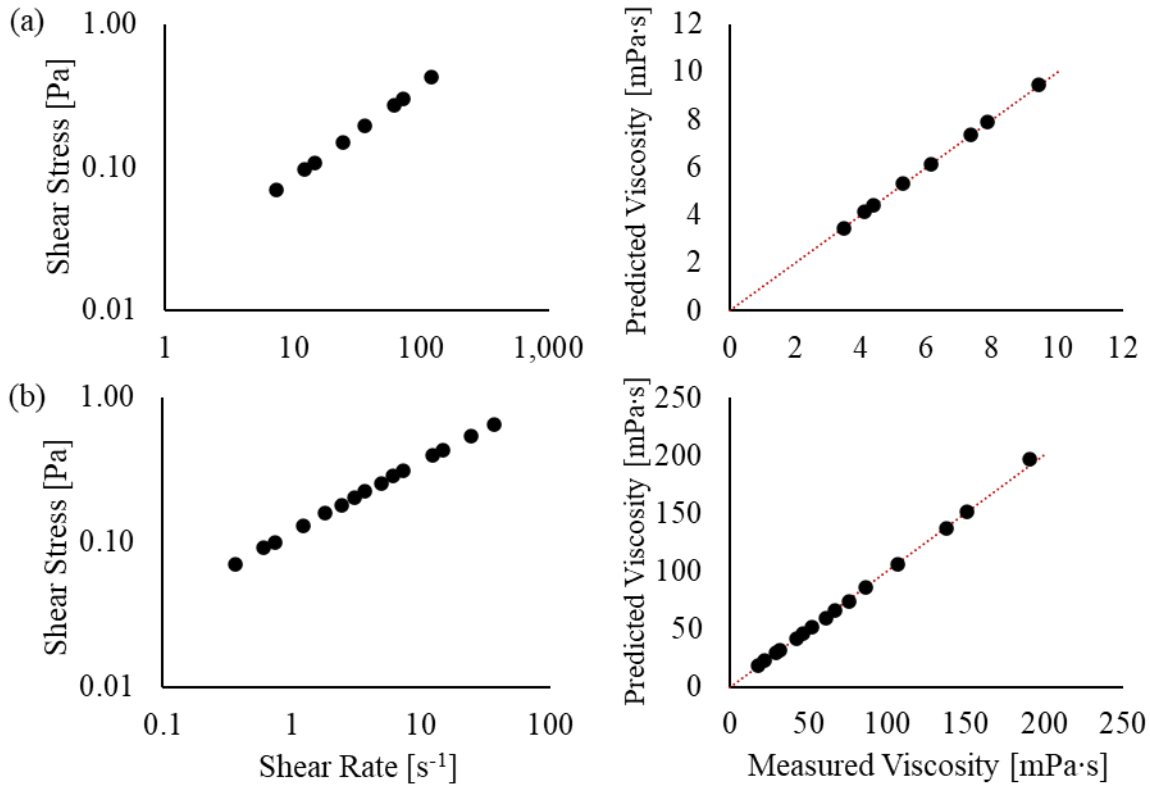

Figure H.1. Shear rate versus shear stress curve and measured viscosity versus predicted viscosity curve, for the fluid of (a) Xanthan Sol B and (b) Xanthan Sol A. The predicted viscosity was calculated using the Power Law model with the parameters fitted from the corresponding shear rate versus shear stress curve ($R^2 > 0.99$, in all the cases). The red dotted line corresponds to the identity line.

Appendix I. Batch Abiotic Systems Mixing Time

The software ImageJ allows the calculation of the mean gray value of a control area for several consecutive time frames. Figure I.1 shows the control area chosen for each analyzed abiotic system. These areas were chosen to reduce the perturbation on the colour analysis, for example, from the vortex formation at the upper liquid level and from the brightness of the light reflected on the glass.

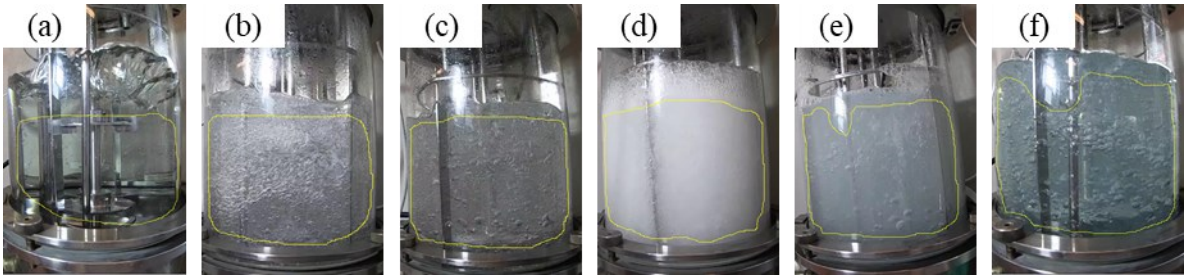

Figure I.1. Control area (defined by the yellow line) used in ImageJ for the mixing time analysis of the batch abiotic systems with (a) water without aeration, (b) water with aeration, (c) PEG Sol A with aeration, (d) PEG Sol B with aeration, (e) Xanthan Sol A with aeration, and (f) Xanthan Sol B with aeration.

For each abiotic system, it was identified the injection time and the maximum mean gray value since the time injection. Thus, for each time frame, it was calculated the difference between the maximum mean gray value and the mean gray value at that time. Afterwards, the maximum difference was identified and used to normalize the mean gray difference at each time frame. Finally, the mixing time was defined as the first time at which the normalized mean gray difference was equal to 0.95. Figure I.2 shows the normalized mean gray difference against time for each analyzed system.

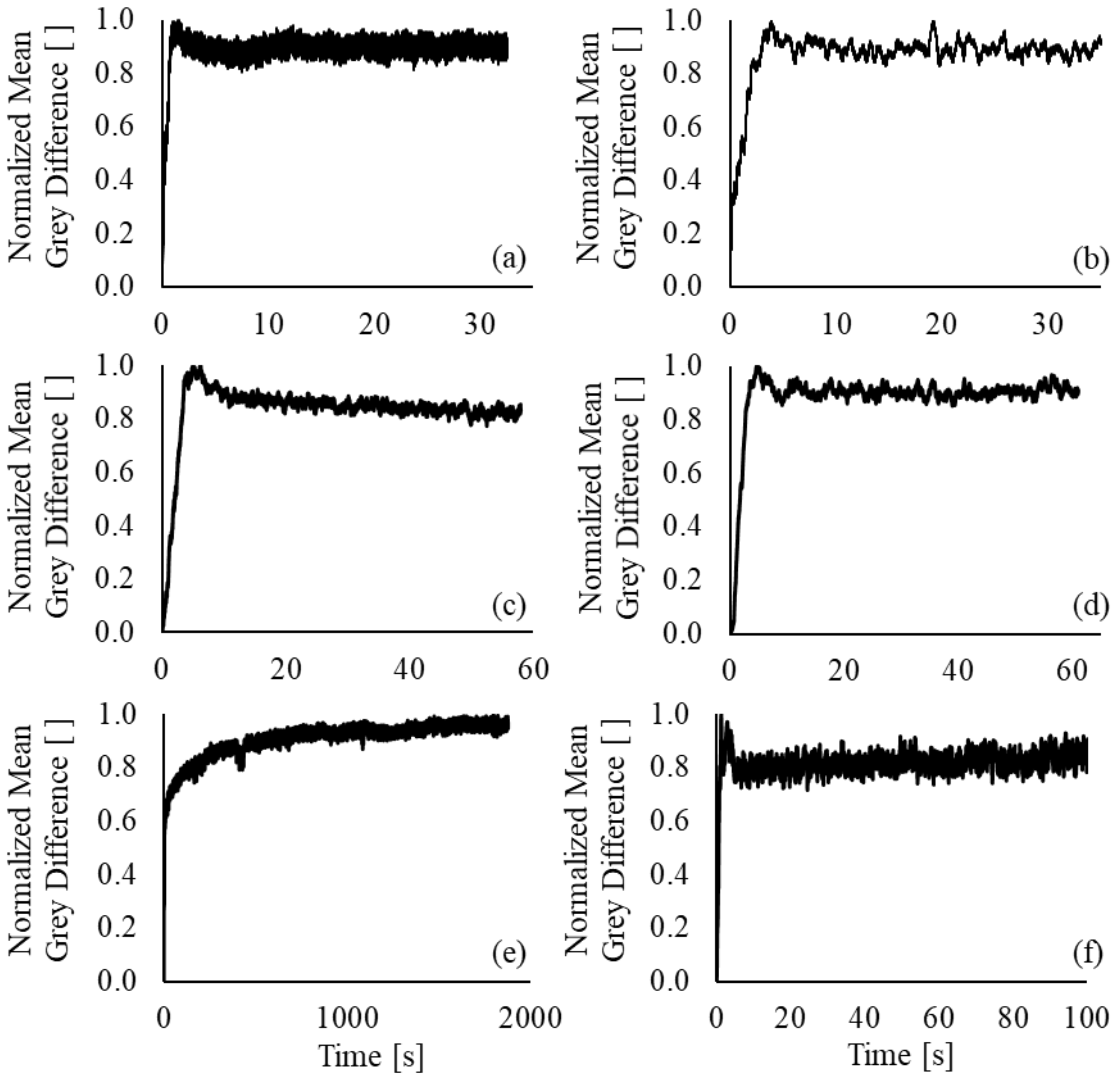

Figure I.2. Normalized mean gray difference against time for the batch abiotic systems (a) water without aeration, (b) water with aeration, (c) PEG Sol A with aeration, (d) PEG Sol B with aeration, (e) Xanthan Sol A with aeration, and (f) Xanthan Sol B with aeration. Time 0 s corresponds to the injection time.

Appendix J. Batch Abiotic Systems Bubble Diameter

Figure J.1 shows one picture for each batch abiotic system with aeration. The software ImageJ allows us the estimation of the dimension of a bubble from the images, based on its pixels. To estimate the pixels of a bubble, a line is drawn over the bubble. For that line, ImageJ supplies the gray value intensity profile, from which the border of the bubble can be identified, and, with that, the dimension of the bubble in pixels. The image must have an object with a known dimension in the metric system, so, with its pixel dimension, it can be defined a measuring units transformation equation. In this case, the thickness of the baffle (2 mm) was used. Thus, the bubble diameter in pixels can be transformed into millimetres. For a better estimation, each bubble diameter was approximated as the averaged of its height and width.

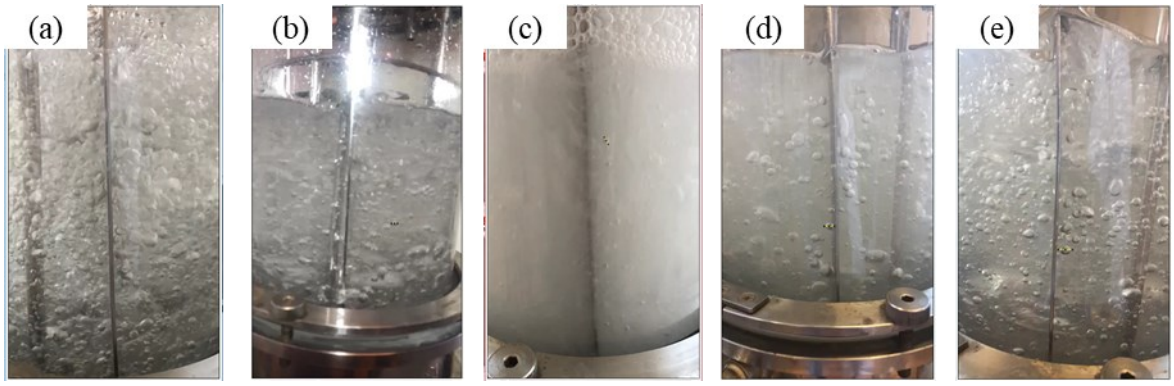

Figure J.1. Example of the analyzed photos to estimate the bubble diameter for the aerated batch abiotic systems with (a) water, (b) PEG Sol A, (c) PEG Sol B, (d) Xanthan Sol A, and (e) Xanthan Sol B.

The procedure will be exemplified for one bubble. Figure J.2 shows the intensity profile across the height and width for a same bubble. Based on an intensity profile of the baffle, in the same image, the baffle thickness was estimated as 8 px. Thus, a conversion factor of 0.25 mm/px was calculated for this image. With that factor, the bubble height and width, which measure 20 and 18 px, were transformed into 5.0 and 4.5 mm, respectively. Finally, its diameter was approximated as 4.8 mm.

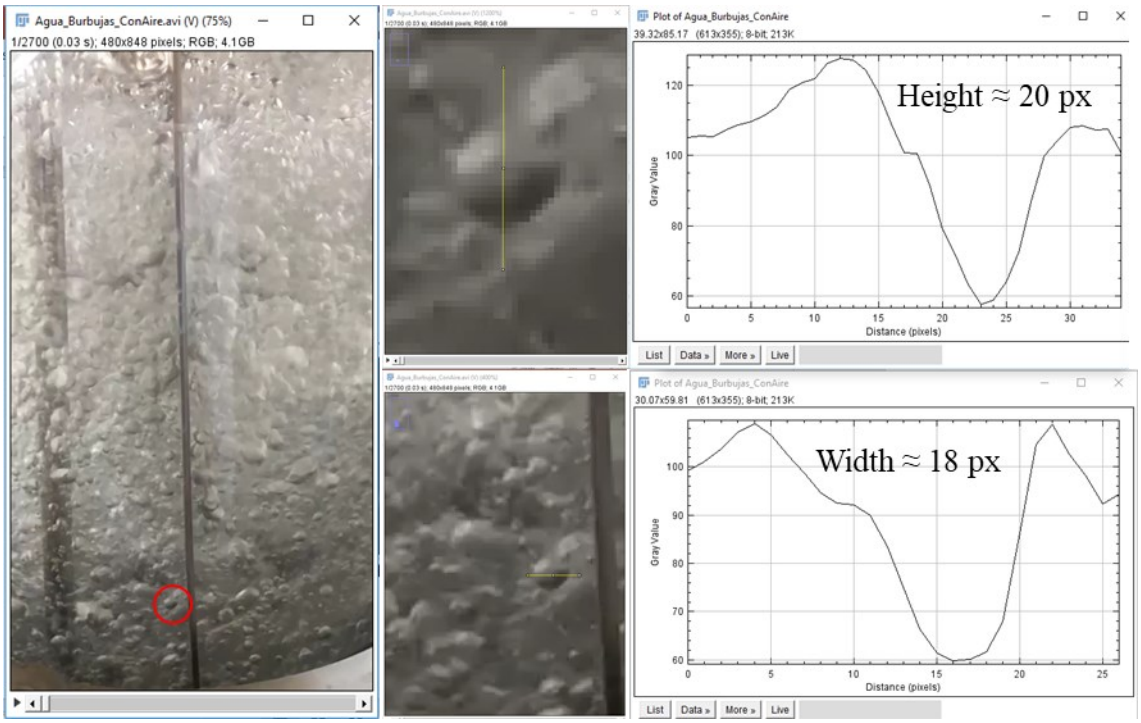

Figure J.2. Example of procedure to estimate the bubble diameter in ImageJ.

Appendix K. Xanthan System Rheological Parameters

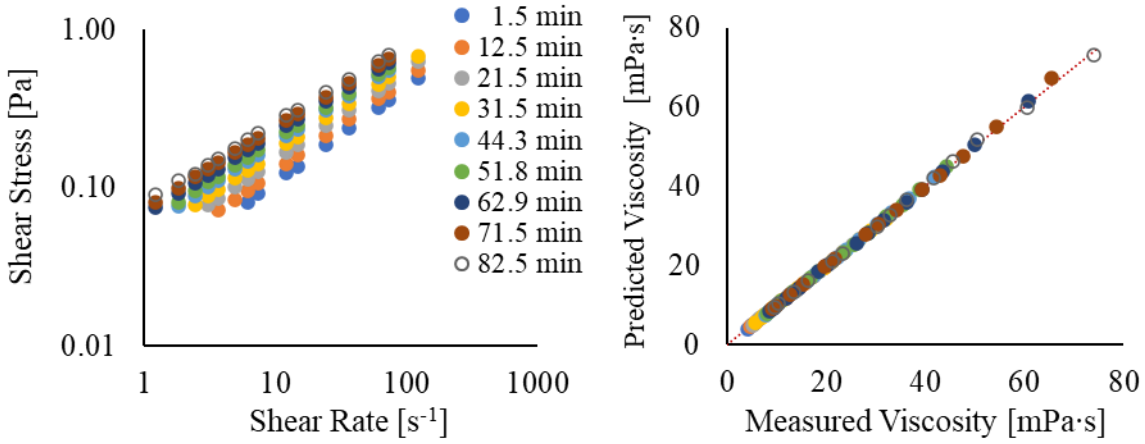

Figure K.1. Shear rate versus shear stress curve and measured viscosity versus predicted viscosity curve, for the samples taken at different times from the outflow of the continuous Xanthan system. The predicted viscosity was calculated using the Power Law model with the parameters fitted from the shear rate versus shear stress curve ($R^2 > 0.99$, in all the cases). The red dotted line corresponds to the identity line.

Appendix L. Batch Abiotic Systems Torque Data

In the experimental system, the impeller was moved by a pulsed force, not by a continuous force. The frequency and the magnitude of the pulses were controlled to keep the set-up agitation speed. Thus, the torque meter, which registers data each $9 \cdot 10^{-3}$ s, will register zero and non-zero values (see Figure L.1). To analyze the torque as a continuous variable (ie. not as a pulse), the pulses were averaged every 500 consecutive data (including zero and non-zero values). This treatment is important because the experimental torque is being used for the validation of the CFD models, and the torque is a continuous variable in the models.

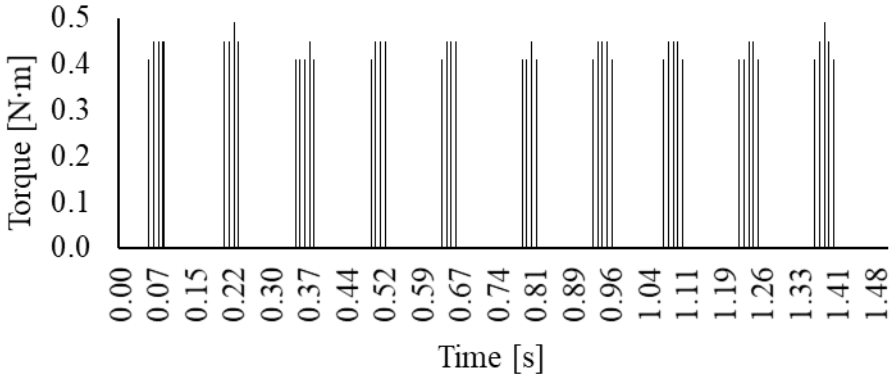

Figure L.1. Example of the registered zero and non-zero pulses at the impeller by the torque meter.

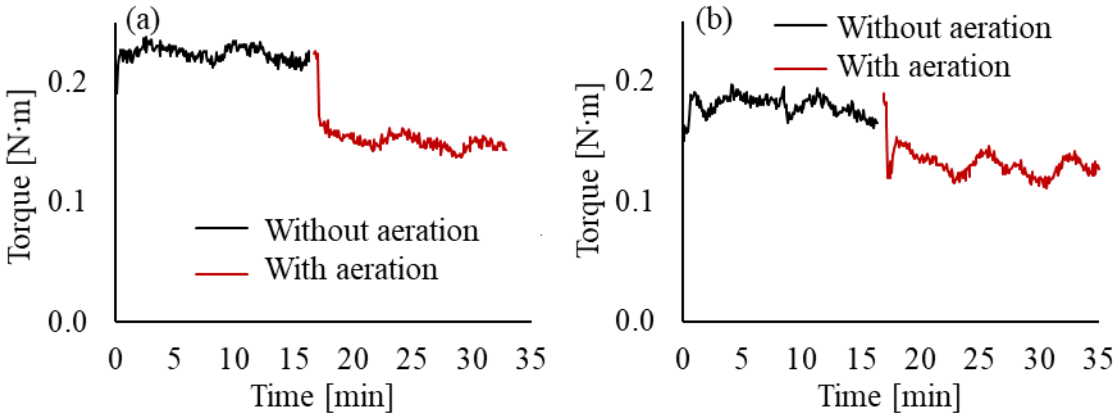

Figure L.2. Torque temporal evolution for the batch abiotic systems with (a) PEG Sol A and (b) PEG Sol B, without and with aeration, in the tank configuration with probes. The curves for PEG Sol A correspond to the discarded data (with ** in Table 3.4).

Figure L.2-L.6 show the temporal variation of the torque (as a continuous variable) for the abiotic systems, without and with aeration. The plots not included in this appendix can be found in Figure 3.4.

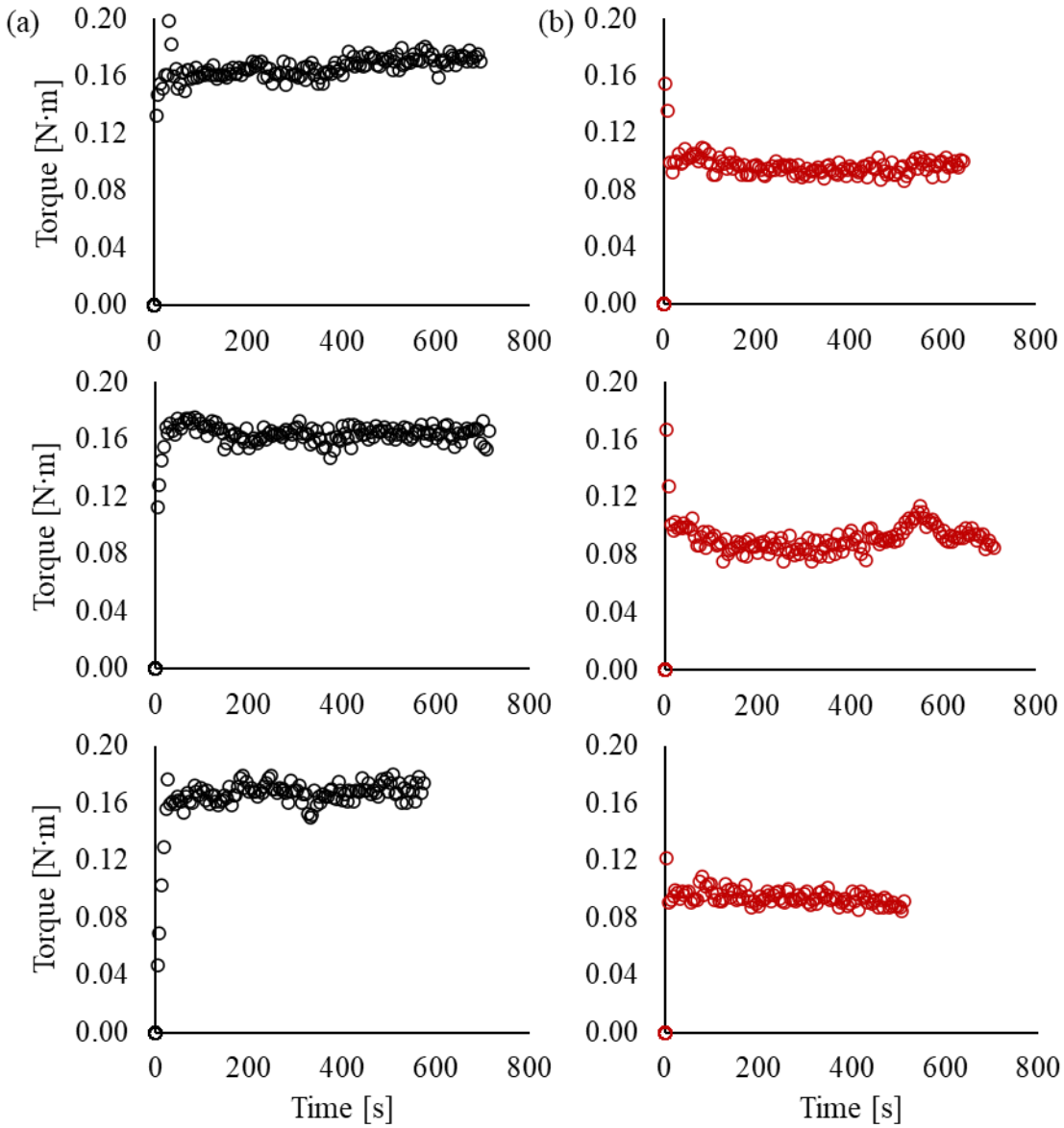

Figure L.3. Torque temporal evolution for the batch abiotic system with PEG Sol A, (a) without and (b) with aeration, in the tank configuration with probes. These measurements replaced the discarded data.

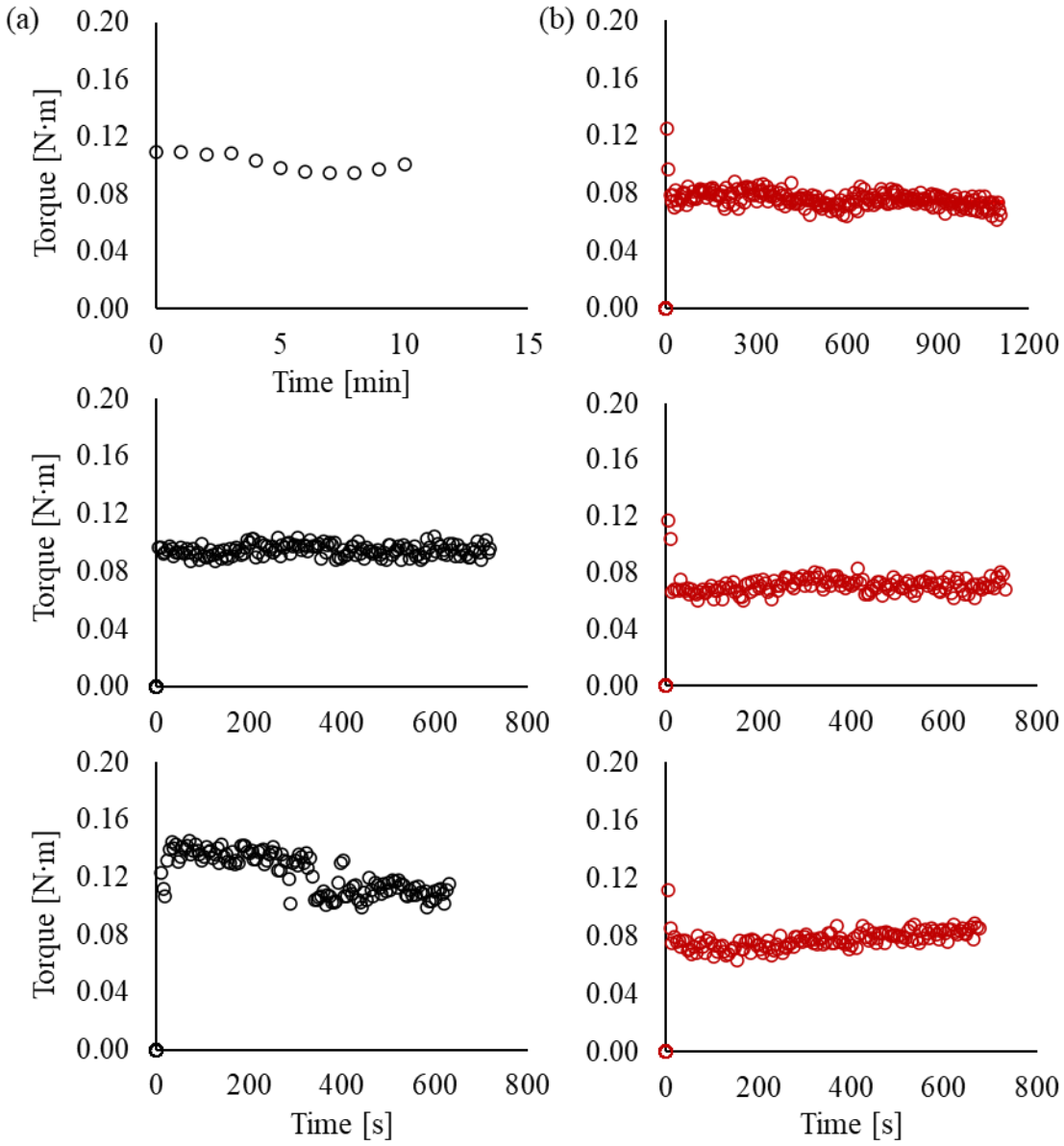

Figure L.4. Torque temporal evolution for the batch abiotic system with water, (a) without and (b) with aeration, in the tank configuration without probes.

Figure L.4 shows the temporal variation of the torque for the triplicates of the abiotic system with water, without probes and without aeration. The triplicate #1 is the only exception regarding the methodology of averaging consecutive pulses. In this case, the pulses were averaged over each minute of the experiment. This was the initial methodology applied to analyze the experimental data. Later, the methodology was replaced by the idea of

averaging every 500 consecutive pulses. However, for triplicate #1, it was not possible to modify the analysis because the original data file was lost. This does not impact the averaged torque, based on the results of the other analyzed experimental cases.

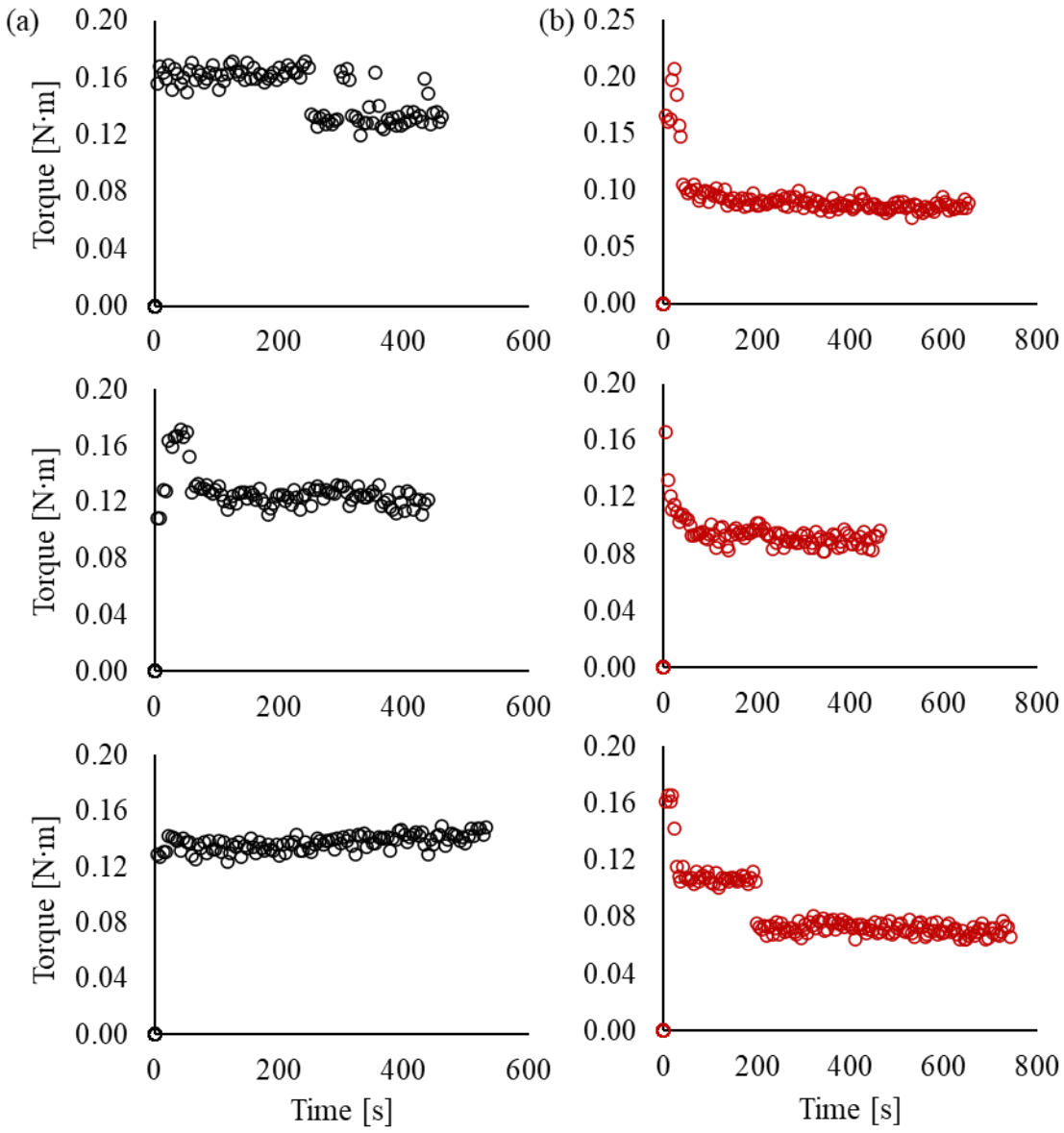

Figure L.5. Torque temporal evolution for the batch abiotic system with PEG Sol A, (a) without and (b) with aeration, in the tank configuration without probes.

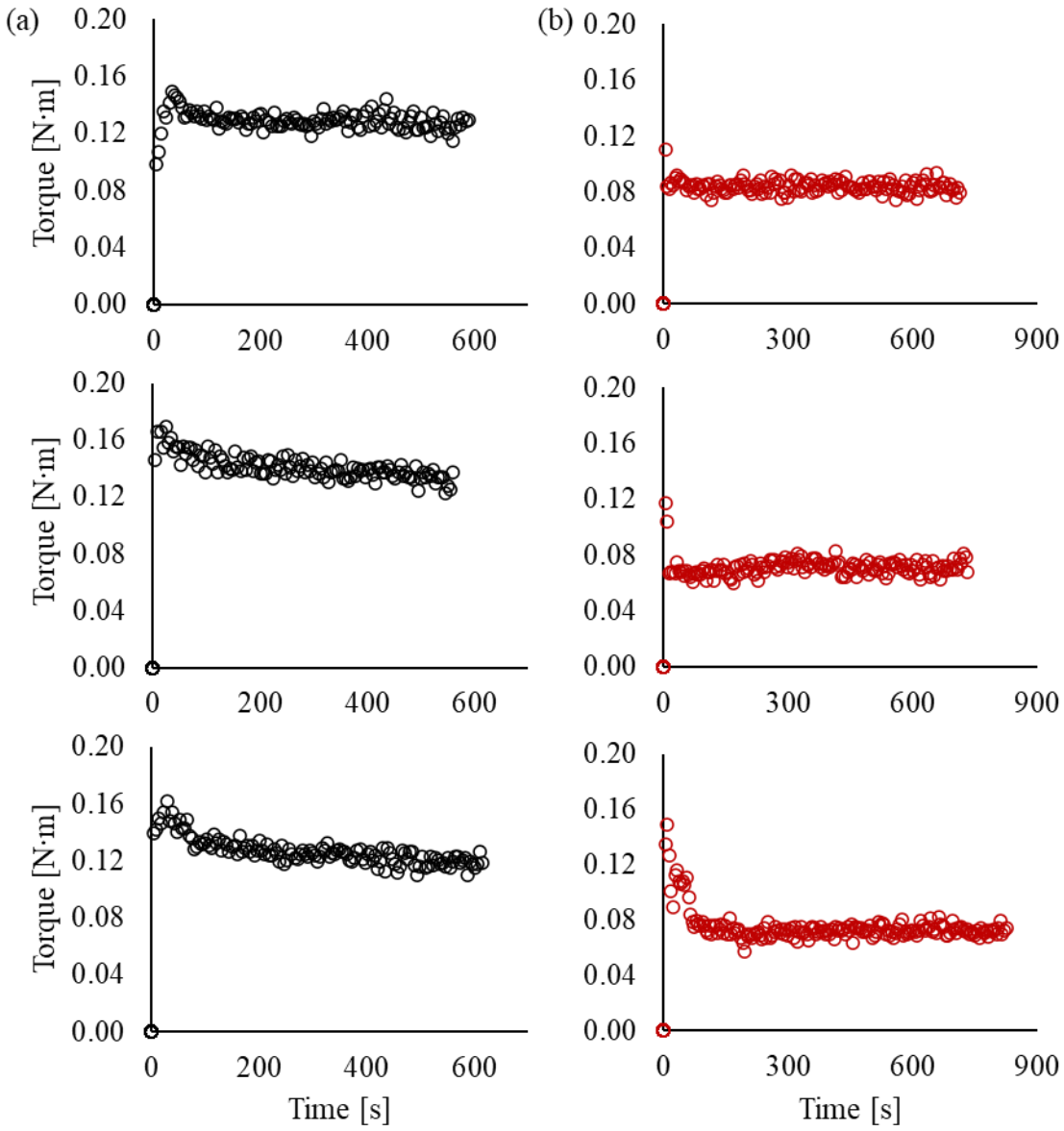

Figure L.6. Torque temporal evolution for the batch abiotic system with PEG Sol B, (a) without and (b) with aeration, in the tank configuration without probes.

Appendix M. Preliminary Simulations Step 1

Geometry. The preliminary geometry of the 4 L tank contained only the baffles and the sparger ring, apart from the dual impeller. The domain was divided into smaller bodies to set the moving reference frames around the axis (see Figure M.1). Unlike GeomA, the stationary zone, where are located the baffles and the sparger ring, was not divided into smaller bodies.

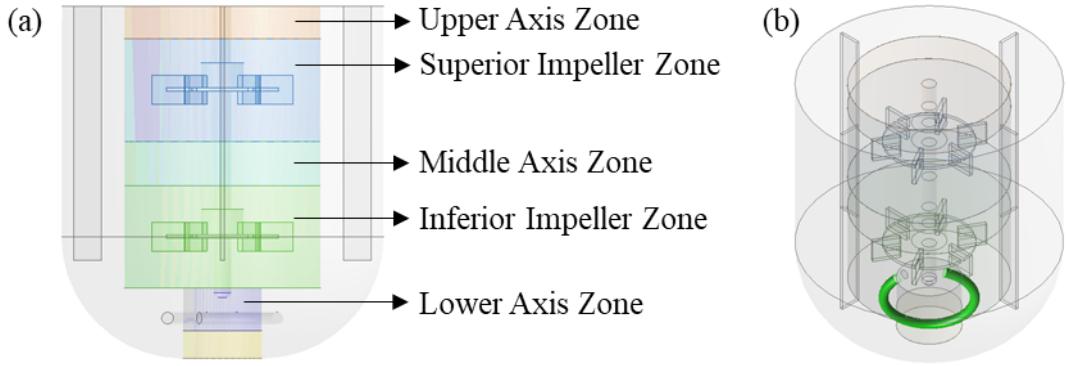

Figure M.1. Preliminary CFD domain of the tank. (a) Side view, identifying the moving reference frames, and (b) isometric view, with the ring of the sparger highlighted in green.

Mesh. An unstructured mesh was implemented (see Figure M.2). CFD and Fluent were selected, respectively, under the physics and solver preferences of the software. For the general sizing settings, the curvature function was set with coarse relevance center. The maximum face size, minimum size and maximum tetrahedral size were modified from their default values to 2.2, 1 and 2.2 mm, respectively.

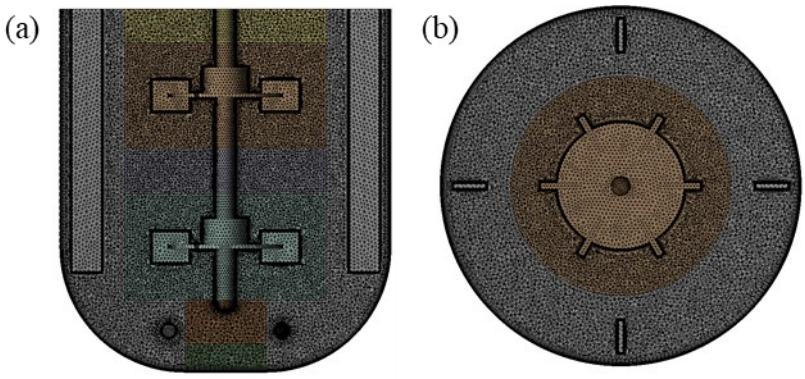

Figure M.2. Preliminary mesh. Views at (a) vertical plane across the tank center, and (b) horizontal plane across the upper impeller.

Face and body sizing methods were used to locally refine the mesh. Also, inflation layers were implemented next to each wall (see Table M.1). Using these features, the spatial mesh resulted in 1,419,083 nodes. The quality of the grid is reported in Table M.2.

Table M.1. Methods and sizes used for the local refinement of the preliminary grid.

Body sizing, with curvature	Impeller zones (1.8 mm)
	Middle axis zone (1.8 mm)
Face sizing, with curvature	Impeller wall (1.8 mm)
	Exterior wall (2 mm)
	Baffles' wall (2 mm)
	Air sparger wall (2 mm)
Inflation layers, applied to	Total thickness
* Impeller walls	Layers: 15
* Baffles walls	Growth rate: 1.2
** Exterior wall	Max. Thickness: 2 mm *
** Sparger wall	Max. Thickness: 3 mm **

Table M.2. Quality indices of the preliminary grid.

Index Value	Skewness	Orthogonal quality	Aspect Ratio
Minimum	2.3e-07	9.8e-02	1.16
Maximum	0.90	1	171
Average	0.22	0.78	7.41

Model settings. To simulate the mixing without aeration, a single-phase model was implemented for the batch abiotic systems with water, PEG Sol A and PEG Sol B. The properties of the fluids were set up according to Table 3.1. The sliding mesh approach was used, with a rotating velocity of 400 rpm for each moving zone: upper, middle and lower axis, and impeller zones. The gravity force was included as a body force in the negative Y-direction. The standard k-epsilon turbulence model was set with standard wall functions. An additional simulation was developed for PEG Sol A, using the laminar model. The boundary conditions were as follows: for the top wall, symmetry; for the impellers and axis walls, 0 rpm as relative velocity with respect to the moving zones; and no-slip condition for the other walls. As initial condition, the velocity in every direction was set to 0 m/s and the turbulence parameters values were set to 0.1.

To solve the equations, the SIMPLE pressure-velocity coupling scheme with the absolute velocity formulation was chosen. The following discretization methods were set: least-squares cell-based for gradient; second-order for pressure; first-order upwind for momentum, turbulent kinetic energy, and turbulent dissipation; and first-order implicit for the transient formulation. The warped-face gradient correction was activated, and some under-relaxation factors were modified from its default value (density 0.7; body forces 0.7; turbulent viscosity 0.8). The simulations were solved using double precision, with a time step size of 0.0004 s and 50 iterations per time step. After running 35 impeller turns, the discretization methods were changed to second-order. Afterwards, the near-wall treatment was modified based on Y^+ values.

For each simulation, the velocity magnitude at different points and the impeller torque were registered after every time step. The monitoring points were placed over the vertical

plane shown in Figure 4.4. Furthermore, the residual values were tracked, along with any alert of cells with turbulent viscosity ratio exceeding the maximum allowed value (10^5). At the end of each time step, residuals values below 10^{-5} were expected.

Simulation results. All the simulations with first-order discretization methods reached residuals values below 10^{-5} and did not present numerical issues. In particular, there were no alerts of turbulent viscosity ratio above 10^5. From the simulations with the standard k-epsilon model, the turbulent viscosity ratio data was analyzed to check whether a laminar model should be used or not. For the systems with water and PEG Sol B, it was confirmed that the use of a turbulence model is appropriate. On the other hand, for the case with PEG Sol A, a laminar model should be used. Furthermore, for the cases with water and PEG Sol B, the Y^+ values next to the walls suggest that the enhanced wall treatment would be more appropriate than the standard wall functions.

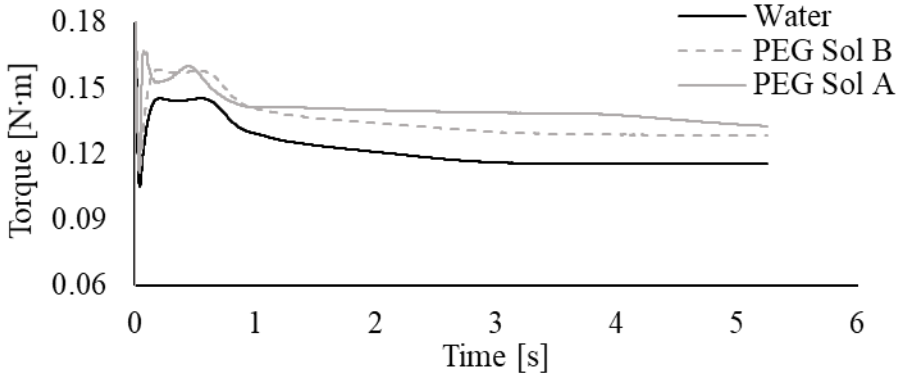

Figure M.3. Impeller torque evolution simulated with the preliminary CFD models of the batch abiotic systems with Newtonian fluids, using first-order discretization methods.

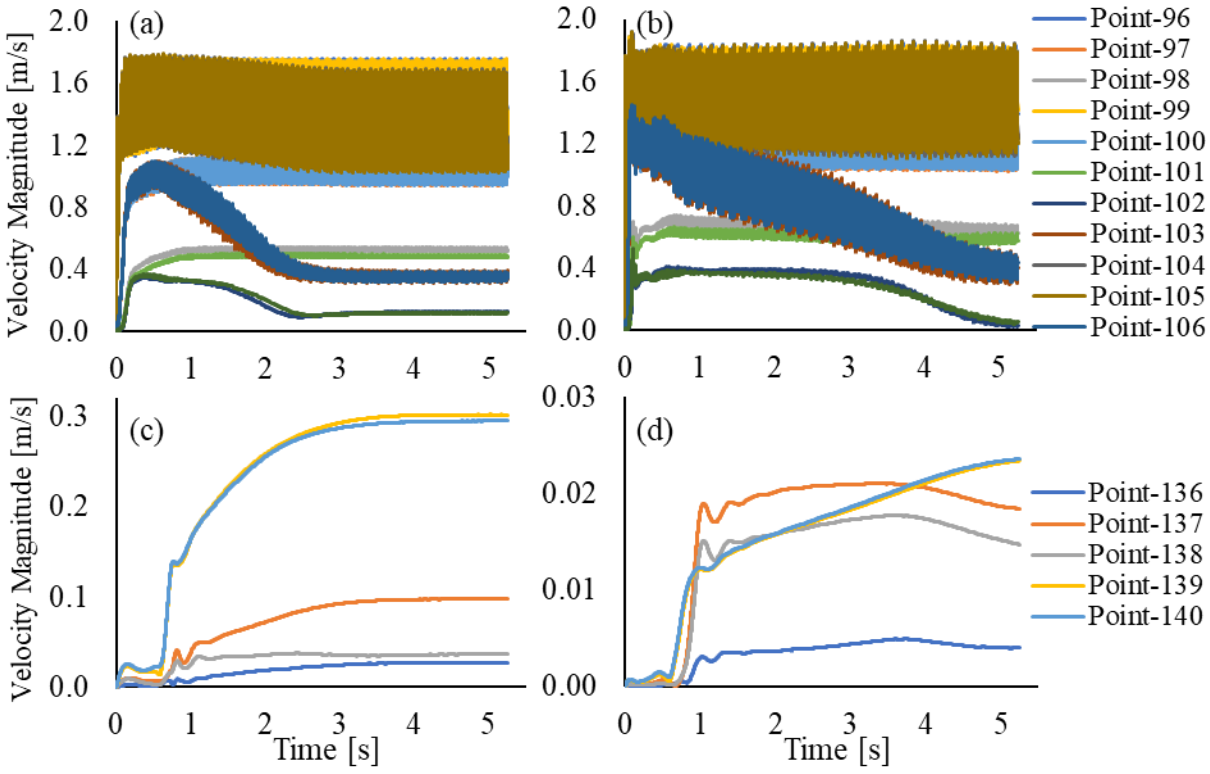

Figure M.4. Velocity magnitude evolution simulated with the preliminary CFD models of the systems with (a, c) water and (b, d) PEG Sol A, using first-order discretization methods.

After the simulation of 35 impeller turns, the torque shows a stationary state for the systems with water and PEG Sol B but not for PEG Sol A (see Figure M.3). Something similar was observed when comparing the fluid velocity magnitude of the different systems. Figure M.4 shows the fluid velocity at the monitoring points for the cases with water and PEG Sol A. While the water velocity magnitude has reached the stationary state in all the monitoring points, from the closest to the impellers to the more distant ones; PEG Sol A velocity magnitude has not reached that state yet. That can be explained by the higher viscosity of PEG Sol A, which decreases and delays the momentum transferred from the impellers to the other zones of the tank. In fact, the maximum velocity magnitude close to the tank bottom is one order of magnitude lower in the system with PEG Sol A than with water.

An averaged torque value was calculated over the torque data of the last simulated impeller turn. For the abiotic systems with water, PEG Sol A and PEG Sol B, the simulated averaged torque was compared with the triplicates' average of the experimental results

without probes (see Table M.3). The simulated averaged torque for the system with water has the biggest error, although it is as low as 13%, while the simulated averaged torque for PEG Sol A and PEG Sol B match satisfactorily the experimental results. Thus, so far, the CFD model is able to predict the torque when a Newtonian fluid is mixed in the tank. Furthermore, in agreement with the experiments, the highest and lowest simulated torques correspond to the systems with PEG Sol A and water, respectively. Also, PEG Sol A registered a higher torque than PEG Sol B.

Table M.3. Validation of the preliminary CFD models, using first-order discretization methods, against experimental torque data. Simulated torque is given as $T_{AVG_{sim}} \pm T_{SD_{sim}}$, in units of [N·m], and $|E|$ in unit of [%].

Fluid	**Turbulence Model**	**Torque**	$\|E\|$
Water	Standard k-epsilon	0.1153 ± 0.00001	13%
PEG Sol B	Standard k-epsilon	0.1285 ± 0.00002	0.3%
PEG Sol A	Standard k-epsilon	0.1392 ± 0.00003	2.1%
	Laminar	0.1328 ± 0.00012	2.6%

The solutions of the simulations with first-order discretization methods were used as initial condition to run the corresponding models with second-order discretization methods. All the other settings remained the same. 15 impeller turns were run for the abiotic systems using the standard k-epsilon model, while 20 impeller turns were run for the system with the laminar model. The residuals reached values below 10^{-5}, except for the model of PEG Sol A with the k-epsilon model. Furthermore, it was confirmed that the laminar model should be used for PEG Sol A. Thus, the model of PEG Sol A with k-epsilon was discarded.

For the systems with water and PEG Sol B, a few cells presented a turbulent viscosity ratio above 10^5, which is a numerical issue. Aside, similar to the simulations with first-order methods, the Y^+ value indicates that the enhanced wall treatment should be applied in these cases. Thus, these solutions were used as initial condition to run simulations with the enhanced wall treatment. 8 impeller turns were simulated for each abiotic system. Again, all

the residuals reached values below 10^{-5} and the Y^+ values were consistent with the use of the enhanced wall treatment, but the simulations still presented cells with numerical issues. Inspecting the contour of turbulent viscosity ratio for PEG Sol B, it was possible to identify that the cells with problems were mainly located in the interfaces between the moving and stationary bodies (see Figure M.5).

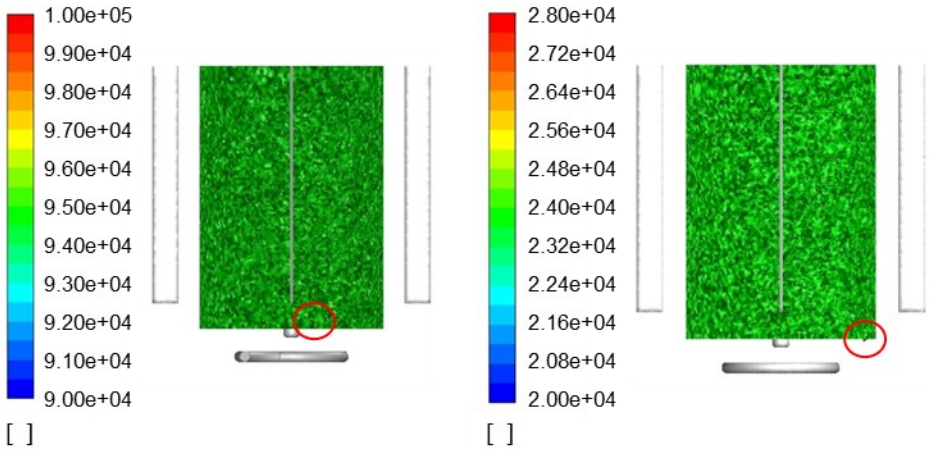

Figure M.5. Identification of cells with turbulent viscosity ratio above 10^5. Images were obtained from the simulation of the batch abiotic system with PEG Sol B.

Table M.4 shows the averaged torque, calculated from the last impeller turn, simulated with second-order methods, for each abiotic system. For the systems with water and PEG Sol B, the simulated averaged torques, obtained with the enhanced wall treatment, match satisfactorily the experimental averaged torques. The laminar model for PEG Sol A reasonably predicted the averaged torque as well.

Table M.4. Validation of the preliminary CFD models, using second-order discretization methods, against experimental torque data. Simulated torque is given as $T_{AVG_{sim}} \pm T_{SD_{sim}}$, in units of [N·m], and $|E|$ in units of [%].

Fluid	**Turbulence Model**	**Torque**	$\boldsymbol{\lvert E \rvert}$
Water	Standard k-epsilon	0.1005 ± 0.00004	1.3%
PEG Sol B	Standard k-epsilon	0.1231 ± 0.00004	4.5%
PEG Sol A	Laminar	0.1268 ± 0.00109	7.0%

Appendix N. GeomA & GeomB Coarse Grid Settings

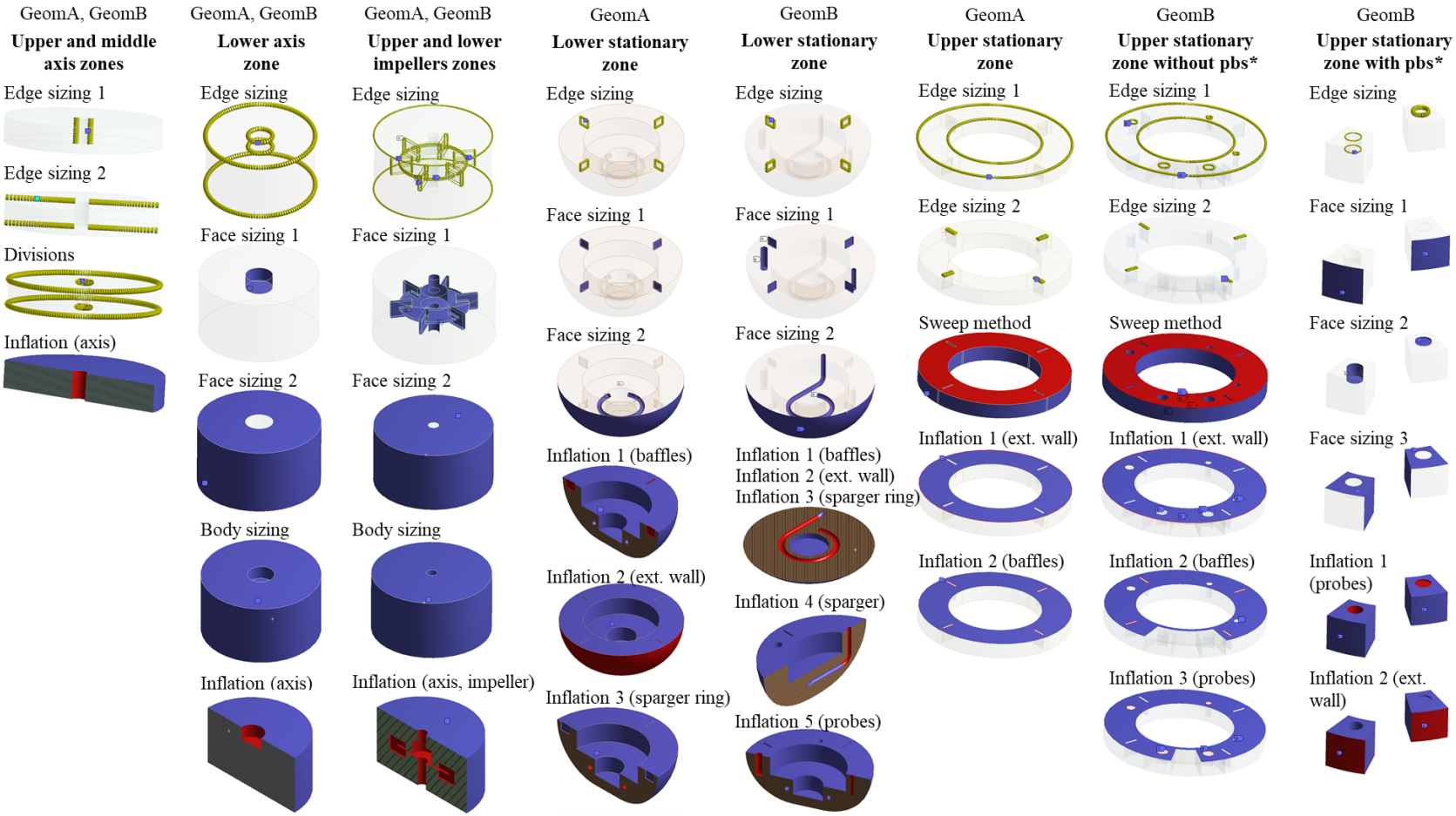

Figure N.1. Sizing methods and inflation layers used to mesh and refine the grid of specific bodies of GeomA and GeomB (pbs*, probes bottom section). Figure from Sadino-Riquelme et al. (2021), reprinted with permission of John Wiley and Sons.

Table N.1. Methods and sizes used for the coarse grid's local refinement of GeomA and GeomB. Table from Sadino-Riquelme et al. (2021), reprinted with permission of John Wiley and Sons.

Body	Feature	Size [mm]
Upper and middle axis zones (GeomA, GeomB)	Edge sizing 1	1.5
	Edge sizing 2	1
	Divisions	100 (-)
	Inflation (Pre)	2
Lower axis zone (GeomA, GeomB)	Edge sizing	1
	Face sizing 1	1.8
	Face sizing 2	1.8
	Body sizing	1.8
	Inflation (Pre)	2
Upper and lower impeller zones (GeomA, GeomB)	Edge sizing	1
	Face sizing 1	1.8
	Face sizing 2	1.8
	Body sizing	1.8
	Inflation	2
Lower stationary zone (GeomA)	Edge sizing	1
	Face sizing 1	1.5
	Face sizing 2	2
	Inflation 1 (Pre)	2
	Inflation 2 (Post)	3
	Inflation 3 (Post)	3
Upper stationary zones (GeomA)	Edge sizing 1	1
	Edge sizing 2	1
	Sweep method	1.5
	Inflation 1 (Pre)	3
	Inflation 2 (Pre)	2
Lower stationary zone (GeomB)	Edge sizing	1
	Face sizing 1	1.5
	Face sizing 2	2
	Inflation 1 (Pre)	2
	Inflation 2 (Post)	3
	Inflation 3 (Post)	3
	Inflation 4 (Post)	2
	Inflation 5 (Pre)	2
Upper stationary zones without probes bottom section (GeomB)	Edge sizing 1	1
	Edge sizing 2	1
	Sweep method	1.5
	Inflation 1 (Pre)	3
	Inflation 2 (Pre)	2
	Inflation 3 (Pre)	2
Upper stationary zones with probes bottom section (GeomB)	Edge sizing	1
	Face sizing 1	2
	Face sizing 2	1.5
	Face sizing 3	1.8
	Inflation 1 (Pre)	2
	Inflation 2 (Pre)	3

Appendix O. CFD Single-Phase Governing Equations

Water. The CFD models of the batch abiotic system with water and without aeration are governed by conservation equations that describe a three-dimensional, single-phase, transient system, with turbulent flow. The conservation of mass and momentum, for a laminar flow, in an inertial reference frame is described given by Equation O.1 and O.2, respectively.

$$\frac{\partial \rho}{\partial t} + \nabla \cdot (\rho \vec{v}) = 0 \tag{O.1}$$

$$\frac{\partial}{\partial t}(\rho \vec{v}) + \nabla \cdot (\rho \vec{v}\vec{v}) = -\nabla p + \nabla \cdot (\bar{\bar{\tau}}) + \rho \vec{g} + \vec{F} \tag{O.2}$$

$$\bar{\bar{\tau}} = \eta \left[(\nabla \vec{v} + \nabla \vec{v}^{t}) - \frac{2}{3} \nabla \cdot \vec{v} \bar{\bar{I}} \right] \tag{O.3}$$

where ρ is the fluid density, t is the fluid flow time, $\vec{v}$ is the fluid velocity vector, p is the static pressure, $\vec{g}$ is the gravity acceleration, and $\vec{F}$ represents external body forces. The stress tensor, $(\bar{\bar{\tau}})$, is given by Equation O.3, where $\bar{\bar{I}}$ is the unit tensor.

Two turbulence models for RANS equation closure were compared, the standard k-epsilon model and the SST k-omega model. The standard k-epsilon model uses Equation O.4 and O.5 to describe, respectively, the turbulence kinetic energy (k) and the rate of dissipation (ε).

$$\frac{\partial}{\partial t}(\rho k) + \frac{\partial}{\partial x_i}(\rho k v_i) = \frac{\partial}{\partial x_j}\left[\left(\eta + \frac{\eta_t}{\sigma_k} \right) \frac{\partial k}{\partial x_j} \right] + G_k - \rho \varepsilon \tag{O.4}$$

$$\frac{\partial}{\partial t}(\rho \varepsilon) + \frac{\partial}{\partial x_i}(\rho \varepsilon v_i) = \frac{\partial}{\partial x_j}\left[\left(\eta + \frac{\eta_t}{\sigma_\varepsilon} \right) \frac{\partial \varepsilon}{\partial x_j} \right] + C_{1\varepsilon} \frac{\varepsilon}{k} G_k - C_{2\varepsilon} \rho \frac{\varepsilon^2}{k} \tag{O.5}$$

$$\eta_t = \rho C_\eta \frac{k^2}{\varepsilon} \tag{O.6}$$

where G_k is the generation of turbulence kinetic energy due to the mean velocity gradients and η_t is the turbulent viscosity, which is given by Equation O.6. The constants $C_{1\varepsilon}$, $C_{2\varepsilon}$, C_η, σ_k and σ_ε have default values: 1.44, 1.92, 0.09, 1.0 and 1.3, respectively.

The SST k-omega model uses Equation O.7 and Equation O.8 to describe the turbulence kinetic energy and the specific dissipation rate (ω).

$$\frac{\partial}{\partial t}(\rho k) + \frac{\partial}{\partial x_i}(\rho k v_i) = \frac{\partial}{\partial x_j}\left[\left(\eta + \frac{\eta_t}{\sigma_k}\right)\frac{\partial k}{\partial x_j}\right] + G_k - Y_k \quad \text{(O.7)}$$

$$\frac{\partial}{\partial t}(\rho \omega) + \frac{\partial}{\partial x_i}(\rho \omega v_i) = \frac{\partial}{\partial x_j}\left[\left(\eta + \frac{\eta_t}{\sigma_\omega}\right)\frac{\partial \omega}{\partial x_j}\right] + G_\omega - Y_\omega + D_\omega \quad \text{(O.8)}$$

$$\eta_t = \rho \frac{k}{\omega} \frac{1}{max\left[\frac{1}{\alpha^*}, \frac{S_R F_2}{a_1 \omega}\right]} \quad \text{(O.9)}$$

where G_k and G_ω are the generation of k and ω, respectively; while Y_k and Y_ω are the dissipation of k and ω, respectively. D_ω is the cross-diffusion term. Equation O.9 gives the turbulent viscosity, for which α^*, S_R, F_2 and a_1 can be estimated (Ansys, 2009).

For the standard k-epsilon turbulence model, a near-wall treatment must be selected based on the non-dimensional distance (Y^+) at the wall, defined by Equation O.10.

$$Y^+ \equiv \frac{\rho v^* y}{\eta} \quad \text{(O.10)}$$

where v^* is the friction velocity and y is the dimensional distance from the wall. Available wall treatments are standard wall functions ($30 < Y^+ < 300$) and enhanced wall treatment ($Y^+ < 5$).

To simulate the impeller rotation, the SM method was applied, which uses rotating reference frames. Thus, all the conservation equations need modifications to include the grid motion (Ansys, 2009).

Non-Newtonian fluids. For the CFD model of the batch abiotic systems with non-Newtonian fluids within the transitional flow regime, the k-kl-omega transition model was evaluated. This model uses Equation O.11 to O-13 to estimate, respectively, the turbulence kinetic energy, the laminar kinetic energy (k_L) and the specific dissipation rate (Furst, 2013).

$$\frac{D}{Dt}(\rho k) = \rho(P_k + R + R_{NAT} - \omega k - D_T) + \frac{\partial}{\partial x_j}\left[\left(\eta + \frac{\rho \alpha_T}{\sigma_k}\right)\frac{\partial k}{\partial x_j}\right] \quad \text{(O.11)}$$

$$\frac{D}{Dt}(\rho k_L) = \rho(P_{k_L} - R - R_{NAT} - D_L) + \frac{\partial}{\partial x_j}\left[\eta \frac{\partial k_L}{\partial x_j}\right] \tag{O.12}$$

$$\frac{D}{Dt}(\rho\omega) = \rho\left[C_{\omega 1}\frac{\omega}{k}P_k + \left(\frac{C_{\omega R}}{f_W} - 1\right)\frac{\omega}{k}(R + R_{NAT}) - C_{\omega 2}\omega^2 + C_{\omega 3} f_\omega \alpha_T f_W^2 \frac{\sqrt{k}}{y^3}\right] + \frac{\partial}{\partial x_j}\left[\left(\eta + \frac{\rho\alpha_T}{\sigma_\omega}\right)\frac{\partial\omega}{\partial x_j}\right] \tag{O.13}$$

where P_k and P_{k_L} are the production of turbulent and laminar kinetic energy, respectively; R and R_{NAT} are related to the laminar-turbulent transition of energy from k to k_L; and D_T and D_L correspond to the anisotropic dissipation rate. f_W and f_ω are damping functions, and α_T the turbulent diffusivity. The constants $C_{\omega 1}$, $C_{\omega 2}$, $C_{\omega 3}$, $C_{\omega R}$, σ_k and σ_ω have default values (Furst, 2013).

However, to initialize the simulations, the standard k-omega model was used. This model uses the same transport equations as the SST k-omega model, except that it does not include the cross-diffusion term for ω and the turbulent viscosity is estimated by Equation O.14 (Ansys, 2009).

$$\eta_t = \alpha^* \frac{\rho k}{\omega} \tag{O.14}$$

Appendix P. GeomA & GeomB Grid Quality

Table P.1. Quality indices of the grids used for GeomA and GeomB. Table from Sadino-Riquelme et al. (2021), reprinted with permission of John Wiley and Sons.

GEOMETRY	**GeomA**			**GeomB**		
MESH	**Coarse**	**Medium**	**Fine**	**Coarse**	**Medium**	**Fine**
Nodes	2,615,336	3,365,649	4,401,802	2,843,027	3,646,519	4,726,656
Elements (cells)	5,321,110	7,063,334	9,495,590	5,641,625	7,454,307	9,930,614
Skewness						
Minimum	9.4e-005	2.1e-004	8.6e-005	9.4e-005	3.0e-004	2.1e-004
Maximum	0.85	0.84	0.86	0.86	0.83	0.86
Average	0.20	0.20	0.20	0.20	0.19	0.19
Standard Dev.	0.16	0.16	0.15	0.16	0.16	0.15
Orthogonal quality						
Minimum	1.6e-002	1.8e-002	1.9e-002	1.6e-002	1.8e-002	1.9e-002
Maximum	1	1	1	1	1	1
Average	0.80	0.80	0.80	0.80	0.81	0.81
Standard Dev.	0.18	0.18	1.7	0.18	0.17	0.17
Aspect Ratio						
Minimum	1.16	1.16	1.17	1.16	1.17	1.16
Maximum	726	713	832	726	713	832
Average	8.69	8.21	7.63	9.15	8.67	8.10
Standard Dev.	15.3	15.0	14.1	15.4	15.2	14.4

Appendix Q. Additional Results Step 2

Table Q.1. Range of Y^+ next to the walls, obtained as instantaneous values, after the simulation of 58 impeller turns, for the batch abiotic systems with non-Newtonian fluids. Y^+ is given in units of [ ].

Walls	**XSolA-kklω**	**XSolB-kklω**	**XSolB-SSTkω**
Exterior walls	0.003 – 1.38	0.023 – 2.1	0.013 – 3.0
Impeller and axis	0.005 – 5.81	0.018 – 6.8	0.016 – 6.5
Baffles	0.003 – 0.634	0.015 – 1.1	0.009 – 1.9
Probes	0.001 – 1.69	0.006 – 2.9	0.010 – 2.4
Sparger	0.001 – 1.79	0.016 – 2.7	0.008 – 3.2

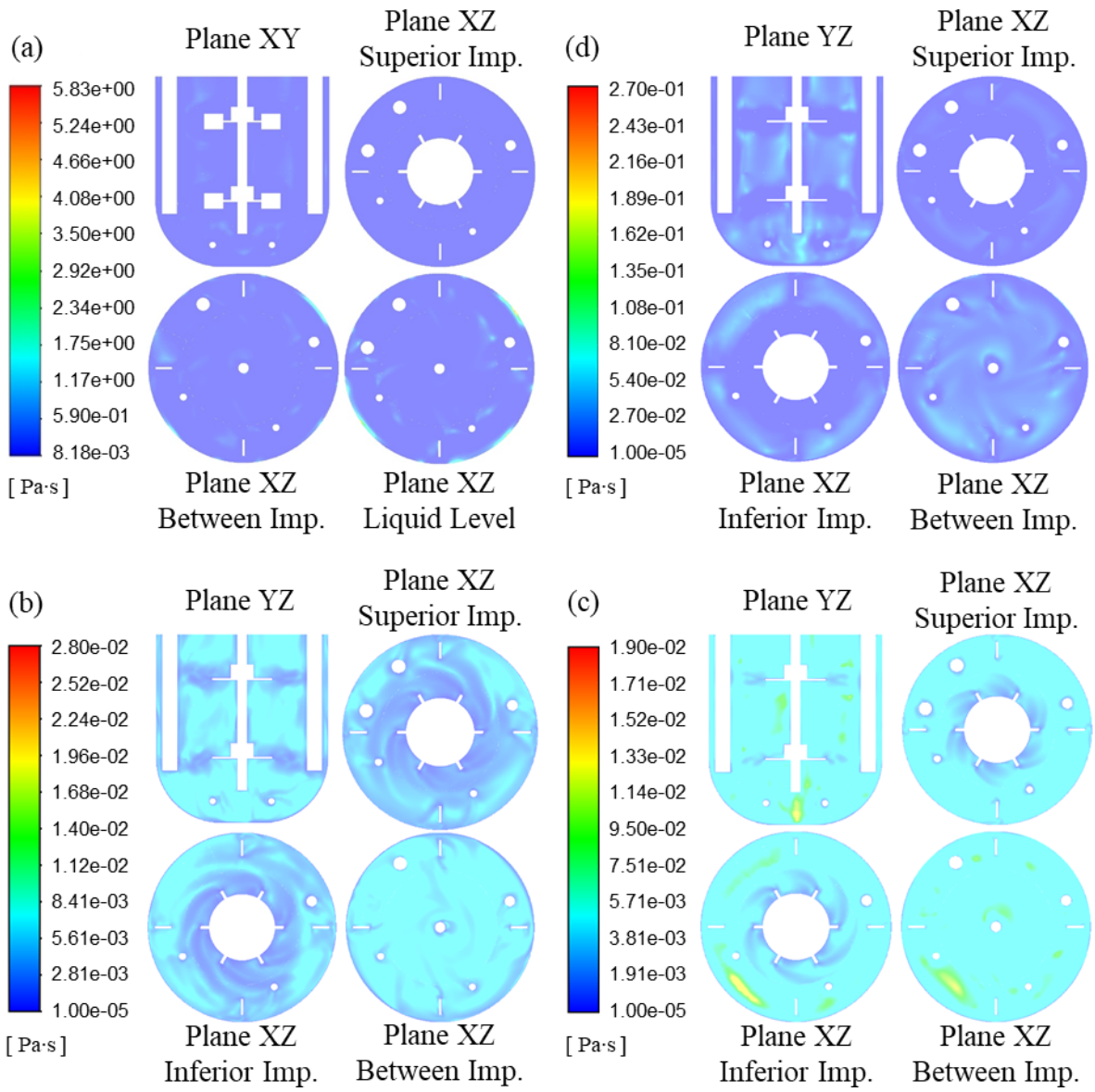

Figure Q.1. Contours of instantaneous viscosity, computed after 58 impeller turns, for the batch abiotic systems (a) Xanthan Sol C, (b) XSolB-SSTkω, (c) XSolB-kklω, and (d) XSolA-kklω.

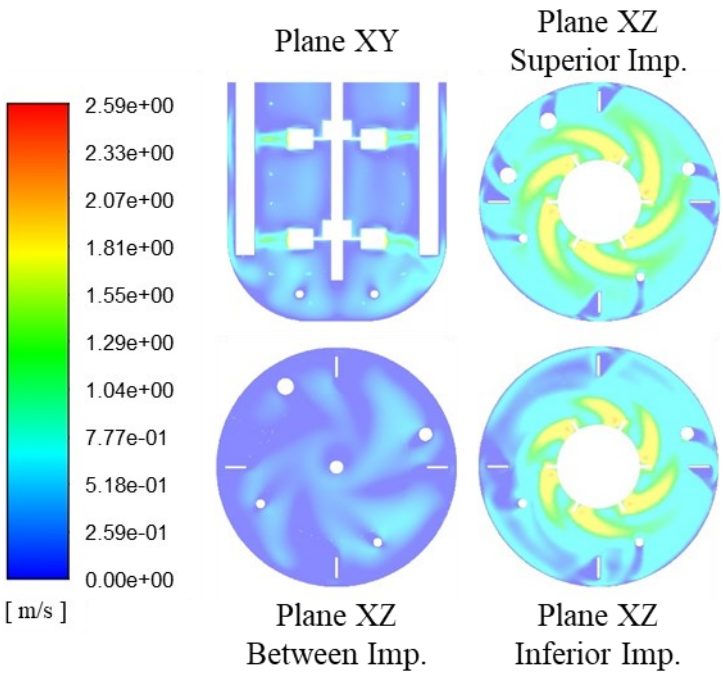

Figure Q.2. Contours of instantaneous velocity magnitude, computed after 58 impeller turns, for Xanthan Sol C.

Appendix R. Preliminary Simulations Step 3

***Geometry and mesh*.** The preliminary CFD domain and mesh, described in Appendix M, were used. Importantly, the sparger ring has four holes equally sized (1 mm diameter).

***Model settings*.** To simulate the mixing with aeration, a multi-phase model was adapted for the batch abiotic systems with water, PEG Sol A and PEG Sol B, in the software ANSYS Fluent version 18.2. The multi-phase Eulerian model with implicit volume fraction parameters formulation was applied. Two phases were defined for each abiotic system, the liquid fluid (primary phase) and air (secondary phase). The properties of the fluids were set up according to Table 3.1. The air bubble diameter was set based on experimental data from Table 3.6. As interphase interaction, only the drag force was included, using the universal drag model. This model requires the surface tension, which was estimated from literature for each abiotic system (see Table R.1). The ia-particle model was set for the calculation of the interfacial area. Under operating conditions, the air density was specified as operating density and the reference pressure was set as 1 atm at the liquid level.

Table R.1. Surface tension values used for the modelling of the aerated batch abiotic systems, with Newtonian fluids, in units of [mN/m].

Fluid	Surface Tension	Reference
Water	71	Engineering ToolBox (2004)
PEG Sol B	57	Amooey and Fazlollahnejad (2014)
PEG Sol A	51	Amooey and Fazlollahnejad (2014)

The sliding mesh approach was used, with a rotating velocity of 400 rpm for each moving zone. The gravity force was included as a body force in the negative Y-direction. The per-phase standard k-epsilon turbulence model was set, with standard wall functions. An additional simulation was developed for PEG Sol A, using the laminar model. The boundary conditions were as follows: for the top wall, degassing; for the impellers and axis walls, 0

rpm as relative velocity with respect to the moving zones; velocity inlet at the sparger holes (see Table R.2); and no-slip condition for the other walls. As initial condition, the velocity in every direction was set to 0 m/s, the turbulence parameters values were set to 0.1, and the volume fraction of air was defined as 0.

Table R.2. Characteristics of the velocity inlet boundary condition set at the sparger holes.

Water's velocity inlet	0 m/s
Air's velocity inlet	21.15 m/s (upwards)
Turbulent intensity	5%
Hydraulic diameter	0.001 m
Air's volume fraction	1

To solve the equations, the phase coupled SIMPLE pressure-velocity coupling scheme with the absolute velocity formulation was chosen. The following discretization methods were set: least-squares cell-based for gradient; modified HRIC for volume fraction; first-order upwind for momentum, turbulent kinetic energy, and turbulent dissipation; and first-order implicit for the transient formulation. The warped-face gradient correction was activated, and some under-relaxation factors were modified from its default value (density 0.7; body forces 0.7; volume fraction 0.2; turbulent viscosity 0.8). The simulations were solved using double precision, with a time step size of 0.0004 s and 50 iterations per time step.

For each simulation, the velocity magnitude at different points and the impeller torque were registered after every time step. The monitoring points were placed over the vertical plane shown in Figure 4.4. Also, the airflow through the liquid level was monitored. Furthermore, the residual values were tracked, along with any alert of cells with turbulent viscosity ratio exceeding the maximum allowed value (10^5). At the end of each time step, residuals values below 10^{-5} were expected.

Simulation results. All the simulations with the k-epsilon model presented numerical issues, showing an alert for turbulent viscosity ratio above 10^5. In particular, the simulation for PEG Sol A, using the turbulence model, diverged. For the batch abiotic systems with water and PEG Sol B, were simulated, respectively, 25 and 20 impeller turns. None of these simulations got all residuals values below 10^{-5}. Overall, the residuals of the continuity and volume fraction equations reached values as low as $3 \cdot 10^{-3}$ and $2 \cdot 10^{-5}$, respectively; while the residuals for the air's momentum equations decreased to around $4 \cdot 10^{-4}$. The numerical issues significantly affected the output variables, which is clearly reflected in the torque evolution of each case (see Figure R.1).

The analysis of the Y^+ values next to the walls suggests that the enhanced wall treatment should be applied, for the cases with water and PEG Sol B. However, due to the numerical issues, these results are not reliable.

The simulation of PEG Sol A, with the laminar model, showed a poor convergence after the simulation of 25 impeller turns. Especially for the continuity equation, whose residual decreased only to 10^{-5}. As well as for the other cases, the numerical error is apparent in the torque curve (see Figure R.1).

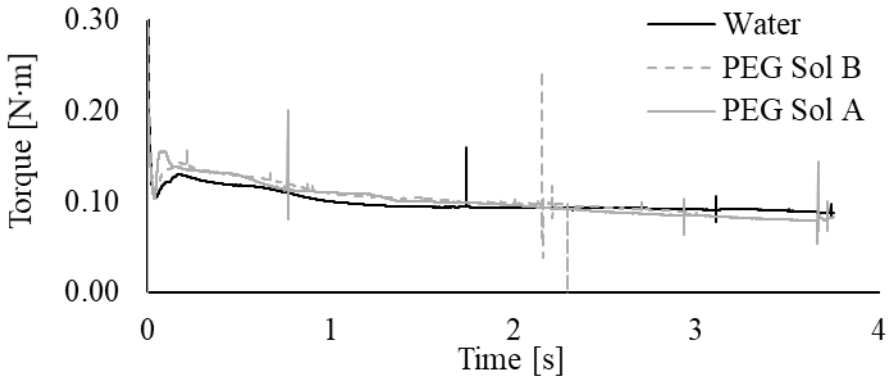

Figure R.1. Impeller torque evolution simulated with the preliminary CFD models of the batch abiotic systems with Newtonian fluids, under aerated conditions, using first-order discretization methods.

For each abiotic system, the averaged torque was calculated over the data of the last simulated impeller turn (see Table R.3.). The match between the experimental and simulated

torque values is not as good as for the preliminary simulations without aeration (see Appendix M). However, for all the cases, a better agreement would be out of explanation due to the numerical issues already identified.

Table R.3. Validation of the preliminary CFD models, with aeration, using first-order discretization methods, against experimental torque data. Simulated torque is given as $T_{AVG_{sim}} \pm T_{SD_{sim}}$, in units of [N·m], and $|E|$ in units of [%].

Fluid	**Turbulence model**	**Torque**	$\|E\|$
Water	Standard k-epsilon	0.0879 ± 0.0007	17%
PEG Sol B	Standard k-epsilon	0.0888 ± 0.0005	10%
PEG Sol A	Laminar	0.0805 ± 0.0048	3.0%

It is interesting to highlight that, although the numerical issues, the simulations were able to capture the phenomena of air cavities formation behind the blades, as illustrated in Figure R.2 for the batch abiotic system with Water. Furthermore, the effect of these cavities is perceptible on the averaged torque values, as they are lower than in the simulations without aeration. This confirms that the torque is a sensitive parameter, in the experiments as well as in the CFD simulations, able to capture the effects of fluid rheology along with the aeration. Therefore, it can be used for validation purposes.

Due to the several numerical issues, it was not possible to change the discretization methods to second-order neither modify the near-wall treatment. Also, it was not possible to implement additional interphase interactions as turbulent dispersion and turbulence interaction, which are necessary for an accurate multi-phase CFD modelling of the mixing and aerated systems.

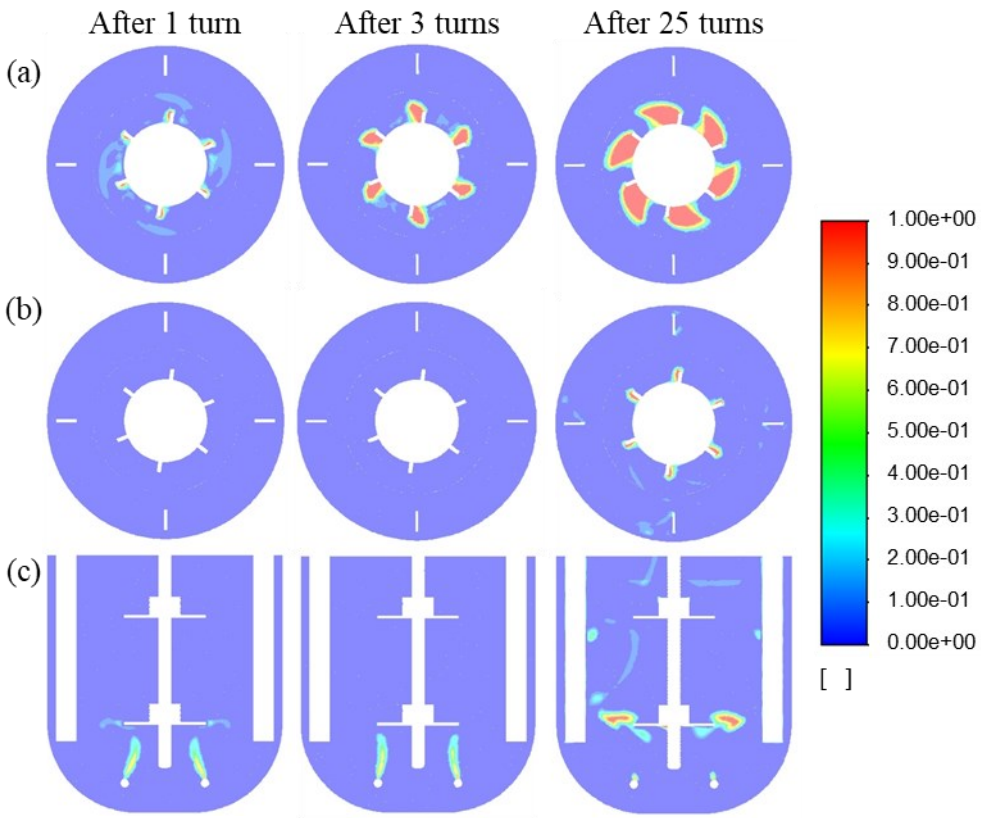

Figure R.2. Temporal evolution of the instantaneous contours of volume fraction of air, simulated for the batch abiotic system with water, with aeration. Planes XZ across the (a) lower and (b) upper impeller, and (c) plane XY across the middle of the tank.

Appendix S. GeomC Grid Settings and Quality

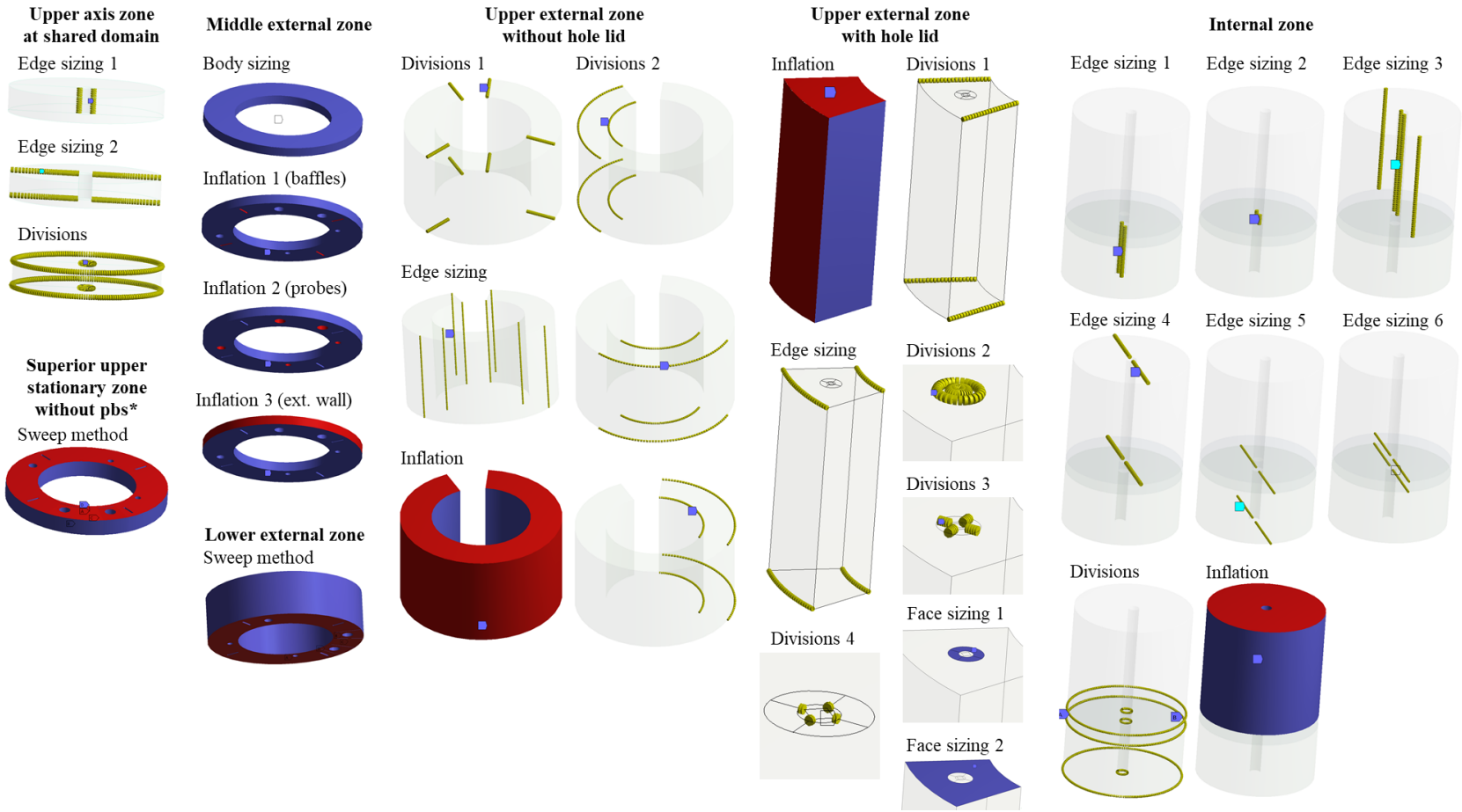

Figure S.1. Sizing methods and inflation layers used to mesh and refine the grid of specific bodies of GeomC. This figure only details the settings that differ from the grid of GeomB (pbs*, probes bottom section).

Table S.1. Methods and sizes used for the grid local refinement of the domain GeomC. This table only details the settings that differ from the grid of GeomB.

Body	Feature	Size [mm]
Upper axis zone	Edge sizing 1	1.3
	Edge sizing 2	1
	Divisions	100 (-)
	Inflation (Pre)	None
Superior upper stationary zones without probes bottom section	Edge sizing 1	1
	Edge sizing 2	1
	Sweep method	1.3
	Inflation 1 (Pre)	3
	Inflation 2 (Pre)	2
	Inflation 3 (Pre)	2
Middle external zone	Body sizing	1.8
	Inflation 1 (Pre)	2
	Inflation 2 (Pre)	2
	Inflation 3 (Pre)	3
Upper external zone without hole lid	Divisions 1	20
	Divisions 2	52
	Edge sizing	1.7
	Inflation (Pre)	3
Lower external zone	Sweep method	1.3
Upper external zone with lid hole	Divisions 1	20
	Divisions 2	7
	Divisions 3	5
	Divisions 4	2
	Edge sizing	1.7
	Face sizing 1	1.0
	Face sizing 2	1.7
	Inflation (Pre)	3
Internal zone	Edge sizing 1	1.3
	Edge sizing 2	1.5
	Edge sizing 3	2
	Edge sizing 4	1.5
	Edge sizing 5	1
	Edge sizing 6	1.25
	Divisions	100
	Inflation (Pre)	3

Table S.2. Quality indices of the grid used for GeomC.

Index Value	**Skewness**	**Orthogonal quality**	**Aspect ratio**
Minimum	9.4e-005	1.6e-002	1.16
Maximum	0.86	1	815
Average	0.17	0.84	8.5
Standard Dev.	0.16	0.17	14.3

Appendix T. CFD Multi-Phase Governing Equations

The CFD models, adapted to study the effect of the aeration on the fluid dynamics of a stirred bioreactor, are governed by conservation equations that describe a three-dimensional, multi-phase, and transient system. Two multi-phase models were evaluated for that purpose, the Eulerian model and the mixture model, which are described next, assuming a system with two phases without mass transfer between them.

Eulerian model. This approach models the multi-phase system as interacting separated phases. Therefore, the momentum and continuity equations are computed for each phase, but a single pressure is solved for the system. The conservation equations for phase i are described by Equation T.1 and Equation T.2 (Ansys, 2009).

$$\frac{\partial(\varphi_i \rho_i)}{\partial t} + \nabla \cdot (\varphi_i \rho_i \vec{v}_i) = 0 \tag{T.1}$$

$$\frac{\partial}{\partial t}(\varphi_i \rho_i \vec{v}_i) + \nabla \cdot (\varphi_i \rho_i \vec{v}_i \vec{v}_i) = -\varphi_i \nabla p + \nabla \cdot (\bar{\bar{\tau}}_i) + \varphi_i \rho_i \vec{g} + \sum_{j=1}^{2} \vec{R}_{ij} + \vec{F}_i \tag{T.2}$$

$$\bar{\bar{\tau}}_i = \varphi_i \eta_i (\nabla \vec{v}_i + \nabla \vec{v}_i^t) - \varphi_i \left(\kappa_i - \frac{2}{3}\eta_i\right) \nabla \cdot \vec{v}_i \bar{\bar{I}} \tag{T.3}$$

where φ_i is the volume fraction of the phase i, and $\vec{R}_{ij}$ represents the interaction force between the phases i and j. The stress tensor of phase i ($\bar{\bar{\tau}}_i$) is given by Equation T.3, where κ_i is its bulk viscosity. Furthermore, the volume fractions must comply with Equation T.4. Thus, the volume (Ω) occupied by phase i is defined by Equation T.5.

$$\sum_{i=1}^{2} \varphi_i = 1 \tag{T.4}$$

$$\Omega_i = \int_{\Omega} \varphi_i d\Omega \tag{T.5}$$

Additionally, based on the configuration chosen for this thesis, the equations of the turbulence model were applied to each phase. Turbulence model equations are given in Appendix O.

Mixture model. This approach models the multi-phase system by computing the continuity and momentum equations for the mixture, as given by Equation T.6 and T.7, respectively; and solving the volume fraction of the secondary phase, using Equation T.8, The volume fraction of the primary phase is obtained applying Equation T.4 (Ansys, 2009).

$$\frac{\partial(\rho_m)}{\partial t} + \nabla \cdot (\rho_m \vec{v}_m) = 0 \tag{T.6}$$

$$\frac{\partial}{\partial t}(\rho_m \vec{v}_m) + \nabla \cdot (\rho_m \vec{v}_m \vec{v}_m) = -\nabla p + \nabla \cdot [\eta_m (\nabla \vec{v}_m + \nabla \vec{v}_m^t)] + \rho_m \vec{g} + \vec{F} \tag{T.7}$$

$$\frac{\partial(\varphi_2 \rho_2)}{\partial t} + \nabla \cdot (\varphi_2 \rho_2 \vec{v}_2) = 0 \tag{T.8}$$

where ρ_m, $\vec{v}_m$ and η_m correspond to the density, velocity, and viscosity of the mixture, respectively; and ρ_2, $\vec{v}_2$ and φ_2 are the density, velocity, and volume fraction of the secondary phase, respectively. ρ_m, $\vec{v}_m$ and η_m are estimated using Equation T.9 to T.11.

$$\rho_m = \sum_{i=1}^{2} \varphi_i \rho_i \tag{T.9}$$

$$\vec{v}_m = \frac{\sum_{i=1}^{2} \varphi_i \rho_i \vec{v}_i}{\rho_m} \tag{T.10}$$

$$\eta_m = \sum_{i=1}^{2} \varphi_i \eta_i \tag{T.11}$$

Additionally, algebraic expression can be used to calculate relative velocities between the phases. However, for this work, it was assumed that the phases move at the same velocity.

Appendix U. Additional Results Step 3

Table U.1. Range of Y^+ next to the walls, obtained as instantaneous values, after the last impeller turn simulated with the multi-phase CFD models of the batch abiotic system with water without aeration. Y^+ is given in units of [ ].

Walls	**GeomB-EM-kε**	**GeomB-EM-SSTkω**	**GeomC-MM-SSTkω**
Exterior walls	0.059 – 2.5	0.060 – 2.2	0.002 – 2.6
Impeller and axis	0.010 – 5.5	0.072 – 6.1	0.005 – 8.5
Baffles	0.050 – 1.4	0.052 – 1.4	0.004 – 1.4
Probes	0.055 – 1.1	0.036 – 5.6	0.004 – 3.1
Sparger	0.123 – 2.6	0.131 – 2.5	0.003 – 2.1

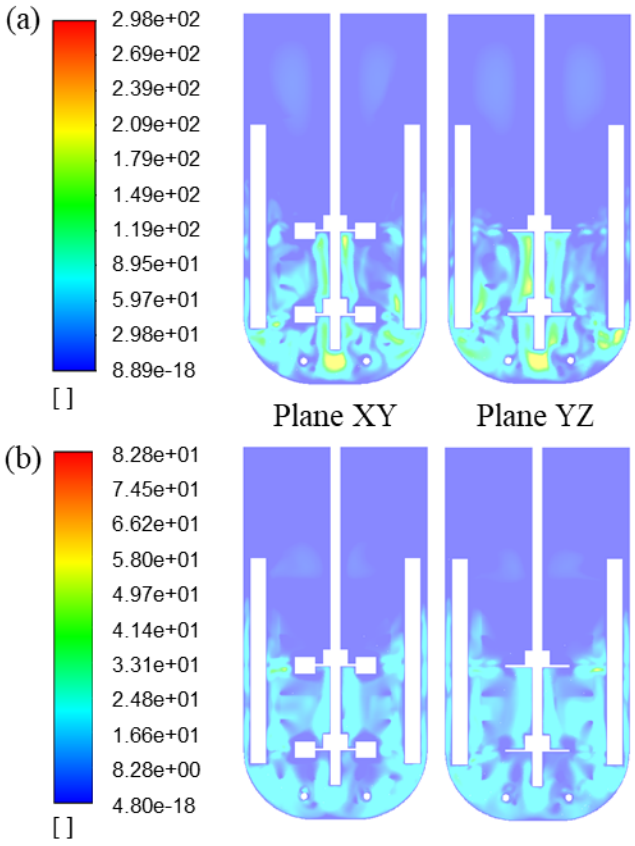

Figure U.1. Instantaneous contours of turbulent viscosity ratio of the mixture, computed with GeomC-MM-SSTkω, for the batch abiotic system with water, (a) without aeration and (b) with aeration.

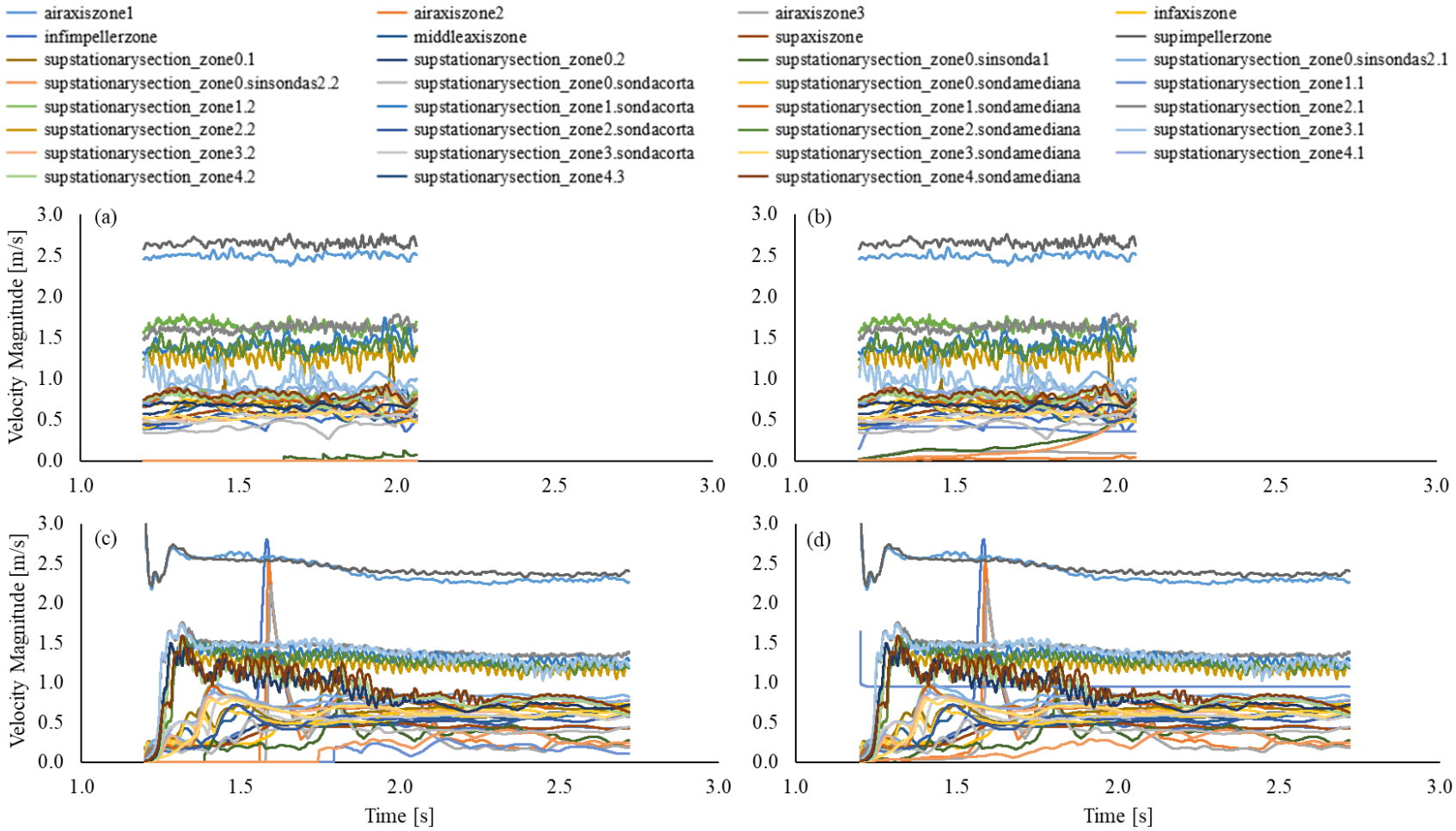

Figure U.2. Temporal evolution of the maximum velocity of (a, c) water and (b, d) air, at different bodies of GeomC. Results computed with GeomC-MM-SSTkω, under (a, b) unaerated and (c, d) aerated conditions. The velocity at the body enclosing the sparger holes was not included in the plots of the simulation with aeration.

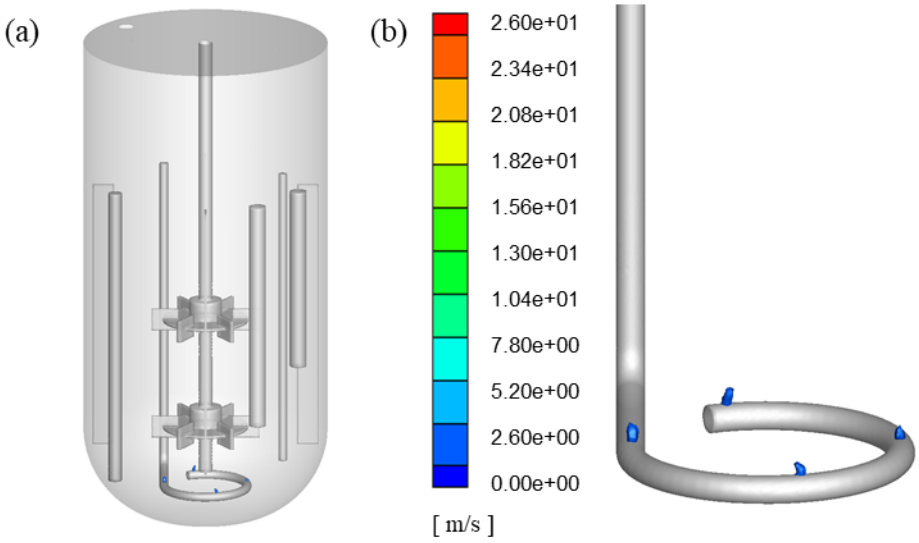

Figure U.3. Instantaneous iso-surface of upward velocity equal to 1 m/s, computed with GeomC-MM-SSTkω, under aerated conditions. View of the (a) entire tank and (b) zoom on the sparger ring.